SEARCH FOR SCALAR TOP QUARK AND SCALAR BOTTOM QUARK IN $p\bar{p}$ COLLISIONS AT $\sqrt{S} = 1.8$ TEV

Christopher Matthew Holck
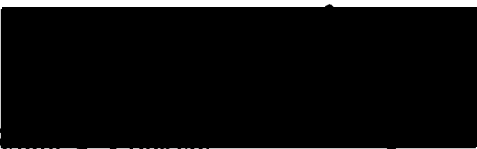
A DISSERTATION

in

PHYSICS AND ASTRONOMY

Presented to the Faculties of the University of Pennsylvania in Partial Fulfillment of the Requirements for the Degree of Doctor of Philosophy

1999

H. H. Williams

Supervisor of Dissertation

Nigel S. Lockyer

Graduate Group Chairperson

UMI

COPYRIGHT

Christopher Matthew Holck

1999

DEDICATION

██

███████████████████████████████

iii

ACKNOWLEDGEMENTS

The journey to my Ph.D. has been long and arduous. From applying to graduate school to passing the qualifying exam to completing this analysis, there were many times where I was not sure I would complete this journey. There have been many people who have helped me overcome these rough patches. The following words are only a shadow of the gratitude I feel towards them.

I would like to thank my advisor Brig Williams for taking a chance on me. He gave me the freedom to pursue this analysis as well as other less sucessful analyses. I appreciate his encouragement when I succeeded and his guidance when I faltered. I will forever be in his debt.

Special thanks go to Regina Demina of Fermilab, Andrei Nomerotski of the University of Florida and Wasiq Bokhari of the University of Pennsylvania. Without their assistance and advice, I would not have been able to complete this analysis.

I would like to thank all the members of the exotics group at CDF who have provided many useful comments and suggestions. I especially thank Maria Spiropulu of Harvard for providing the **FILT2** data sample. Thanks to the rest of the CDF collaboration and to the Fermilab staff. Their hard work and dedication make an experiment of this size possible.

I want to thank the following people who are (or were) at Penn for their friendship, their help and for making my stay at both Fermilab and Penn tolerable: Gary Houk, Guillaume Unal, Rick Wilkinson, Owen Long, Steve Hahn, Scott Metzler, Farrukh Azfar.

Despite what it felt like, not all of my time was spent working. I would like to thank my ex-roommates Pat Brady and William Angerer. I consider their friendship

priceless. Thanks go to my officemate and good friend Brendan Bevensee for tolerating my endless complaining. Thanks go to the entire Champion's crowd: Scott, Pat, Purdue. Ari, Sean, Tom, Hugh (and anyone else I forgot).

v

ABSTRACT

SEARCH FOR SCALAR TOP QUARK AND SCALAR BOTTOM QUARK IN $p\bar{p}$

COLLISIONS AT $\sqrt{S} = 1.8$ TEV

Christopher Matthew Holck

H. H. Williams

We present the results of a search for direct pair production of scalar top (or scalar bottom) quarks followed by the decay of scalar top (or scalar bottom) quark to a charm quark (or bottom quark) and a neutralino using 88 pb^{-1} of data from $p\bar{p}$ collisions at $\sqrt{s} = 1.8$ TeV. The experimental signature is two charm (or two bottom) jets plus significant missing energy. The number of events which pass all our selection criteria is consistent with our expectations from Standard Model processes. We observe 11(5) events in the scalar top (scalar bottom) analysis and expect 14.5 ± 4.2(5.8 ± 1.8). We use a next–to–leading order scalar quark cross section calculation to excluded points, at the 95% C.L., as a function of the scalar top mass (or scalar bottom mass) and the neutralino mass.

Contents

List of Figures

List of Tables

Chapter 1

Introduction

The 20th century has been witness to a tremendous amount of progress in our understanding of the fundamental constituents of nature. From Rutherford's scattering experiments [1] to the discovery of the positron [2] to the discovery of the W/Z bsosons at CERN [3–6] to the discovery of the top quark at Fermilab [7, 8], experimental physicists have made tremendous strides to discover and catalogue the different fundamental particles. At the same time, theorists such as Richard Feynmann, Steven Weinberg, Abdus Salam, and Sheldon Glashow have provided us with the models to understand these particles and how they interact with one another. Physicists have given this theoretical framework an unassuming name: the *Standard Model* (SM). In this chapter, we will give a brief introduction to the Standard Model (see [9–11] for more detailed discussions) and list some of its shortcomings.

1.1 Standard Model

The Standard Model consists of three of the four known forces: the electromagnetic force, the weak force, and the strong nuclear force. An accurate quantum field theory of gravity does not yet exist. Electromagnetism is the most familiar of these forces. It is responsible for the chemical bonds between atoms and molecules. The strong

1

Particle name	Particle symbol	Rest Mass (GeV/c^2)	Electric charge
Electron	e^-	5.11×10^{-6}	-1
Electron neutrino	ν_e	$< 1.5 \times 10^{-8}$	0
Muon	μ^-	106.6×10^{-3}	-1
Muon neutrino	ν_μ	$< 1.7 \times 10^{-4}$	0
Tau	τ^-	1.784	-1
Tau neutrino	ν_τ	$< 1.8 \times 10^{-2}$	0

Table 1.1: Properties of the three generations of leptons.

force binds protons and neutrons together to form stable nuclei. The weak force is responsible for β–decay (e.g. $n \to pe\nu_e$) and for the nuclear fusion processes that power stars.

Matter particles are point-like objects which carry a total spin of $1/2\hbar$[1]. Particles with half–integral spin are called *fermions*. The spin–1/2 fermions are divided into *leptons* and *quarks*. The force between any 2 fermions is mediated by the *exchange* of spin–1 particles called *gauge bosons*. The term *boson* refers to a particle with integral spin.

Leptons are grouped into 3 *generations* or *families*. Each generation consists of 2 particles: an electrically charged particle[2] with non-zero mass and a neutral particle with zero mass[3]. Leptons also carry a quantum number called *isospin* (T) which is the "charge" associated with the weak force. The first generation particles are called an electron (e^-) and an electron–neutrino (ν_e). The second generation

---

[1]The spin of a particle is given in units of $\hbar = h/2\pi$; $h = 6.5821 \times 10^{-16}$ eV $\cdot$ s

[2]The electric charge (Q) of a particle is given as a multiple of the electron charge magnitude: e.

[3]The SM assumes that neutrinos are massless. Current experimental evidence [12] indicates that this assumption is false.

2

Particle name	Particle symbol	Rest Mass (GeV/c^2)	Electric charge
down	d	9×10^{-3}	$-\frac{1}{3}$
up	u	5×10^{-3}	$+\frac{2}{3}$
strange	s	170×10^{-3}	$-\frac{1}{3}$
charm	c	1.4	$+\frac{2}{3}$
bottom	b	4.4	$-\frac{1}{3}$
top	t	173	$+\frac{2}{3}$

Table 1.2: Properties of the three generations of quarks.

consists of a muon (μ^-) and a muon–neutrino (ν_μ). The third generation consists of a tau (τ^-) and a tau–neutrino (ν_τ). Electrons, muons, and taus have the same quantum numbers (electric charge, isospin, spin, etc) but different masses; $M_e = (5.1099906^{+0.0000015}_{-0.0000015}) \times 10^{-4}$ GeV/c^2, $M_\mu = (1.05658389^{+0.00000034}_{-0.00000034}) \times 10^{-1}$ GeV/c^2, $M_\tau = 1.77705^{+0.00029}_{-0.00026}$ GeV/c^2 [13].

Quarks are also grouped into 3 generations. The first generation consists of an up (u) quark with electric charge $+2/3$ and a down quark (d) with an electric charge of -1/3. The second generation contains a $+2/3$ charm (c) quark and a -1/3 strange (s) quark. The third generation quarks are a $+2/3$ top (t) quark and a -1/3 bottom (b) quark. The masses of the quarks span a wide range; they range from ≈ 5 MeV/c^2 for the u quark to 173 ± 5.2 GeV/c^2 for the t quark [13]. Due to the nature of the strong force, free quarks are not observed. We observe groups of quarks as either a *meson* or a *baryon*. A meson is the bound state of a quark and its anti–particle. A baryon is the bound state of three quarks. Collectively, mesons and baryons are referred to as *hadrons*.

Quarks carry isospin quantum numbers as well as an additional quantum number

3

Force	Particle symbol	Rest Mass (GeV/c^2)	Electric charge
electromagnetism	γ	$< 2 \times 10^{-25}$	$< 5 \times 10^{-30}$
weak	$W^{\pm}$	80.41	± 1
	Z^0	91.12	0
strong	$g(\times 8)$	$<$ several MeV	0

Table 1.3: Properties of the gauge bosons.

called *color*. Color is the "charge" associated with the strong force and comes in three varieties: red, green, blue. We have, for example, u(red), u(green), u(blue).

Associated with each force is one or more gauge bosons. Electromagnetism has a single massless boson called the *photon* (γ). The weak force is mediated by 3 massive gauge bosons: a +1 charged boson (W^+), a -1 charged boson (W^-), and a neutral bosons (Z^0). The $W^{\pm}$ have a mass $M_W = 80.41 \pm 0.10$ GeV/c^2 and the Z^0 has a mass $M_Z = 91.187 \pm 0.007$ GeV/c^2 [13]. The strong force is transmitted by the exchange of one of 8 massless neutral bosons called *gluons* (g).

1.2 Field Theory and Symmetries

The twin pillars of particle physics are *quantum field theory* and *symmetries of nature*. The first concept forces us to think of a particle as a many–body field (ψ) instead of a single–particle wavefunction. In classical mechanics, we can derive the equations of motion for fields using Lagrange mechanics [14]. In quantum field theory, we think of this field as a collection of quantum harmonic oscillators. When done properly, quantum field theory allows particle creation/destruction, anti–particles with positive energy, and avoids "action–at–a–distance" [15].

The second concept guides us to the form of the Lagrangian density $\mathcal{L}$ for a

4

particular force. According to Noether's theorem [16], there is a conserved charge for every continuous transformation which leaves the Lagrangian density invariant. For example, translational invariance implies momentum conservation.

For quantum fields, we can study transformations of the phases of the fields which leave the Lagrangian invariant. We call this type of invariance *gauge invariance*. There are two classes of gauge invariance: *global* gauge invariance and *local* gauge invariance. The first type applies a phase transformation which is independent of the space–time coordinate. The second type applies a phase transformation which does depend on the space–time coordinates. Local gauge invariance is the more interesting type because it introduces a new field (called a *gauge* field) which interacts with the matter fields.

The Standard Model consists of 3 local gauge theories: $SU(3)_C \times SU(2)_L \times U(1)_Y$. $SU(3)_C$ is the gauge group for the strong force; the subscript C stands for "color". $SU(2)_L$ is the weak gauge group; the subscript L stands for "left". $SU(2)_L$ is a *chiral* theory. The left–handed and right–handed components[4] of a spin–1/2 fermion interact differently. $U(1)_Y$, when combined with $SU(2)_L$, generates the electromagnetic force. In fact, at high energies, the weak and electromagnetic force are unified into one force called the *electroweak* force. The subscript Y stands for *hypercharge* which satisfies the relationship $Q = T_3 + \frac{1}{2}Y$; T_3 is the third (or "z") component of the total isospin T.

---

[4]Massless spin–1/2 fermions can have two helicity states. The spin polarization can be aligned with the direction of motion (right–handed) or opposite the direction of motion (left–handed).
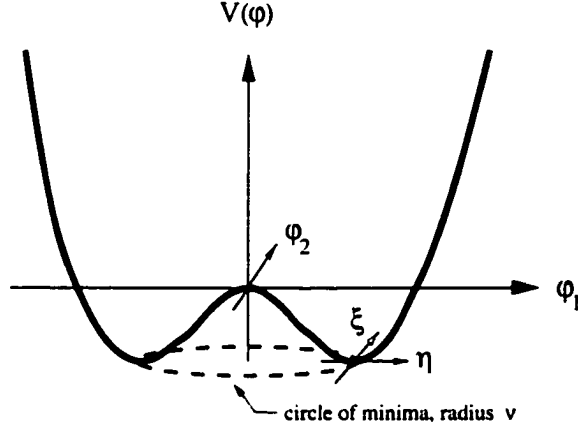
Figure 1.1: The Higgs scalar potential in the Standard Model for $\mu^2 < 0$.

1.3 Higgs boson

The mechanism for generating masses in the Standard Model in a gauge invariant manner is called *Spontaneous Symmetry Breaking* (SSB; see [9–11] for a detailed description). SSB introduces a new field (ϕ) called the *Higgs boson* with a potential $V(|\phi|) = \mu^2|\phi|^2 + \lambda|\phi|^4$ ($\mu^2 < 0$, $\lambda > 0$) into the Standard Model. This is shown in Fig. 1.1. The Higgs boson has Higgs–gauge, Higgs–fermion, and Higgs–Higgs interactions. When the Higgs field is expanded about its minimum ($= \sqrt{\frac{-\mu^2}{\lambda}}$), these interaction terms become the mass terms for the fermions and gauge bosons. The number of free parameters in the Standard Model increases. We now have μ, which is directly related to the Higgs boson mass, and y_i, which is directly related to the fermion masses. There is a different y_i for each fermion type (y_e for an electron, y_t for a top quark, etc).

6
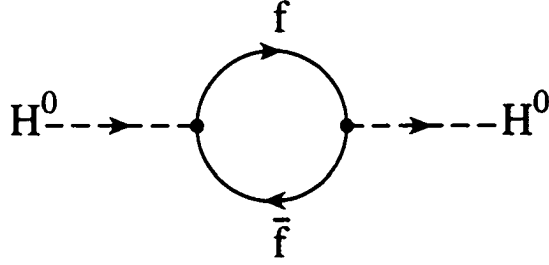
Figure 1.2: One–loop correction from a fermion, f, to the mass of the Higgs boson, H^0.

1.4 Shortcomings of SM

The Standard Model is an amazingly accurate theory. Where applicable, no significant experimental deviation from the theory has been observed [17]. For example, the observed anomalous magnetic moment of the electron ($\equiv \frac{g-2}{2}$) is $(1159.652193 \pm 0.000010) \times 10^{-6}$ [13]. The current theoretical prediction is $1159.652460 \pm 0.000127 \pm 0.000075 \times 10^{-6}$) [18]. Yet there are reasons to believe that the Standard Model is incomplete; that it might be part of some larger theory which will unify all forces and particles into one coherent theory. We list some of these reasons:

1. The Standard Model does not include gravity. At the *Plank* scale ($M_P = 10^{19}$ GeV/c^2), the gravitational force can no longer be ignored.

2. The mass^2 of the Higgs boson, m_H^2, receives corrections, Δm_H^2, from all fermion particles with non-zero mass. The *Feynman Diagram* for these corrections is shown in Fig.1.2. The fermion correction goes like

$$\Delta m_H^2 = \frac{|\lambda_f|^2}{16\pi^2}[-2\Lambda_{UV}^2 + 6m_f^2 \ln(\Lambda_{UV}/m_f) + \ldots]. \qquad (1.1)$$

7
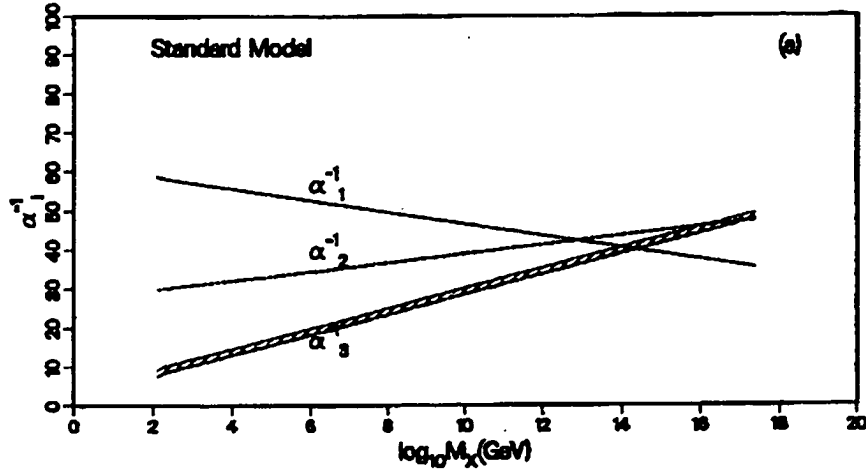
Figure 1.3: The evolution of the coupling constants α_1, α_2, α_3 as a function of the mass scale from data within in the SM [19]. We see that the 3 couplings do not meet at a commom mass.

where λ_f is the fermion–Higgs coupling strength and Λ_{UV} is a large energy scale (say M_P) at which new physics enters. The first term in the bracket is called a *quadratic divergence*. From theoretical and experimental constraints [13] we expect m_H to be $\mathcal{O}(100 \text{ GeV/c}^2)$ while the corrections are 10^{17} larger. This problem is called the *Naturalness* problem.

3. The *coupling constants*[5] for U(1)$_Y$, SU(2)$_L$ unify at a large energy scale ($M_U >$ 10^{12} GeV/c^2). If we believe that the unification of the weak and electromagnetic forces is not an accident, we can attempt to unify all three forces. This is shown

---

[5]The coupling constants α_1, α_2, α_3 are a measure of the strength of the electromagnetic, weak, and strong interactions and are not true constants. Their value depends on the energy at which the interaction takes place. This energy dependence or "running of the coupling" depends on the gauge group and is calculable.

8

for the SM in Fig. 1.3 [19]. Clearly, the constants do not unify at a common point.

4. A related problem is called the *Hierarchy* problem. Why is the electroweak energy scale ($= M_W$) so much lower than the electroweak unification scale?

5. The SM has 19 free parameters. Can we form a theory that has less (or even zero!) free parameters?

6. Why do the fermion masses cover such a large range?

7. The Higgs boson has not yet been discovered. Is spontaneous symmetry breaking the correct method to generate masses in the SM?

Many models have been introduced to solve some or all of these problems. Some models such as Technicolor [20–22] use dynamic electroweak symmetry breaking (DEWSB) to generate fermion/gauge masses. Some models simply unify the SM forces in a larger gauge group (SU(5), SO(10), E_6) [23–29]. We call these models Grand Unified Theories (GUT). Superstring models replace point-particles with strings (fundamental objects which have a length) in higher (10) dimensions [30–32].

Each of these models have significant problems. DEWSB models have difficulty generating large fermion masses such as the top quark. In addition, DEWSB models also have problems predicting the correct amount of flavor–changing neutral currents. Among other problems, GUT models do not unify the gauge couplings (Fig 1.3). String models have many theoretical hurdles chief of which is how the 10 (or 11) dimensions transform (or "compactify") into the 4 dimensions we observe.

This analysis looks for evidence of a model called *Supersymmetry* (SUSY). SUSY models introduce a new gauge symmetry that transforms fermions into bosons and

9

bosons into fermions. We search for two new particles predicted by SUSY: *scalar top quark* ($\tilde{t}_1$) and *scalar bottom quark* ($\tilde{b}_1$). At the Tevatron, $\tilde{t}_1/\tilde{b}_1$ are predicted to be produced in pairs. We assume that $\tilde{t}_1 \longrightarrow c\tilde{\chi}_1^0$ and $\tilde{b}_1 \longrightarrow b\tilde{\chi}_1^0$; $\tilde{\chi}_1^0$, called a *neutralino*, is another particle predicted by Supersymmetry. $\tilde{\chi}_1^0$ is neutral, colorless, and stable. Therefore, $\tilde{\chi}_1^0$ leaves the CDF detector without interacting. The final state for $\tilde{t}_1\bar{\tilde{t}}_1/\tilde{b}_1\bar{\tilde{b}}_1$ production is $c\bar{c} + \tilde{\chi}_1^0\tilde{\chi}_1^0/b\bar{b} + \tilde{\chi}_1^0\tilde{\chi}_1^0$.

We observe these events as 2 clusters of energy in the calorimeter (from $c\bar{c}/b\bar{b}$) plus an imbalance of energy in the calorimeter (from $\tilde{\chi}_1^0\tilde{\chi}_1^0$). The background to this signal from Standard Model processes is dominated by events where the 2 clusters are due to light (u, d, s) quarks and not heavy (b, c) quarks. At CDF we significantly improve our discovery potential by selecting events which contain heavy quarks. Our ability to tag events with c *or* b quarks efficiently and with low fake rates allows us to explore regions of parameter space not available to other experiments.

This thesis is divided as follows. In Ch. 2 we give a brief introduction to Supersymmetry, which introduces a new symmetry of Nature, and describe the experimental signature for which we are looking. In Ch. 3 we describe the experimental apparatus used in this analysis. In Ch. 4 we describe the data selection. In Ch. 5 we describe the heavy quark (b/c) tagger we use to select signal events. In Ch. 6 we present the results of our background and signal estimates after applying the heavy quark tag. In Ch. 7 we discuss the systematic uncertainties in our calculations of our background and signal estimates. In Ch. 8 we present the tagged data results as well as limits on the allowed masses of the scalar top and scalar bottom quarks. Finally, in Ch. 9 we present some thoughts on future extensions of this search as well as applying these results to other new particle searches.

10

Chapter 2

Theory

In this chapter we will first give an experimentalist's introduction to Supersymmetry (SUSY). A detailed description of SUSY is beyond the scope of this analysis; see [33–35] for more details. Next, we will focus on the SUSY physics which is relevant for this analysis. Finally, we will list the current limits on the existence of SUSY particles.

2.1 Minimal Supersymmetry

Supersymmetry postulates a new symmetry, Q, which transforms fermions into bosons and bosons into fermions; $Q\psi_{fermion} = \psi_{boson}$ and $Q\psi_{boson} = \psi_{fermion}$. The spin of the particle is changed by 1/2 but all other quantum numbers remain the same. SM particles and SUSY particles with the same quantum numbers are grouped into *supermultiplets*. For every supermultiplet the number of fermion degrees of freedom $(= n_F)$ must equal the number of boson degrees of freedom $(= n_B)$.

A massless, spin–1/2 fermion has $n_F = 1 \times 2$ so its *superpartners* are 2 real, massless spin–0 bosons $(n_B = 2 \times 1)$. Equivalently, the 2 real bosons can be combined into one complex boson. A spin–1/2 fermion and a complex spin–0 boson form a supermultiplet which is called a *chiral multiplet*. The left and right–handed components of a particle transform differently under $SU(2)_L$ and so belong to separate supermul-

11

tiplets. For a left–handed fermion, ψ_L, the superpartner is a "left–handed" complex scalar, ϕ_L. A right–handed fermion, ψ_R, has a "right–handed" complex scalar partner, ϕ_R[1]. A massless, spin-1 boson has $n_B = 2$ so its the superpartner is a massless, spin-1/2 fermion. This type of supermultiplet is called a *gauge multiplet*.

The names of the fermion superpartners are formed by prefixing a *s-* to the fermion name. To form the SUSY particle symbol, we place a tilde over its SM partner symbol. For example, the superpartner of the electron (e_L/e_R) is called the *selectron* $(\tilde{e}_L/\tilde{e}_R)$. For bosons, the superpartner names are formed by suffixing an *-ino* to the boson name. Again, we place a tilde over the boson symbol to form the superpartner symbol. For example the gluon (g) has a *gluino* $(\tilde{g})$ superpartner. Table 2.1 lists all the chiral and gauge multiplets.

Members of the same multiplet have the same gauge interactions with the same coupling strengths. For example, the $\tilde{e}$–$\tilde{\nu}_e$–$\tilde{W}^-$ interaction has the same coupling strength as the e–ν_e–W^- interaction. There are also interactions between SM and SUSY particles. We have, among others, $\tilde{e}$–e–$\tilde{Z}^0$ and $\tilde{t}$–b–$\tilde{W}^-$ interactions.

To make particles massive via spontaneous symmetry breaking the Higgs spectrum must be modified. Instead of one scalar doublet we need two scalar doublets. Two doublets are needed to cancel certain anomalies as well as to couple to fermions in a SUSY–invariant manner [35]. One doublet, $H_d = \begin{pmatrix} H_d^0 \\ H_d^- \end{pmatrix}$ with $Y = -1$, couples only to the $T_3 = -1/2$ component of an isospin doublet $(d, c, b, e^-, \mu^-, \tau^-)$. The other doublet, $H_u = \begin{pmatrix} H_u^+ \\ H_u^0 \end{pmatrix}$ with $Y = +1$, couples to the $T_3 = +1/2$ component of an isospin doublet (u, s, t). Instead of one neutral scalar boson, we have 5 scalar bosons: H^0, h^0, A^0, H^+, H^-. The superpartners of the Higgs fields, $\tilde{H}_u$ and $\tilde{H}_d$, are massless

---

[1]Scalar particles do not have helicity. The label "left–handed"/"right–handed" is used to indicate that the scalar is the superpartner of a left–handed/right–handed fermion.

12

SM			SUSY		
particle	symbol	spin	particle	symbol	spin
lepton	$(l, \nu_l)_L$	1/2	slepton	$(\tilde{l}, \tilde{\nu}_l)_L$	0
	l_R	1/2		$\tilde{l}_R$	0
quark	$(u', d')_L$	1/2	squark	$(\tilde{u}', \tilde{d}')_L$	0
	u'_R	1/2		$\tilde{u}'_R$	0
	d'_R	1/2		$\tilde{d}'_R$	0
W bosons	$W^\pm, W^0$	1	Winos	$\tilde{W}^\pm, \tilde{W}^0$	1/2
B boson	B^0	1	Bino	$\tilde{B}^0$	1/2
gluon	g	1	Gluino	$\tilde{g}$	1/2
Higgs	H_u	0	Higgsino	$\tilde{H}_u$	1/2
	H_d	0		$\tilde{H}_d$	1/2

Table 2.1: The particle spectrum of the MSSM. $l = e, \mu, \tau$, $u' = u, c, t$, and $d' = d, s, b$. Note that these are the gauge eigenstates. Electroweak symmetry and supersymmetry breaking causes mixing among the gauge eigenstates to form mass eigenstates.

13
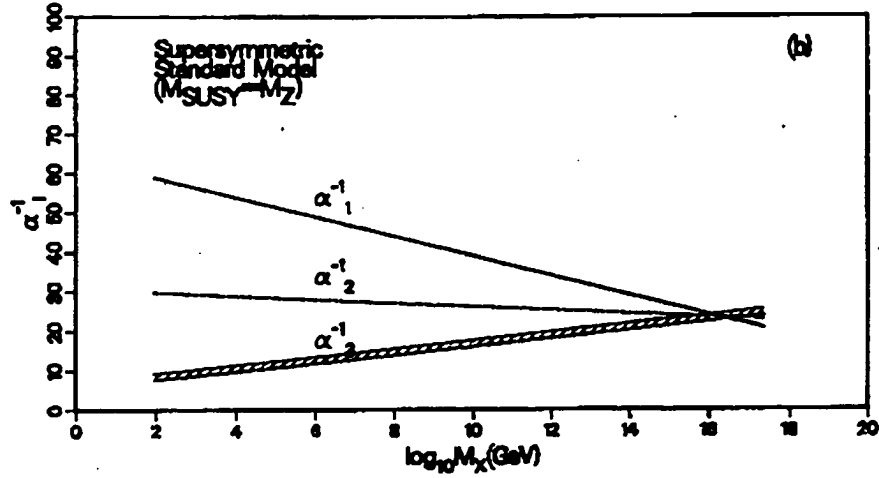
Figure 2.1: The evolution of the coupling constants α_1, α_2, α_3 as a function of the mass scale from data within in the MSSM [19]. We see that the 3 couplings do unify at a commom mass.

spin-1/2 fermions. Therefore, $(H_u, \tilde{H}_u)$ and $(H_d, \tilde{H}_d)$ form separate chiral multiplets.

If SUSY is an exact symmetry of nature then members of the same supermultiplet have the same mass. Since this is ruled out experimentally, SUSY must be a broken symmetry. Supersymmetry breaking is introduced by adding explicit SUSY–breaking terms to the Lagrangian. The most general broken SUSY theory has 105 parameters not found in the SM.

The supersymmetric theory with one generator Q, a pair of Higgs doublets and explicit SUSY–breaking terms is called the Minimal Supersymmetric extension to the Standard Model (*MSSM*). Even though there is no direct experimental evidence for the MSSM, we list some reasons which make it an attractive extension of the Standard Model:

14
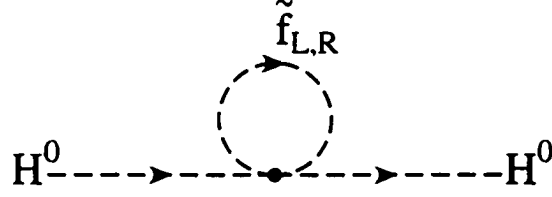
Figure 2.2: One–loop correction from a boson, $\tilde{f}$, to the mass of the Higgs boson, H^0.

1. In Supersymmetric extensions of the Standard Model, the gauge couplings do unify at a common energy scale $M_U \approx 10^{16}$ GeV/c^2. This is shown in Fig. 2.1 [19].

2. We can incorporate quantum gravity if we demand that supersymmetry be a local gauge symmetry. This introduces the graviton (G) and the gravitino ($\tilde{G}$).

3. The Naturalness problem is eliminated. For every spin–1/2 fermion, f, which couples to the Higgs boson (see Fig. 1.2) there are a pair of scalar bosons, $\tilde{f}_{L,R}$, which also couple to the Higgs boson. This is shown at the one–loop level in Fig. 2.2. The correction for the bosons is

$$\Delta m_H^2 \;\; = \;\; \frac{\lambda_S}{16\pi^2}[\Lambda_{UV}^2 - 2m_S^2 \ln(\Lambda_{UV}/m_S) + \ldots] \qquad (2.1)$$

If $|\lambda_f|^2 = \lambda_S$ then the Λ_{UV}^2 terms (see Eqn. 1.1) cancel exactly and there is no quadratic divergence. This condition holds in unbroken supersymmetry because f and $\tilde{f}_{L,R}$ belong to the same multiplet.

4. Cosmological studies have shown that the Universe contains more mass than is visible [13, 36]. A good candidate for this *dark matter* is the lightest neutral electroweak gaugino $\tilde{\chi}_1^0$.

15

2.1.1 R-Parity

It is possible to make more complicated SUSY theories. For instance, we can suppose that there is more than one generator, Q_i, of supersymmetric transformations. These *extended supersymmetry theories* do not allow chiral fermions or parity violation [35] so we do not consider these models. One can also add terms which violate baryon or lepton number. However, limits on proton decay [13] severely restrict baryon/lepton-violating terms. Therefore one often assumes, as we do in this analysis, an additional symmetry called *R-parity* which forbids lepton/baryon violating terms in the Lagrangian.

R-parity is an exact, discrete symmetry with quantum number $R = (-1)^{3B-L+2S}$; $B = $ baryon number, $L = $ lepton number[2] and $S = $ spin. For SM particles $R = 1$ and for SUSY particles $R = -1$. This means that the Lightest Supersymmetric Particle (LSP) is absolutely stable whereas all other SUSY particles decay to states with an odd number of LSP's.

2.1.2 Renormalization Group Equations

In classical electrodynamics, the effective charge (q_{eff}) of a charged particle (q) depends on the polarization of the medium in which it is situated. Far away from the particle, $q_{eff} < q$ because the molecules will align themselves along the electric field of the charged particle and the net charge inside a radius r will be less than q. For r less than the molecule size, this screening effect disappears.

A similar effect occurs in particle physics. As the energy (Q^2) of an interaction

---

[2]B equals +1/3 for quarks, -1/3 for anti-quarks and 0 for leptons. L equals +1 for leptons, -1 for anti-leptons, and 0 for quarks/anti-quarks.

16
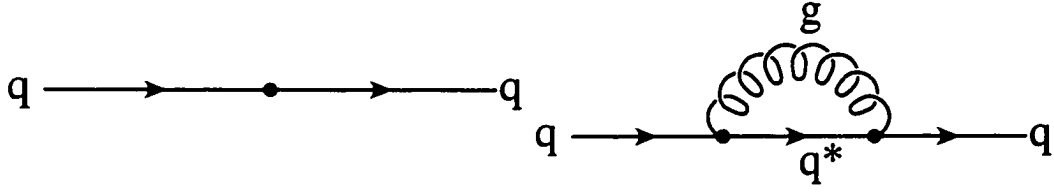
Figure 2.3: Figure (a) shows the tree-level diagram for the quark mass. Figure (b) shows a one-loop correction to the quark mass.

increases, the contribution from higher-order diagrams to the lowest-order diagram becomes important. Consider the QCD diagram shown in Fig. 2.3(a). The one-loop corrections to this diagram are shown in Fig. 2.3(b). These loops introduce integrals which depend on the momentum p of the virtual particles. Since p can range from 0 to ∞, the integrals become infinite. One can remove these infinities be absorbing them in a redefinition of the observed quantities (such as m_q or α_s). This redefinition or *renormalization* introduces a new energy scale μ. However, all observable amplitudes must be independent of the specific renormalization procedure (hence independent of μ) when all possible loops are included. The set of renormalization procedures as a function of μ form a group called the *Renormalization Group*

For each gauge group ($SU(3)_C$, $SU(2)_L$, $U(1)_Y$) there is a unique set of differential equations, called the *Renormalization Group Equations* (RGE), which determines the energy dependence of the observable parameters. The equations in the MSSM are different than their SM counterparts because the MSSM has a greater number of particles which leads to more loop diagrams. This difference explains why the coupling constants converge in the MSSM but not in the SM (see Figs. 1.3,2.1). In Sec. 2.3.1, we discuss how the RGE affect the mass spectrum of the third generation scalar quarks.

17

2.2 Charginos/Neutralinos

Because of electroweak symmetry and supersymmetry breaking the gauge eigenstates $(\tilde{B}, \tilde{W}^0, \tilde{H}_d^0, \tilde{H}_u^0)$ mix to form the mass eigenstates $(\tilde{\chi}_1^0, \tilde{\chi}_2^0, \tilde{\chi}_3^0, \tilde{\chi}_4^0)$. The $\tilde{\chi}_i^0$ are called *neutralinos* and obey the mass ordering $m_{\tilde{\chi}_i^0} < m_{\tilde{\chi}_{i+1}^0}$. The mixing matrix is:

$$
\begin{pmatrix}
M_1 & 0 & -m_Z \sin\theta_W \cos\beta & m_Z \sin\theta_W \sin\beta \\
0 & M_2 & m_Z \cos\theta_W \cos\beta & -m_Z \cos\theta_W \sin\beta \\
-m_Z \sin\theta_W \cos\beta & m_Z \cos\theta_W \cos\beta & 0 & -\mu \\
m_Z \sin\theta_W \sin\beta & -m_Z \cos\theta_W \sin\beta & -\mu & 0
\end{pmatrix}
\quad (2.2)
$$

M_1, M_2 are the mass terms from the SUSY–breaking Lagrangian terms for the $U(1)_Y$, $SU(2)_L$ gauginos. μ comes from the mass term in the Higgs scalar potential. θ_W is the Weinberg angle and β is defined so that $\tan\beta$ is the ratio of Vacuum Expectation Values (VEVs) of the Higgs fields; $\tan\beta = < H_d > / < H_u >$.

The charged gauginos, $(\tilde{W}^+, \tilde{H}_u^+, \tilde{W}^-, \tilde{H}_d^-)$, also mix. The mass eigenstates, called *charginos*, are $(\tilde{\chi}_1^\pm, \tilde{\chi}_2^\pm)$ with $M_{\tilde{\chi}_i^+} = M_{\tilde{\chi}_i^-}$ and $M_{\tilde{\chi}_1^\pm} < M_{\tilde{\chi}_2^\pm}$. The mixing matrix is:

$$
\begin{pmatrix}
0 & 0 & M_2 & \sqrt{2}m_W \cos\beta \\
0 & 0 & \sqrt{2}m_W \sin\beta & \mu \\
M_2 & \sqrt{2}m_W \sin\beta & 0 & 0 \\
\sqrt{2}m_W \cos\beta & \mu & 0 & 0
\end{pmatrix}
\quad (2.3)
$$

Searches for massive, charged, stable particles rule out the $\tilde{\chi}_i^\pm$ as the LSP [37,38]. In gravity–mediated susy–breaking models, the $\tilde{\chi}_1^0$ is the LSP. In gauge–mediated susy–breaking models, the gravitino is the LSP. In this scenario, the decay of $\tilde{\chi}_1^0$ produces a photon plus gravitino. However, if this decay occurs outside the detector, then the SUSY decay topologies will be the same as in the gravity–mediated case. In this analysis, we assume that $\tilde{\chi}_1^0$ is the LSP. Since $\tilde{\chi}_1^0$ is neutral and colorless, it will

18

leave the detector without interacting. This causes a measurable amount of missing energy which we will use to select our signal events.

2.3 3rd Generation Squarks

This thesis looks for evidence of the lighter mass eigenstates of the third generation scalar quarks. They are called *scalar top quark/scalar bottom quark* or *stop/sbottom* and their particle symbols are $\tilde{t}_1/\tilde{b}_1$. We will now show how these mass eigenstates can be light (< 150 GeV/c^2) even if the gauge eigenstates are heavy. We will also show that light $\tilde{t}_1/\tilde{b}_1$ can have a cross section large enough to be detectable at the Tevatron.

2.3.1 Mass Spectra

The one–loop RGE for the mass of $\tilde{t}/\tilde{b}$ is [39–41]:

$$16\pi^2 \frac{d}{dt} m^2_{\tilde{t}_L} = X_t + X_b - \frac{32}{3} g_3^2 |M_3|^2 - 6 g_2^2 |M_2|^2 - \frac{2}{15} g_1^2 |M_1|^2 \qquad (2.4)$$

$$16\pi^2 \frac{d}{dt} m^2_{\tilde{t}_R} = 2X_t - \frac{32}{3} g_3^2 |M_3|^2 - \frac{32}{15} g_1^2 |M_1|^2 \qquad (2.5)$$

$$16\pi^2 \frac{d}{dt} m^2_{\tilde{b}_L} = X_t + X_b - \frac{32}{3} g_3^2 |M_3|^2 - 6 g_2^2 |M_2|^2 - \frac{2}{15} g_1^2 |M_1|^2 \qquad (2.6)$$

$$16\pi^2 \frac{d}{dt} m^2_{\tilde{b}_R} = 2X_b - \frac{32}{3} g_3^2 |M_3|^2 - \frac{8}{15} g_1^2 |M_1|^2 \qquad (2.7)$$

M_3 is the SU(3)$_C$ SUSY–breaking mass term and $t = \ln(Q/Q_0)$. Q is the energy at which the parameter is evaluated and Q_0 is the "input scale" (say M_U). The terms X_t, X_b (which are positive) are due to the Yukawa couplings which are assumed to be non–negligible for the third generation quark/squarks. Since the first and second generation quarks are very light compared to the SUSY–breaking masses M_i, we can ignore the X_q terms of the RGEs for these generations. Therefore, the RGEs for

19

these generations contain only gaugino contributions and the right side of the RGE will be strictly negative. If all squarks have the same mass $(m_{\tilde{q}})$ at the input scale, then at the electroweak scale (≈ 100 GeV/c^2), the third generation squarks will have smaller masses than the first and second generation. Since $m_{\tilde{q}}$ and the other SUSY parameters are unknown, it is quite possible that neither $\tilde{t}_L/\tilde{t}_R$ nor $\tilde{b}_L/\tilde{b}_R$ is light enough to be detected.

There is still hope, however. Supersymmetry breaking can lead to large mixing between the left/right–handed third generation squarks. The mixing matrix for $\tilde{t}_L/\tilde{t}_R$ is:

$$\begin{pmatrix} m^2_{\tilde{t}_L} & M_t(A_t + \mu \cot \beta) \\ M_t(A_t + \mu \cot \beta) & m^2_{\tilde{t}_R} \end{pmatrix} \qquad (2.8)$$

A_t, called the stop *trilinear coupling*, is the Higgs–stop–stop SUSY–breaking coupling constant. Looking at the off–diagonal terms, we see that even if A_t is small, the top mass can make this term large. This can lead to a substantial mixing between $\tilde{t}_L$ and $\tilde{t}_R$. The mass eigenvalues ($m_{\tilde{t}_1} < m_{\tilde{t}_2}$) are:

$$m^2_{\tilde{t}_{1,2}} = \tfrac{1}{2}[m^2_{\tilde{t}_L} + m^2_{\tilde{t}_R} \mp \sqrt{(m^2_{\tilde{t}_L} - m^2_{\tilde{t}_R})^2 + 4m^2_t(A_t + \mu \cot \beta)^2}] \qquad (2.9)$$

The mixing between the light/heavy partners is parameterized by a mixing angle $\theta_{\tilde{t}}$:

$$\begin{pmatrix} \tilde{t}_1 \\ \tilde{t}_2 \end{pmatrix} = \begin{pmatrix} \cos \theta_{\tilde{t}} & \sin \theta_{\tilde{t}} \\ -\sin \theta_{\tilde{t}} & \cos \theta_{\tilde{t}} \end{pmatrix} \begin{pmatrix} \tilde{t}_L \\ \tilde{t}_R \end{pmatrix} \qquad (2.10)$$

where $\tilde{t}_1/\tilde{t}_2$ are the light/heavy mass eigenstates.

The mixing matrix for $\tilde{b}_L/\tilde{b}_R$ is:

$$\begin{pmatrix} m^2_{\tilde{b}_L} & M_b(A_b + \mu \tan \beta) \\ M_b(A_b + \mu \tan \beta) & m^2_{\tilde{b}_R} \end{pmatrix} \qquad (2.11)$$

Since m_b is much smaller than m_t, we need to rely on $\tan\beta$ and A_b to make the off-diagonal term large and cause a large mixing. The mass eigenvalues $(m_{\tilde{b}_1} < m_{\tilde{b}_2})$ are:

$$m_{\tilde{b}_{1,2}}^2 = \tfrac{1}{2}[m_{\tilde{b}_L}^2 + m_{\tilde{b}_R}^2 \mp \sqrt{(m_{\tilde{b}_L}^2 - m_{\tilde{b}_R}^2)^2 + 4m_b^2(A_b + \mu\,\tan\beta)^2}] \qquad (2.12)$$

The mixing between the light/heavy partners is parameterized by a mixing angle $\theta_{\tilde{b}}$:

$$\begin{pmatrix} \tilde{b}_1 \\ \tilde{b}_2 \end{pmatrix} = \begin{pmatrix} \cos\theta_{\tilde{b}} & \sin\theta_{\tilde{b}} \\ -\sin\theta_{\tilde{b}} & \cos\theta_{\tilde{b}} \end{pmatrix} \begin{pmatrix} \tilde{b}_L \\ \tilde{b}_R \end{pmatrix} \qquad (2.13)$$

where $\tilde{b}_1/\tilde{b}_2$ are the light/heavy mass eigenstates.

In Figs. 2.4-2.5 we show the mass eigenstates for $\tilde{t}/\tilde{b}$ as a function of μ for 2 sets of parameters. In Fig. 2.4, $M_{\tilde{t}_L} = 370$ GeV/c^2, $M_{\tilde{t}_R} = 372$ GeV/c^2, $M_{\tilde{b}_L} = 335$ GeV/c^2, $M_{\tilde{b}_R} = 331$ GeV/c^2, $A_t = A_b = -330$ GeV/c^2, and $\tan\beta = 20$. In Fig. 2.5, $M_{\tilde{t}_L} = 371$ GeV/c^2, $M_{\tilde{t}_R} = 372$ GeV/c^2, $M_{\tilde{b}_L} = 333$ GeV/c^2, $M_{\tilde{b}_R} = 331$ GeV/c^2, $A_t = A_b = -330$ GeV/c^2, and $\tan\beta = 20$. We see that it is quite possible for either $\tilde{t}_1$ or $\tilde{b}_1$ to be light (< 150 GeV/c^2) even if the gauge eigenstates ($\tilde{t}_L/\tilde{t}_R$ or $\tilde{b}_L/\tilde{b}_R$) are heavy and nearly degenerate.

2.3.2 Production mechanism

At a $p\bar{p}$ collider machine such as the Tevatron, $\tilde{t}_1/\tilde{b}_1$ quarks are produced in pairs if R-parity is conserved. The Leading Order (LO) QCD production mechanisms are shown in Fig. 2.6. The LO and NLO cross sections have been calculated [42]. Even at NLO, the change in the cross section as the SUSY parameters (such as $\tan\beta$, A_t/A_b, etc.) are varied is less than 1%. The NLO cross section as a function of squark ($\tilde{t}_1$ or $\tilde{b}_1$) mass is shown in Fig. 2.7 for three different values of the QCD renormalization

21
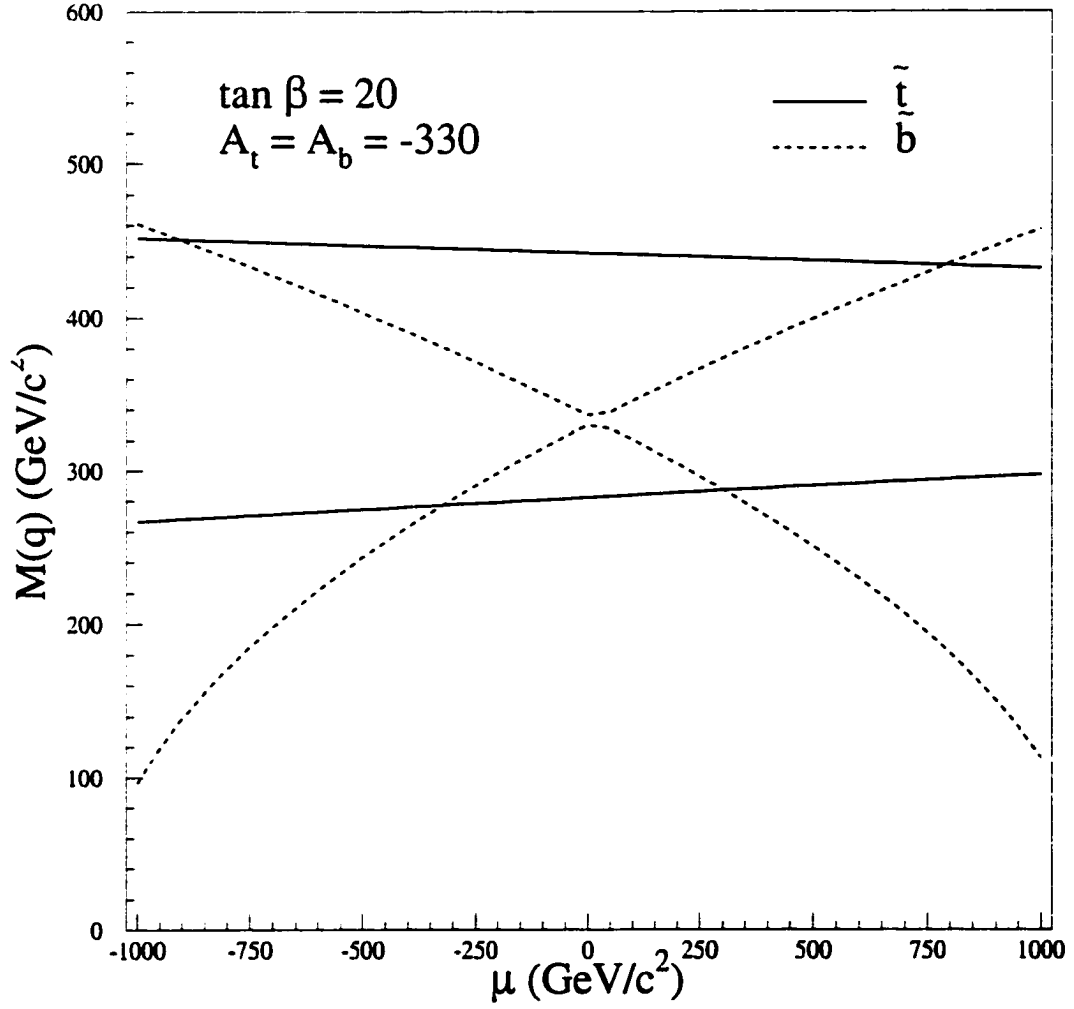
Figure 2.4: The mass splitting of the $\tilde{t}_L/\tilde{t}_R$ and $\tilde{b}_L\tilde{b}_R$ gauge eigenstates as a function of the SUSY parameter μ. For this choice of $\tan\beta$ and $A_{t,b}$, the lightest eigenstate is usually $\tilde{b}_1$. We also see that there are parts of parameter space where $\tilde{b}_1 < 150$ GeV.

22
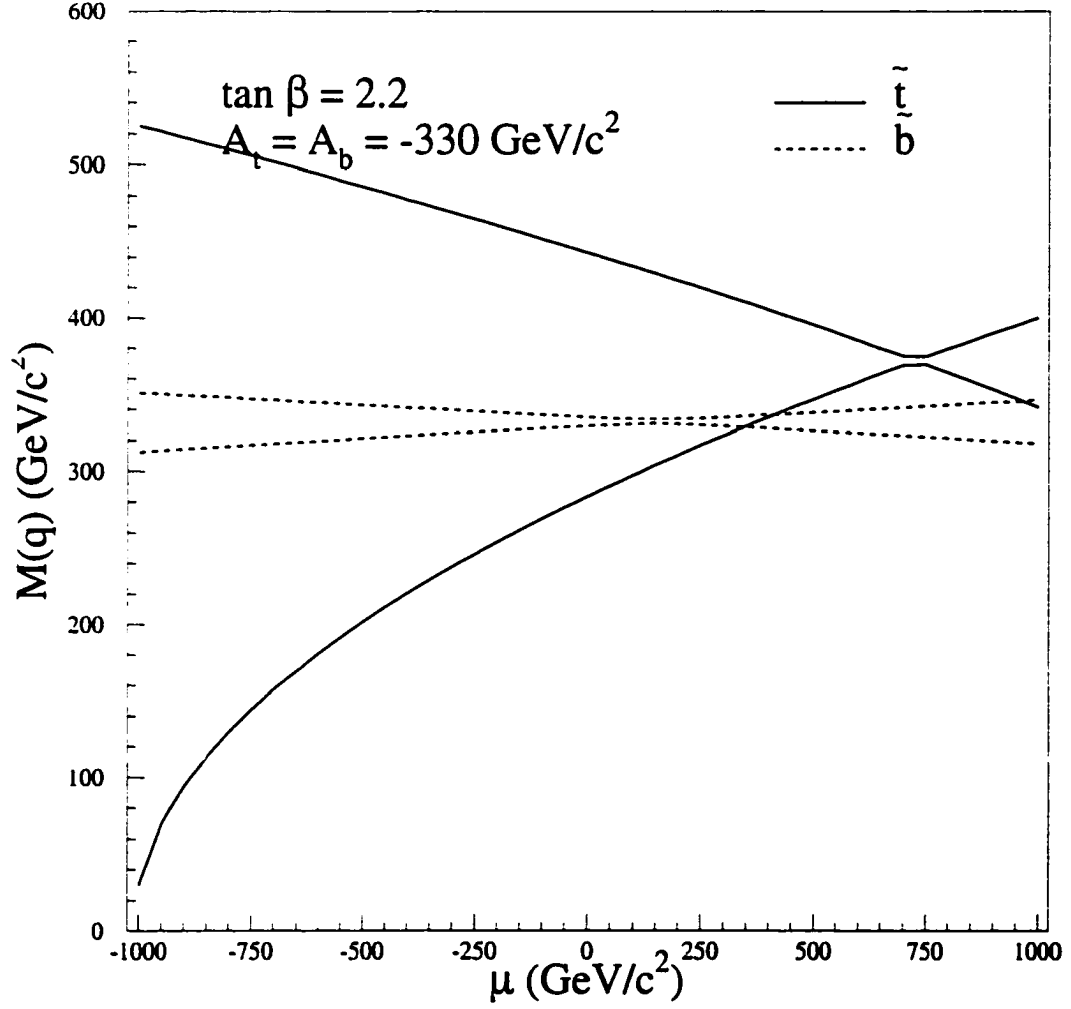
Figure 2.5: The mass splitting of the $\tilde{t}_L/\tilde{t}_R$ and $\tilde{b}_L\tilde{b}_R$ gauge eigenstates as a function of the SUSY parameter μ. For this choice of $\tan\beta$ and $A_{t,b}$, the lightest eigenstate is usually $\tilde{t}_1$. We also see that there are parts of parameter space where $\tilde{t}_1 < 150$ GeV.

23
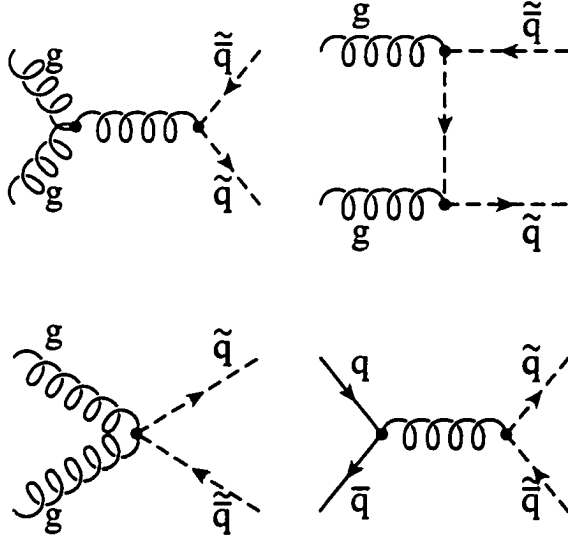
Figure 2.6: Leading Order (LO) QCD production for squark $(\tilde{q}=\tilde{t}_1/\tilde{b}_1)$ pair-production.

scale μ. For example, $m_{\tilde{q}} = 110$ pb, $\sigma_{NLO}(\mu = m_{\tilde{q}}) = (7.4 \pm 1.1)$ pb; the error refers to the change in σ when μ is varied to $m_{\tilde{q}}/2$ and $2m_{\tilde{q}}$. We note that this is essentially the same cross-section for $t\bar{t}$ production at the Tevatron as measured by CDF [7].

2.3.3 Decay Topologies

We now discuss the possible decay patterns of $\tilde{t}_1$ and $\tilde{b}_1$. We start with $\tilde{t}_1$. The tree-level decays of $\tilde{t}_1$ are:

$$\tilde{t}_1 \longrightarrow t\tilde{\chi}_i^0 \tag{2.14}$$

$$\tilde{t}_1 \longrightarrow t\tilde{g} \tag{2.15}$$

$$\tilde{t}_1 \longrightarrow b\tilde{\chi}_i^+ \tag{2.16}$$

Since $M_t = 175$ GeV/c^2, we have no hope of observing (2.14) or (2.15) at the Tevatron. The current limit on $M_{\tilde{\chi}_1^+}$ is $M_{\tilde{\chi}_1^+} > 90$ GeV/c^2 [43]. Therefore, $\tilde{t}_1 \longrightarrow b\tilde{\chi}_1^+$ is possible

24
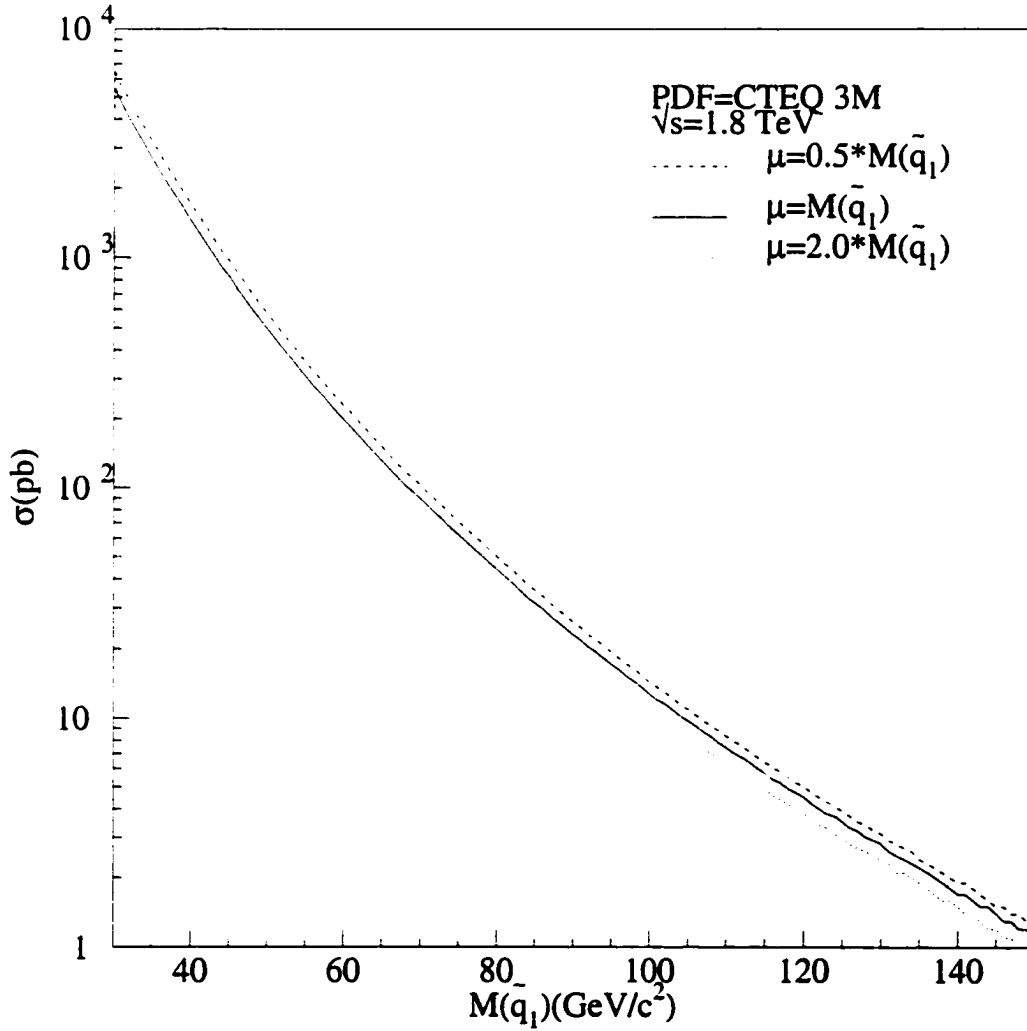
Figure 2.7: The NLO cross section for $\tilde{t}_1\tilde{t}_1$ or $\tilde{b}_1\tilde{b}_1$ production in $p\bar{p}$ collisions at $\sqrt{s} = 1.8$ TeV [42]. The central value sets the QCD μ scale $= m_{\tilde{q}}$. The cross–sections when QCD $\mu = 2m_{\tilde{q}}$ and $0.5m_{\tilde{q}}$ are also shown.

25

in our region of interest ($M_{\tilde{t}_1} < 150$ GeV/c^2).

If $M_{\tilde{t}_1} < M_t$ and $M_{\tilde{t}_1} < M_b + M_{\tilde{\chi}_1^+}$, the $\tilde{\chi}_1^+$ in (2.16) is virtual and the following decays are possible:

$$\tilde{t}_1 \longrightarrow bq'\bar{q} \tag{2.17}$$

$$\tilde{t}_1 \longrightarrow bl\bar{\nu}_l \tag{2.18}$$

$$\tilde{t}_1 \longrightarrow b\nu_l\bar{l} \tag{2.19}$$

$$\tilde{t}_1 \longrightarrow bW\tilde{\chi}_1^0 \tag{2.20}$$

$$\tilde{t}_1 \longrightarrow c\tilde{\chi}_1^0 \tag{2.21}$$

The current limit on $M_{\tilde{q}}$ is $M_{\tilde{q}} > 216$ GeV/c^2 [44]; $\tilde{q}$ refers to all squarks except the lightest eigenstate $\tilde{t}_1$ or $\tilde{b}_1$. Therefore, (2.17) is not allowed in our region of interest. The current limit on $M_{\tilde{l}}$ is $M_{\tilde{l}} > 64$ GeV/c^2 [45] and the current limit on $M_{\tilde{\nu}}$ is $M_{\tilde{\nu}} > 43$ GeV/c^2 [13]. Therefore, (2.18) and (2.19) are not forbidden by experiment in our region of interest. However, these decays will be highly suppressed [46]. When $\tilde{l}, \tilde{\nu}, \tilde{q}$ are virtual the four–body decays resulting from (2.17), (2.18), and (2.19) are negligible compared to (2.20) and (2.21) [46]. Finally, it can be shown [47] that the three–body decay (2.20) can, depending on the SUSY parameters, have a large branching fraction. Since this decay will produce topologies very different from (2.21) we restrict our search to the region where $M_{\tilde{t}_1} < M_b + M_W + M_{\tilde{\chi}_1^0}$.

The two competing decays are (2.16) and (2.21). The Feynman diagrams for these decays are shown in Fig. 2.8; note that Fig. 2.8(b) is just one example of the loop-diagrams relevant for this decay. We choose to look for $\tilde{t}_1 \longrightarrow c\tilde{\chi}_1^0$. We do this for several reasons:

1. The limits on $M_{\tilde{\chi}_1^+}(> 90$ GeV$c^2)$ and $M_{\tilde{\chi}_1^0}(> 30$ GeV$c^2)$ [43] give us a small

26
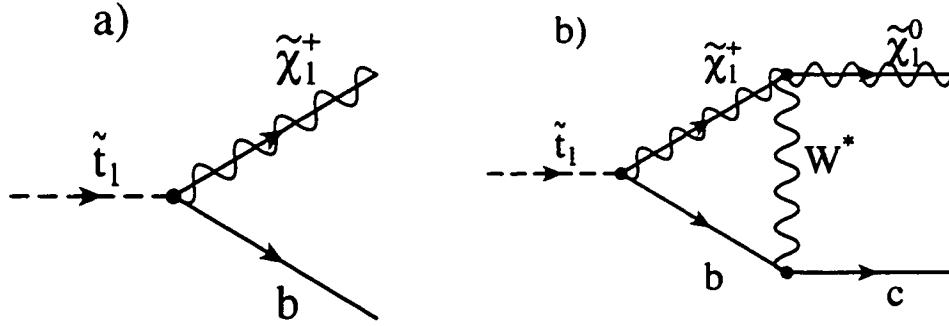
Figure 2.8: (a) Tree–level decay $\tilde{t}_1 \longrightarrow b\tilde{\chi}_1^+$. (b) One example of the one–loop decay $\tilde{t}_1 \longrightarrow c\tilde{\chi}_1^0$.

kinematic region where $\tilde{t}_1 \longrightarrow b\tilde{\chi}_1^+$ is accessible at the Tevatron.

2. This search compliments the direct searches performed at e^+e^- machines (Sec. 2.4.3)

3. With only a slight modification, we can use the same analysis to look for a light $\tilde{b}_1$.

4. As we will show in Ch. 9, the results of this analysis are applicable to other new particle searches.

5. This search has not been performed by the CDF collaboration.

For the purposes of this analysis we **assume** that $M_{\tilde{t}_1} < M_b + M_{\tilde{\chi}_1^+}$. Searches for $\tilde{t}_1$ assuming that (2.16) is allowed have been performed. We will discuss those results in Sec. 2.4.3.

The decay pattern for $\tilde{b}_1$ is much simpler. M_b is $\approx$ 4.5 GeV/c^2 so the decay $\tilde{b}_1 \longrightarrow b\tilde{\chi}_1^0$ is allowed and dominant. All other decays are either forbidden (due to sparticle limits mentioned above) or suppressed.

27

The final state for $\tilde{t}_1/\tilde{b}_1$ in $p\bar{p}$ collisions is $c\bar{c}+\tilde{\chi}_1^0\tilde{\chi}_1^0/b\bar{b}+\tilde{\chi}_1^0\tilde{\chi}_1^0$. The kinematics for these two classes of events are very similar. As we will show in Ch. 4, the same kinematic selection can be used for both searches. Only when we tag for the presence of heavy-flavored quarks can we exploit the difference between b/c quarks.

2.4 Experimental limits

We now discuss the SUSY particle limits which are relevant to our analysis. Some of the limits have been mentioned in Sec. 2.3.3 where we described the possible $\tilde{t}_1/\tilde{b}_1$ decays. We also discuss searches for $\tilde{t}_1/\tilde{b}_1$ at other experiments.

2.4.1 Chargino/Neutralino

At CERN (which is an e^+e^- collider), the lightest chargino ($\tilde{\chi}_1^\pm$) can be pair-produced. The $\tilde{\chi}_1^+$ decays to $\tilde{\chi}_1^0 l^+ \nu_l$ or $\tilde{\chi}_1^0 qq'$ via W^+, $\tilde{l},\tilde{\nu}$, or $\tilde{q}$. The final state topology will be:

1. $l^+l^- + \nu_l\bar{\nu}_l + \tilde{\chi}_1^0\tilde{\chi}_1^0$. This is observed in the detector as a dilepton event with significant missing energy.

2. $l\nu_l + qq' + \tilde{\chi}_1^0\tilde{\chi}_1^0$. This is observed in the detector as a lepton plus two jets[3] event with significant missing energy.

3. $qq' + qq' + \tilde{\chi}_1^0\tilde{\chi}_1^0$. This is observed in the detector as a 4 jet event with significant missing energy.

Looking for an excess of events with respect to Standard Model production in these three channels, one can set a limit on $M_{\tilde{\chi}_1^+}$. This limit depends on the assumed

---

[3]A *jet* is a collimated deposit of energy in the calorimeter. See Sec. 4.1 for a detailed definition.

28

SUSY parameter values. Within the allowed region for the MSSM parameter space, $M_{\tilde{\chi}_1^+} > 90 \text{ GeV}/c^2$ at the 95% Confidence Level (C.L.) if $M_{\tilde{\chi}_1^+} - M_{\tilde{\chi}_1^0} \geq 5 \text{ GeV}/c^2$ [43].

At CERN, $\tilde{\chi}_1^0$ can be produced in association with $\tilde{\chi}_2^0$ ($\tilde{\chi}_1^0\tilde{\chi}_2^0$). $\tilde{\chi}_2^0$ decays to $\tilde{\chi}_1^0\nu_l\bar{\nu}_l$, $\tilde{\chi}_1^0 l^+ l^-$, or $\tilde{\chi}_1^0 q\bar{q}$ via a $Z^0, \tilde{\nu}, \tilde{l}, \tilde{q}, h^0$, or A^0. The observable signal for these events is two jets plus missing energy or two leptons plus missing energy. Again, looking for an excess of events with respect to the Standard Model prediction, one can set a limit on $M_{\tilde{\chi}_1^0}$. Within the allowed SUSY parameter space, the 95% C.L. is $M_{\tilde{\chi}_1^0} > 30$ GeVc^2 [43].

2.4.2 Squark/Gluino

Since squarks ($\tilde{q}$) and gluinos ($\tilde{g}$) are color objects, the best limits come from hadron colliders. At the Tevatron (which is a $p\bar{p}$ collider), one looks for $\tilde{q}\bar{\tilde{q}}$, $\tilde{q}\tilde{g}$, and $\tilde{g}\tilde{g}$ production assuming that 5 of the 6 flavors of quarks are degenerate in mass. The exact branching fractions for the different sequence of decays (which are called *cascade decays*) depends on ($M_{\tilde{q}}, M_{\tilde{g}}$) and the value of the SUSY parameters.

The topology of three or more jets plus missing energy and no lepton has been studied at the Tevatron. The 95% C.L. limit is set by looking for an excess of events with respect to the Standard Model prediction. The limits from CDF [44] are:

- $M_{\tilde{g}} > 173 \text{ GeV}/c^2$ (independent of $M_{\tilde{q}}$, $M_{\tilde{q}} \gg M_{\tilde{g}}$).

- $M_{\tilde{g}} > 216 \text{ GeV}/c^2$ ($M_{\tilde{q}} = M_{\tilde{g}}$)

The limits from DØ [48] are:

- $M_{\tilde{g}} > 180 \text{ GeV}/c^2$ (independent of $M_{\tilde{q}}$, $M_{\tilde{q}} \gg M_{\tilde{g}}$).

- $M_{\tilde{g}} > 218 \text{ GeV}/c^2$ ($M_{\tilde{q}} = M_{\tilde{g}}$)

29

A complimentary channel for squark/gluino discovery is to look for same–sign dileptons plus ≥ 2 jets plus missing energy. The gluino is a Majorana fermion so that when pair–produced both gluinos can decay to a chargino of the same sign: $\tilde{g}\tilde{g} \rightarrow 4q + \tilde{\chi}_1^{\pm}\tilde{\chi}_1^{\pm}$. At CDF, preliminary results [49] in this channel give the following limits:

- $M_{\tilde{g}} > 171$ GeV/c^2 (independent of $M_{\tilde{q}}$, $M_{\tilde{q}} \gg M_{\tilde{g}}$).

- $M_{\tilde{q}} > 225$ GeV/c^2 ($M_{\tilde{q}} = M_{\tilde{g}}$)

2.4.3 Stop/Sbottom

At CERN, light $\tilde{t}_1\bar{\tilde{t}}_1$ or $\tilde{b}_1\bar{\tilde{b}}_1$ can be pair–produced. The cross–section depends on the mixing angle $\theta_{\tilde{t}}$ or $\theta_{\tilde{b}}$ because light squarks are produced via γ/Z^0. The $\tilde{t}_1$ search is sensitive to $\tilde{t}_1 \longrightarrow c\tilde{\chi}_1^0$ and $\tilde{t}_1 \longrightarrow bl\bar{\nu}_l$ [50]. The limit in the channel $\tilde{t}_1 \longrightarrow c\tilde{\chi}_1^0$ is $M_{\tilde{t}_1} > 81$ GeV/c^2 independent of $\theta_{\tilde{t}}$ and assuming $M_{\tilde{t}_1} - M_{\tilde{\chi}_1^0} > 10$ GeV/c^2. The limit in the channel $\tilde{t}_1 \longrightarrow bl\bar{\nu}_l$ is $M_{\tilde{t}_1} > 75$ GeV/c^2 independent of $\theta_{\tilde{t}}$ and assuming $M_{\tilde{t}_1} - M_{\tilde{\nu}} > 10$ GeV/c^2. The limit, independent of $\theta_{\tilde{b}}$, for $\tilde{b}_1 \longrightarrow b\tilde{\chi}_1^0$ is $M_{\tilde{b}_1} > 54$ GeV/c^2 if $M_{\tilde{b}_1} - M_{\tilde{\chi}_1^0} > 7$ GeV/c^2.

D∅ has searched for $\tilde{t}_1$ in the $\tilde{t}_1 \longrightarrow c\tilde{\chi}_1^0$ channel [51]. They look for an excess of events with 2 jets plus missing energy plus no high P_T lepton. Due to the missing energy trigger requirement, the 95% C.L. depends on $(M_{\tilde{t}_1}, M_{\tilde{\chi}_1^0})$. The maximum excluded $M_{\tilde{t}_1}$ is $M_{\tilde{t}_1} = 93$ GeV/c^2 where $M_{\tilde{\chi}_1^0} = 8$ GeV/c^2. The maximum excluded value of $M_{\tilde{\chi}_1^0}$ is $M_{\tilde{\chi}_1^0} = 44$ GeV/c^2 for $M_{\tilde{t}_1} = 85$ GeV/c^2.

D∅ has also searched for $\tilde{b}_1$ in the $\tilde{b}_1 \longrightarrow b\tilde{\chi}_1^0$ channel [52]. They combine the results for the $\tilde{t}_1$ search mentioned above with the results from a third generation

30

leptoquark[4] search. The leptoquark search uses the presence of muons associated with a jet to preferentially select events which contain a b quark. Combining the results from both analyses, the maximum $M_{\tilde{b}_1}$ excluded is $M_{\tilde{b}_1} = 115$ GeV/c^2 for $M_{\tilde{\chi}_1^0} < 20$ GeV/c^2. The maximum excluded $M_{\tilde{\chi}_1^0}$ is $M_{\tilde{\chi}_1^0} = 47$ GeV/c^2 for $M_{\tilde{b}_1} = 85$ GeV/c^2.

---

[4]A *leptoquark* (LQ) is a particle which carries both lepton and baryon numbers and is predicted to exist in Grand Unified Theories such as SU(5). The DØ search looked for the decay of $LQ \rightarrow \nu_\tau + b$.

Chapter 3

Experimental Apparatus

3.1 Tevatron

The Tevatron is a proton–antiproton ($p\bar{p}$) collider located at the Fermi National Accelerator Laboratory (FNAL) in Batavia, Illinois. The energy of each beam is 900 GeV for a total center–of–mass energy ($\equiv \sqrt{s}$) of 1.8 TeV in head–on collisions. The protons are accelerated in several steps from an initial energy of 0.025 eV to the final beam energy of 900 GeV. The antiprotons are generated using part of the proton beam and are also accelerated to 900 GeV. We will give a brief synopsis of how this is done. A schematic overview of the accelerator complex is shown in Fig. 3.1. For a detailed description see [53].

The proton beam starts as a hydrogen gas (H_2) source. The H_2 is converted into negatively charged ions (H^-) by a *magnetron* source which is shown in Fig. 3.2. The H_2 gas is turned into a plasma by static magnetic and electric fields. Positive ions and energetic particles strike the cathode surface releasing H atoms which have been absorbed. A small percentage of these atoms capture an electron to produce a H^- ion. Cesium is added to increase the efficiency of electron capture. The extractor plate draws the H^- ions to the *Cockcroft–Walton* accelerator which is located at the

32
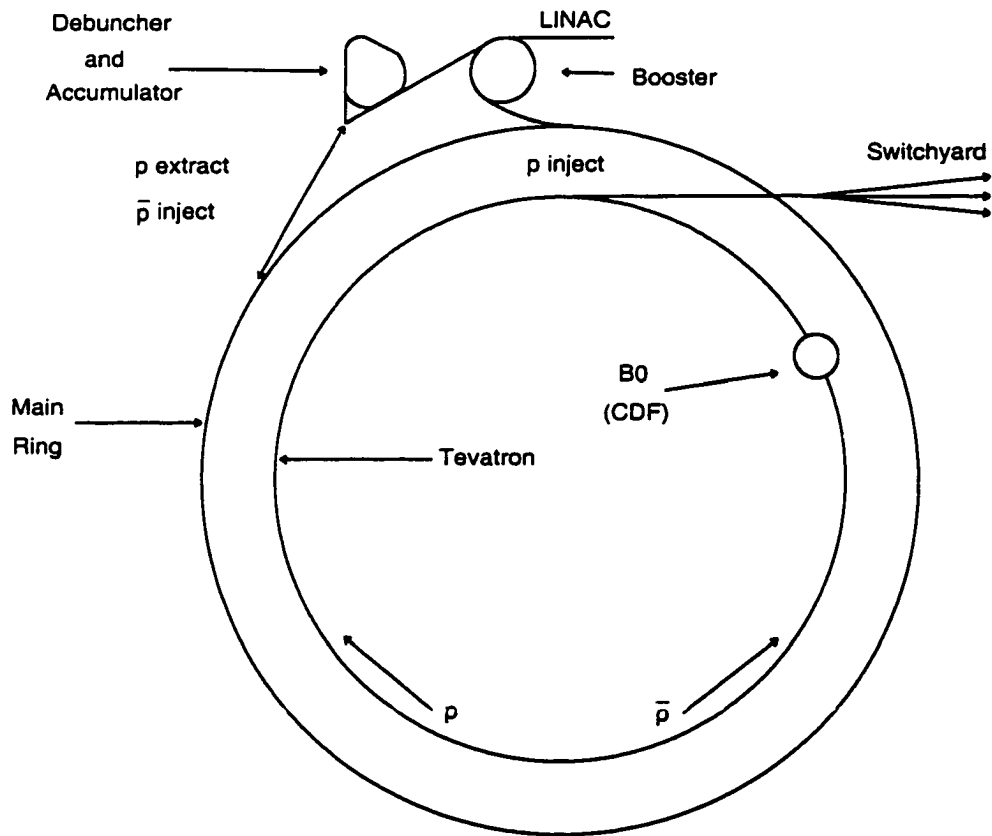
Figure 3.1: Diagram of the Tevatron accelerator complex. All the accelerator subsystems, except the Switchyard, are described in the text. The Switchyard transfers beam from the Tevatron to fixed target experiments.

33
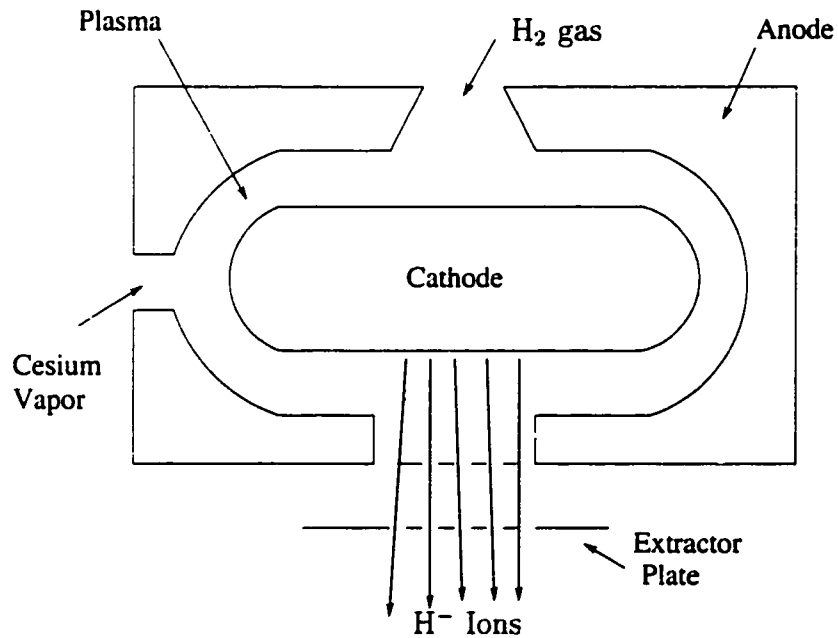
Figure 3.2: Schematic diagram of the magnetron. The magnetron creates the H^- source from H_2 gas.

beginning of the Linac. The Cockcroft-Walton is a dome–shaped capacitor held at a potential difference of -750 kV which accelerates the H^- ions to an energy of 750 keV.

The 750 keV H^- beam is then fed to the *Linear Accelerator* (*Linac*). This accelerator uses Radio Frequency (RF) techniques to accelerate the beam. A time–varying sinusoidal electric field is created inside a conducting, cylindrical cavity. When the electric field is negative, the H^- ions undergo a positive acceleration. When the field is positive, the beam is negatively accelerated. If the beam is accelerated for an entire cycle then the beam will simply oscillate inside the RF cavity. If, instead, the beam passes through a grounded, conducting tube (called a *drift tube*) when the field is positive then the beam undergoes a positive acceleration. Since the frequency of

34

the RF voltage is fixed, the length of the drift tubes must increase as the beam is accelerated.

The Linac consists of two RF accelerators. The first is called an *Alvarez* drift–tube linac. It is 79 m long and has 5 RF cavities. Each RF cavity resonates at 201.24 MHz and is powered by its own 5 MW power source. The second RF accelerator is a 67 m *side-coupled* linac. The RF principle is the same but the construction is different. These cavities resonate at 805 MHz. Since this is the fourth multiple of the Alvarez linac frequency, only every fourth RF bucket[1] is filled with beam. The beam leaves the Linac at an energy of 400 MeV.

Upon leaving the Linac, the H^- beam is put into a parallel path with the existing proton beam in the *Booster*. The proton and H^- beams are merged into a single beam by passing through the same magnetic dipole field. The merged beam is passed through a carbon foil target which strips the H^- ions of their electrons, converting the ions into protons. The beam is passed through a magnetic dipole field of the opposite polarity which bends the protons back into the correct Booster orbit. The left over beam remnant (H^-, H_2, etc.) is sent to a beam dump.

The *Booster* is a circular accelerator (*synchrotron*) of radius 75.5 m. The Booster contains 17 RF cavities plus 96 combined dipole/quadrupole magnets. The dipole magnets are *bending* magnets. They force the beam into a circular orbit. The quadrupole magnets are *focusing* magnets. If a particle deviates from the ideal orbit in a transverse direction (say the x–plane), the particle feels a restoring force in the x–plane from a quadrupole magnet and is forced back towards the ideal orbit. Unfortunately, a quadrupole magnet that focuses in the x–plane defocuses in the y–

---

[1]The sinusoidal electric field creates standing waves in the RF cavity. These standing wave packets are called RF buckets. If a RF bucket contains beam it is called a *bunch*.

plane. Therefore, quadrupole magnets which focus in the x-plane are alternated with quadrupole magnets which focus in the y-plane. As the particle travels around the synchrotron, it will oscillate about the ideal orbit in the transverse directions as it is alternately focused/defocused in the transverse planes. These oscillations are called *betatron* oscillations. Particles which deviate in the longitudinal direction (or equivalently in time) undergo *synchrotron* oscillations about the ideal orbit. This allows particles which deviate from the ideal orbit to make multiple stable orbits around the ring and still undergo acceleration.

The Booster frequency increases from 37.9 MHz to 52.813 MHz as the beam is accelerated from 400 MeV to 8 GeV. The magnetic fields are increased in sync with the increase of the RF fields. The acceleration takes $\approx$ 33 msec and the Booster cycle time is $\approx$ 66 msec ($\Leftrightarrow$ 15 Hz). The Booster contains 84 RF buckets. One bunch is lost when beam is transfered from the Booster to the *Main Ring*.

The Main Ring is a synchrotron accelerator with a radius of 1000 m. The Main Ring consists of 17 RF cavities as well as 774 dipole and 240 quadrupole magnets. The RF frequency varies from 52.8 MHz to 53.1 MHz as the proton is accelerated. The Main Ring operates in two modes. In one mode, the Main Ring accelerates protons to 150 GeV and then transfers the proton beam to the *Tevatron*. In the other mode, the Main Ring accelerates protons to 120 GeV and then transfers the beam to the *Antiproton Source* where it strikes a target producing antiprotons. In either mode, there are 1113 RF buckets.

The Tevatron and the Main Ring are housed in the same tunnel with the Tevatron located 25.5 in below the Main Ring. The Tevatron consists of 8 RF cavities operating at a frequency of 53.103 MHz to 53.104 MHz. This accelerates the proton/antiproton

36

beams to 900 GeV. The beam is kept in a stable orbit using 774 dipole and 216 quadrupole superconducting magnets. There are 1113 RF buckets in the Main Ring. This is the same number of buckets as the Main Ring which leads to a nearly 100% transfer efficiency between the Main Ring and the Tevatron. When the Tevatron is in colliding mode, there are 6 bunches of protons (15×10^{10} protons per bunch) and 6 bunches of antiprotons (5×10^{10} antiprotons per bunch) which interact every 3.5 μsec at one of 6 points along the ring. The interaction points are labeled A0–F0. CDF is located at the B0 interaction point. The other colliding beam experiment at FNAL, called D∅, is located at the D0 interaction point.

The antiprotons are made using the Main Ring plus a nickel target. The Main Ring accepts a full *batch* (83 bunches) from the Booster and accelerates them to 120 GeV. Just before transfer to the target station, the proton bunches are rotated in phase space by appropriately changing the phase of the RF fields. Before *bunch rotation*, the bunches have a large time spread but small momentum spread. After bunch rotation, the bunches have a small time spread but large momentum spread. The protons strike the nickel target producing a spray of particles which includes antiprotons. This spray then passes through a cylindrical magnet made of lithium. A 0.5 mA current is pulsed through the conductor creating a magnetic field which focuses the spray along the axis. Eight GeV antiprotons are selected from this spray by a pulsed dipole magnet which bends the antiprotons into a transport line which transfers the beam to the *Debuncher*.

The Debuncher prepares the antiprotons for transfer to the *Accumulator*. Upon entering the Debuncher, antiprotons have a large momentum spread and small time spread. The Debuncher performs a bunch rotation which turns the large momen-

37

tum/small time spread into a large time/small momentum spread. The momentum spread is reduced from 4% to 0.2%. This process takes about 0.4 s. Since a Main Ring cycle takes 2.4 s, there is 2 s in which the Debuncher can "cool" the beam before transferring it to the Accumulator. The Debuncher performs betatron and momentum stochastic cooling.

A detailed description of stochastic cooling is beyond the scope of this thesis (see [54]). A simple understanding will suffice. Consider a single particle circulating around the ring and performing betatron and synchrotron oscillations. Pickup electrodes measure the displacement of the particle relative to the ideal orbit. At a later point in the orbit, a *kicker* electrode deflects the particle in direct proportion to the signal from the pickup electrode thereby reducing the oscillation amplitude. Since this deflection is very small, it takes many orbits (say 10^6) to substantially reduce the amplitude of the oscillations. The term *stochastic* refers to applying this cooling process to a large number of particles.

Only one antiproton is produced for every 10^5 protons which strike the target. Therefore. the above process must be repeated many times to create a large collection of antiprotons. The Accumulator stores antiprotons from the Debuncher while new antiprotons are created. Beam from the Debuncher is cooled by 150 MeV reducing the orbital radius by 63 mm. Fresh antiprotons are added over the course of several hours creating a dense collection of antiprotons. This collection is called the *core*. When antiprotons are needed for collisions, a small RF field is applied to the core. This RF field captures a small portion of the core while leaving the rest undisturbed. The captured antiprotons are put in the same orbit as the injected antiprotons. These antiprotons are injected into the Main Ring where they are accelerated to 150 GeV

38
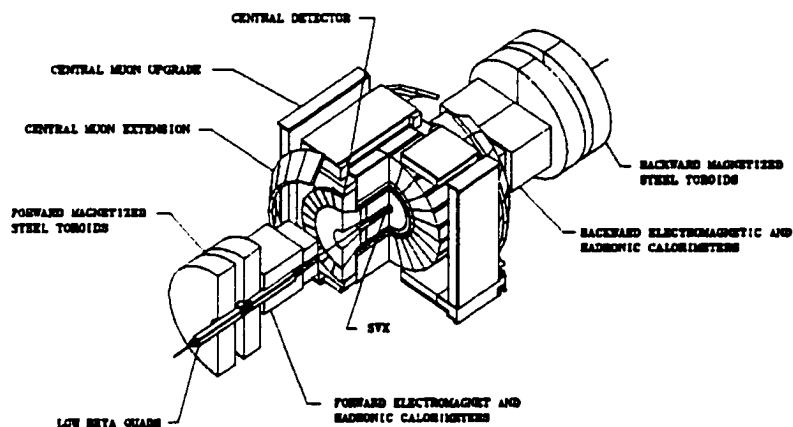
Figure 3.3: Isometric view of the CDF detector.

and injected into the Tevatron in the same manner as protons.

3.2 CDF

The Central Detector at Fermilab (CDF) detector is a cylindrical detector located at one of the 6 interaction points along the Tevatron ring (see Fig. 3.1). The CDF detector is azimuthally and forward/backward symmetric, covering nearly the entire 4π area surrounding the interaction point. The detector contains tracking chambers inside a 1.4 T superconducting solenoidal magnet 4.8 m long and 1.5 m in radius. Outside the magnet are calorimeters to measure the energy of electrons, photons, and

39

hadrons. Outside the calorimeters are muon chambers to identify energetic muons.

The CDF coordinate system is a right–handed system with the positive z–axis along the proton beam direction. The x–axis points radially away from the center of the Tevatron and the y–axis points up. More commonly, the coordinate system used is r–ϕ–η; r is the radial distance perpendicular to the beam line, ϕ is the usual azimuthal angle and η, called the *pseudorapidity*, is defined as $-\ln(\tan\frac{\theta}{2})$ where θ is the usual polar angle. For energetic particles ($E \gg m$), pseudorapidity is equivalent to *rapidity* y, $y \equiv \frac{1}{2}\ln\frac{E+p_z}{E-p_z}$. Rapidity is a convenient variable because it is a Lorentz invariant and it is additive. We also define several basic physics quantities which are used throughout this analysis. Transverse momentum (P_T) is defined as $P_T = P \cdot \sin\theta$. Transverse energy (E_T) is similarly defined as $E_T = E \cdot \sin\theta$.

An isometric diagram of the entire detector is shown in Fig. 3.3. In Fig. 3.4, we show one quadrant of the detector along with the definition of the coordinate system. Below, we briefly describe the CDF sub-systems used for this analysis.

Tracking

The magnetic field generated by the supercounducting magnet lies along the z–axis ($\vec{B} = 1.4\ T\ \hat{z}$). This causes charged particles to trace helical paths with the helix axis parallel to the z–axis. The helix is described by 5 parameters:

1. the half–curvature C (sign equals the sign of the particle)

2. the signed impact parameter D (distance of closest approach to the primary vertex; the sign is determined by the charge and the curvature)

3. z_0 (z position at closest approach)

40
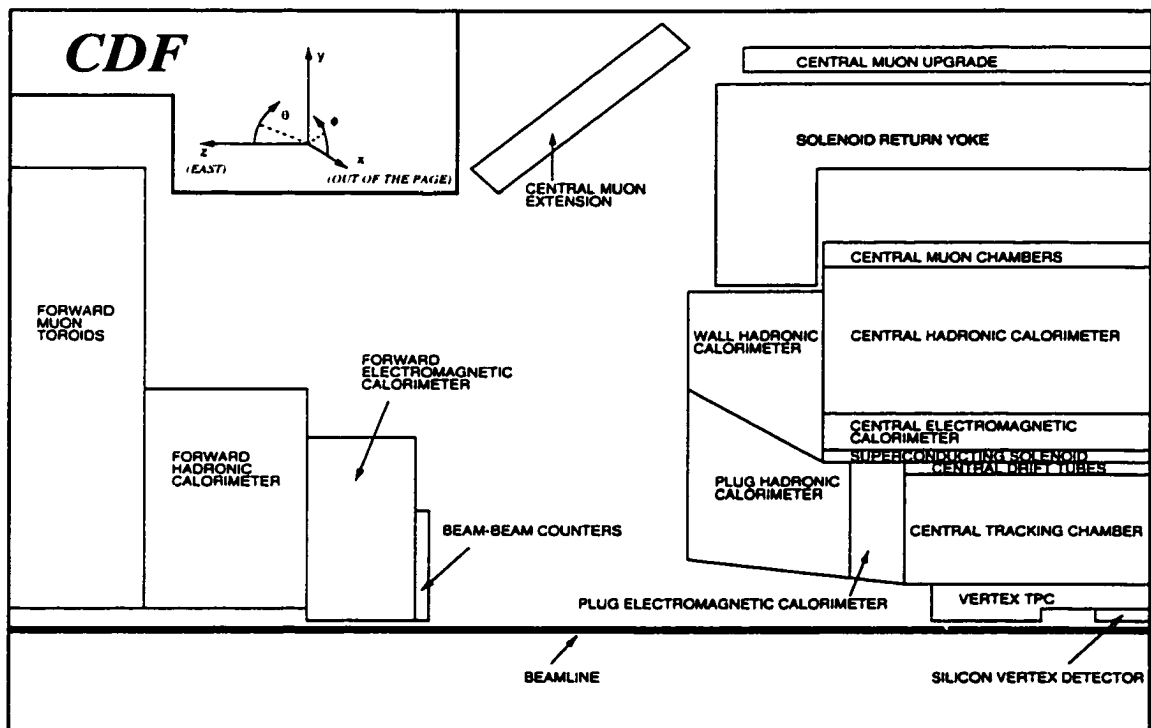
Figure 3.4: A diagram of one quadrant of the CDF detector. The CDF detector is azimuthally and forward/backward symmetric.

4. ϕ_0 (measured at closest approach)

5. $\cot \theta$ (measured at closest approach)

CDF uses 3 complimentary systems to measure these parameters: the Silicon Vertex Detector (SVX) which provides very precise tracking in the $r-\phi$ plane, the Vertex Drift Chamber (VTX) which provides $r-\phi-z$, and the Central Tracking Chamber (CTC) which also provides $r-\phi-z$ information. Below, we describe each of these detectors.

3.2.1   Silicon Vertex Detector

The Silicon Vertex Detector detector, shown in Fig. 3.5, is a silicon microstrip vertex detector that provides tracking information in the $r-\phi$ plane. The goal of the SVX is to

41
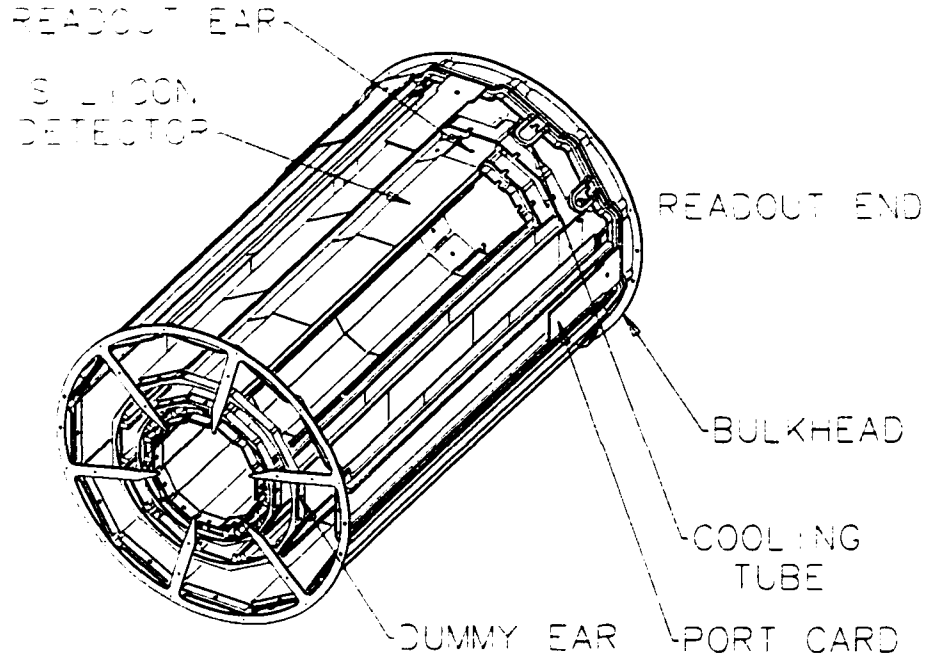
Figure 3.5: Schematic diagram of the Silicon Vertex Detector (SVX). The SVX measures the r-ϕ of tracks which have small displacements from the primary vertex.

measure tracks which have small (order 300 μm) displacements relative to the primary vertex. This allows the identification of particles (such as B hadrons) produced in the primary interaction which travel a short distance before decaying.

The original SVX was installed for the 1992-1993 data taking run (called Run 1A) [55]. An upgraded detector was installed for the 1994-1995 data taking run (Run 1B) [56]. Since this thesis uses data from Run 1B only, we will only describe the upgraded SVX detector which we refer to as the SVX'.

The SVX' is located closest to the beam pipe and covers the entire ϕ range. The

42

SVX' is cylindrically shaped and consists of 2 modules (called *barrels*) separated by a 2.15 cm gap at z=0. The active region of the SVX' covers 51.1 cm in the z–axis which corresponds to a pseudorapidity range of $|\eta| < 1.9$. Each barrel is concentric with the beam pipe and consists of 4 layers of silicon (called layers 0–3) which lie at a radius of 2.86 cm, 4.26 cm, 5.69 cm, and 7.87 cm respectively. Each layer is divided into 12 30° segments called *ladders*. Each ladder consists of 3 detector elements 8.5 cm long for a total strip length of 25.5 cm. The detector width and pitch depends on the layer. Layers 0–2 have a pitch of 60 μm and a width of 1.536 cm, 2.304 cm, and 3.072 cm respectively. Layer 3 has a pitch of 55 μm and a width of 4.224 cm. There are a total of 46080 channels.

The cluster, or hit, position resolution is 13 μm, 11 μm, 19 μm for one, two, three strip clusters respectively. Rather than form tracks from SVX' hits only, hits are added to CTC tracks in an iterative process. Starting with CTC tracks, the track parameters are extrapolated to the next tracking layer taking into account multiple scattering and ionization energy loss. A 4σ "road" or region in ϕ is defined. For each hit in the "road", the hit is added to the track candidate to form a new track candidate with a new χ^2. This process is repeated for all hits in all layers in the "road". Only those tracks with χ^2 below a pre–set maximum are kept. If there exits 4–hits tracks, the candidate with the lowest χ^2 is selected. Otherwise, the 3–hit candidate with the lowest χ^2 is selected. If no 3–hit track is selected, 2–hit candidates are searched. Single hit tracks are not considered. The impact parameter resolution for CTC+SVX' tracks is $(15 + 40/p_T)$ μm as determined from data.

43
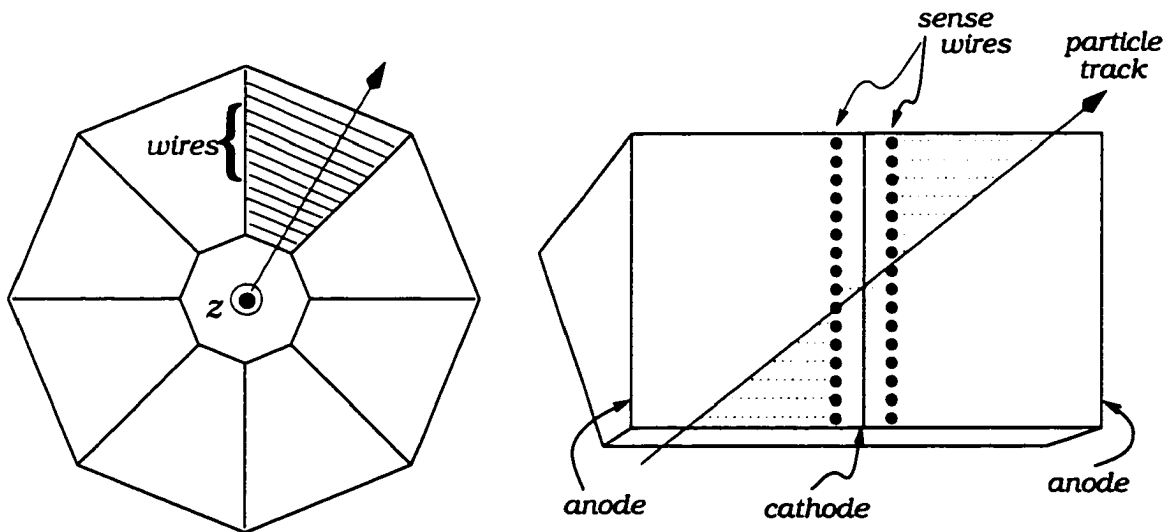
Figure 3.6: Schematic diagram of the Vertex Drift Chamber (VTX). The primary purpose of the VTX is to measure the z–vertex of the primary event.

3.2.2 Vertex Drift Chamber

The Vertex Drift Chamber [57] is a gas drift chamber located outside the SVX'. The primary purpose of the VTX is to provide an accurate (resolution = 1 mm) measurement of the z position of the primary $p\bar{p}$ interaction (called the z-vertex). In addition, the VTX can reconstruct multiple z–vertices in a single crossing. Crossings with multiple z-vertices occurred often during Run 1B because of the high instantaneous luminosities. The VTX also provides tracking information for tracks with $|\theta| < 10°$.

The VTX is cylindrically shaped with an inner radius of 8 cm and an outer radius of 22 cm. It is 2.8 m long covering the range $|\eta| < 3.25$. The VTX is divided into 28 modules. Each module is divided into 2 drift regions separated by a high voltage plane. Each drift region is divided into 8 45° segments to provide a full coverage in ϕ. The outer 10 modules have 24 sense wires strung azimuthally while the inner 18

44

modules have 16 sense wires to create space for the SVX'. Each module is rotated 15° in ϕ relative to its neighbor.

3.2.3 Central Tracking Chamber

The Central Tracking Chamber [58], shown in Fig. 3.7, is located between the VTX and the superconducting magnet. The CTC is a gas (49.6% argon:49.6% ethane:0.8% alcohol) drift chamber which provides precise 3-dimensional single particle tracking and momentum measurement.

The CTC is cylindrically shaped with a length of 3.2 m, an inner radius of 31 cm, and an outer radius of 132 cm. This covers the range $|\eta| < 1$. The CTC has 84 layers of sense wires which are divided into 9 groups called *superlayers*. Five of the 9 superlayers are called *axial* superlayers and contain 12 sense wires grouped together to form an axial *super cell*. Four of the 9 superlayers are called *stereo* superlayers and contain 6 sense wires (called a stereo super cell) which are tilted ±3° degrees relative to the beamline. By alternating axial layers with stereo layers, the CTC provides tracking in the z–plane and not just the r–ϕ plane. The number of super cells depends on the super layer. The axial super layers are layers 0,2,4,6,8 and contain 30,48,72,96,120 cells respectively for a total of 4,392 sense wires. The stereo super layers are layers 1,3,5,7 and contain 42,60,84,108 cells for a total of 1,764 sense wires.

Each super cell contains shaper wires which create a constant radial electric field ($\sim$ 1350 V/m) called a drift field. The maximum drift distance is 40 mm corresponding to a drift time of 800 ns. In a region with magnetic and electric fields perpendicular to each other a charged particle moves at an angle (called the *Lorentz* angle) to the electric field. The Lorentz angle for the CTC is 45°. Therefore, cells are
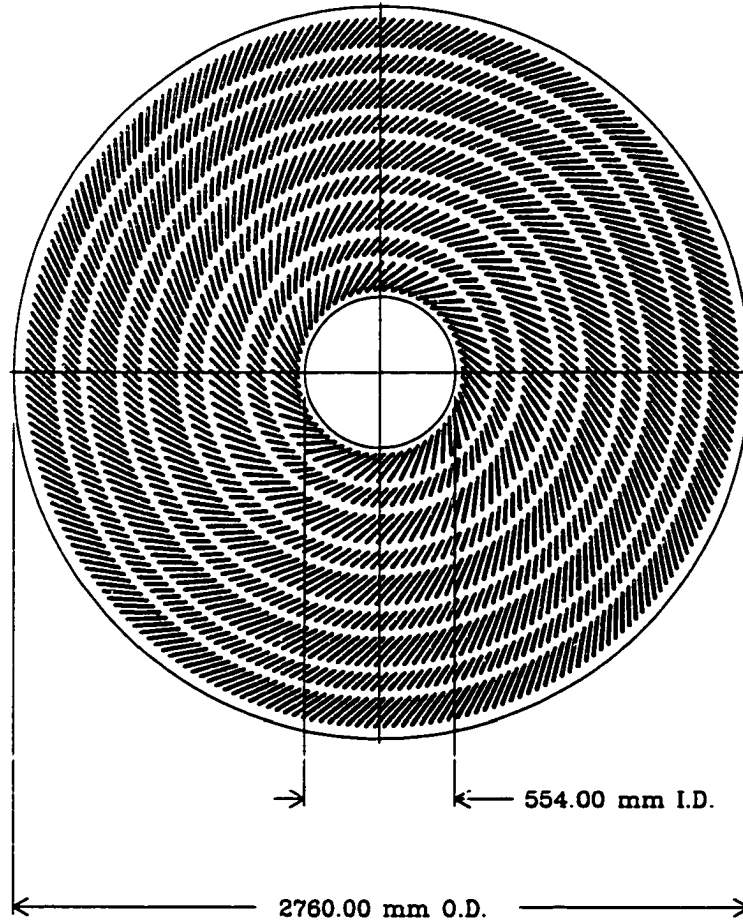
Figure 3.7: Schematic diagram of the Central Tracking Chamber (CTC). The CTC provides 3-d tracking in the central region ($|\eta| < 1.0$.)

46

placed at a 45° angle to the radial direction. This resolves the left/right ambiguity when reconstructing tracks. Only the correct left/right assignment will point to the primary vertex.

Calorimetry

Electromagnetic (EM) and hadronic (HAD) calorimeters are located outside of the solenoid. The calorimeters cover the entire ϕ range and $|\eta| < 4.2$ and are roughly divided into 3 regions: the central region ($|\eta| < 1.1$), the plug region ($1.1 < |\eta| < 2.4$), and the forward region ($2.2 < |\eta| < 4.2$). Each calorimeter is segmented in η–ϕ in a projective "tower" geometry with a tower pointing to the interaction region. Towers have an EM calorimeter lying in front of a HAD calorimeter.

All calorimeters are sampling calorimeters. This means that each component alternates layers of absorber material (lead for EM calorimeters and steel for HAD calorimeters) with the active medium (scintillator or proportional chambers). Thus, only a portion or sample of the entire energy deposition of a particle is measured. The true energy of a particle is equal to the measured energy times a scale factor. Test beam data is used to determine this scale factor. Table 3.1 shows the energy resolution of each calorimeter as determined from test beam data. Below, we give brief descriptions of each of the calorimeter sub–systems.

3.2.4 Central Calorimeter

The Central Calorimeter is divided into 48 wedges; Fig. 3.9 shows a diagram of one wedge. The EM calorimeter (CEM) lies closest to the beam line [59]. A CEM wedge is segmented into 10 towers; $\Delta\eta \times \Delta\phi = 0.11 \times 15°$ per tower. This covers the range

47

Component	η range	Energy resolution
CEM	$|\eta| < 1.1$	$13.7\%/\sqrt{E_T} \oplus 2\%$
PEM	$1.1 < |\eta| < 2.4$	$22\%/\sqrt{E_T} \oplus 2\%$
FEM	$2.2 < |\eta| < 4.2$	$26\%/\sqrt{E_T} \oplus 2\%$
CHA	$|\eta| < 0.9$	$50\%/\sqrt{E_T} \oplus 3\%$
WHA	$0.7 < |\eta| < 1.3$	$75\%/\sqrt{E_T} \oplus 4\%$
PHA	$1.3 < |\eta| < 2.4$	$106\%/\sqrt{E_T} \oplus 6\%$
FHA	$2.3 < |\eta| < 4.2$	$137\%/\sqrt{E_T} \oplus 3\%$

Table 3.1: A list of the η coverage and the energy resolution of the different calorimeters. The symbol "$\oplus$" means add in quadrature.

$|\eta| < 1.1$. Nominally, there are 31 layers of 5 mm thick scintillator alternated with 31 layers of 3.2 mm thick lead absorber. However, to maintain a constant radiation length [2] as a function of polar angle, acrylic was substituted for lead in certain layers.

Embedded in the CEM between the eighth absorber layer and ninth scintillator layer is a strip chamber called the CES. The CES measures the shower position and the transverse shower development. The measurements are made using 64 anode wires which are orthogonal to 128 cathode strips. Fig. 3.8 shows a diagram of one CES chamber.

In the central region, there are actually 2 hadron calorimeters: the Central Hadron Calorimeter (CHA) and the Endwall Hadron Calorimeter (WHA) [60]. The CHA lies directly behind the CEM and is segmented into 8 towers; $\Delta\eta \times \Delta\phi = 0.11 \times 15°$ per tower. The WHA is segmented into 6 towers; $\Delta\eta \times \Delta\phi = 0.11 \times 15°$ per tower. The CHA and WHA overlap with the CHA covering $|\eta| < 0.9$ and the WHA covering

---

[2]The radiation length, X_0, of a material is defined as the distance an electron must travel through the material to lose all but $1/e$ of its energy.

48

Strip Spacing = 1.67 cm in Towers 0–4
2.01 cm in Towers 5–9

Wire Spacing = 1.45 cm Throughout

Cathode Strips →

z

x

Anode Wires (ganged in pairs)
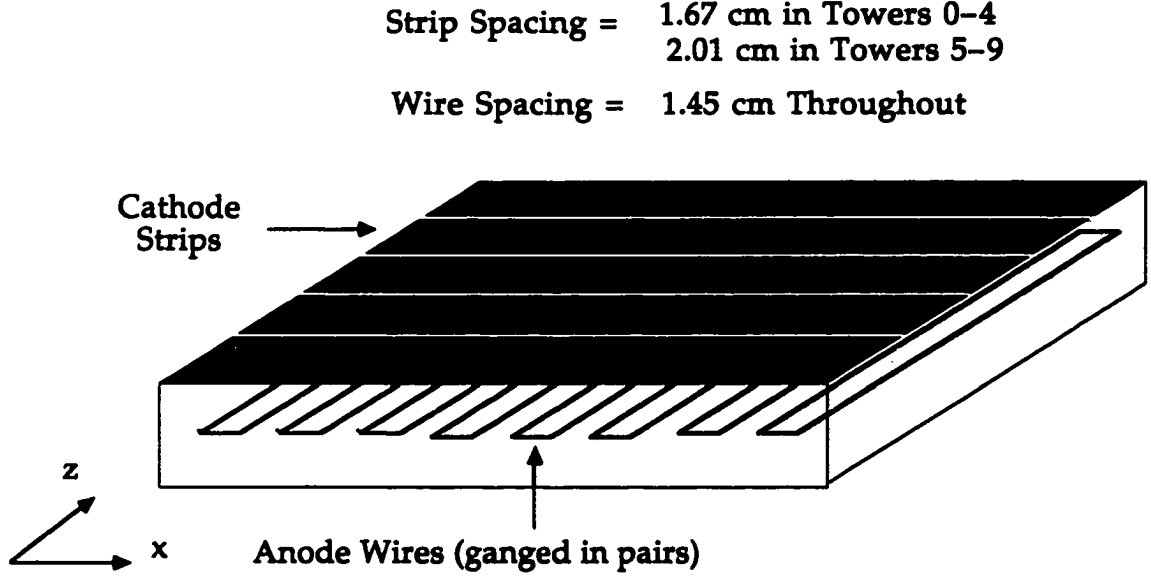
Figure 3.8: Schematic diagram of the Central Strip Chamber (CES). The CES measures the transverse development of electromagnetic showers in the Central Electromagnetic calorimeter.

$0.7 < |\eta| < 1.3$. Both the WHA and the CHA use steel as the absorber and scintillator as the active medium. The CHA has 32 layers of 10 mm thick absorber and 25 mm thick scintillator. The WHA has 15 layers of 10 mm thick absorber and 51 mm thick scintillator.

3.2.5 Plug Calorimeter

The Plug Calorimeter is divided into two modules located at each end of the solenoid (see Fig. 3.4) which are divided into 4 quadrants. Each module contains an electromagnetic calorimeter (PEM) [61] and a hadronic calorimeter (PHA). The PEM and PHA have the same tower size: $\Delta\eta \times \Delta\phi = 0.09 \times 5°$. The PEM covers the range $1.1 < |\eta| < 2.4$ while the PHA covers the range $1.3 < |\eta| < 2.4$.

The PEM uses 34 layers of 2.7 mm thick lead absorber and 34 layers of plastic

49
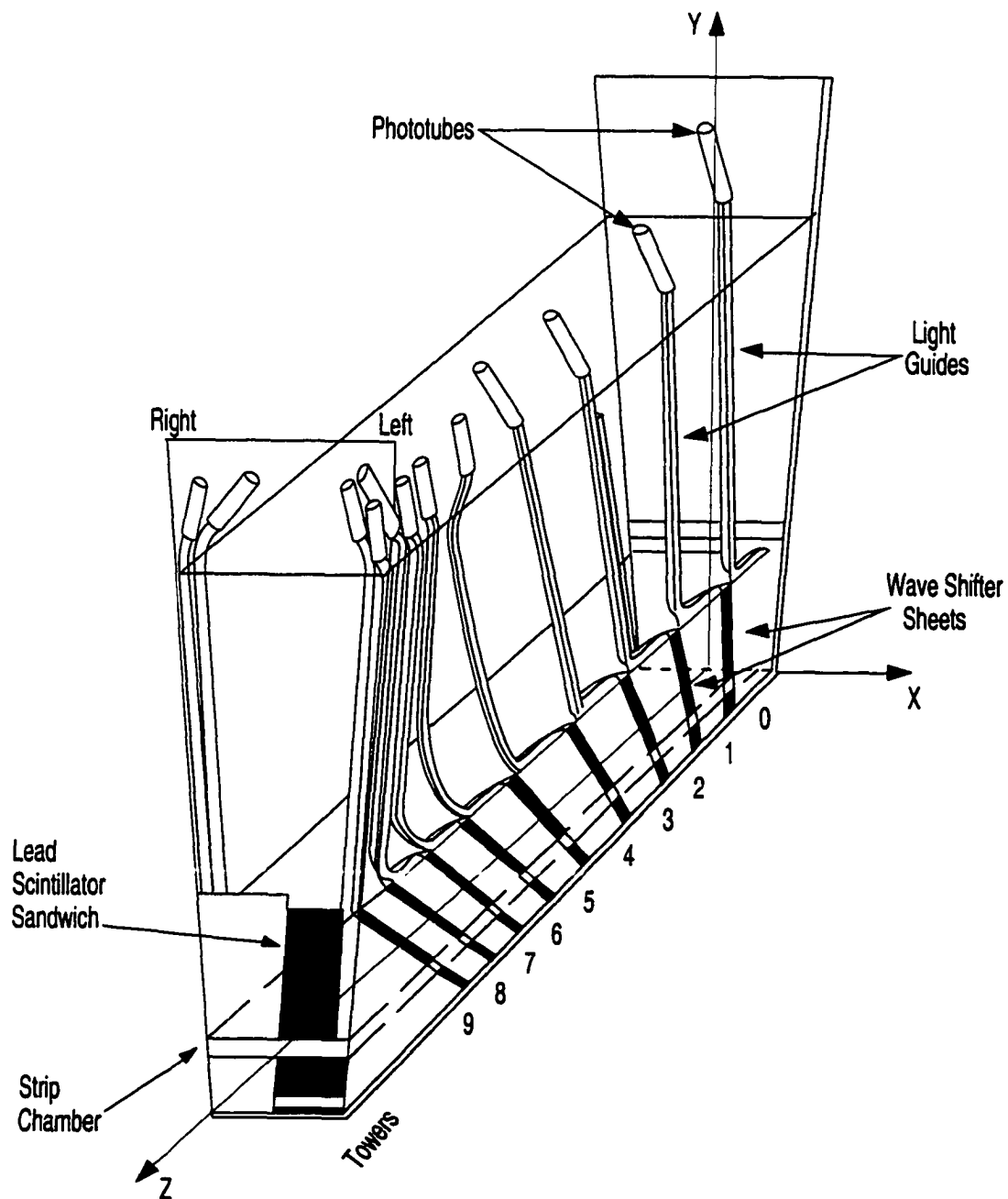
Figure 3.9: Schematic diagram of one wedge of the Central Calorimeter. Shown are the waveshifter and waveguide elements which transfer light from the scintillator to the phototubes.

50

proportional tubes. The proportional tubes, which use a 50–50 mixture of argon-ethane, have a square cross section of 7 mm × 7 mm. The anode wire is 50 μm diameter gold–plated tungsten. Longitudinally, the PEM is divided into 3 segments. The first and third segments contain 5 layers while the second segment contains 24 layers.

The PHA has a design similar to the PEM. The PHA uses 20 layers of 51 mm thick steel and plastic proportional tube chambers. The PHA proportional tubes are 14 mm × 8 mm. The PHA has only one longitudinal segment.

3.2.6 Forward Calorimeter

The Forward Calorimeter is very similar to the Plug Calorimeter. The Forward Calorimeter is divided into two modules which are further divided into 4 quadrants. The Forward Calorimeter has an EM calorimeter (FEM) [62] and a HAD calorimeter (FHA) [63]. The FEM covers the range $2.2 < |\eta| < 4.2$ with a tower size of $\Delta\eta \times \Delta\phi = 0.1 \times 5°$. The FHA covers the range $2.3 < |\eta| < 4.2$ with the same tower size as the FEM.

The FEM uses 30 layers of lead and 30 layers of proportional tubes. The lead sheets are 4.8 mm thick and the proportional tubes are 10 mm × 7 mm. Longitudinally, the FEM is divided into 2 segments, 15 layers thick.

The FHA uses 27 layers of steel and 27 layers of proportional tubes. The steel sheets are 51 cm thick and the proportional tubes are 15 mm × 10 mm. The FHA has only 1 longitudinal segment.

51

Muon subs-systems

Energetic muons traverse the detector without depositing much energy in the hadronic or electromagnetic calorimeters. Therefore, drift chambers are placed outside the calorimeters to detect muons. The EM and HAD calorimeters act as shielding, reducing the backgrounds from hadrons and other non–muon particles in the muon detectors. We describe the muon sub–systems below.

3.2.7 Central Muon Detector

The Central Muon Detector (CMU) [64] lies directly behind the central calorimeter wedges. Each CMU wedge covers $|\eta| < 0.6$ and $12.6°$ leaving a $2.4°$ gap in coverage per wedge. Each CMU wedge is further divided into 3 modules which cover $4.2°$.

Each module consists of 4 layers of 4 rectangular drift tubes which use a 50–50 mix of argon–ethane bubbled through ethanol as the active gas. The drift tube dimensions are 63.5 mm wide × 26.8 mm high × 2261 mm long. A 50 μm sense wire lies at the center of the tube. Two of the four sense wires (from alternating layers) lie on a radial vector which points to the interaction point. The other two sense wires lie along a radial vector which is shifted by 2 mm at the midpoint of the chamber. Shifting the sense wires resolves the ϕ ambiguity when reconstructing tracks as well as providing a crude measure of the muon p_T for triggering purposes. Charge division measurements give the track position along the sense wire. Fig. 3.10 is a diagram of a muon track traveling through a single module.
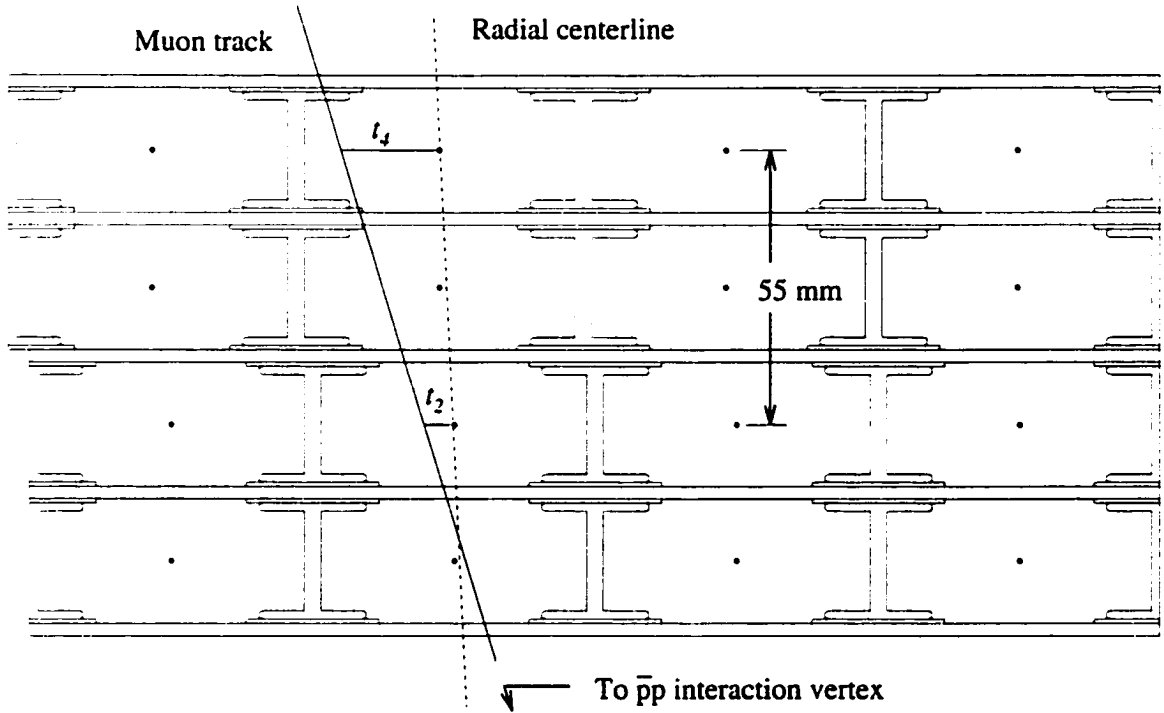
Figure 3.10: Schematic diagram of one Central Muon module. Shown is a track going through a 4 × 4 array of drift tubes.

3.2.8 Central Muon Upgrade

The Central Muon Upgrade (CMP) [65] lies behind the CMU with a 0.6 m thick layer of steel separating the two detectors. The extra layer of steel reduces the background from "punch throughs" which are hadronic jets that make it through the calorimeters to the muon chambers. The CMP uses 4 layers of drift tubes to measure the position/momentum of muon tracks.

3.2.9 Central Muon Extension

The Central Muon Extension (CMX) [65] extends the muon cover to $0.6 < |\eta| < 1.0$. The CMX consists of 4 free-standing arches. The CMX uses 4 drift tube layers for

53

muon detection. The drift tubes are sandwiched between 2 layers of scintillator which are used for triggering purposes.

Luminosity

At CDF, the luminosity is measured using the Beam–Beam Counters (BBC). The BBC is a plane of scintillator located in front of each FEM module (see Fig. 3.4) 5.8 m along the beamline from the nominal interaction point. Each module consists of 16 scintillator plates plus photomultiplier tubes forming a rectangle around the beam pipe. The BBC covers the range $3.2 < |\eta| < 5.9$. If we know the cross-section for tracks from a $p\bar{p}$ interaction to generate hits in the BBC (σ_{BBC}), then the instantaneous luminosity can be derived from the number of counts registered in the BBC.

3.2.10 Trigger System

A crossing time of 3.5 μs corresponds to a raw event rate of 280 kHz. Storing the information for every event is impossible. CDF implements a three level trigger system to reduce the amount of data to a manageable level. The first two triggers (Level 1 and Level 2) are hardware triggers while the third trigger (Level 3) is a software trigger.

The Level 1 trigger uses the analog outputs from the various detector components. Calorimetry information is grouped into 42×24 trigger towers in η–ϕ space; $\Delta\eta \times \Delta\phi = 0.2 \times 15°$ per tower. The calorimeter triggers, used to identify jets and electrons, require at least one trigger tower above a preset threshold (which depends on the calorimeter component). Muon triggers require multiple hits in the muon chambers.

54

Tracking information is not used.

The Level 2 trigger uses the same analog outputs as Level 1 but in a more sophisticated manner. Calorimeter towers are clustered using a nearest-neighbor algorithm. The E_T, ϕ, and η of each cluster are calculated. Tracks in r-ϕ from the CTC are reconstructed by the Central Fast Tracker (CFT) with a momentum resolution of $\delta P_T/P_T \approx 0.035 \times P_T$. Track segments from the 3 central muon chambers are also reconstructed.

Information from different detector sub–systems can be combined to form Level 2 trigger decisions. For example, CFT tracks which point to energetic EM clusters form electron candidates. Muon candidates are formed from CFT tracks which point to muon track segments. The Level 2 triggers can also be *prescaled.* Instead of keeping every event that passes a trigger, one can keep 1 of every N events that pass the trigger. N is the prescale factor. N can be either a *static* prescale or a *dynamic* prescale. A dynamic prescale changes value as the instantaneous luminosity changes. A static prescale is independent of the instantaneous luminosity.

The Level 3 trigger is implemented by commercial processors which can execute approximately one billion instructions per second. These processors use the same algorithm as the offline analysis. Full three–dimensional CTC track reconstruction is performed. Also, complex physics object identification (such as tau or jets) is performed. Events passing Level 3 are written to tape at a rate of $\approx$ 5 Hz.

Chapter 4

Data Selection

We remind the reader of the signals for which we are searching:

$$p\bar{p} \to \tilde{t}_1\bar{\tilde{t}}_1 \to c\bar{c} + \tilde{\chi}_1^0\tilde{\chi}_1^0 \tag{4.1}$$

$$p\bar{p} \to \tilde{b}_1\bar{\tilde{b}}_1 \to b\bar{b} + \tilde{\chi}_1^0\tilde{\chi}_1^0 \tag{4.2}$$

In the detector, we observe these events as events with large $\not{E}_T$, 2 high E_T jets, and no high P_T lepton(s). Further, the jets are due to heavy (c or b) quark hadrons which have a long (for quarks) lifetime. These hadrons travel a short distance before decaying to lighter hadrons. In Chapter 5, we describe how we use the SVX′ to select events with heavy flavor jets. In this chapter, we describe the kinematic requirements applied to select a sample of events enriched in stop or sbottom (if they exist). We call this sample the **Pretagged** sample.

4.1 Jet Algorithm

Jets are collimated collections of particles formed by quarks and gluons traveling through the calorimeter. CDF uses a fixed–cone (in η–ϕ space) algorithm to identify jets [66]. The algorithm starts by generating a list of towers (called seed towers) that

56

have an energy $E_T > 1$ GeV [1]. Preclusters are formed from seed towers by chaining together contiguous seed towers with decreasing E_T. If the tower is outside a 7×7 window around the seed tower, then the tower is used to form a new precluster.

For each precluster, the E_T weighted centroid in η–ϕ is calculated. A cone of radius $R = \sqrt{(\Delta\eta)^2 + (\Delta\Phi)^2} = 0.4$ is formed around the centroid. All towers with $E_T > 100$ MeV and which have their centroid lying within the cone of the precluster are added to the precluster to form a cluster. The E_T weighted centroid of the cluster is calculated and a new cone around the centroid is drawn. The process of adding/removing clusters and recomputing the centroid is iterated until the tower list is stable.

There are several cluster overlap situations to consider. If one cluster is completely contained in another cluster, then the smaller cluster is dropped. If there is only a partial overlap, then the overlap fraction is computed. The overlap fraction is equal to the sum of the E_T of the common towers divided by the E_T of the smaller cluster. If this fraction is greater than 0.75, then the clusters are merged. If the fraction is less than 0.75, then the common towers are associated to the cluster closest in η–ϕ space. The centroid is recomputed and the overlap procedure is iterated until the tower list for each cluster is stable.

The jet four–vector, (E, p_x, p_y, p_z), is computed by summing the tower four–vectors. The tower four–vectors are computed assuming all particles are massless and the direction is defined as above. From the jet four–vector, we can compute the E_T, ϕ, η, etc. of the jet.

---

[1] The transverse energy, E_T, is defined as $E_T \equiv E \cdot \sin\theta$. E is the energy deposited in the calorimeter tower and the direction is defined as the unit vector from the origin to the face of the calorimeter tower at shower maximum.

Calorimeter	Energy threshold (MeV)
CEM	100
CHA	100
WHA	100
PEM	300
PHA	500
FEM	500
FHA	800

Table 4.1: Energy thresholds for a calorimeter tower to be included in the $\vec{\not{E}}_T$ calculation.

4.2 $\not{E}_T$

Neutral, stable, weakly–interacting particles (such as ν or possibly $\tilde{\chi}_1^0$) traverse the detector without interacting. We infer their presence by an imbalance of energy in the calorimeter. The transverse missing energy ($\equiv \vec{\not{E}}_T$) is defined as the negative of the vector sum of transverse energy in all calorimeter towers with $|\eta| < 3.6$ [67] above a minimum energy threshold (see Table 4.1):

$$\vec{\not{E}}_T \equiv \sum_{|\eta|<3.6} \vec{E}_T$$

4.2.1 Monte Carlo programs

We use several different Monte Carlo (MC) programs to simulate the signal samples and the background samples. $\tilde{t}_1\bar{\tilde{t}}_1/\tilde{b}_1\bar{\tilde{b}}_1$ kinematics and acceptances are modeled using the PYTHIA generator [68]. The PYTHIA Monte Carlo generator includes production and decay of supersymmetric particles [69]. PYTHIA uses a leading

58

order QCD matrix calculation to simulate the hard–scattering sub–process. The partons are then evolved into final state particles using coherent parton showering and string hadronization. The $W(\to l\nu_l)+$ jets ($l = e/\mu/\tau$) backgrounds are simulated using the VECBOS generator [70]. VECBOS is a tree–level matrix calculation of the parton final states. VECBOS is interfaced with HERWIG [71] to evolve the partons into hadrons. HERWIG uses coherent parton showering and cluster hadronization. VECBOS is also used to simulate $Z^0(\to l^+l^-)+$ jets ($l = e/\mu/\nu$) backgrounds. $Z^0(\to \tau\bar\tau)$ and $WW/WZ/ZZ$ (diboson) backgrounds are simulated using ISAJET [72]. Like PYTHIA, ISAJET uses a leading–order QCD matrix element calculation for the hard–scattering subprocess. However, ISJAET uses incoherent gluon emission and independent fragmentation to evolve the outgoing partons. Collectively, the $W(\to l\nu_l)$, $Z^0(\to l^+l^-)$, and diboson backgrounds are referred to as *electroweak* or $W/Z/t\bar{t}/Diboson$ backgrounds. We use PYTHIA to simulate QCD multijet backgrounds, which have only quarks and gluons in the final state. All MC samples are processed through a full simulation of the CDF detector. This simulation produces the same output as real data. Therefore, we can apply the same reconstruction code to MC as we do to data.

In general, the number of events due to each process (background or signal) is given by:

$$\# \ of \ events \ = \ \sigma \cdot \int \mathcal{L}dt \cdot a_{tot}$$

where σ is the cross-section, $\int \mathcal{L}dt$ is the integrated luminosity, and a_{tot} is the total acceptance as determined by MC. For $\tilde{t}_1\bar{\tilde{t}}_1$ and $\tilde{b}_1\bar{\tilde{b}}_1$ we use the NLO cross section from [42]. For $t\bar{t}$ we use the cross section as measured by CDF: $\sigma_{t\bar{t}} = 7.5 \pm 1.8$ pb^{-1}. The diboson backgrounds ($WW/WZ/ZZ$) and $Z^0(\to \tau\bar\tau)+ \geq 0$ jets are normalized

59

Sample	σ (pb)	scale factor
$W(\to l\nu_l)+ \geq 1$ jets	333	1.
$W(\to l\nu_l)+ \geq 2$ jets	837	0.9
$Z^0(\to l^+l^-)+ \geq 2$ jets $(l = e/\mu)$	32.1	1.
$Z^0(\to l^+l^-)+ \geq 2$ jets $(l = \nu)$	64.1	1.

Table 4.2: VECBOS MC cross section scale factors [73].

to the ISAJET cross sections: $\sigma_{WW} = 6.4$ pb, $\sigma_{WZ} = 0.86$ pb, $\sigma_{ZZ} = 0.73$ pb, and $\sigma_{Z^0(\to \tau\bar{\tau})} = 8.0$ pb. For the $W(\to l\nu_l)+$ jets and $Z^0(\to l^+l^-)+$ jets backgrounds, we use the cross sections returned by VECBOS scaled by an appropriate factor. The scale factor is determined by comparing the measured cross section for these processes with the predicted cross section from VECBOS [73]. The cross sections and the scale factors for the various VECBOS samples are given in Table 4.2. Since the $W/Z+$ jets backgrounds are the largest source of backgrounds in our final sample, in Sec. 4.6.1 we check the normalization and kinematics using a control data sample.

4.3 $\not{E}_T$ data sample

There are two distinct trigger paths one could follow at CDF to select events with large $\not{E}_T$ and 2 large E_T jets. One could start with data samples created from triggers that require at least one jet with $E_T > X$ GeV where X = 20,50,70, or 100. These samples are called the *JET20/JET50/JET70/JET100* samples, respectively. Or one could start with a data sample created from a trigger that requires $\not{E}_T > 30$ GeV. This sample is called the $\not{E}_T$ sample.

We choose to start with the $\not{E}_T$ sample. We do this because the jet samples are prescaled (see Sec 3.2.10) thus lowering the integrated luminosity of our data sample.

60

calorimeter	threshold (GeV)
CEM	8
PEM	11
FEM	51
CHA	12
PHA	51
FHA	51

Table 4.3: Tower E_T thresholds for the Level 1 calorimeter trigger.

This, in turn, reduces our sensitivity at large squark mass where we are statistics-limited. The drawback to using the $\not{E}_T$ sample is that we are not sensitive in the region of low squark mass and low neutralino mass. As described in Sec. 2.4.3, that region of parameter space is addressed by other experiments. Below, we describe the Level 1/2/3 triggers used in this analysis.

4.3.1 Level 1 trigger

There is no explicit Level 1 $\not{E}_T$ trigger. $\not{E}_T$ is a global variable combining information from multiple calorimeter sub–systems. The Level 1 calorimeter trigger works on a tower–by–tower basis; at least one trigger tower must be above threshold. We show the trigger tower E_T thresholds used in Table 4.3. We assume that any event with offline $\not{E}_T > 30$ GeV has at least one trigger tower that is over threshold. We therefore assume the Level 1 trigger efficiency is 100%.

4.3.2 Level 2 trigger

The Level 2 trigger is the first trigger to combine information across different detector elements. Using the same trigger tower segmentation as Level 1 (see 3.2.10), the Level 2 $\vec{E}_T$ is formed by taking the negative of the vector sum of E_T over all calorimeter towers (EM+HAD) with $|\eta| < 3.6$. There are 3 Level 2 $\rlap{/}{E}_T$ triggers. The first trigger (MET_20_CEM_16_XCES) requires Level 2 $\rlap{/}{E}_T > 20$ GeV plus a central photon with $E_T(EM) > 16$ GeV. Our signal topology does not contain a photon so we do not use this trigger. The second trigger (MET_35_TEX_2_NOT_GAS) requires Level 2 $\rlap{/}{E}_T > 35$ GeV plus at least 2 clusters which have $E_T > 1$ GeV and are not in the forward calorimeter. The third trigger (MET_35_TWO_JETS) also requires $\rlap{/}{E}_T > 35$ GeV but only requires at least 1 central cluster with $E_T(EM) > 2$ GeV. The second and third triggers are appropriate for our signal topology. We therefore require events to pass either of these triggers which we collectively refer to as the L2_MET_35* trigger.

Trigger simulation

To simulate the L2 MET_35* trigger, we use a parameterization derived from [74]. This note determines the trigger efficiency as a function of $\rlap{/}{E}_T$ from $W^{\pm}(\to e^{\pm}\nu_e) + 0$ jet and $W^{\pm}(\to \tau^{\pm}\nu_\tau) + 0$ jet events. We fit the data for $W^{\pm}(\to \tau^{\pm}\nu_\tau)$ to the function:

$$\epsilon(\rlap{/}{E}_T) \;=\; A + \frac{1 - A}{1 + exp(-(\rlap{/}{E}_T - B)/C)}$$

The fitter returns $A = 0.0051 \pm 0.0056$, $B = 39 \pm 1$, and $C = 3.1 \pm 0.5$ with a $\chi^2/dof = 1.5$. The data+fit is shown in Fig. 4.1. If we fit the electron sample to the
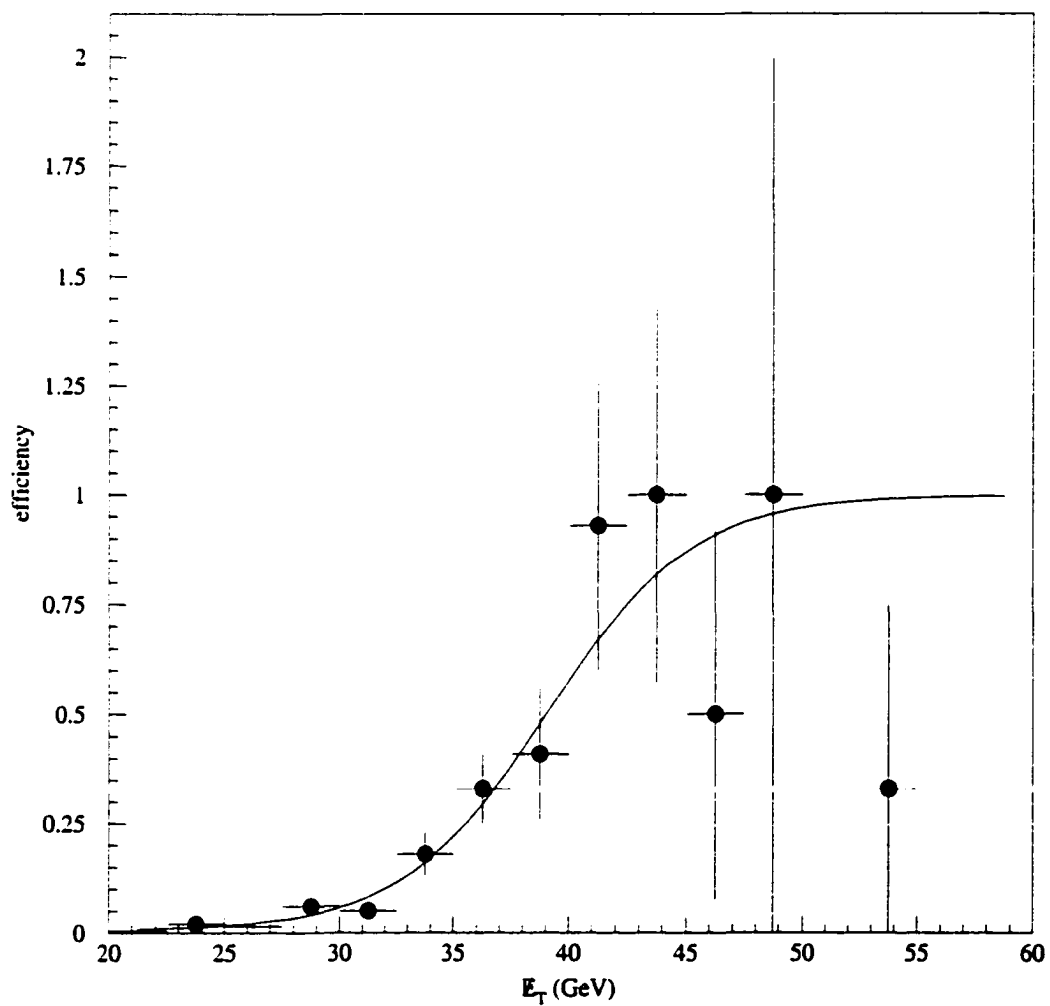
62

Figure 4.1: Parameterization of the L2 MET_35* trigger using $W^{\pm}(\to \tau^{\pm}\nu_{\tau})$ data from [74].
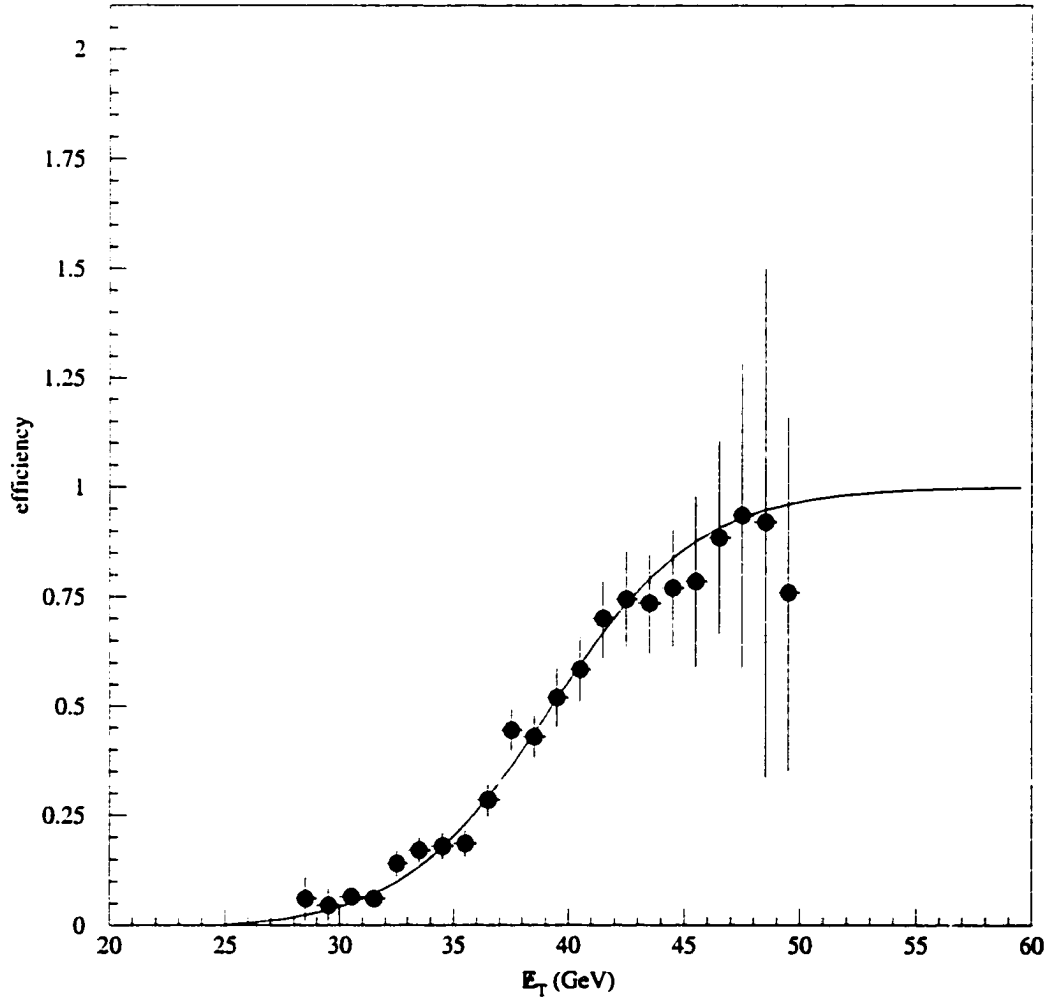
63

Figure 4.2: Parameterization of the L2 MET_35* trigger using $W^{\pm}(\to e^{\pm}\nu_e)$ data from [74].

64

same function (Fig. 4.2), we get $A = -0.011 \pm 0.030$, $B = 39 \pm 0.3$, and $C = 3.2 \pm 0.4$ with a $\chi^2/dof = 0.6$. We use the fit from the $W^\pm(\rightarrow e^\pm \nu_e) + 0$ jet data for our trigger simulation.

4.3.3 Level 3 Trigger

The Level 3 trigger uses the natural tower size of the calorimeters (see 3.2.4–3.2.6) to compute the offline $\not{E}_T$. The Level 3 $\not{E}_T$ trigger, called COMBINED_EXOB_MET, requires offline $\not{E}_T > 30$ GeV. The $\not{E}_T$ data sample consists of all events which pass the COMBINED_EXOB_MET trigger. It is important to note that the $\not{E}_T$ data sample does not require the L2_MET_35* trigger.

4.4 FILT1 sample

The $\not{E}_T$ data sample, which has an integrated luminosity of 89.6 ± 3.7 pb^{-1}, contains 2,517,998 events. There are several ways for events to populate the $\not{E}_T$ sample:

Accelerator effects: As mentioned in Sec 3.1, the Main Ring is run while CDF is taking data. Since the Main Ring is directly above the CDF detector, stray particles from the Main Ring beam can hit the CDF detector and preferentially deposit energy at the top of the calorimeters. We call this energy deposition *Main Ring splash*. If the Main Ring splash occurs while the detector is readout, the extra energy will cause an apparent imbalance of energy. In Run 1B, the high luminosities lead to events having multiple $p\bar{p}$ collisions within the same bunch. An incorrect choice of the z vertex of the $p\bar{p}$ collision can also lead to large $\not{E}_T$.

Detector effects: Noise in the detector electronics and other electronic malfunctions can cause towers to appear to have energy. These "spikes" in energy can lead to large

65

$\not{E}_T \geq 35$ GeV using highest $\sum P_T$ z–vertex
E_T of out–of-time towers ≤ 10 GeV
# of out–of-time towers ≤ 5

Table 4.4: Selection requirements used to create the **FILT1** sample [75]

$\not{E}_T$.

Fake–$\not{E}_T$ Physics: Cosmic rays which pass through the detector coincident with a $p\bar{p}$ collision can create a large $\not{E}_T$ signal. QCD multijet events, which are $p\bar{p}$ collisions with only quarks and gluons in the final state, can also have large $\not{E}_T$, if the jet energy is mis–measured by the calorimeter; in this case the event has $\not{E}_T$ that lies preferentially along the jet axis. The energy mis–measurement is caused by non–linearities in the calorimeter response, cracks in the calorimeter coverage, and random fluctuations in the energy sampling.

Real–$\not{E}_T$ Physics: Some $p\bar{p}$ collisions produce high P_T vector bosons (W or Z). The vector bosons can then decay to final states that contain neutrinos: $W(\rightarrow l\nu_l)$ and $Z^0(\rightarrow \nu\bar{\nu})$. Neutrinos are neutral, stable and colorless. They leave the detector without interacting causing an imbalance in energy. Our signal also contains neutral, stable, colorless particles (neutralinos). As we will show, vector boson production is the biggest source of backgrounds to our final signal sample.

Table 4.4 shows the 3 selection requirements we apply to create what we call the **FILT1** sample. The goal of these cuts is to remove accelerator backgrounds. We now describe each requirement and the motivation for using them.

66

Δz pair	$R(|\Delta z|)$
$z(default) - z(\sum P_T)$	12.
$z(jet1) - z(jet2)$	1.
$z(jet1) - z(default)$	11.
$z(jet1) - z(\sum P_T)$	1.

Table 4.5: Z–vertex association. $R(|\Delta z|)$ is the percentage of events in a QCD data sample which have the pair of z–vertices greater than 2.5 cm from each other [75]. See Sec 4.4.1 for the definition of the z–vertex pairs.

4.4.1 Missing E_T with highest $\sum P_T$ z–vertex

To calculate physics quantities of interest ($\not{E}_T$, jet energies, track momenta/position, etc.) one must know the primary vertex on an event by event basis. The spatial distribution of primary vertices over the course of a single data taking run depends on the beam profile. In the x and y directions, the beam has a low emittance [2]. The x and y components of the primary vertex are Gaussian–distributed about zero with a sigma of 36 μm each [76]. In the z direction, the emittance is much higher. The z–vertex is Gaussian–distributed about zero with a sigma of 30 cm. For events with multiple primary vertices, the difference in the z–vertex can be quite large.

The default z–vertex when calculating the offline $\not{E}_T$ and jet energies is the z–vertex with the most number of VTX hits. An alternate choice of the z–vertex is the z–vertex with the highest $\sum P_T$ of tracks associated to the z–vertex. For QCD data samples, these choices of z–vertices differ in 12% of events [75]. We determine the "correct" vertex by comparing how often the z–vertex of the first and second leading E_T jet is the default z–vertex versus the highest $\sum P_T$ vertex in a QCD sample of

---

[2] *Emittance* is defined as the area in phase space that contains 95% of the beam.

67

events [75]. The following procedure is used to find the z–vertex of a jet:

1. All tracks in the event are associated to a jet by requiring $\Delta R \leq 0.4$ between the jet axis and the track.

2. Using the track z_0, each track is associated to the closest z–vertex with a maximum $|\Delta z|$ of 5 cm.

3. For each jet k, we define the vertex occupancy, Q_j^k, for each vertex j:

$$Q_j^k = \frac{V_j^k}{T^k}$$

where T^k is the total number of tracks associated to the jet k and V_j^k is the number of tracks in jet k associated to z–vertex j. The z–vertex with the highest Q_j^k is called the jet z–vertex.

Let $R(|\Delta z|)$ be the percentage of events with $|\Delta z| > 2.5$ cm for any two z–vertices. Table 4.5 shows the $R(|\Delta z|)$ values for different pairs of z–vertices [75].

As we can see, the highest $\sum P_T$ z–vertex is the "correct" z–vertex. Therefore, we re–calculate the $\not{E}_T$ and re–cluster the jets using the highest $\sum P_T$ z–vertex and require that $\not{E}_T > 35$ GeV.

4.4.2 Out–of–time Energy

Every tower in the Central and End Wall hadron calorimeters is equipped with Time–to–Digital Converters (TDC's) in addition to Analog–to–Digital Converters (ADC's). The ADC's are enabled 196 ns before the beam crossing. The TDC's, which are enabled 46 ns before the beam crossing, measure the time relative to the beam crossing

$E_{HAD} > 1$ GeV and ($\Delta t < -20$ ns or $\Delta t > 35$ ns) - Central Calorimeter	
$E_{HAD} > 1$ GeV and ($\Delta t < -25$ ns or $\Delta t > 55$ ns) - End Wall Calorimeter	
Energy is only deposited during the 150 ns that the ADC's are	
enabled but the TDC's are not	

Table 4.6: Definitions used to declare a hadron calorimeter tower (central or end wall) *Out-of-Time* [75].

(Δt) when energy is deposited in the calorimeter tower. Table 4.6 lists the requirements for a tower to be labeled *Out-of-time.*

Fig. 4.3 shows the distribution of the energy out-of-time (EOT) versus the number of out-of-time towers (NOT) for a data sample of QCD events [75]. We clearly see a significant number of events with large amount of EOT and/or a large number of NOT.

Region I, EOT > 10 GeV and NOT > 20, is almost entirely due to Main Ring splash. We see this by plotting the tower η versus the tower ϕ for these events. This is shown in Fig. 4.4 [75]. We clearly see the signature of a MR splash; energy almost entirely deposited at small η and near 90° where the MR passes closest to the CDF detector.

The IETA vs. IPHI plots for Region II, EOT > 10 GeV and $5 <$ NOT ≤ 20, and Region III, EOT > 10 GeV and NOT < 5, are shown in Fig. 4.5 and Fig. 4.6 respectively [75]. Region II has a small amount of MR splash mixed in with cosmic ray events whereas Region III is dominated by cosmic ray events.

Region IV, EOT < 10 GeV and NOT ≤ 5, is the signal region. The events in this region almost all come from a $p\bar{p}$ collision with only a residual amount of MR splash
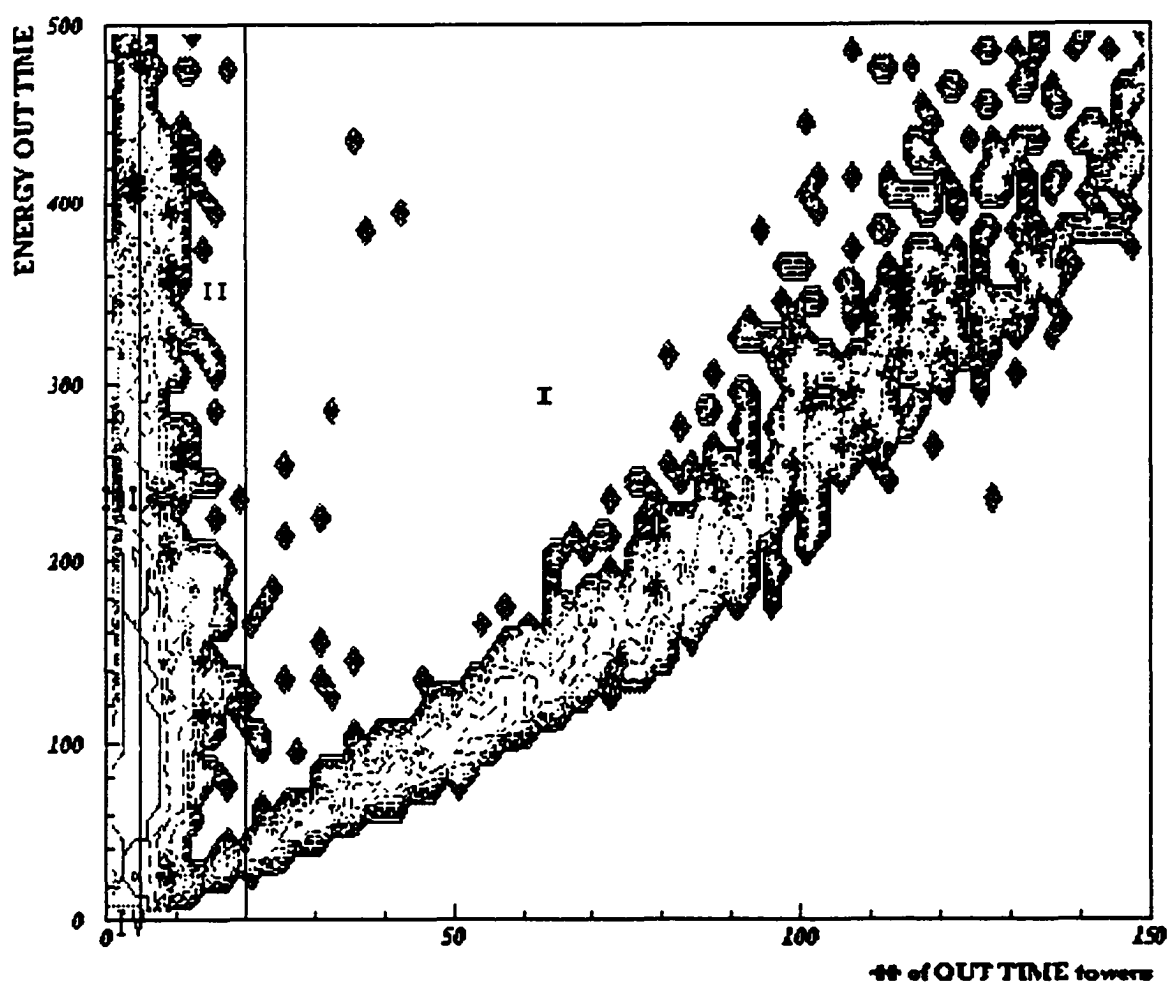
69

Figure 4.3: Plot of EOT versus NOT for a QCD data sample [75].

70

$$\not{E}_T \text{ total} = 2517998$$

Selection	Number of events fail
$\not{E}_T > 35$ GeV	1123734
Out–of–Time	506241
$\not{E}_T \oplus$ Out–of–Time	1625603
Total FILT1 (pass)	892395

Table 4.7: Data reduction due to the **FILT1** requirements [75].

and cosmic ray events. A plot of IETA vs. IPHI for this region, Fig. 4.7 shows none of the structure seen in Fig. 4.4 or Fig. 4.6 [75].

We apply the requirement that EOT < 10 GeV and NOT ≤ 5 to the $\not{E}_T$ data sample. Fig. 4.8 shows the EOT vs. NOT distribution of the $\not{E}_T$ events that fail this requirement [75]. Fig. 4.9 compares the $\not{E}_T$ distribution of the $\not{E}_T$ sample before and after the Out–of–Time requirement is made [75]. Note that the $\not{E}_T$ plotted is the re–clustered $\not{E}_T$ for both distributions. We see that the Out–of–Time requirement removes a large fraction of the large $\not{E}_T$ events. Table 4.7 shows the number of events failing the **FILT1** selection requirements [75]. We are left with 892395 events in the **FILT1** sample.

4.5 FILT2 sample

The **FILT1** cuts remove the bulk of Main Ring splashes and comsic ray events. However, a fraction of these events do occur in–time with the $p\bar{p}$ collision and are not removed by the Out–of–Time cuts. We therefore apply the selection requirements listed in Table 4.8 [77].
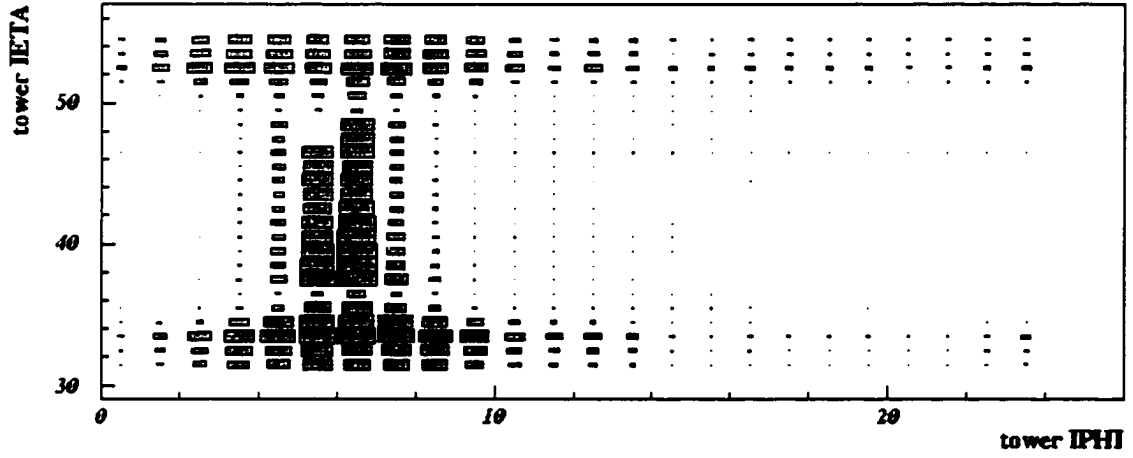
71

Figure 4.4: Plot of tower η (IETA) versus tower ϕ (IPHI) for the region EOT > 10 GeV and NOT > 20 for the QCD data sample [75]. The IPHI towers (0-23) are evenly segmented from 0° to 360°. See Appendix A for IETA to η translations.
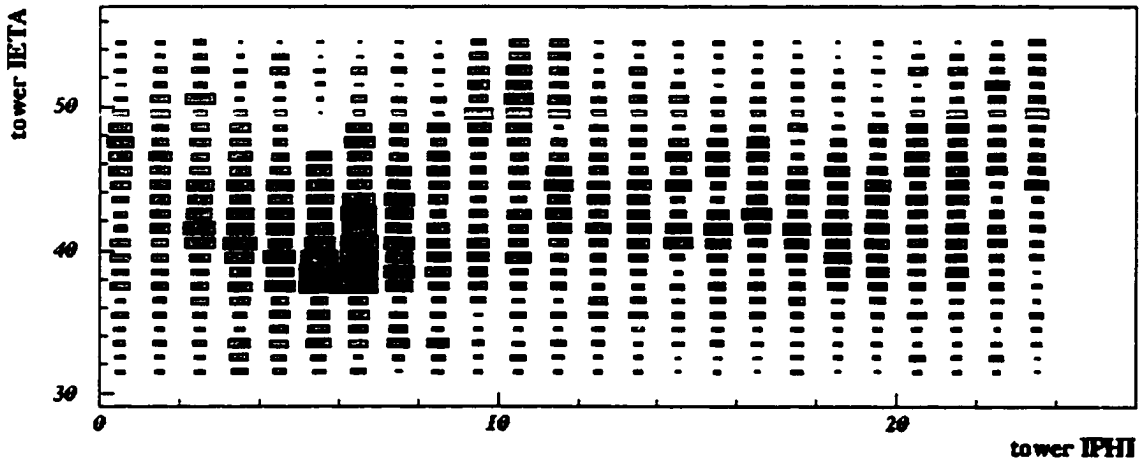

Figure 4.5: Plot of tower η (IETA) versus tower ϕ (IPHI) for the region EOT > 10 GeV and 5 < NOT ≤ 20 for the QCD data sample [75]. The IPHI towers (0-23) are evenly segmented from 0° to 360°. See Appendix A for IETA to η translations.

72

Figure 4.6: Plot of tower η (IETA) versus tower ϕ (IPHI) for the region EOT > 10 GeV and NOT < 5 for the QCD data sample [75]. The IPHI towers (0-23) are evenly segmented from 0° to 360°. See Appendix A for IETA to η translations.
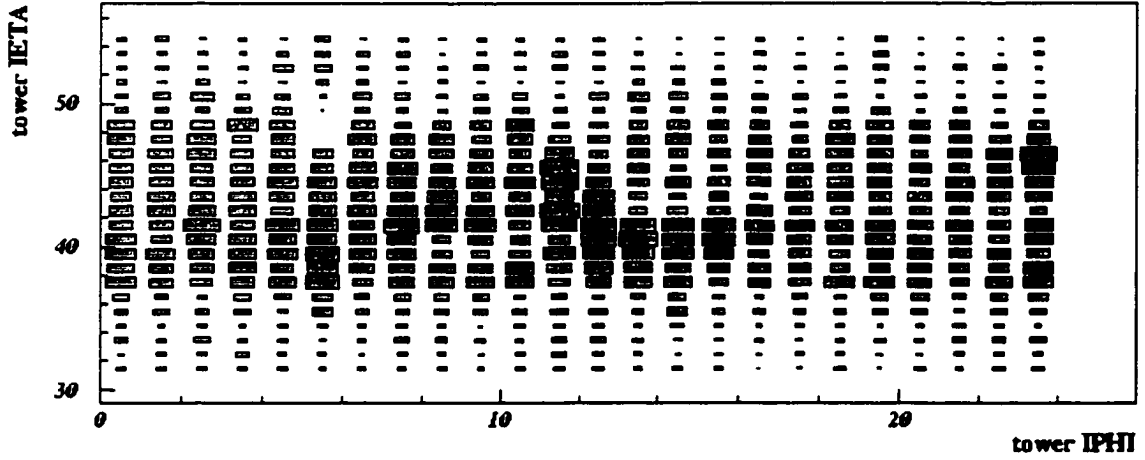

Figure 4.7: Plot of tower η (IETA) versus tower ϕ (IPHI) for the region EOT > 10 GeV and NOT > 20 for the QCD data sample [75]. The IPHI towers (0-23) are evenly segmented from 0° to 360°. See Appendix A for IETA to η translations.
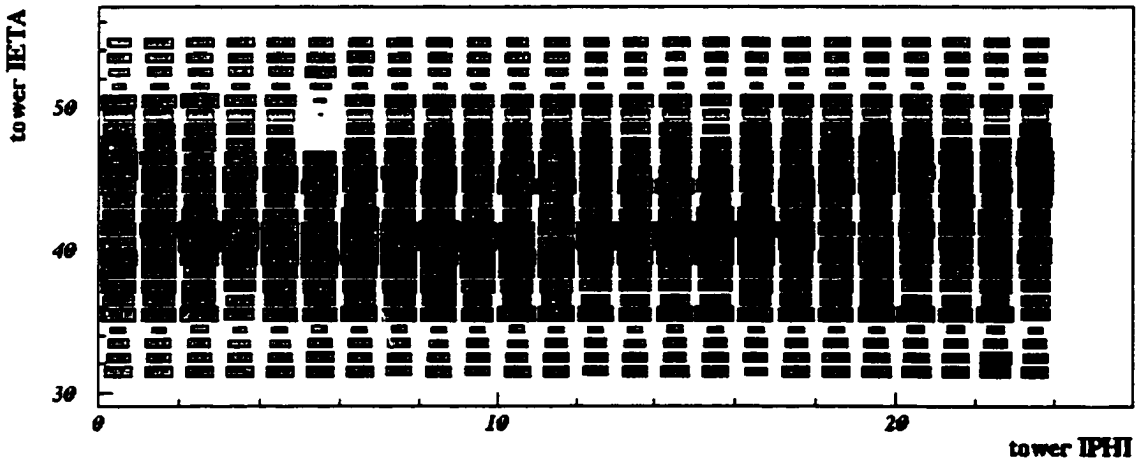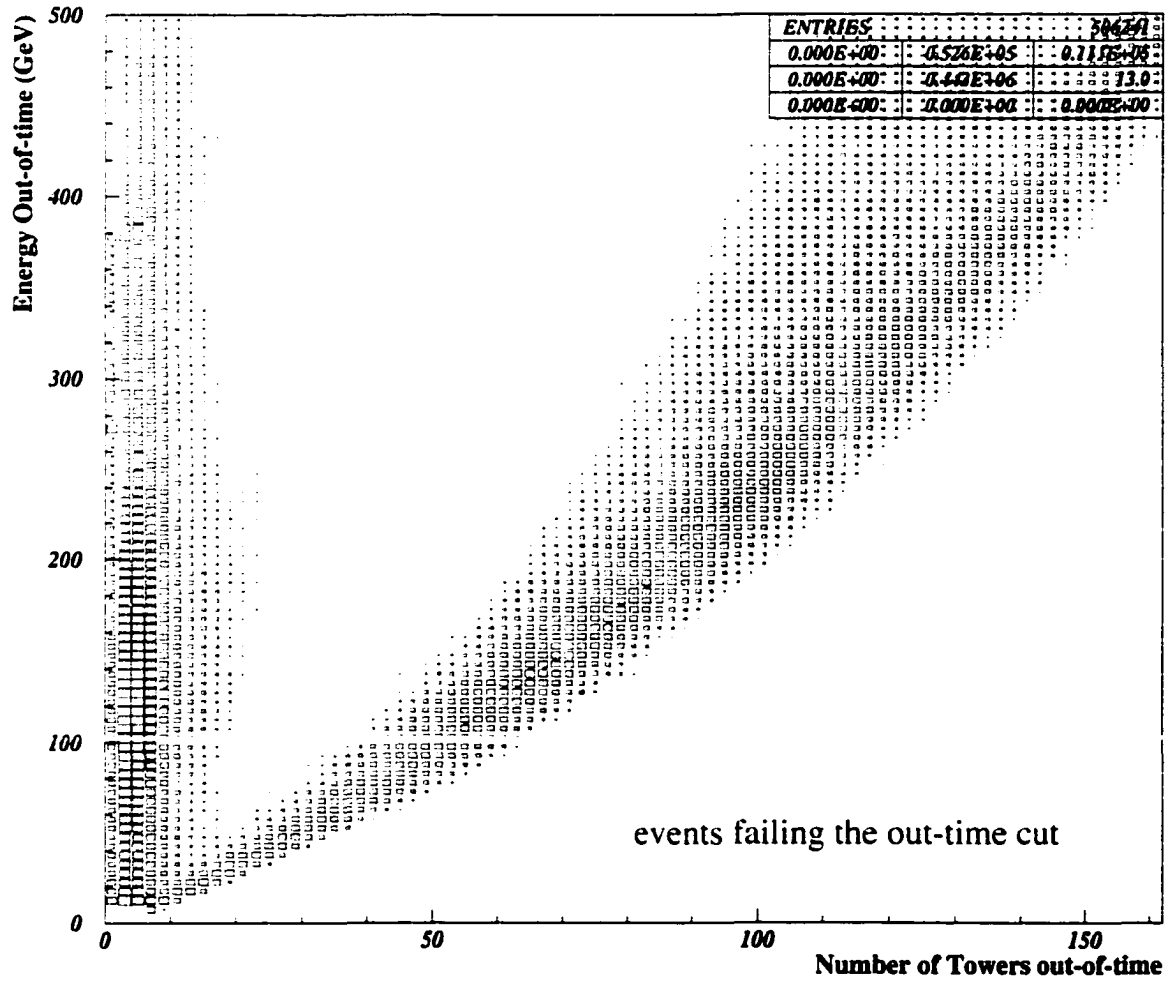
73

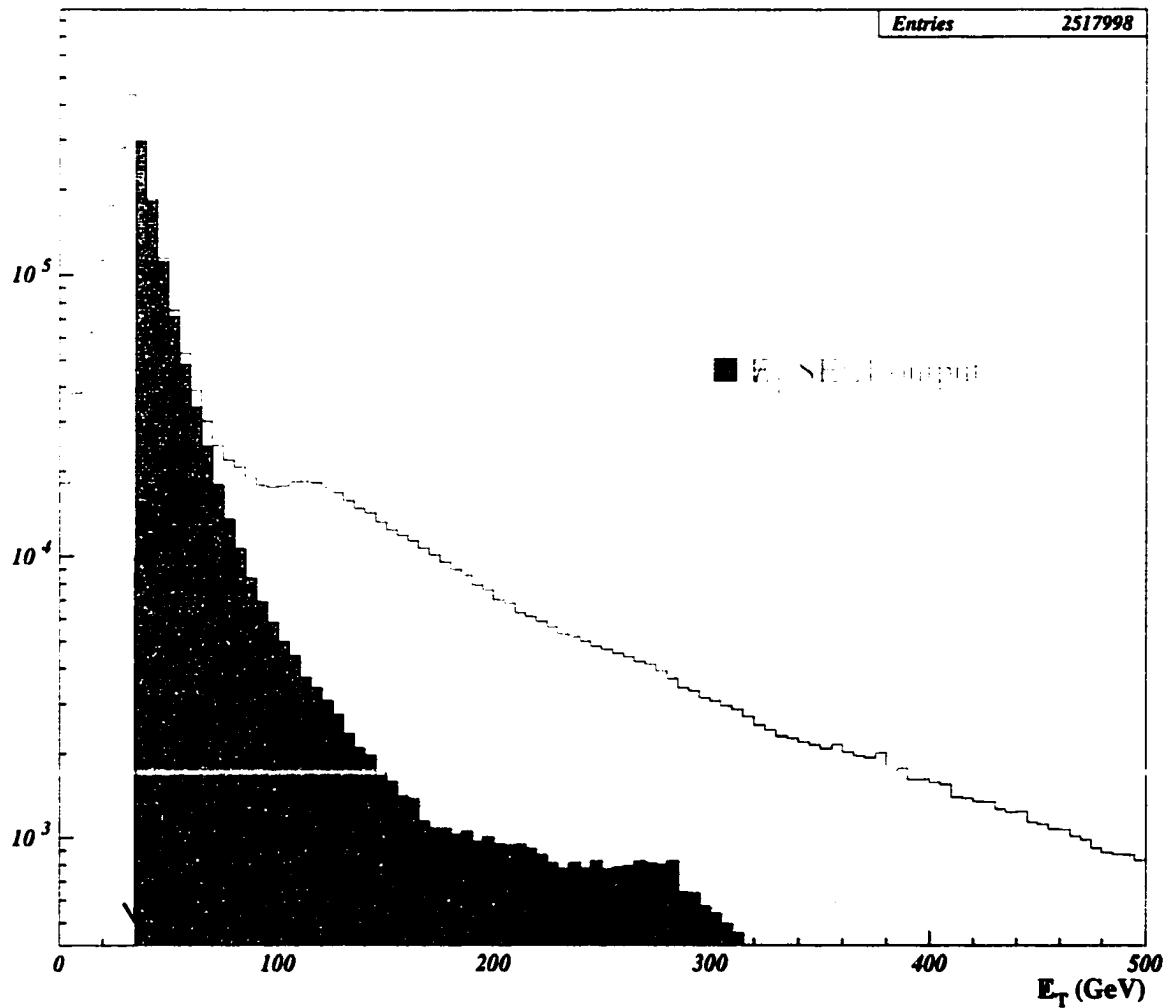Figure 4.8: Plot of EOT versus NOT for the $\not{E}_T$ data sample [75].

74

Figure 4.9: Plot of $\rlap{/}{E}_T$ in the $\rlap{/}{E}_T$ data sample before(light shaded histogram) and after(dark shaded histogram) the Out–of–Time requirement [75].

75

FITL2 selection

at least one jet with $E_T > 10$ GeV and $|\eta| < 0.9$
Event E-M fraction (EEMF) ≥ 0.1
Event Charge fraction (ECHF) ≥ 0.175

Table 4.8: Selection requirement used to create the **FILT2** sample [77]

4.5.1 Event E-M fraction

Let E_{EM} be the energy deposited in the electromagnetic calorimeter and E_{HAD} be the energy deposited in the hadron calorimeter. Then, the E-M fraction (EMF) of a jet is:

$$EMF = \frac{E_{EM}}{E_{EM} + E_{HAD}}$$

For jets due to quarks and gluons, we expect EMF to be between 0 and 1. For jets due to cosmic rays we expect all the energy to be deposited in the electromagnetic calorimeter or the hadronic calorimeter. Therefore, we expect the EMF to be near 0 or near 1 for cosmic rays. For Main Ring splashes, we expect the energy to be deposited in the hadron calorimeters only. Therefore, EMF is near 0 for jets due to Main Ring splashes.

We want to use the individual jet EMF's in a global fashion. We therefore define the Event E-M fraction ($EEMF$) [77]:

$$EEMF = \frac{\sum_j E_T^j \times EMF_j}{\sum_j E_T^j}$$

where the sum is over all jets with $E_T > 10$ GeV (no η requirement). Cutting on the
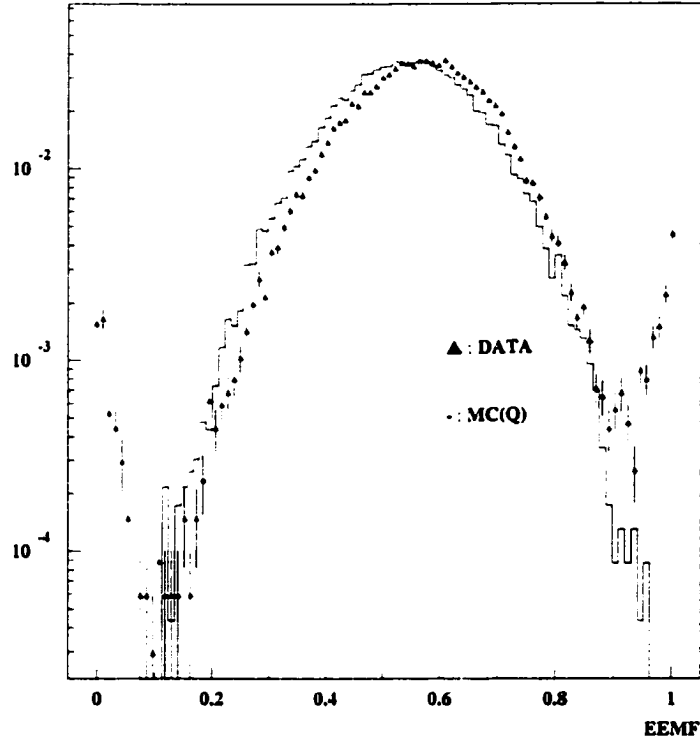
76

Figure 4.10: Event E–M Fraction for a QCD data sample [77].

$EEMF$ allows us to retain events which are jet like but might still contain interesting physics. In Fig. 4.10 we plot the $EEMF$ for a QCD data sample along with the expectations from MC [77]. This plot shows clearly the contributions of QCD events near 0.7 and background events near 0. We see that requiring $EEMF \geq 0.1$ removes a large fraction of the accelerator-induced background events. The excess of events near $EEMF = 1$. contain real physics events where an electron or photon fakes a jet. We do not remove these events at this point because we use events with a single electron to check the normalization of our background estimates (see Sec. 4.6.1.
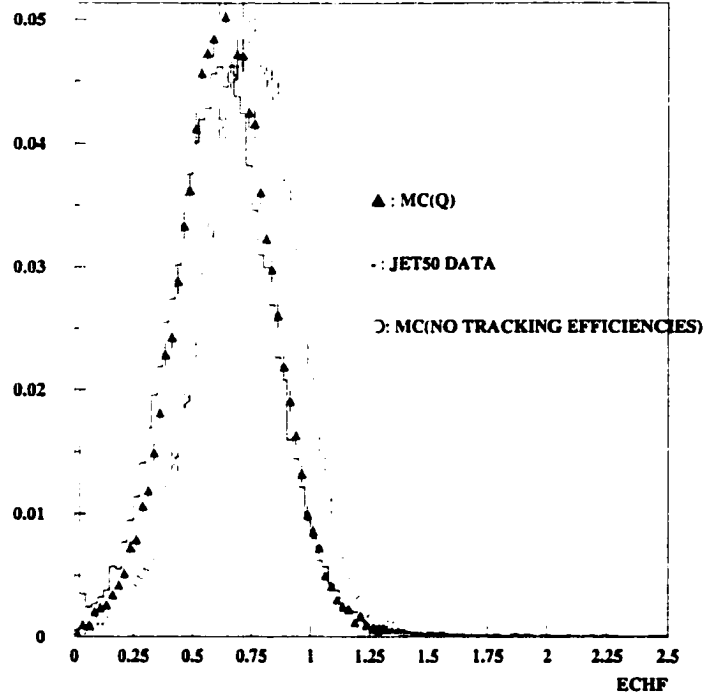
77

Figure 4.11: Event Charge Fraction for a QCD data sample [77]. Tracking degradation is described in Sec. 5.1.2.

4.5.2 Event Charge fraction

Let $\sum P_T$ be the scalar sum of the P_T of tracks associated to a jet and E_T be the total (electromagnetic+hadronic) transverse energy of a jet. Then the charge fraction (CHF) of a jet is:

$$CHF = \frac{\sum P_T}{E_T}$$

Quarks and gluons that originate from the $p\bar{p}$ collision produce charged and neutral particles as they travel through the detector. The charged particles are measured by the CTC and the track momenta are reconstructed. The charged and neutral particles deposit energy in the electromagnetic and hadronic calorimeters. Therefore,
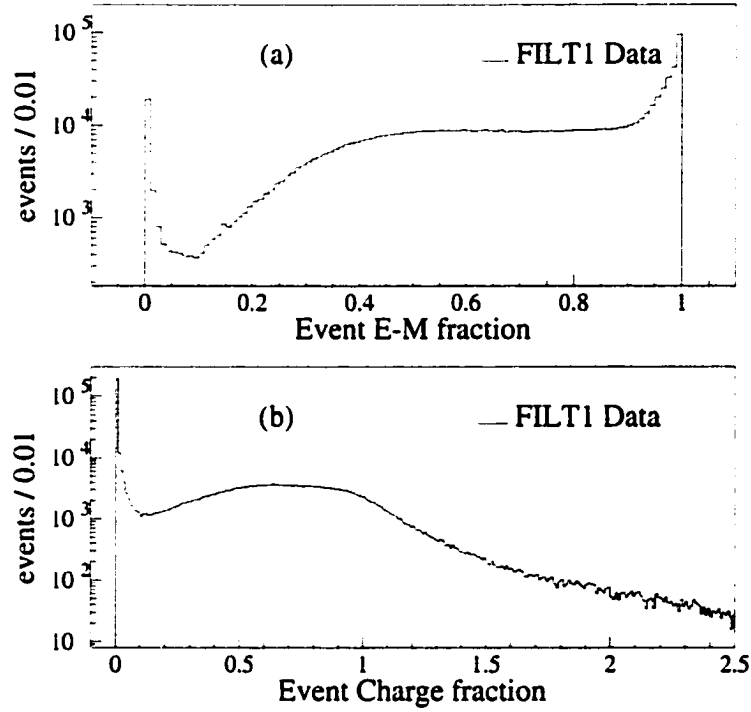
78

Figure 4.12: (a) Event E-M fraction of the **FILT1** data sample. (b) Event Charge fraction of the **FILT1** data sample.

we expect the CHF of jets from the $p\bar{p}$ collision to be non-zero. Cosmic rays and Main Ring splashes, on the other hand, do not necessarily travel through the CTC. Often, these types of events have no tracks pointing to the calorimeter towers in which the energy is deposited. We expect these background events to have jets with CHF near zero. Just as we use the EMF of jets in a global fashion by defining $EEMF$ so to we want to use the CHF in a global fashion. We define the Event Charge Fraction ($ECHF$) [77]:

$$ECHF = \langle CHF_j \rangle$$

79

FILT1 total = 892395

Selection	Number of events fail
$\geq$ 1 jet w/E_T > 10 GeV and $|\eta|$ < 0.9	290323
Event E–M Fraction	26646
Event Charge Fraction	566403
Total FILT2 (pass)	304582

Table 4.9: Data reduction due to the **FILT2** requirements.

where the average is over jets with E_T > 10 GeV and $|\eta|$ < 0.9. The $ECHF$ is plotted for the QCD data sample in Fig. 4.11 [77]. We see the large peak near 0 due to cosmic ray events and other backgrounds. We require $ECHF \geq 0.175$.

Fig. 4.12 shows the $EEMF$ and the $ECHF$ for the **FILT1** data sample. The **FILT1** data sample has the same peaks as the QCD data sample near $ECHF = 0$ and $EEMF = 0, 1$.

As a final requirement, we demand that the event contain at least one jet with E_T > 10 GeV and $|\eta|$ < 0.9. We do this for several reasons. First, we ensure that the $ECHF$ is a well defined quantity. Second, the jets from our signal are due to the decay of heavy scalar quarks. These jets tend to lie in the central calorimeter as opposed to QCD events which tend to populate the forward calorimeter.

We call the data sample which pass these 3 requirements the **FILT2** data sample. Table 4.9 shows the number of events which fail the requirements individually and combined.

4.6 **Pretagged** sample

Now that we have substantially reduced the accelerator and non–physics backgrounds, we must turn our attention to physics backgrounds (real and fake $\rlap{/}{E}_T$ sources). The physics backgrounds to the stop/sbottom signal are:

1. QCD multijet events where the $\rlap{/}{E}_T$ in an event is due to jet energy mismeasurement.

2. $W^{\pm}(\to \tau^{\pm}\nu_{\tau})+\ \geq 1$ jets where $l = \tau$ and the τ can be counted as a jet. For $W + 1$ jet events (see Fig. 4.13(a)), the tau must be counted as a jet while for $W + 2$ jets events (see Fig. 4.13(b)), the tau *might* be counted as a jet.

3. $W(\to l\nu_l)+\ \geq 2$ jets where $l = e/\mu$ and we fail to identify the lepton

4. $Z^0(\to \nu\bar{\nu})+\ \geq 2$ jets

5. $Z^0(\to l^+l^-)+\ \geq 0$ jets where $l = \tau$ and one or both of the τ's can be counted as a jet depending on the number of jets produced in association with the Z boson.

6. $Z^0(\to l^+l^-)+\ \geq 2$ jets where $l = e/\mu$ and we fail to identify both the leptons.

7. $t\bar{t}$ production

8. Diboson production: WW,WZ,ZZ

Fig. 4.13 shows a Feynman diagram for $W + 1$ jet and for $W + 2$ jet production. The next stage of data selection uses kinematic quantities to remove these backgrounds while still being efficient for the scalar squark signal. These selection requirements are listed in Table 4.10.
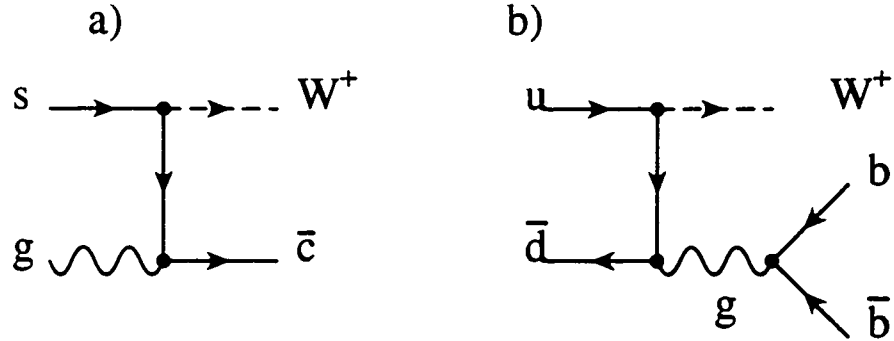
81

Figure 4.13: (a) Example Feynman diagram of W boson produced in association with 1 quark (b) Example Feynman diagram of W boson produced in association with 2 quarks.

$|z\ vertex| \leq 60\ cm$

Bad run removal

L2_MET_35* Trigger requirement

$\not{E}_T \geq 40$ GeV

$N_J = 2$ or 3 - $E_T \geq 15$ GeV, $|\eta| \leq 2$)

min $\Delta\Phi(\not{E}_T, j) > 45°$

$\Delta\Phi(\not{E}_T, j_1) < 165°$

$45° < \Delta\Phi(j_1, j_2) < 165°$

No other jets with $E_T > 7$ GeV, $|\eta| < 3.6$

$0.1 \leq$ jet em–fraction ≤ 0.9

Lepton veto

Table 4.10: Selection requirements used to create the **Pretagged selection**

82

The z–vertex requirement ensures that the vertex is well–measured. The z–vertex distribution for the **FILT2** sample is shown in Fig. 4.14. We require $|z\ vertex| \leq 60$ cm.

CDF keeps what is called a Bad Run list. The status of the detector sub–systems is checked for each run. If a component malfunctions during a run then the event is flagged as bad. We require that all components are working properly. This requirement reduces the integrated luminosity ($\int \mathcal{L}dt$) of the $\not{E}_T$ data sample from 88.6 pb^{-1} to 88 pb^{-1}.

Events from many different Level 2 trigger paths have offline $\not{E}_T > 30$ GeV and populate the $\not{E}_T$ data sample. We explicitly demand that the event pass the L2_MET_35* triggers (see Sec 4.3.2). In Sec 4.3.2 we discussed how to model the L2_MET_35* trigger efficiency for both the background and signal.

As a first step in reducing the background, especially from QCD processes, we increase the $\not{E}_T$ requirement to 40 GeV. The optimal value for this requirement depends on the $\tilde{t}_1$ and $\tilde{\chi}_1^0$ masses. Fig. 4.15 shows the $\not{E}_T$ distribution for data, $\tilde{t}_1\bar{\tilde{t}}_1$ MC with $M_{\tilde{t}_1} = 110$ GeV/c^2 and $M_{\tilde{\chi}_1^0} = 40$ GeV/c^2. and $\tilde{b}_1\bar{\tilde{b}}_1$ MC with $M_{\tilde{t}_1} = 140$ GeV/c^2 and $M_{\tilde{\chi}_1^0} = 40$ GeV/c^2 before the $\not{E}_T \geq 40$ GeV requirement

As described in Sec 2.3.2, the pair production of $\tilde{t}_1$ or $\tilde{b}_1$ leads to two high–P_T quarks in the final state. We therefore require 2 or 3 jets with $E_T \geq 15$ GeV and $|\eta| \leq 2$. The requirement that the event contain less than 4 jets with $E_T \geq 15$ GeV and $|\eta| \leq 2$ removes a significant fraction of $t\bar{t}$ events. Fig. 4.16 shows the jet multiplicity distribution for stop, sbottom, and $t\bar{t}$ before the jet multiplicity requirement is applied: the solid histogram is $M_{\tilde{t}_1} = 110$ GeV/c^2, $M_{\tilde{\chi}_1^0} = 40$ GeV/c^2, the dashed histogram is $M_{\tilde{b}_1} = 140$ GeV/c^2, $M_{\tilde{\chi}_1^0} = 40$ GeV/c^2 and the dotted histogram is $t\bar{t}$. The
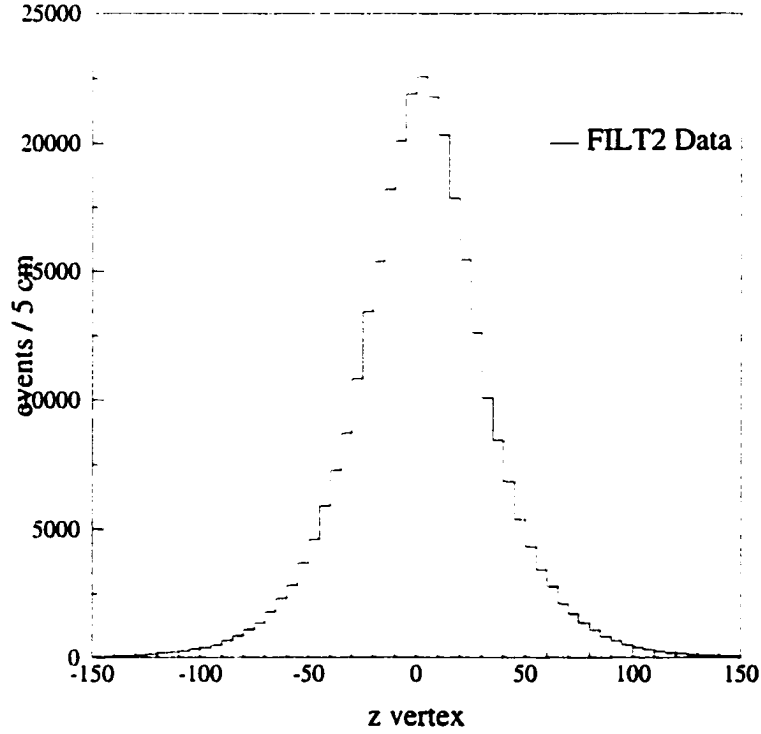
83

Figure 4.14: Distribution of the z–vertex for the **FILT2** data sample.

histograms are normalized to unit area.

At this point, we are still dominated by QCD multijet background. If the $\rlap{/}{E}_T$ of an event is due to the energy mismeasurement of a jet, then the $\rlap{/}{E}_T$ will be either parallel or anti-parallel (in the Φ direction) with the jet. In Fig. 4.17 we plot the distribution of the minimum $\Delta\Phi$ between the $\rlap{/}{E}_T$ and the jets (which we call min $\Delta\Phi(\rlap{/}{E}_T, j)$) for data, $t_1\bar{t}_1$ MC, and $b_1\bar{b}_1$ MC. The histograms are normalized to unit area. We use data as our QCD background shape because the expected contribution from signal at this stage is small. Further, the contribution to the data sample from vector boson production is small compared to the QCD multijet contribution. We require that the event have min $\Delta\Phi(\rlap{/}{E}_T, j) > X°$ where X is chosen by maximizing
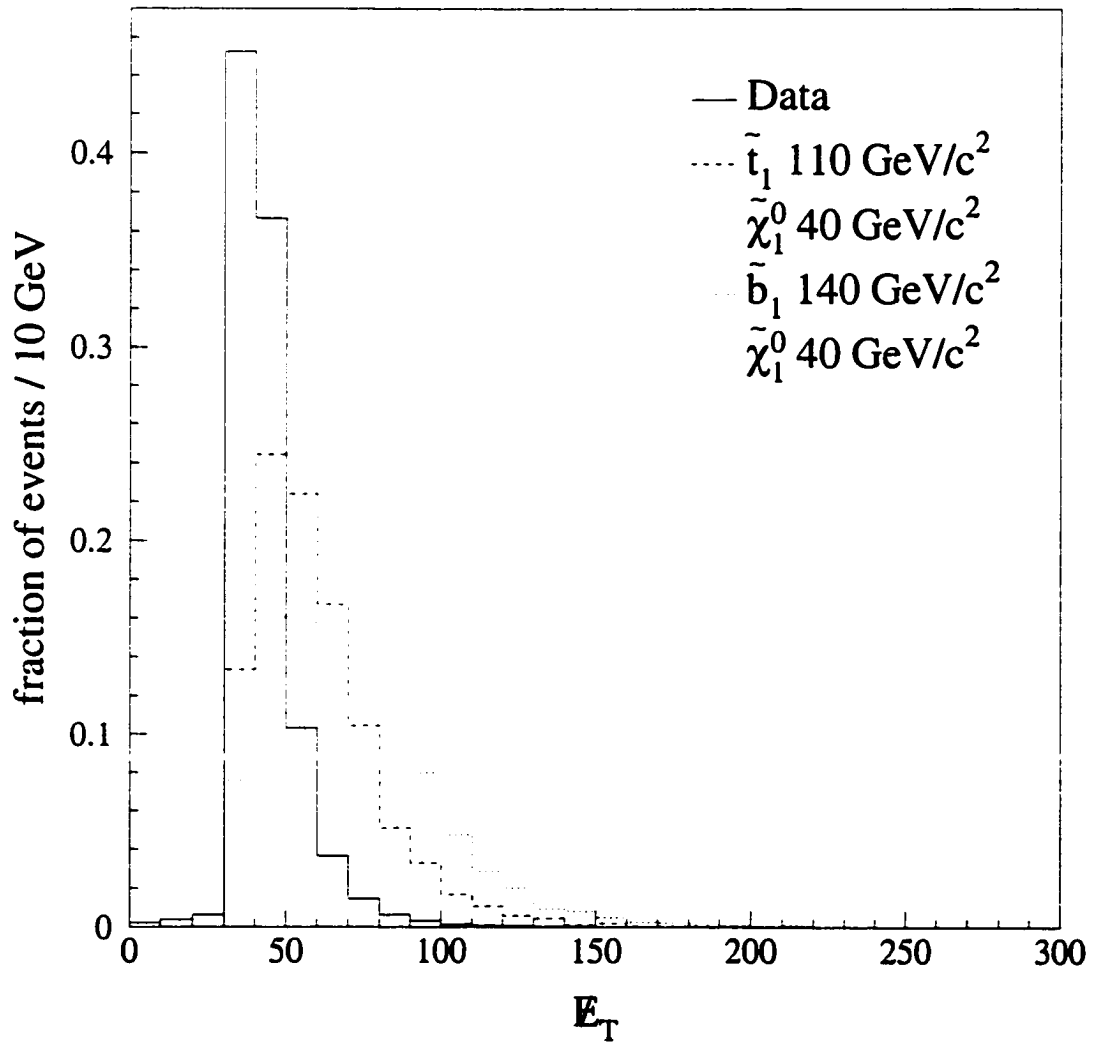
84

Figure 4.15: $\not{E}_T$ distribution *before* applying $\not{E}_T \geq 40$ GeV requirement. The solid histogram is data, the dashed histogram is stop MC, and the dotted histogram is sbottom MC. All histograms are normalized to unit area.
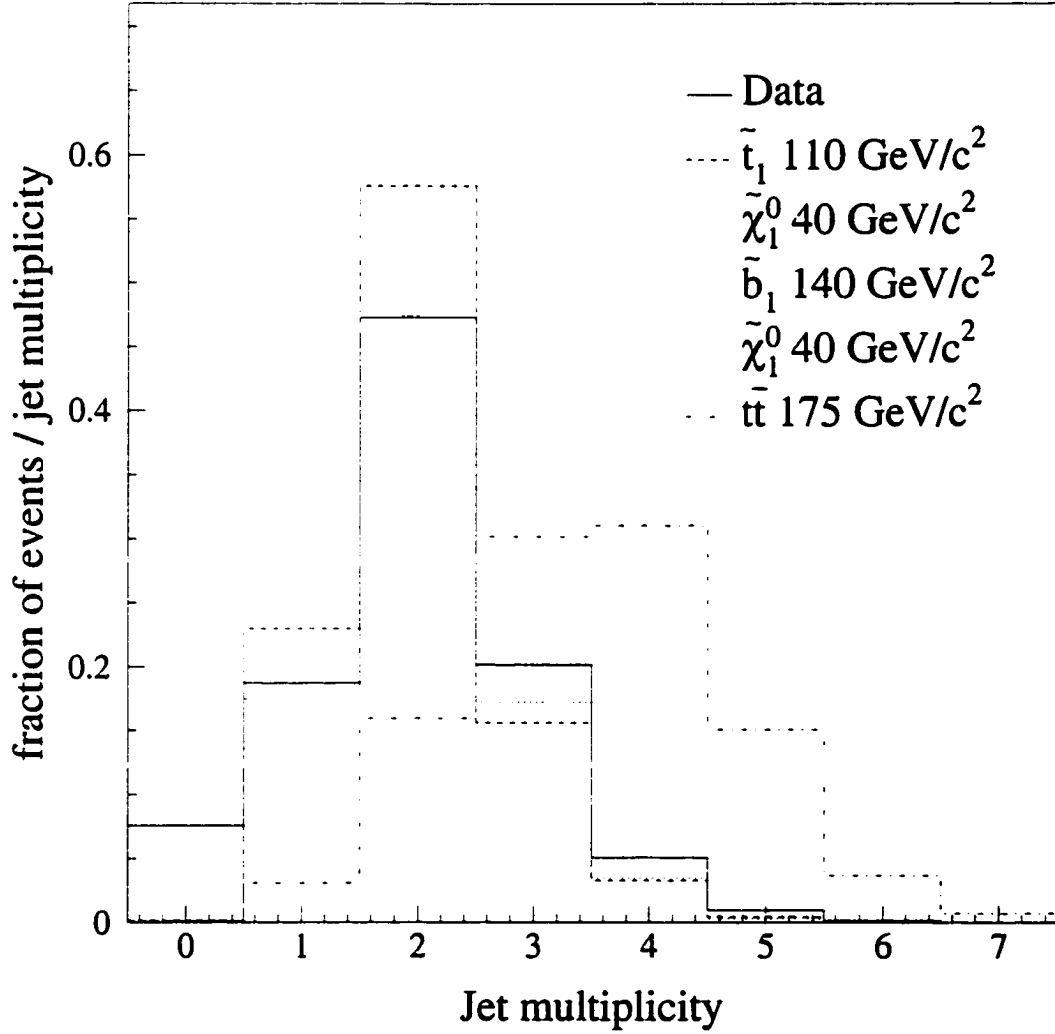
85

Figure 4.16: N_J distribution *before* applying 2 or 3 jet requirement. The solid histogram is data, the dashed histogram is stop MC, the dotted histogram is sbottom MC and the dashed-dotted histogram is $t\bar{t}$ MC. All histograms are normalized to unit area.

86

the value $Signal/\sqrt{Background} \equiv S/\sqrt{B}$. We plot this quantity in Fig. 4.18 using the $\tilde{t}_1\bar{\tilde{t}}_1$ distribution for signal and the data distribution for background. We see that requiring min $\Delta\Phi(\not{E}_T, j) > 45°$ is a good choice.

The $\not{E}_T$ direction is also correlated with the direction of the jet with the highest E_T in QCD multijet events. In Fig. 4.19, we plot the $\Delta\Phi$ between the $\not{E}_T$ and the highest E_T jet (which we call $\Delta\Phi(\not{E}_T, j_1)$) for data, $\tilde{t}_1\bar{\tilde{t}}_1$ MC, and $\tilde{b}_1\bar{\tilde{b}}_1$ MC after making the min $\Delta\Phi(\not{E}_T, j) > 45°$ selection. The histograms are normalized to unit area. We require that $\Delta\Phi(\not{E}_T, j_1) < X°$ and choose X by maximizing $S/\sqrt{B}$. The $S/\sqrt{B}$ distribution is shown in Fig. 4.20. Again, we use data for background and $\tilde{t}_1\bar{\tilde{t}}_1$ for signal. We require that $\Delta\Phi(\not{E}_T, j_1) < 165°$.

The two highest E_T jets in QCD events are preferentially back to back in the Φ direction. In addition, we expect the angle between these jets to be uniformly distributed for the vector boson backgrounds. Fig. 4.21 shows the distribution of the opening angle in Φ between the two leading E_T jets (which we call $\Delta\Phi(j_1, j_2)$) after the $\Delta\Phi(\not{E}_T, j_1) < 165°$ requirement. The $\tilde{t}_1\bar{\tilde{t}}_1$, $\tilde{b}_1\bar{\tilde{b}}_1$, and data distributions are normalized to 1. We require events to have $X° < \Delta\Phi(j_1, j_2) < Y°$ where we choose X and Y by maximizing $S/\sqrt{B}$. We use the $\tilde{t}_1\bar{\tilde{t}}_1$ distribution for signal and the data for background. This is shown in Fig. 4.22. We select events with $45° < \Delta\Phi(j_1, j_2) < 165°$.

After the above requirements are made, we are still dominated by QCD multijet events. QCD multijet events with large $\not{E}_T$ often have extra, low–E_T jets (which we call soft jets). These soft jets are due to gluon radiation. Gluon radiation off the initial state partons is called *Initial State Radiation* (ISR) and gluon radiation off the final state partons is called *Final State Radiation* (FSR). In Fig. 4.23 we show the soft jet multiplicity distribution (normalized to unit area) in QCD MC, $\tilde{t}_1\bar{\tilde{t}}_1$ MC, and
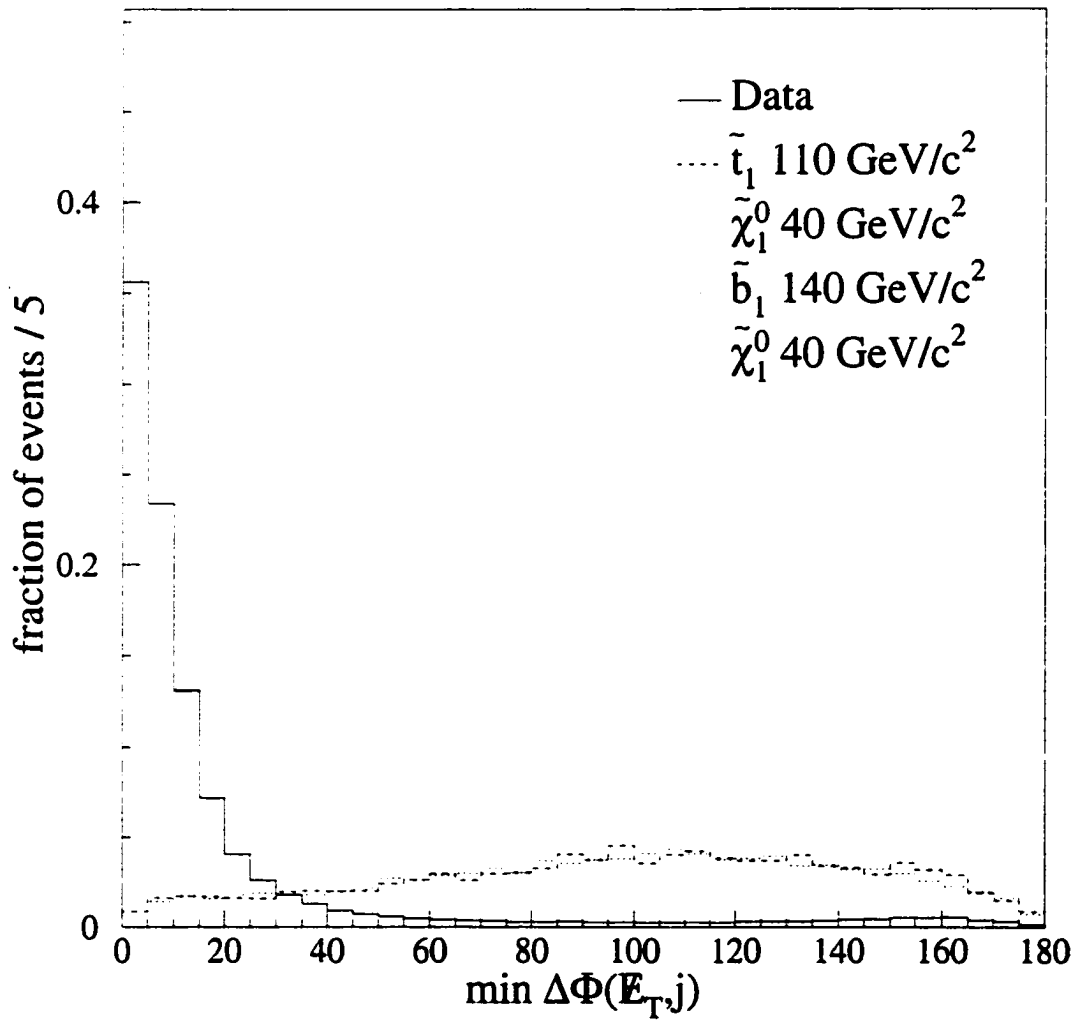
87

Figure 4.17: min $\Delta\Phi(\not{E}_T, j)$ distribution *before* applying min $\Delta\Phi(\not{E}_T, j) >$ 45° requirement. The solid histogram is data, the dashed histogram is stop MC, and the dotted histogram is sbottom MC. All histograms are normalized to unit area.

88

Figure 4.18: Optimization of min $\Delta\Phi(\not{E}_T, j)$ requirement. The arrow indicates the value chosen.

89

Figure 4.19: $\Delta\Phi(\not{E}_T, j_1)$ distribution *before* applying $\Delta\Phi(\not{E}_T, j_1) < 165°$ requirement. The solid histogram is data, the dashed histogram is stop MC, and the dotted histogram is sbottom MC. All histograms are normalized to unit area.
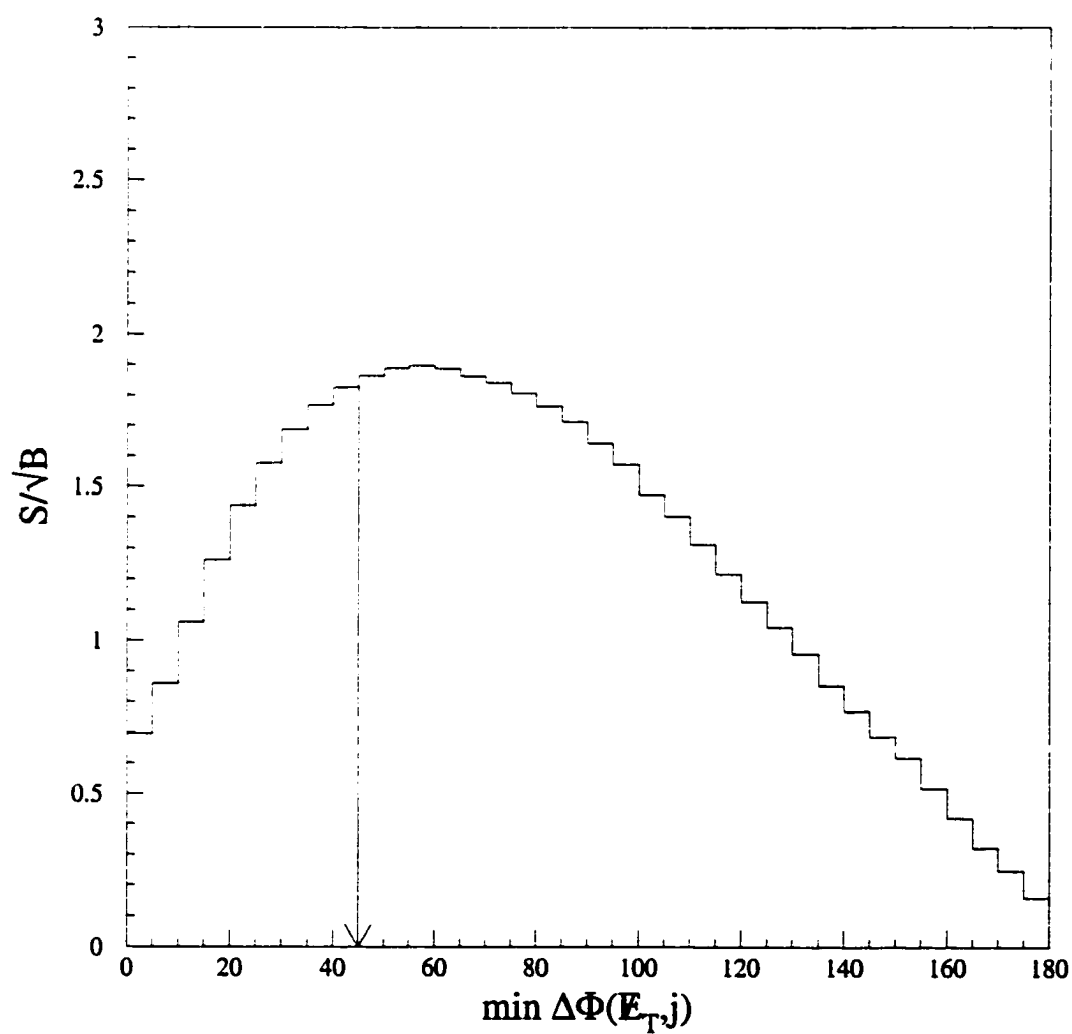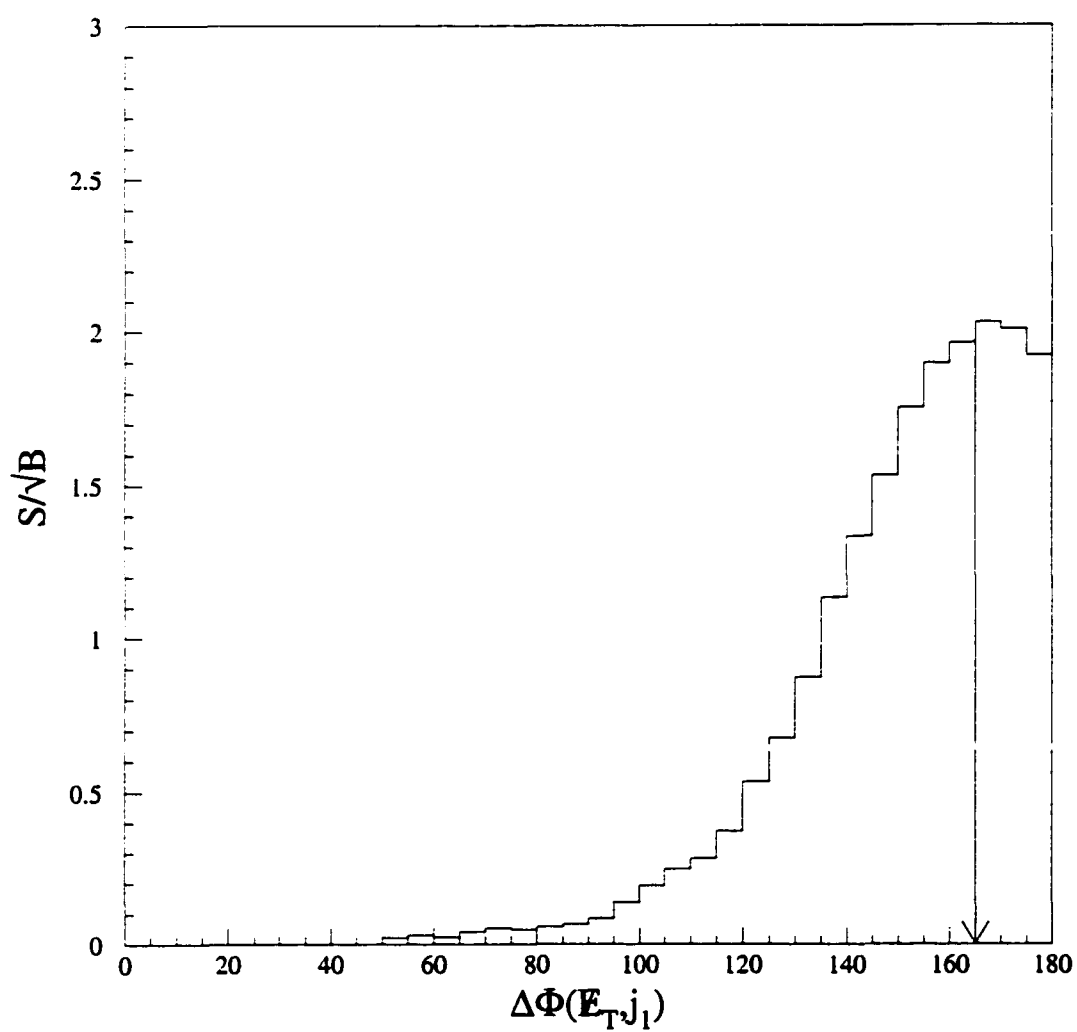
Figure 4.20: Optimization of $\Delta\Phi(\not{E}_T, j_1)$ requriement. The arrow indicates the value chosen.

91

Figure 4.21: $\Delta\Phi(j_1, j_2)$ distribution *before* applying $45° < \Delta\Phi(j_1, j_2) < 165°$ requirement. The solid histogram is data, the dashed histogram is stop MC, and the dotted histogram is sbottom MC. All histograms are normalized to unit area.

92

Figure 4.22: Optimization of $\Delta\Phi(j_1, j_2)$ requirement. The arrow indicates the value chosen.
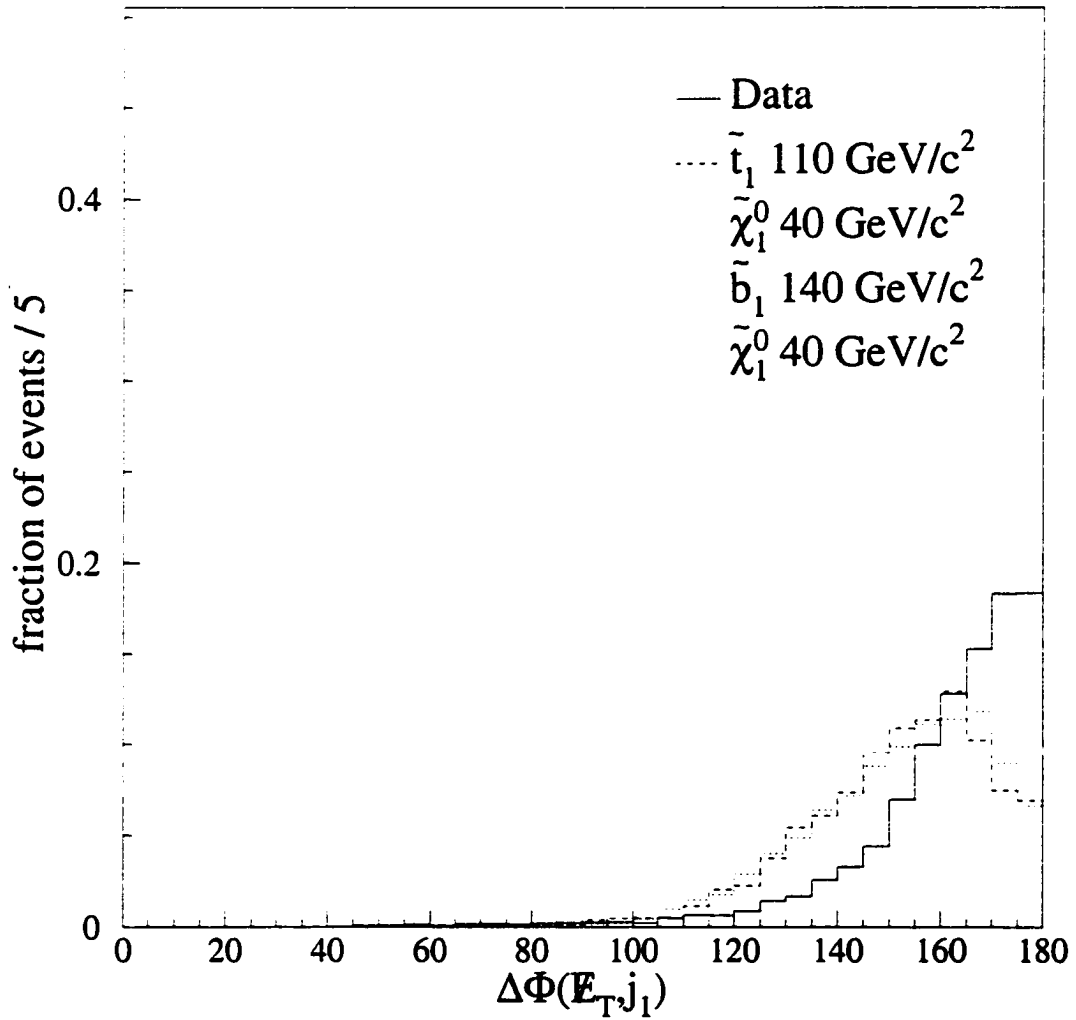
93

Figure 4.23: Multiplicity of jets with $7 < E_T < 15$ GeV and $|\eta| < 3.6$. The solid histogram is data, the dashed histogram is stop MC, and the dotted histogram is sbottom MC. All histograms are normalized to unit area.
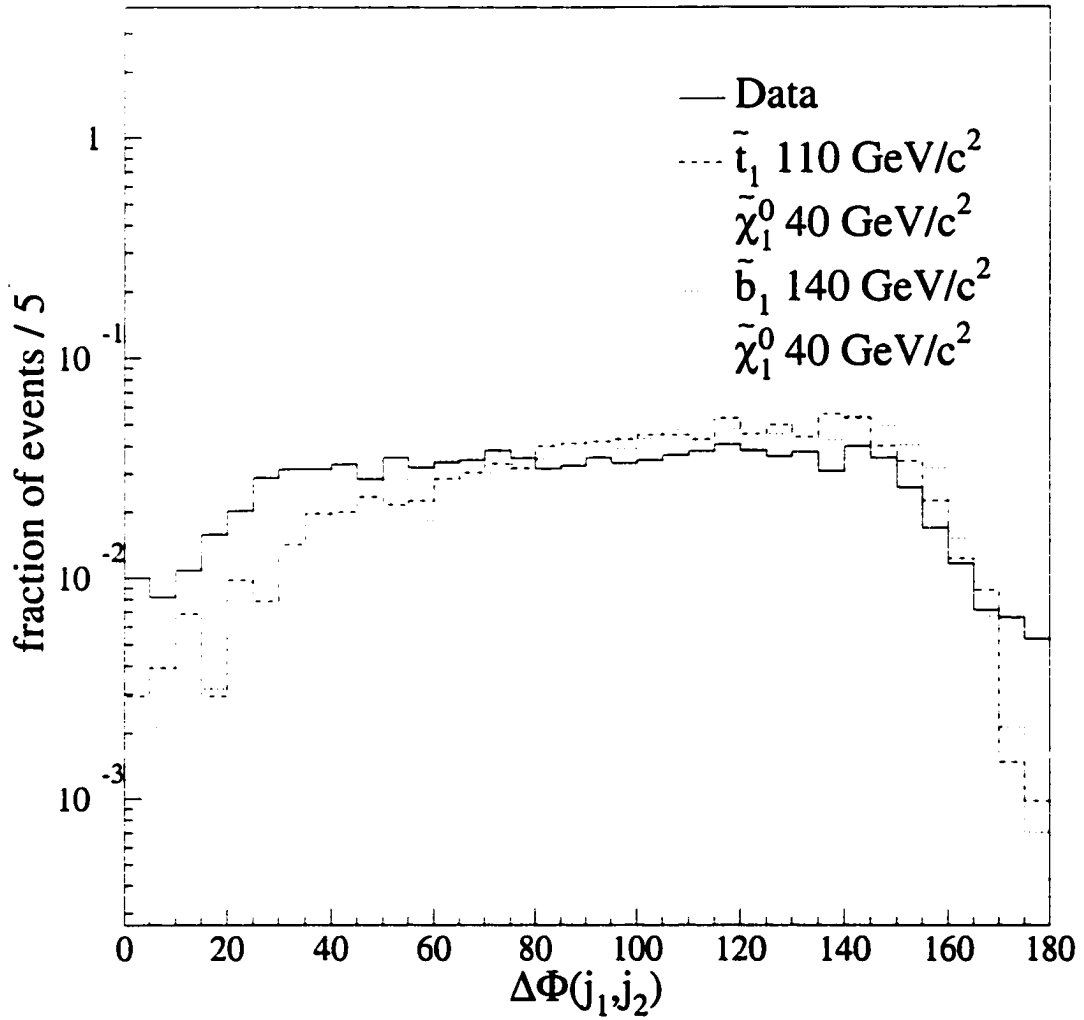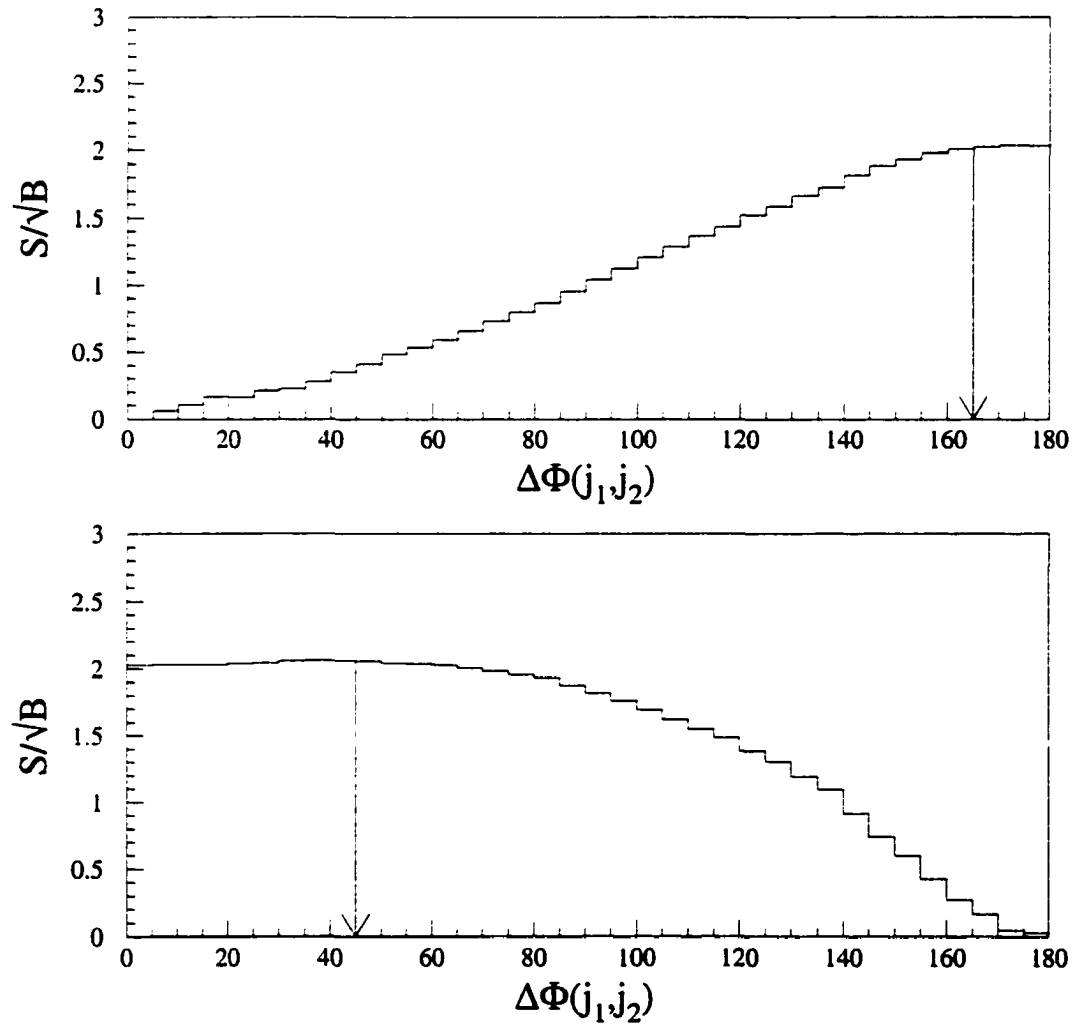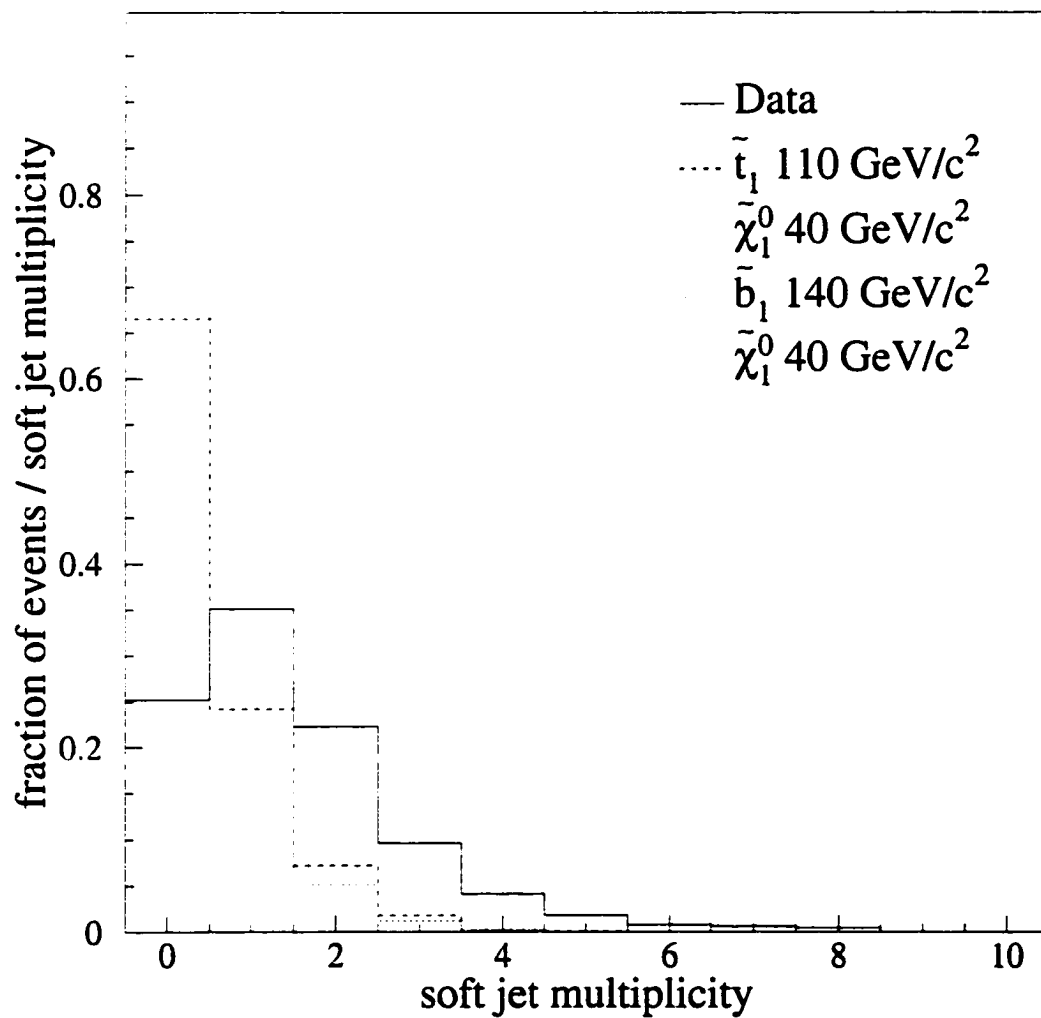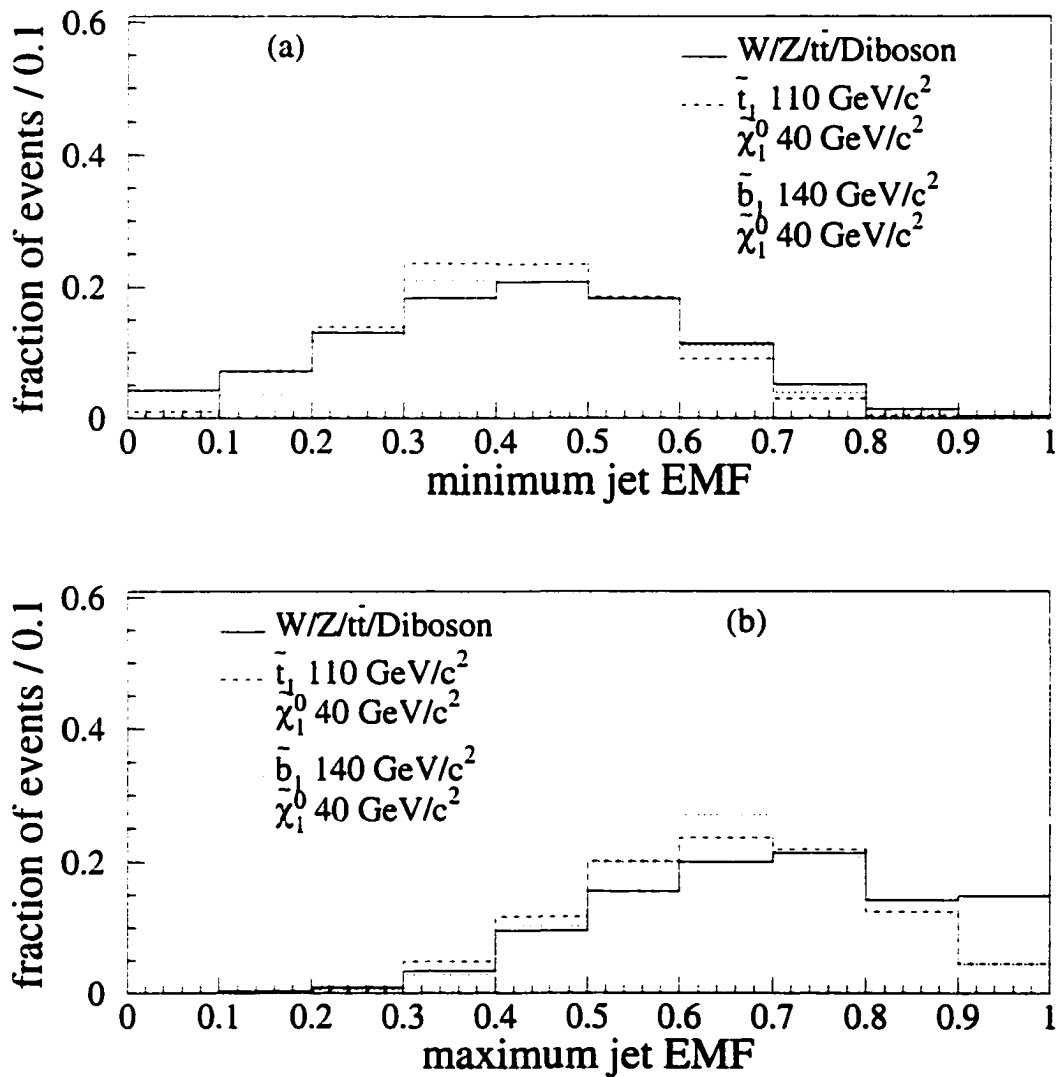
94

Figure 4.24: (a) Distribution of the minimum EMF_j for jets with $E_T > 15$ GeV and $|\eta| < 2$. (b) Distribution of the maximum EMF_j for jets with $E_T > 15$ GeV and $|\eta| < 2$

95

$\tilde{b}_1\tilde{\bar{b}}_1$ MC for soft jets with $7 < E_T < 15$ GeV and $|\eta| < 3.6$. We require that an event contain no jets with $7 < E_T < 15$ GeV and $|\eta| < 3.6$.

The above requirements significantly reduce the QCD multijet contribution. The electroweak backgrounds, on the other hand, are only minimally addressed by the above cuts. As a first step in removing events with lepton(s), we require all jets with $E_T > 15$ GeV and $|\eta| < 2$. to have $0.1 < EMF_j < 0.9$ (see Sec 4.5.1). Fig. 4.24(a) shows the minimum EMF_j for $\tilde{t}_1\tilde{\bar{t}}_1$ MC, $\tilde{b}_1\tilde{\bar{b}}_1$ MC, and electroweak MC while Fig. 4.24(b) shows the maximum EMF_j for the sample samples. The distributions have been normalized to unit area. The minimum EMF_j distribution shows a slightly higher fraction of electroweak events in the $EMF_j < 0.1$ bin. This is due to the $W^{\pm}(\to \tau^{\pm}\nu_\tau)$ background where one of the jets is really a tau which decays hadronically. The maximum EMF_j distribution shows a pronounced excess of electroweak events in the $EMF_j > 0.9$ bin. This excess is due to $W^{\pm}(\to e^{\pm}\nu_e)$, where the electron is counted as a jet and to a lesser extent $W^{\pm}(\to \tau^{\pm}\nu_\tau)$.

The final requirement to create the **Pretagged** sample is to explicitly identify leptons ($=e/\mu$) and veto events that contain at least one lepton. The lepton identification requirements are listed in Tables 4.12–4.15. The identification requirements for electrons and CMUO muons are inspired by the requirements used in the PRD [65] that presented first evidence of the top quark existence. The identification variables are described in detail in [65].

Table 4.11 summarizes the data reduction with the **Pretagged** requirements. Table 4.16 lists the expected amount of background in the **Pretagged** sample from each source. Both the statistical and systematic uncertainties are listed; see Chapter 7 for a description of the uncertainty estimates. The $W/Z/t\bar{t}/Diboson$ estimates are

96

Total after FILT2 cuts	304582
Cut	# events left
z vertex	281042
Bad Run	263126
$E_T \geq 40$ GeV	140842
L2 MET_35*	116954
$N_J = 2$ or 3	78899
min $\Delta\Phi$	7912
$\Delta\Phi(E_T, j_1)$	3799
$\Delta\Phi(j_1, j_2)$	3007
No jet with $E_T > 7$GeV	757
jet em-fraction	569
Lepton veto	396

Table 4.11: Data reduction due to the **Pretagged** requirements.

97

$$E_T > 10 \text{ GeV}$$
$$E/P < 2$$
$$E_{HAD}/E_{EM} < 0.1$$
$$Strip \; |\Delta x| < 3 \; cm$$
$$Strip \; |\Delta z| < 5 \; cm$$
$$L_{SHR} < 0.2$$
$$\chi^2_{strip} < 10$$

Table 4.12: Central Electron identification requirements. See [65] for a description of the identification variables.

$$E_T > 10 \text{GeV}$$
$$E_{HAD}/E_{EM} < 0.1$$
$$\chi^2_{3X3} < 10$$

Table 4.13: Plug Electron identification requirements. See [65] for a description of the identification variables.

98

$$P_T > 10 \text{ GeV}$$

$$E_{EM} < 2 \text{ GeV}$$

$$E_{HAD} < 6 \text{ GeV}$$

$$E_{EM} + E_{HAD} > 0.1 \text{GeV}$$

$$Impact\ parameter\ |d_0| < 0.5\ cm$$

$$|d_z| < 2\ cm\ (CMU)$$

$$|d_z| < 5\ cm\ (CMP, CMX)$$

Table 4.14: Central Muon identification requirements. See [65] for a description of the identification variables.

$$P_T > 15 \text{ GeV}$$

$$E_{EM} < 2 \text{ GeV}$$

$$E_{HAD} < 6 \text{ GeV}$$

$$E_{EM} + E_{HAD} > 0.1 \text{GeV}$$

$$Impact\ parameter\ |d_0| < 0.5\ cm$$

$$Isolation\ E_T(cone = 0.4) < 5 \text{ GeV}$$

$$Good\ Track\ = \geq 2 \text{ CTC stereo layers } (\geq 3 \text{ hits / layer})$$

$$AND \geq 2 \text{ CTC axial layers } (\geq 6 \text{ hits / layer})$$

Table 4.15: CMIO identification requirements. See [65] for a description of the identification variables.

99

given by our MC samples normalized to an integrated luminosity of 88 pb^{-1}. We assume that the entire excess in data above electroweak backgrounds is due to QCD multijet sources. When we estimate the QCD multijet background for the tagged sample (Chapter 6), we normalize the background rate to this excess. Fig. 4.25 shows the acceptance after each requirement for $\tilde{t}_1\bar{\tilde{t}}_1$ MC as a function of the $\tilde{t}_1\bar{\tilde{t}}_1$ mass for $M_{\tilde{\chi}_1^0} = 40$ GeV/c^2. Fig. 4.26 shows the same plot for $\tilde{b}_1\bar{\tilde{b}}_1$ MC.

To verify our hypothesis that the data is composed of QCD+$W/Z/t\bar{t}/Diboson$ processes, we compare the data to our QCD+$W/Z/t\bar{t}/Diboson$ distributions from MC. $W/Z/t\bar{t}/Diboson$ MC is normalized to the integrated luminosity of our data sample (88 pb^{-1}) and QCD MC is normalized to the difference between data and $W/Z/t\bar{t}/Diboson$. In Fig. 4.27, we plot the N_J spectrum (# of jets with $E_T \geq$ 15 GeV, $|\eta| \leq 2$) and the $\not{E}_T$ distribution. In Fig. 4.28 we plot the E_T of the jets where the jets are ordered in descending E_T; $E_T^1 > E_T^2 > E_T^3$. In Fig. 4.29 we plot the various angular distributions: $\Delta\Phi(\not{E}_T, j_1)$, min $\Delta\Phi(\not{E}_T, j)$, and $\Delta\Phi(j_1, j_2)$.

Fig. 4.27–Fig. 4.29 also include the expected contribution from $\tilde{t}_1\bar{\tilde{t}}_1$ MC where $M_{\tilde{t}_1} = 110$ GeV/c^2 and $M_{\tilde{\chi}_1^0} = 40$ GeV/c^2. We expect a total of 70 events in the **Pretagged** sample. The background sources dwarf our signal at this stage. Chapter 5 shows how we use the presence of 2 c quarks (or 2 b quarks for $\tilde{b}_1\bar{\tilde{b}}_1$) to create a sample where the expected signal is comparable to the expected background.

We observe in most cases that the agreement is quite good. The $\not{E}_T$ is the only variable where the QCD background is not modeled correctly by MC. The disagreement between data and $W/Z/t\bar{t}/Diboson$+QCD in $\not{E}_T$ does <u>not</u> affect our estimate of QCD in the **Tagged** samples. For our **Tagged** samples, we use the excess of data events in our **Pretagged** sample to determine the normalization of our QCD

100

Sample	N_{exp}
$W^{\pm}(\to e^{\pm}\nu_e)+\geq 2$ jets	$16.9 \pm 2.3 \pm 5.0$
$W^{\pm}(\to \mu^{\pm}\nu_\mu)+\geq 2$ jets	$63.0 \pm 4.4 \pm 18.6$
$W^{\pm}(\to \tau^{\pm}\nu_\tau)+\geq 1$ jets	$143.9 \pm 6.9 \pm 41.8$
$Z^0(\to \nu\bar{\nu})+\geq 2$ jets	$38.9 \pm 2.1 \pm 11.3$
$t\bar{t}$	$1.90 \pm 0.40 \pm 0.69$
$Diboson$ (WW, WZ, ZZ)	$5.5 \pm 0.4 \pm 1.5$
Total $W/Z/t\bar{t}/Diboson$ bkg	$270.1 \pm 8.7 \pm 75.7$
Total QCD	125.9 ± 83.4
Total DATA	396

Table 4.16: The number of data events and expected background events for the **Pretagged** sample. The first error is statistical, the second systematic.

background estimate.

4.6.1 Cross-check

This analysis is, in essence, a counting experiment (albeit an expensive one!). Therefore, it is very important to make sure that the normalization (or total rates) of the backgrounds is well understood. For single vector boson processes, we have a handle to determine the normalization. We can simply reverse the lepton veto requirement while applying all other **Pretagged** requirements and look at events with a single lepton ($=e/\mu/\tau$). In addition, if the kinematic distributions are modeled correctly in events <u>with</u> an identified lepton then we have confidence these distributions are modeled correctly in events <u>without</u> an identified lepton.
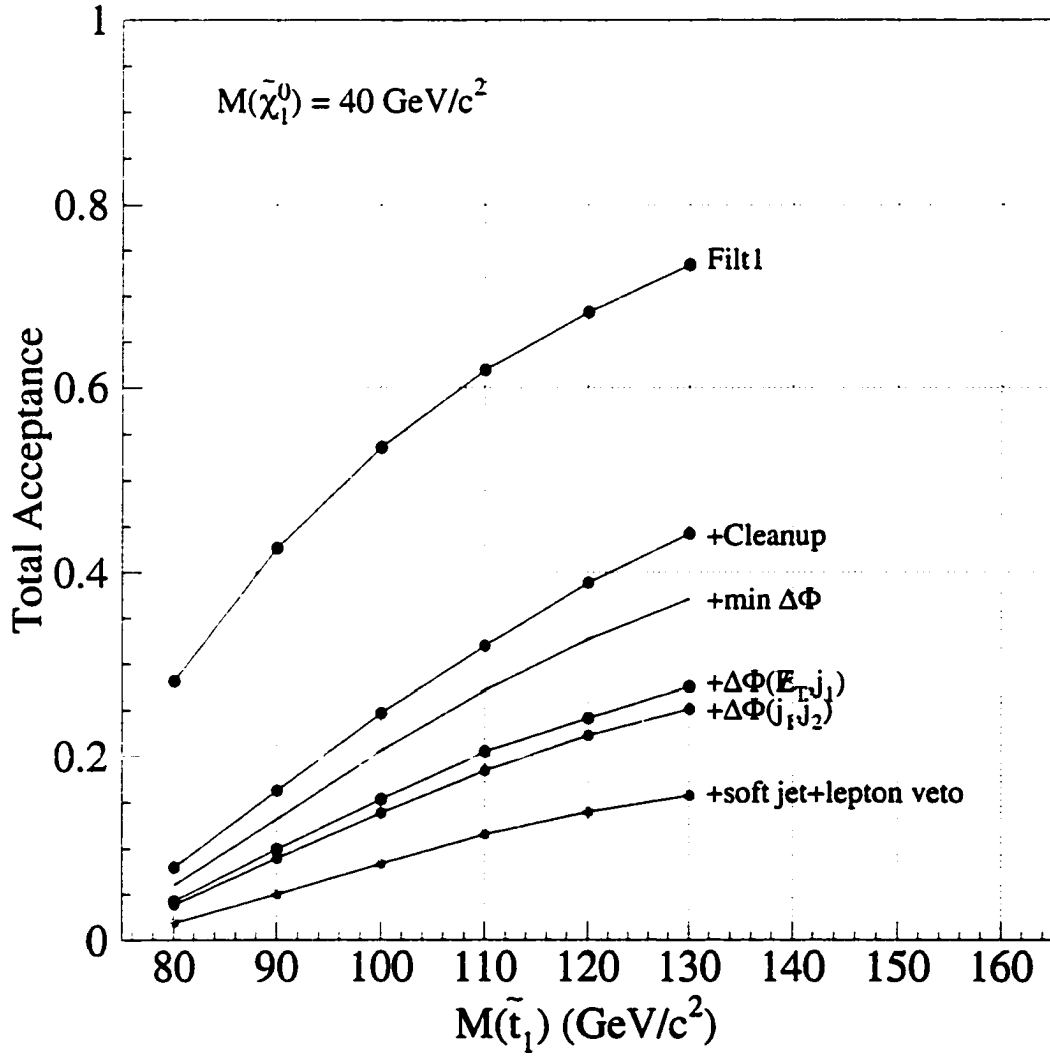
101

Figure 4.25: The total $\tilde{t}_1\bar{\tilde{t}}_1$ acceptance after each requirement is applied (see Table 4.10) as a function of $M_{\tilde{t}_1}$ for $M_{\tilde{\chi}_1^0}=40$ GeV/c^2.

102

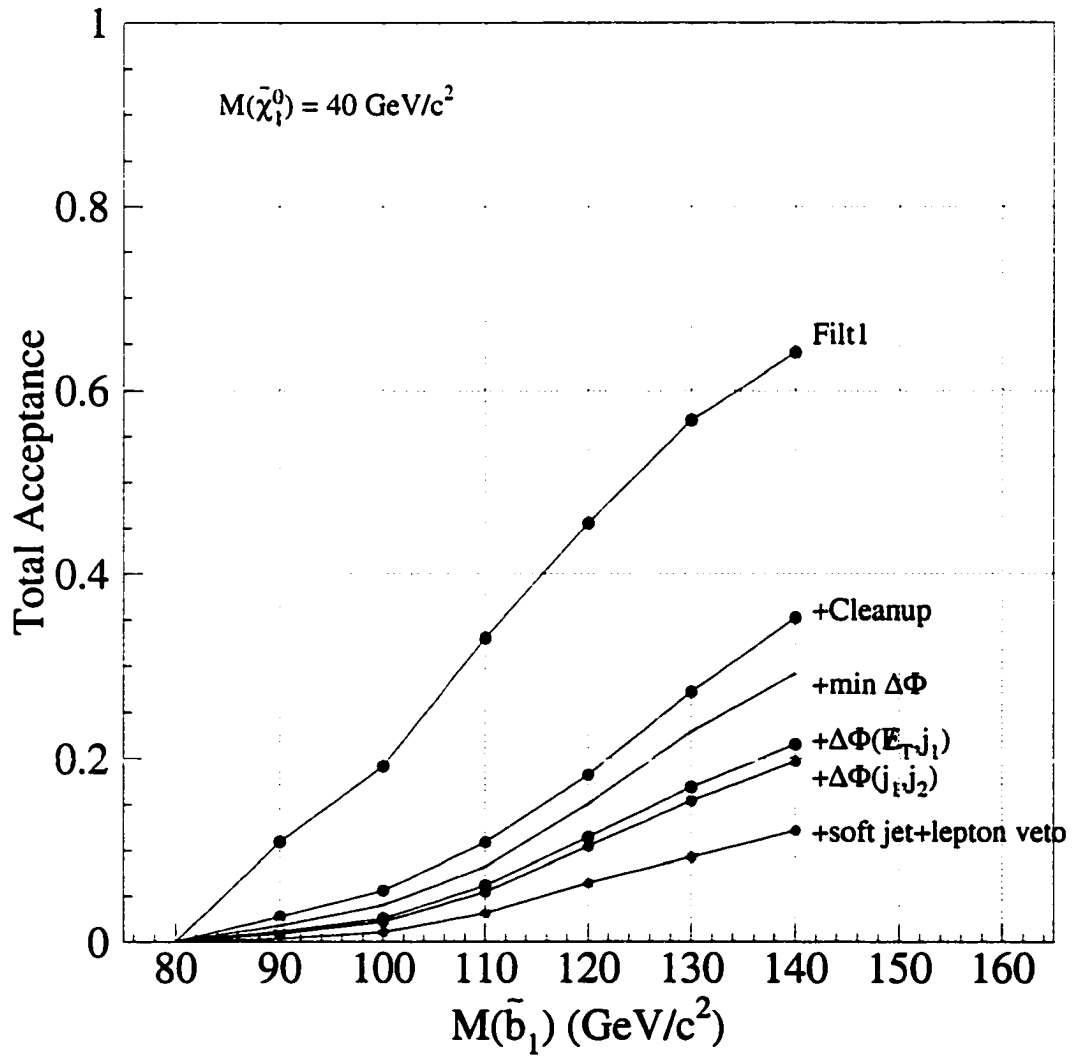Figure 4.26: The total $\tilde{b}_1\bar{\tilde{b}}_1$ acceptance after each requirement is applied (see Table 4.10) as a function of $M_{\tilde{b}_1}$ for $M_{\tilde{\chi}_1^0}=40$ GeV/c^2.

103

Figure 4.27: Kinematic distributions for events in the **Pretagged** sample. The $\tilde{t}_1\bar{\tilde{t}}_1$ sample has $M_{\tilde{t}_1} = 110$ GeV/c^2 and $m_{\tilde{\chi}_1^0} = 40$ GeV/c^2.

104

Figure 4.28: Kinematic distributions for events in the **Pretagged** sample. The $\tilde{t}_1\bar{\tilde{t}}_1$ sample has $M_{\tilde{t}_1} = 110 \text{ GeV}/c^2$ and $m_{\tilde{\chi}_1^0} = 40 \text{ GeV}/c^2$
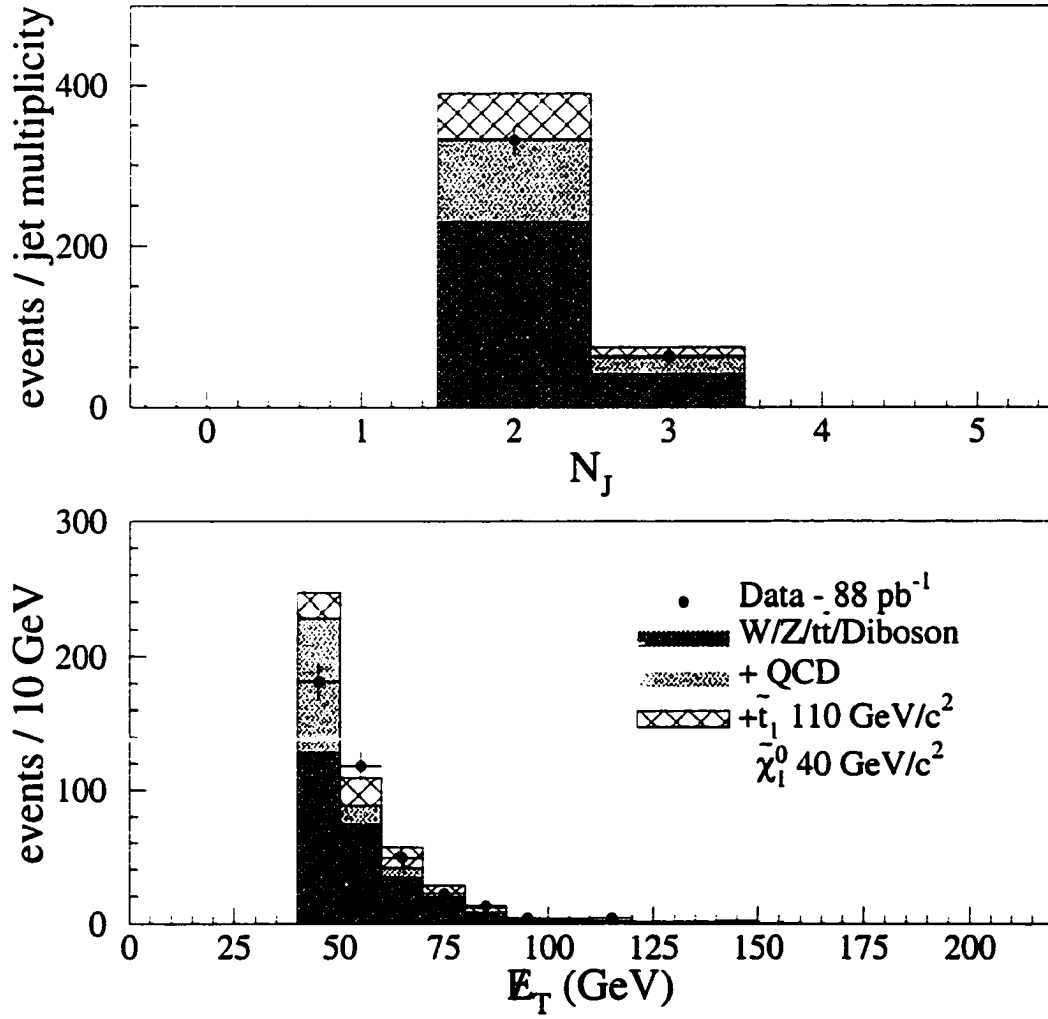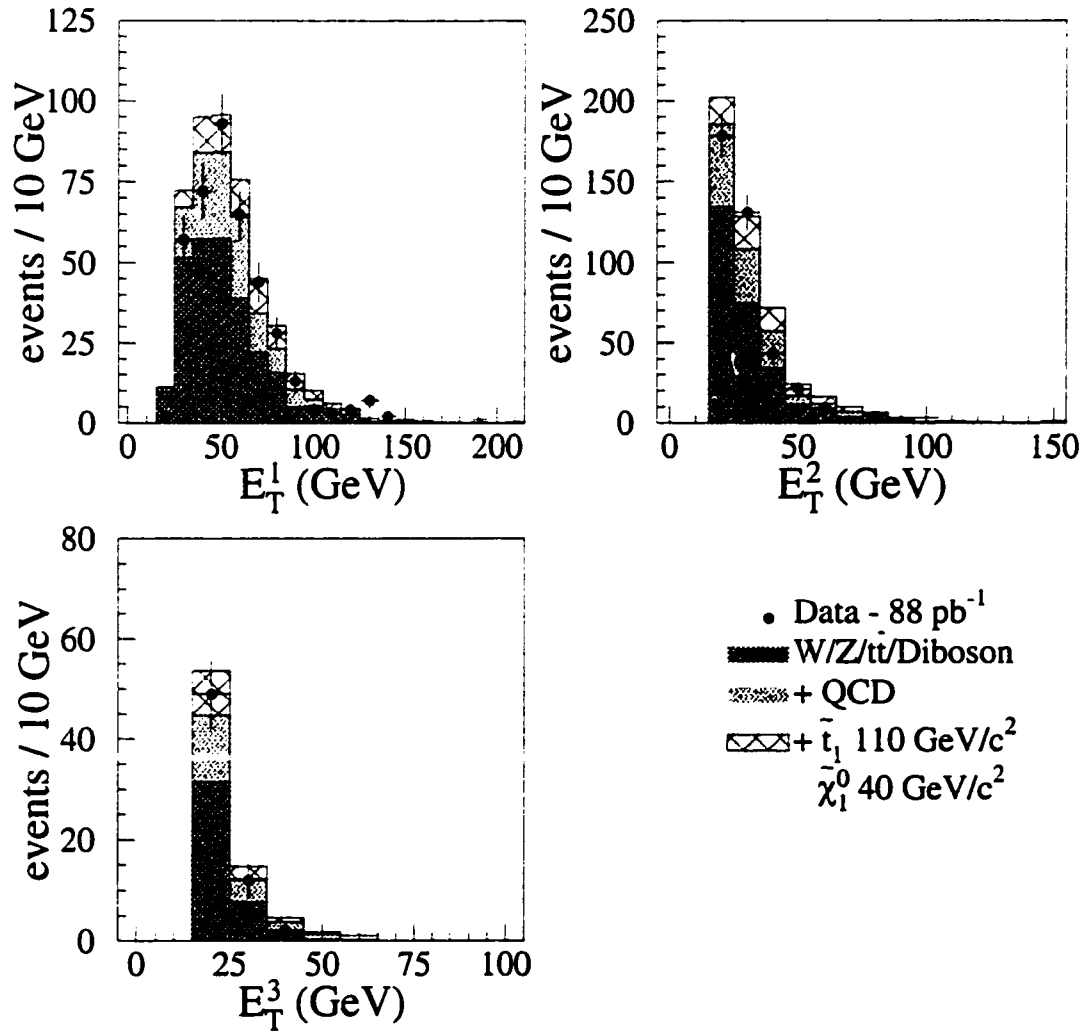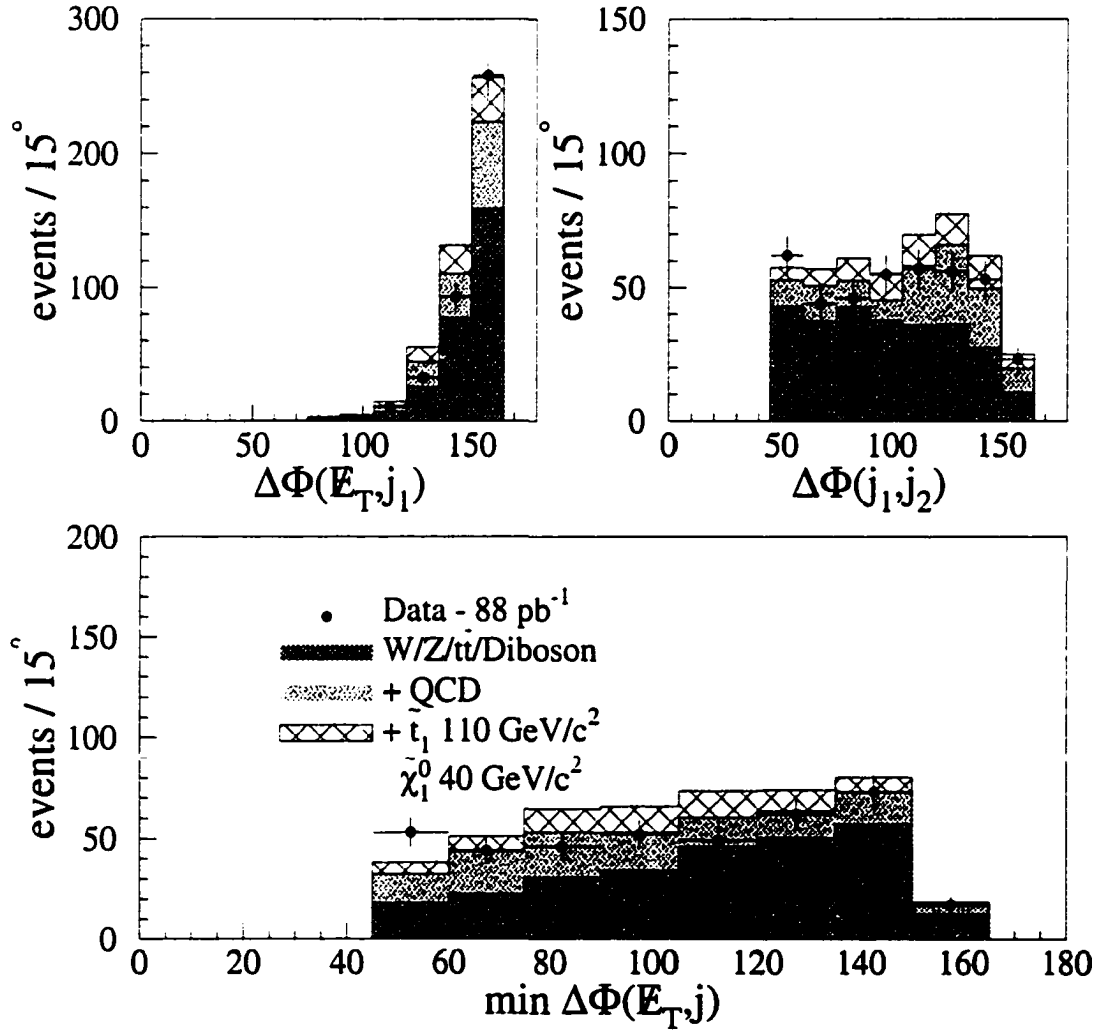
Figure 4.29: Kinematic distributions for events in the **Pretagged** sample. The $\tilde{t}_1\bar{\tilde{t}}_1$ sample has $M_{\tilde{t}_1} = 110$ GeV/c^2 and $m_{\tilde{\chi}_1^0} = 40$ GeV/c^2

106

Sample	N_{exp}
$W^\pm(\to e^\pm \nu_e){+}{\geq} 2$ jets	$69.7 \pm 4.6 \pm 20.6$
$W^\pm(\to \tau^\pm \nu_\tau){+}{\geq} 1$ jets	$2.3 \pm 0.9 \pm 0.7$
$Z^0(\to e\bar{e}){+}{\geq} 2$ jets	$0.4 \pm 0.2 \pm 0.1$
$Z^0(\to \mu\bar{\mu}){+}{\geq} 2$ jets	$0.4 \pm 0.2 \pm 0.1$
$Z^0(\to \tau\bar{\tau}){+}{\geq} 2$ jets	$0.1 \pm 0.1 \pm 0.03$
$t\bar{t}$	$2.6 \pm 0.5 \pm 0.9$
Diboson (WW+WZ+ZZ)	$2.0 \pm 0.3 \pm 0.6$
total EWK bkg	$77.5 \pm 4.7 \pm 22.3$
total DATA	78

Table 4.17: The number of data events and expected background events for the **Pre-tagged** central electron sample. The first error is statistical, the second is systematic.

Central Electrons

Table 4.17 shows the composition of the **Pretagged** single central electron sample. We see there is an excellent agreement between expected number of events and the number of observed events. Figure 4.30 shows the N_J, $\not{E}_T$ and M_T distributions. Figure 4.31 shows the jet E_T spectrum as well as the the lepton E_T. Figure 4.32 shows various $\Delta\Phi$ distributions. We draw the reader's attention to the transverse mass plot in Figure 4.30. The Jacobian peak near the W mass tells us that this sample is dominated by $W^\pm(\to e^\pm \nu_e)$. In Figures 4.30–4.32, the "W" in the label "$W/Z/t\bar{t}/Diboson$" refers to $W^\pm(\to \mu^\pm \nu_\mu)$ and $W^\pm(\to \tau^\pm \nu_\tau)$ only.

Plug Electrons

For plug electrons, we observe 36 events while we expect $47.4 \pm 3.74 \pm 13.78$ events; an overestimate of $\approx 33\%$. This means that we are underestimating our plug electron
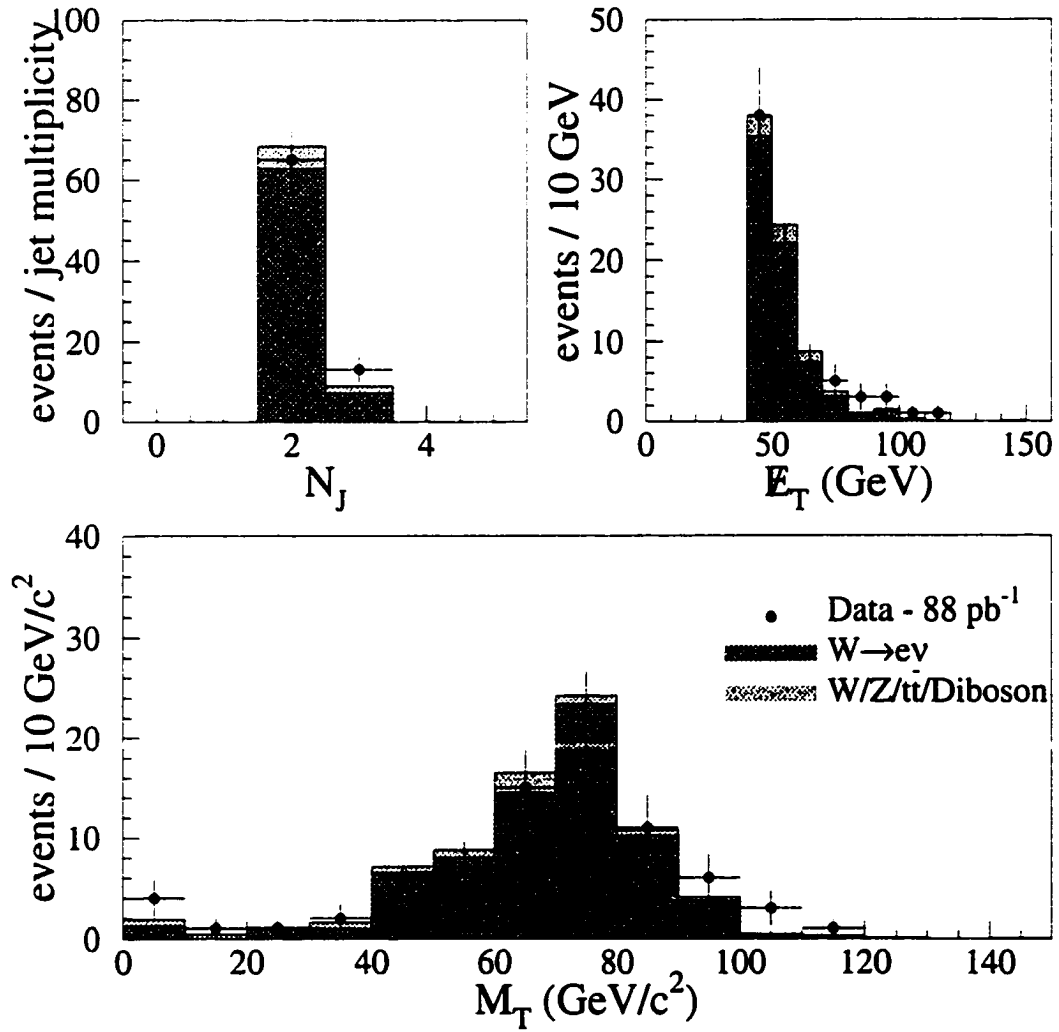
107

Figure 4.30: Kinematic distributions for events in the **Pretagged** central electron sample.
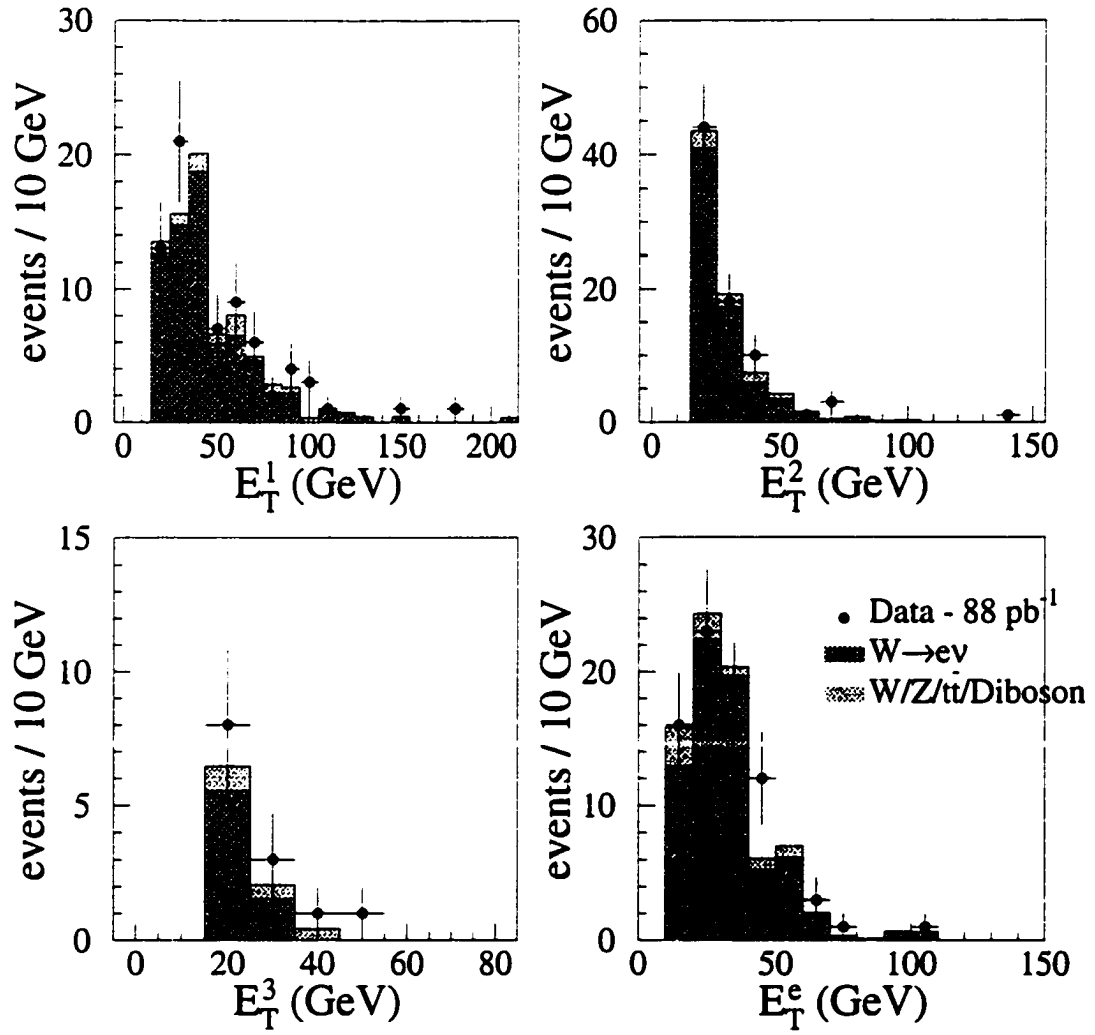
108

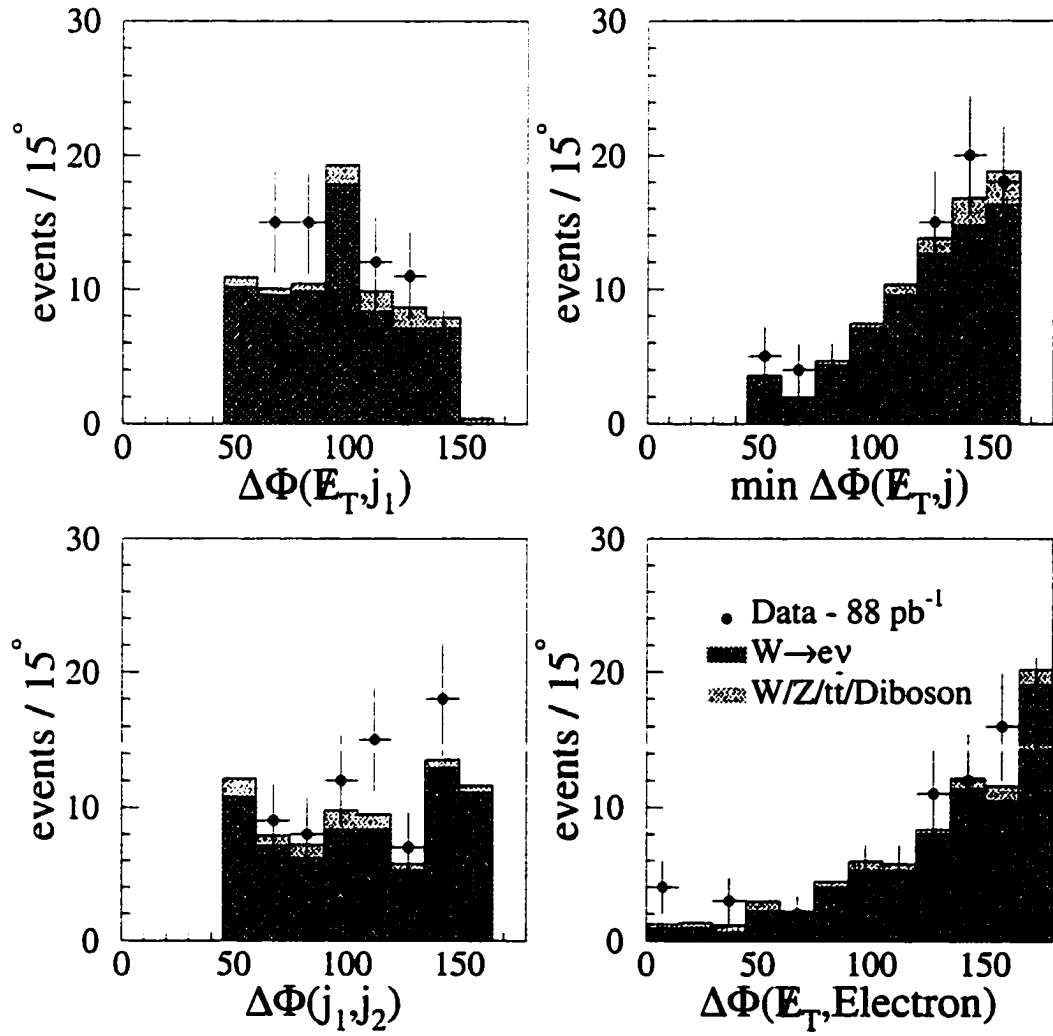Figure 4.31: Kinematic distributions for events in the **Pretagged** central electron sample.

109

Figure 4.32: Kinematic distributions for events in the **Pretagged** central electron sample.

110

Sample	N_{exp}
$W^{\pm}(\to e^{\pm}\nu_e) + \geq 2$ jets	$0.9 \pm 0.5 \pm 0.3$
$W^{\pm}(\to \mu^{\pm}\nu_{\mu}) + \geq 2$ jets	$47.3 \pm 3.8 \pm 13.9$
$W^{\pm}(\to \tau^{\pm}\nu_{\tau}) + \geq 1$ jets	$5.6 \pm 1.37 \pm 1.6$
$Z^0(\to \nu\bar{\nu}) + \geq 2$ jets	$0.1 \pm 0.1 \pm 0.03$
$t\bar{t}$	$2.1 \pm 0.4 \pm 0.8$
Diboson (WW+WZ+ZZ)	$2.0 \pm 0.3 \pm 0.5$
total EWK bkg	$58.0 \pm 4.1 \pm 16.7$
total Data	55

Table 4.18: The number of data events and expected background events for the **Pretagged** central muon sample. The first error is statistical, the second is systematic.

background by up to 33% in the Pretagged sample. The background from plug electrons is $\approx 40\%$ of the total electron background. Therefore, we have underestimated the total electron background by $\approx 13\%$. In the **Pretagged** sample, this equals ≈ 2 events. In the tagged sample, this is ≈ 0.04 events.

Central Muons

Table 4.18 shows the expected composition of the **Pretagged** central muon sample. As with the central electrons, the agreement is quite good between data and calculation. In addition, the sample is dominated by $W^{\pm}(\to \mu^{\pm}\nu_{\mu})$. Figures 4.33–4.35 show the agreement between data and MC for the same variables which are plotted for the central electron sample. Again we note the Jacobian peak in the transverse mass plot (Figure 4.33). In Figures 4.33–4.35, the "W" in the label "$W/Z/t\bar{t}/Diboson$" refers to $W^{\pm}(\to e^{\pm}\nu_e)$ and $W^{\pm}(\to \tau^{\pm}\nu_{\tau})$ only.
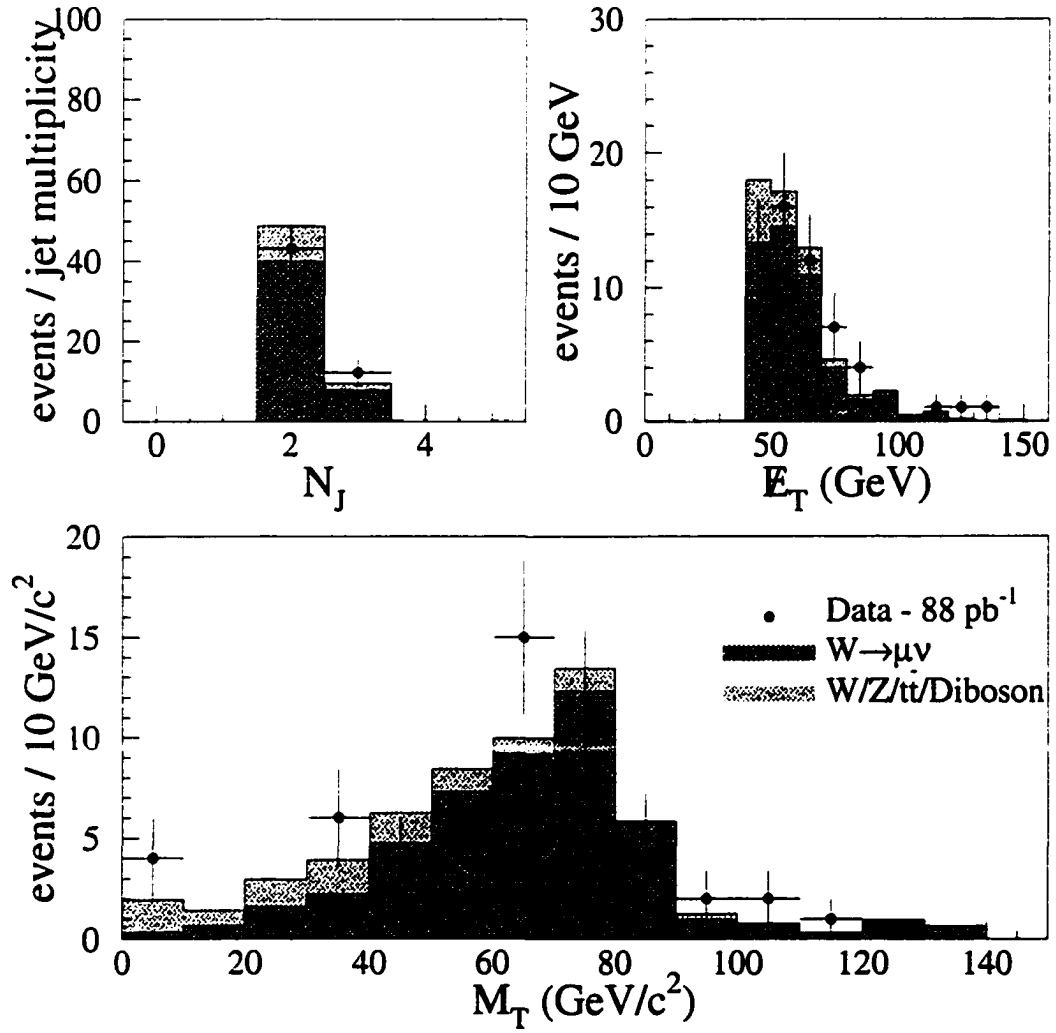
111

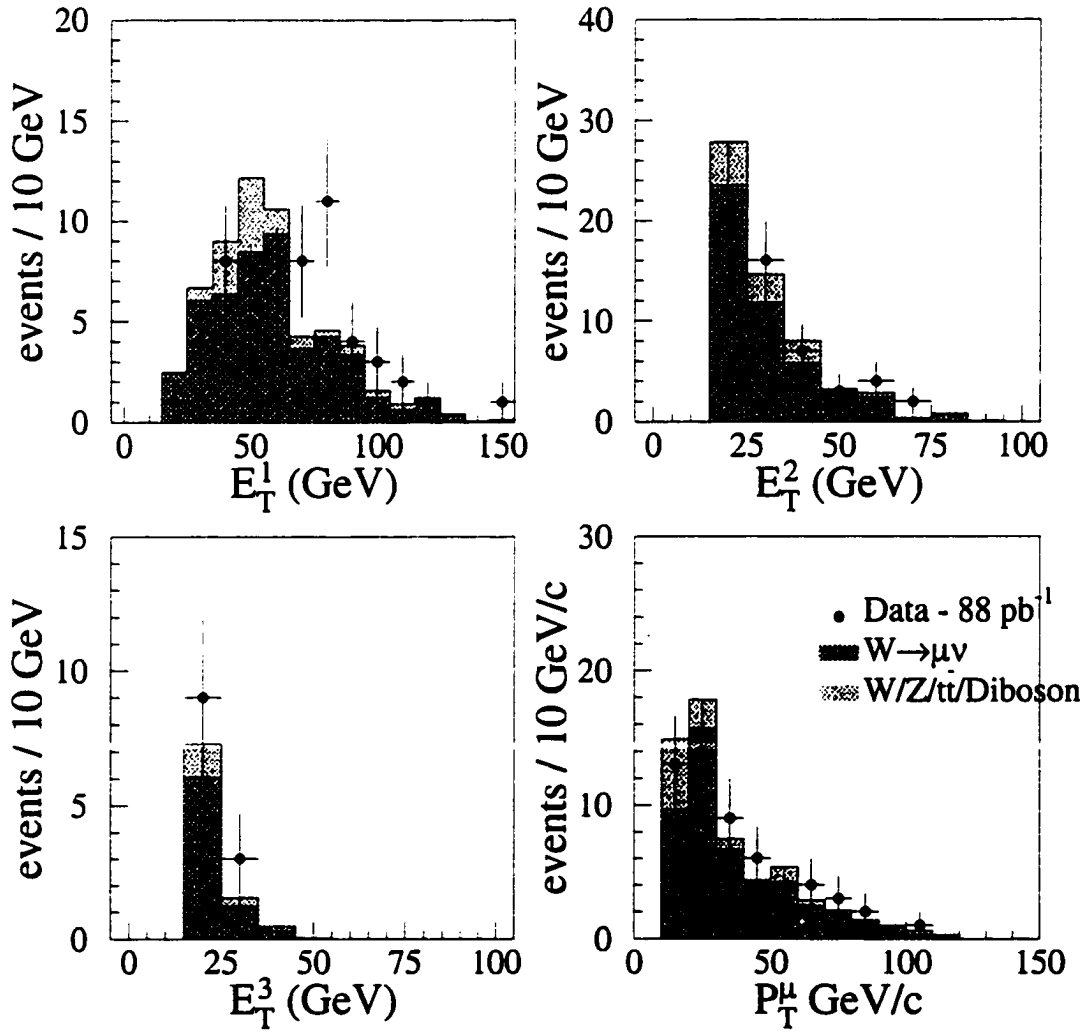Figure 4.33: Kinematic distributions for events in the **Pretagged** central muon sample.

112

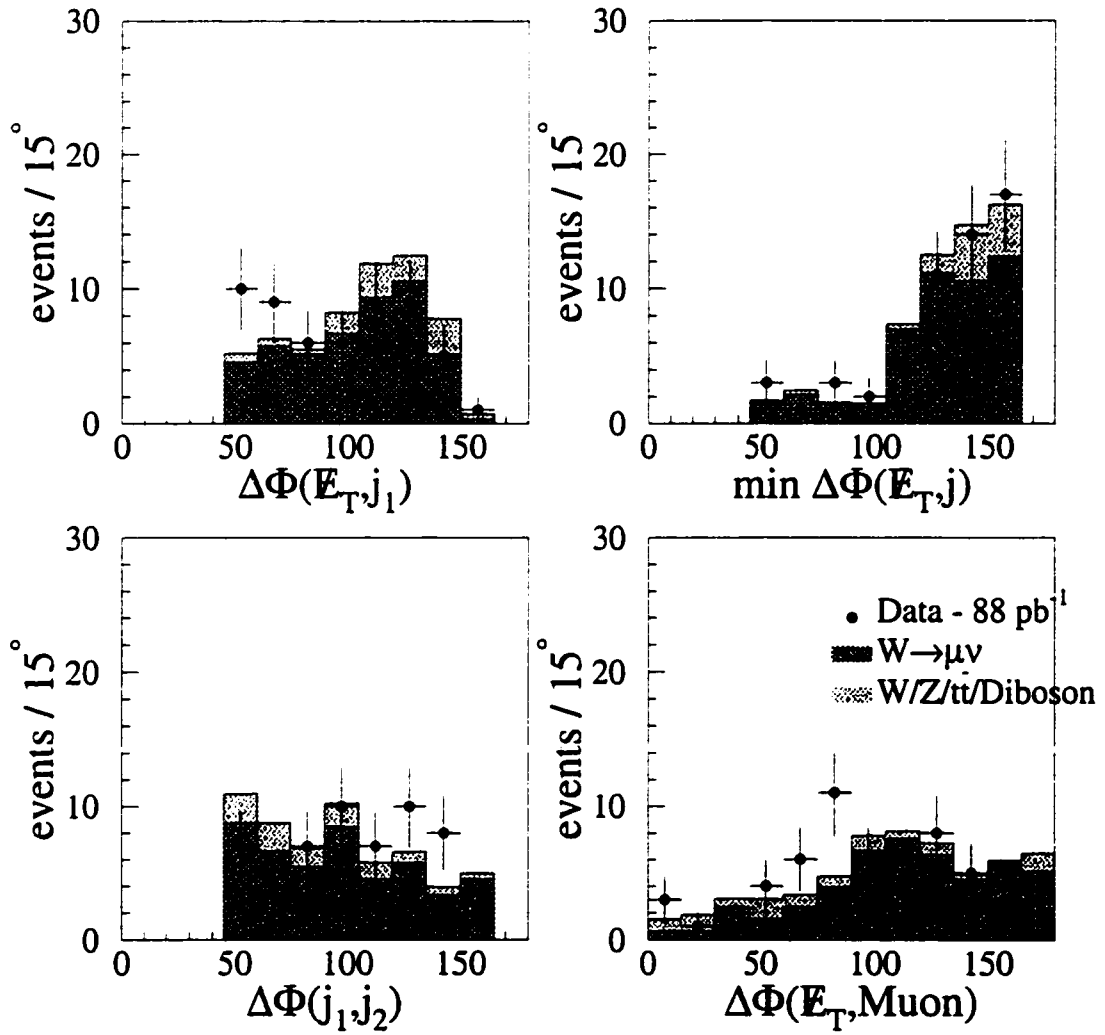Figure 4.34: Kinematic distributions for events in the **Pretagged** central muon sample.

113

Figure 4.35: Kinematic distributions for events in the **Pretagged** central muon sample.

114

$$E_T > 10 \text{ GeV}$$

$$P_T(seed\ track) > 10 \text{ GeV/c}$$

$$|\eta| < 1.$$

$$\#tracks\ (10°\ cone) = 1\ or\ 3$$

$$|Q_\tau| = 1$$

$$\#tracks\ (10° - 30°\ annulus) = 0$$

$$\zeta > 0.15$$

Table 4.19: Tau ID requirements. See [57, 78] for a description of the identification variables.

Taus

For tau events, we use the id algorithm described in [57, 78] with one exception. We do not cut on the tau mass as reconstructed from tracks and π^0's. In consultation with the authors of [57, 78], we see that we are not reconstructing the π^0's correctly. We believe that the cross-check of the tau MC normalization is still valid using the modified set of id requirements. The requirements we use are listed in Table 4.19 for completeness.

Table 4.20 shows the expected composition of the **Pretagged** tau sample. For this sample, we look at events with one identified tau and one or two high–E_T jets. Since a tau can be mis–identified as a jet, it is these types of events which populate our **Pretagged** sample. We see there is an excellent agreement between data and our background calculation. We again plot kinematic distributions to show the agreement between MC and data; these are shown in Figures 4.36–4.38.

We consider the possibility of rejecting identified taus from the final sample. Tau rejection does suppress our background, while still being efficient to signal and thus increase our sensitivity to stop. Indeed after tau veto the $S/\sqrt(B)$ goes from 5.1 to

115

Sample	N_{exp}
$W^{\pm}(\to e^{\pm}\nu_e)+\geq 2$ jets	$0.6 \pm 0.4 \pm 0.2$
$W^{\pm}(\to \mu^{\pm}\nu_\mu)+\geq 2$ jets	$2.4 \pm 0.9 \pm 0.7$
$W^{\pm}(\to \tau^{\pm}\nu_\tau)+\geq 1$ jets	$45.7 \pm 3.9 \pm 13.3$
$Z^0(\to \nu\bar{\nu})+\geq 2$ jets	$0.3 \pm 0.2 \pm 0.1$
$t\bar{t}$	$0.2 \pm 0.1 \pm 0.06$
Diboson (WW+WZ+ZZ)	$0.3 \pm 0.1 \pm 0.09$
total EWK bkg	$49.5 \pm 4.0 \pm 14.3$
total Data	46

Table 4.20: The number of data events and expected background events for the **Pretagged** tau sample. The first error is statistical, the second is systematic.

5.7 for $M_{\tilde{t}_1} = 110$ GeV/c^2, $m_{\tilde{\chi}_1^0} = 40$ GeV/c^2. Yet there is a problem with applying tau id veto. We find that it rejects 4% of our signal events. This is not a problem by itself, but this number does not agree with the fake tau rate estimate from generic jets samples [57], which is 1% per jet (2% for dijet events). This fact is not surprising, because our signal contains charm jets, while the fake rate study was done on a mostly gluon jet sample. This means we need to do more studies to understand the fake tau rate in a heavy–flavor enriched sample. The modest enhancement of the sensitivity is more than offset by the increase in the systematic uncertainties.

Looking at the M_T for the tau sample, we note that the expected shape does not agree well with the observed shape. If we perform a K–S [3] test on the shapes, we get a probability of 0.02. Whether this low value is due to a poor modeling of taus in MC or to a severe statistical fluctuation in the 40–50 GeV/c^2 bin is something that would need studying. Since this is not a tau analysis and the total number of events

---

[3]The Kolmogorov–Smirnov (K–S) test is a measure of the probability that two distributions are consistent with coming from the same parent distribution.

116

is consistent, we choose not to pursue this farther. For completeness, the K–S test returns a value of 0.87 for the central electron sample and 0.48 for the central muon sample.
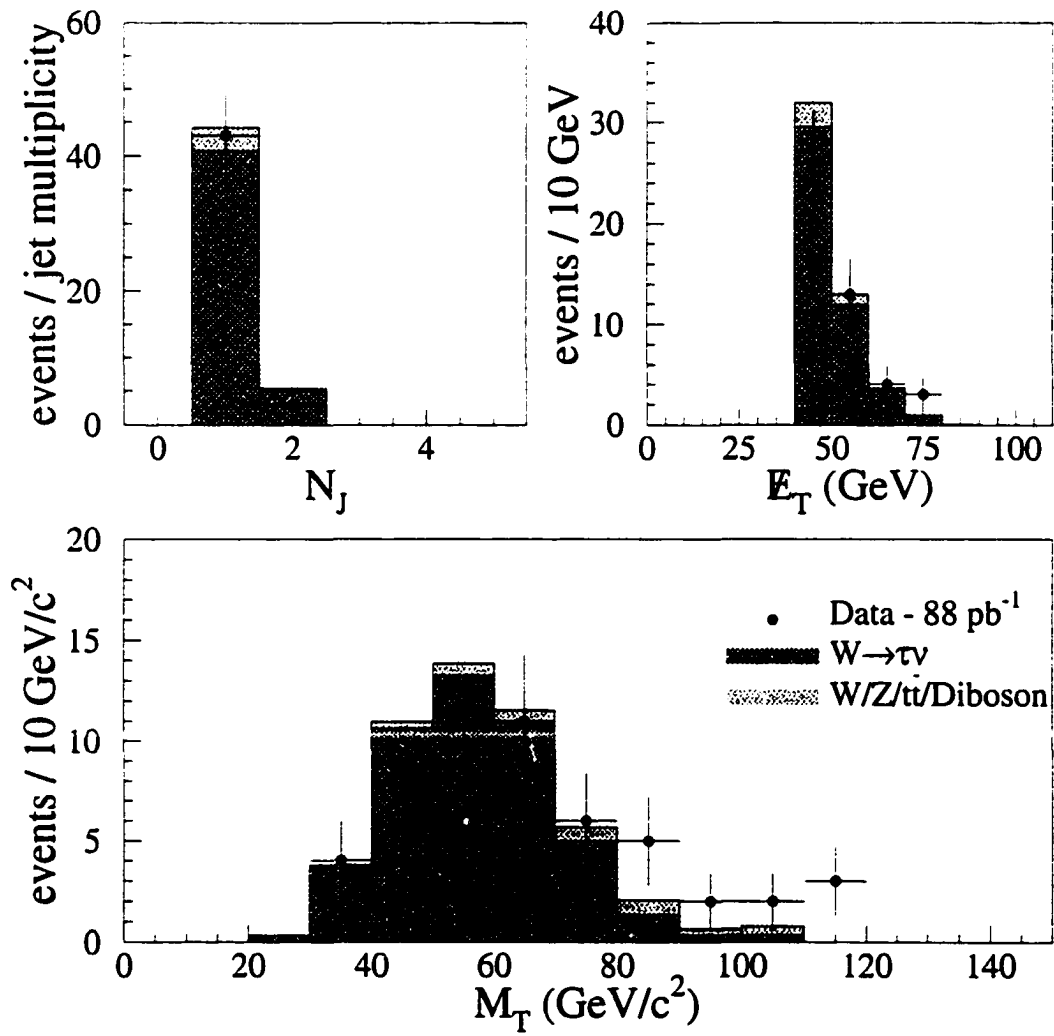
117

Figure 4.36: Kinematic distributions for events in the **Pretagged** tau sample.
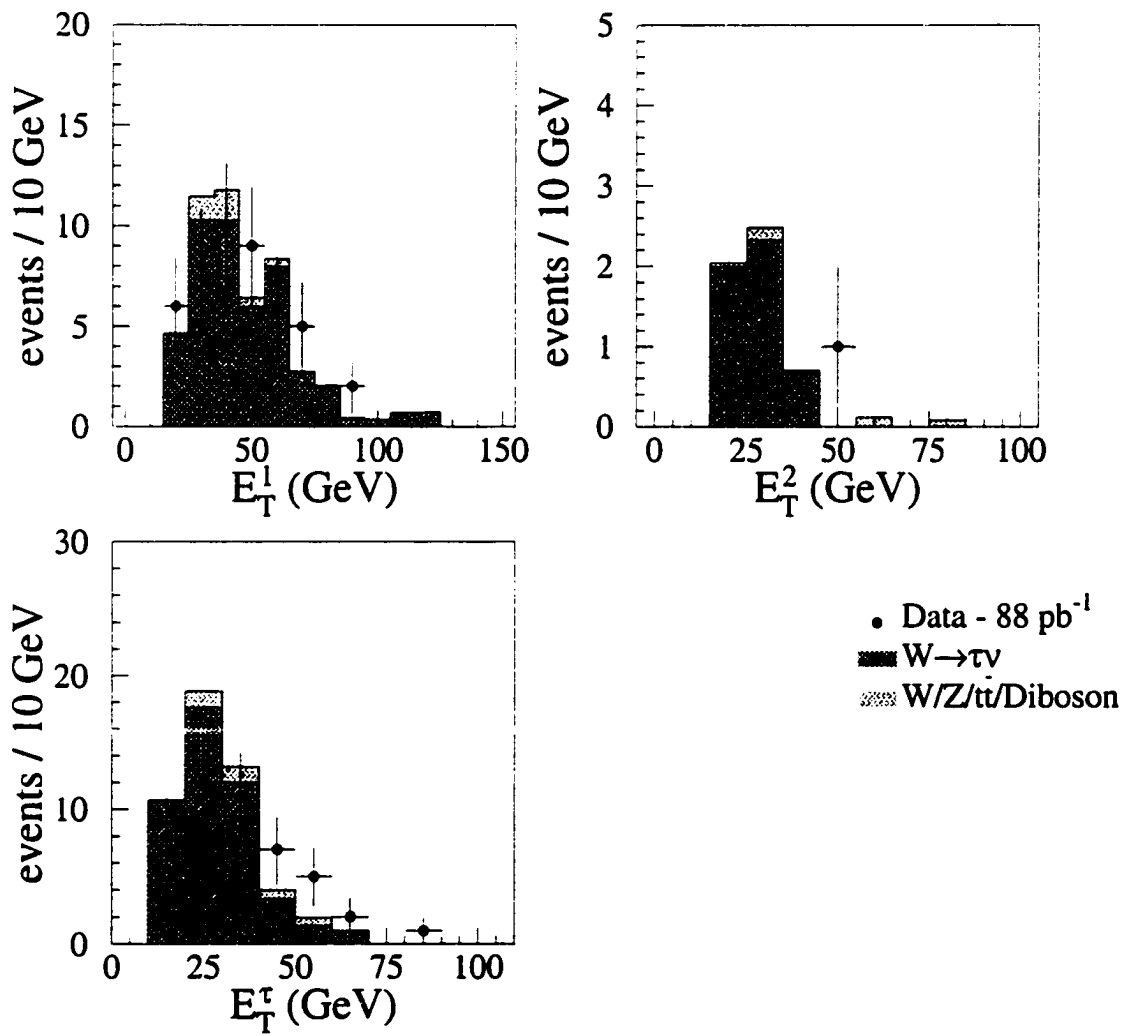
118

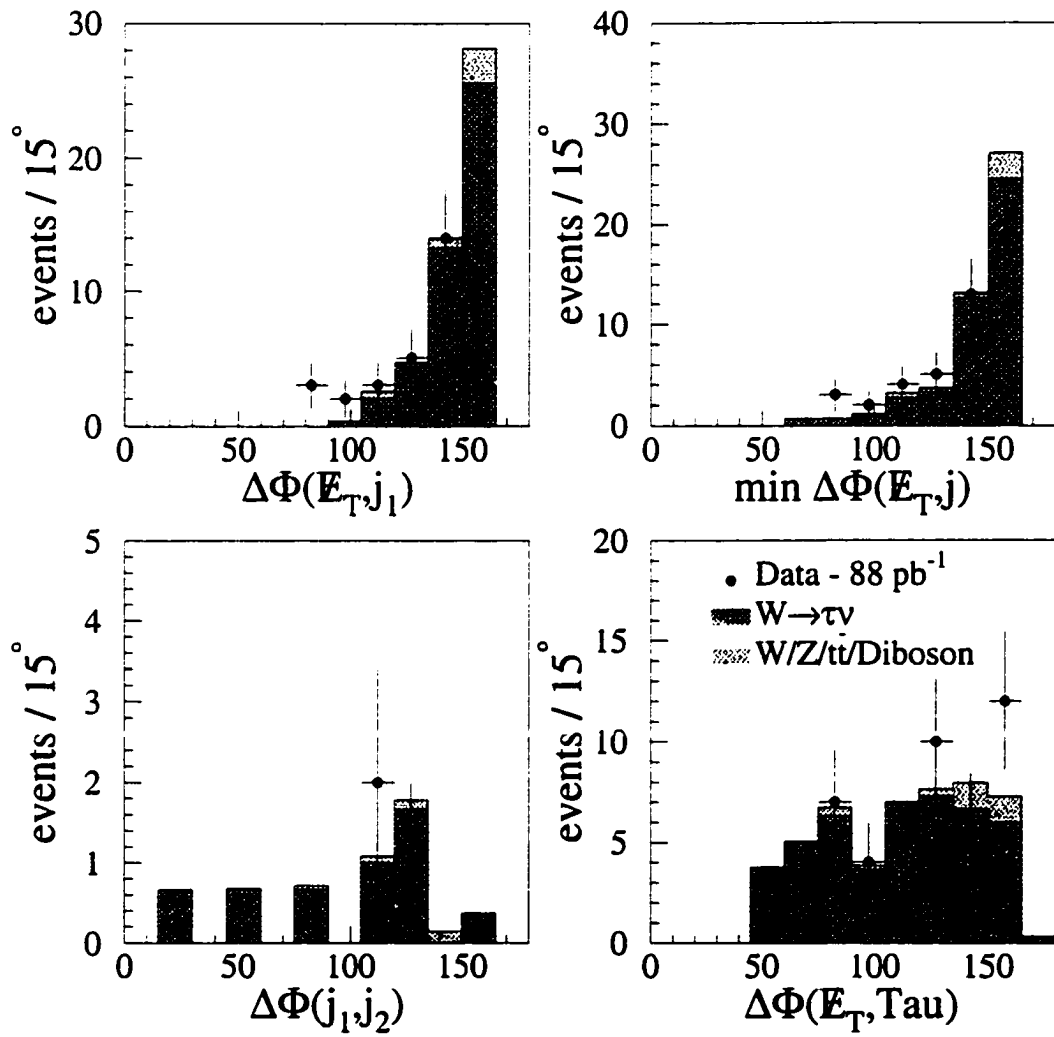Figure 4.37: Kinematic distributions for events in the **Pretagged** tau sample.

119

Figure 4.38: Kinematic distributions for events in the **Pretagged** tau sample.

120

Chapter 5

Heavy Flavor Tagger

After applying our **Pretagged** requirements, we expect (based on MC studies) 99% of $\tilde{t}_1\bar{\tilde{t}}_1$ events ($M_{\tilde{t}_1} = 110$ GeV/c^2, $M_{\tilde{\chi}_1^0} = 40$ GeV/c^2) to contain at least one c jet ($E_T > 15$ GeV, $|\eta| < 2$) and 99% of $\tilde{b}_1\bar{\tilde{b}}_1$ events ($M_{\tilde{b}_1} = 140$ GeV/c^2, $M_{\tilde{\chi}_1^0} = 40$ GeV/c^2) to contain at least one b jet ($E_T > 15$ GeV, $|\eta| < 2$). For background, the percentage is much lower (see Table 5.1). If we can efficiently tag heavy flavor jets (jets due to a b/c hadron) while having a low tag rate for primary jets (jets due to a $u/d/s$ hadron), then we can significantly improve the expected signal significance ($S/\sqrt{B}$).

According to [13], the lifetimes for hadrons containing c quarks is ≈ 1 ps. This translates to a proper decay distance ($c\tau$) of ≈ 300 μm. c hadrons produced in the primary hard–scattering process travel a finite distance before decaying. CTC+SVX$'$ tracks from these decays appear to be displaced from the primary vertex in the transverse (x–y) plane. That is, the impact parameter in the transverse plane, d, for these tracks is large and positive. From Sec 3.2.1, we see that for tracks with $p_T > 1$ GeV the impact parameter error for tracks reconstructed from the CTC+SVX$'$ is much smaller than $c\tau$. These decay tracks have a large positive signed [1] impact

---

[1] The sign of a track's impact parameter is the sign of the scalar product of the impact parameter
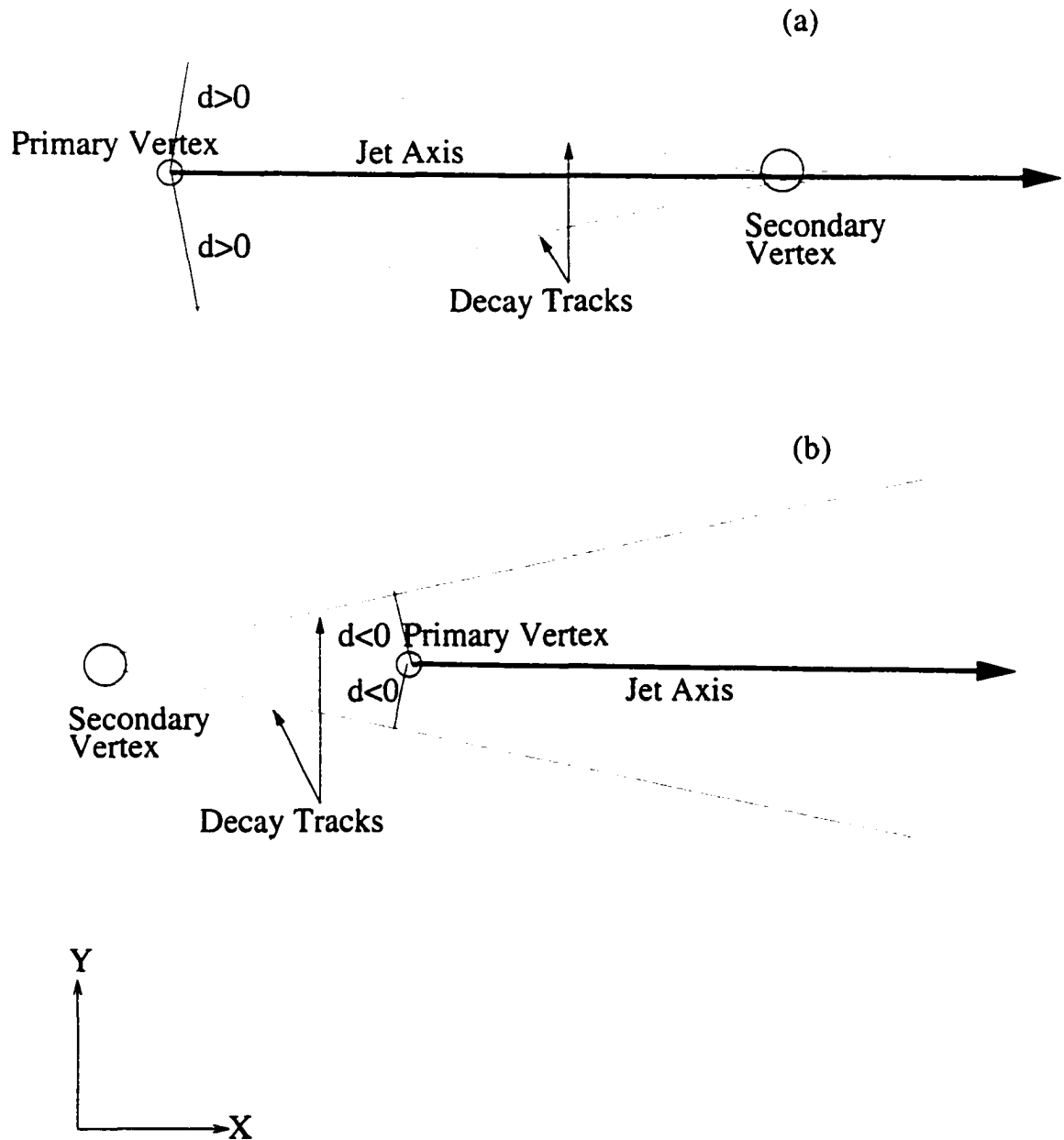
121

Figure 5.1: (a) Diagram of a secondary vertex composed of positive $(d > 0)$ impact parameter tracks. (b) Diagram of a secondary vertex composed of negative $(d < 0)$ impact parameter tracks.

122

Sample	1 c	2 c	1 b	2 b
$\tilde{t}_1\bar{\tilde{t}}_1$	6.6	93.2	0.1	0
$\tilde{b}_1\bar{\tilde{b}}_1$	1	0	10	89
QCD	8.9	0.9	4.5	1.8
$W^{\pm}(\rightarrow \tau^{\pm}\nu_{\tau})+ \geq 1$ jet	3.2	0.7	0	0
$W^{\pm}(\rightarrow \mu^{\pm}\nu_{\mu})+ \geq 2$ jet	6.2	0.5	1.4	0
$W^{\pm}(\rightarrow e^{\pm}\nu_{e})+ \geq 2$ jet	1.8	1.8	1.8	0
$Z^0(\rightarrow \nu\bar{\nu})+ \geq 2$ jet	3.1	0	0.3	0
$t\bar{t}$	30	4.3	52	43

Table 5.1: Percentage of events with $1c/2c/1b/2b$ jet(s) as determined by MC. Jets are required to have $E_T > 15$ GeV and $|\eta| < 2$. The $\tilde{t}_1\bar{\tilde{t}}_1$ sample has $M_{\tilde{t}_1} = 110$ GeV/c^2, $M_{\tilde{\chi}_1^0} = 40$ GeV/c^2 and the $\tilde{b}_1\bar{\tilde{b}}_1$ sample has $M_{\tilde{b}_1} = 140$ GeV/c^2, $M_{\tilde{\chi}_1^0} = 40$ GeV/c^2.

parameter significance $s_0 \equiv d \cdot \sigma_d$ with respect to the primary vertex; σ_d includes both the track uncertainty and the primary vertex uncertainty. In $\tilde{b}_1\bar{\tilde{b}}_1$ events, this effect is even greater. b hadrons have a lifetime of ≈ 1.5 ps [13] which translates to a $c\tau$ of ≈ 450 μm. In addition, the large b mass leads to decay tracks which have, on average, a larger p_T. The larger track p_T leads to a smaller impact parameter error. The combination of longer decay distance and smaller impact parameter error leads to a greater, on average, impact parameter significance.

On the other hand, light quark ($= u, d, s$) hadrons or gluons do not have a measurable lifetime. Tracks from light quark hadrons or gluons, which we call primary tracks, are consistent with coming from the primary vertex. The SVX' resolution causes the signed impact distribution of these tracks to be gaussian–distributed around zero

and E_T vector of its associated jet. A track is associated to a jet if the track lies within a cone of R=0.4 of the jet.

123

while multiple scattering adds an exponential tail at large impact parameter significance. Fig. 5 is a diagram of an event with both primary and displaced tracks.

In this analysis, we use a probability technique [79] called Jet Probability (JP) to distinguish heavy flavor jets (jets containing b/c hadrons) from prompt jets (jets containing $u/d/s/$ hadrons or gluons). CDF has an alternate heavy flavor tagger, called SECVTX [7], that reconstructs the secondary vertex formed by the decay of the heavy flavor hadrons. We choose JP over SECVTX for several reasons:

1. JP is twice as efficient for charm jets as SECVTX.

2. JP is a robust tagger that works well in different data samples.

3. JP returns a continuous variable. We can easily optimize the JP requirement for different analyses.

4. JP allows us to use a single tagger for both $\tilde{t}_1\bar{\tilde{t}}_1$ and $\tilde{b}_1\bar{\tilde{b}}_1$ analyses.

5.1   Jet Probability

5.1.1   Description

Fig. 5.2 shows the signed impact parameter significance (s) distribution of tracks from the JET50 data sample [79]. The gaussian core is due to the SVX' resolution while the negative tail is due to multiple scattering and the positive tail is due to multiple scattering plus long–lived particles. We fit the data to a pair of gaussians plus two exponentials; one exponential for the negative tail and one exponential for the positive tail. Because negative impact parameter significance tracks are due only to resolution effects, we can use the fitted curve in this region as our resolution function: $R(s_0)$.
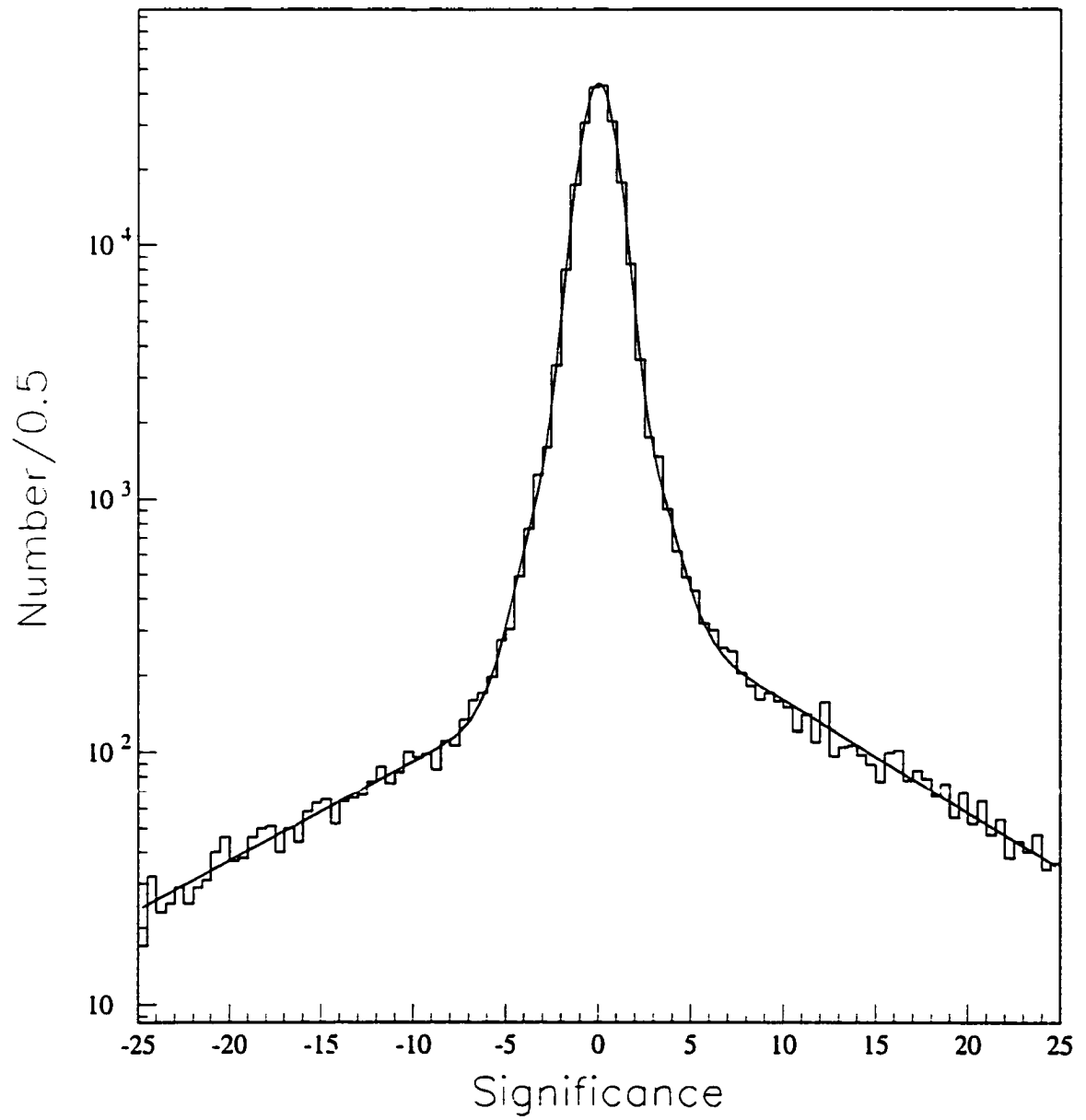
124

Figure 5.2: Signed impact parameter significance, s, for JET50 data sample [79].
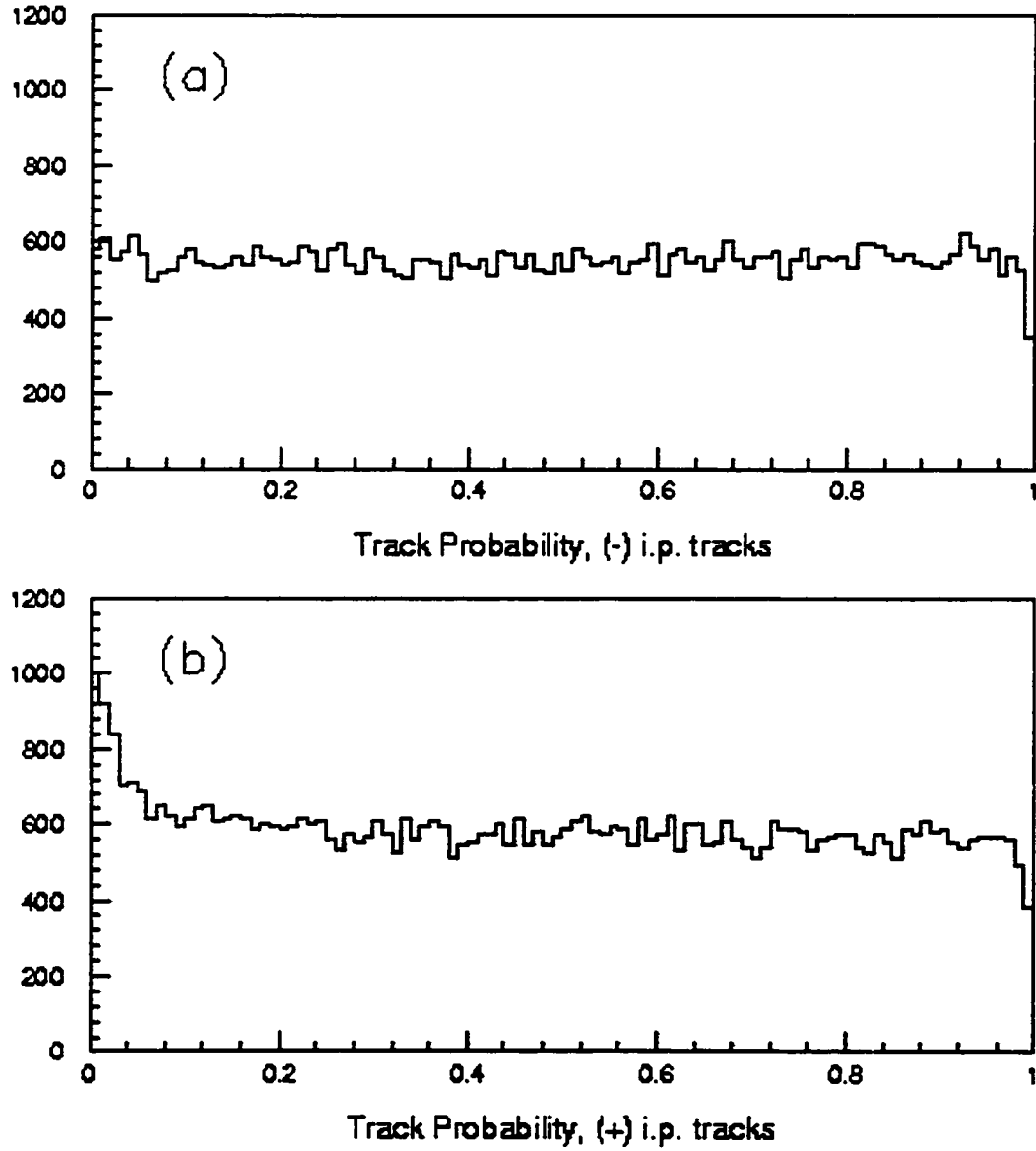
125

Track Probabilities, QCD sample

Figure 5.3: (a) Track probability distribution of *negative* impact parameter (-i.p.) tracks for QCD sample [80]. (b) Track probability distribution of *positive* impact parameter (+i.p.) tracks for QCD sample [80].

126

We then define the probability, $P(s_0)$, that a track with a signed impact parameter significance of s_0 or greater comes from the primary vertex:

$$P(s_0) = \frac{\int_{-\infty}^{-|s_0|} R(s)ds}{\int_{-\infty}^{0} R(s)ds} \qquad (5.1)$$

In practice, R and P are functions of s_0, N_{hits} (the number of SVX' hits), and N_{shared} (the number of shared SVX' hits). N_{hits} ranges from 2 to 4 and N_{shared} ranges from 0 to N_{hits}. Therefore, there are 12 independent resolution functions. In addition, we use separate sets of resolution functions for data and MC. Fig. 5.3(a) shows the track probability distributions in the QCD sample for negative impact parameter (-i.p) tracks [80]. As expected, the distribution is flat. The positive impact parameter (+i.p) tracks, Fig. 5.3(b), exhibit an excess of tracks at low probability [80].

We can now define jet probability, JP, as the probability that the ensemble of tracks in a jet are consistent with originating from the primary vertex:

$$JP = \prod \sum_{k=0}^{N-1} \frac{(-\ln \prod)^k}{k!} \qquad (5.2)$$

where $\prod = P_1 \cdot P_2 \cdot P_3 \ldots P_N$.

Positive jet probability, JP_+, is the jet probability for the ensemble of tracks with positive impact parameter and negative jet probability, JP_-, is the jet probability for the ensemble of tracks with negative impact parameter. The resolution functions for data are derived from the JET50 data sample. Fig. 5.4 plots the JP_- and the JP_+ for the QCD data sample [80]. The JP_- is flat and the JP_+ has an excess of jets at low jet probability indicating the presence of heavy flavor jets.
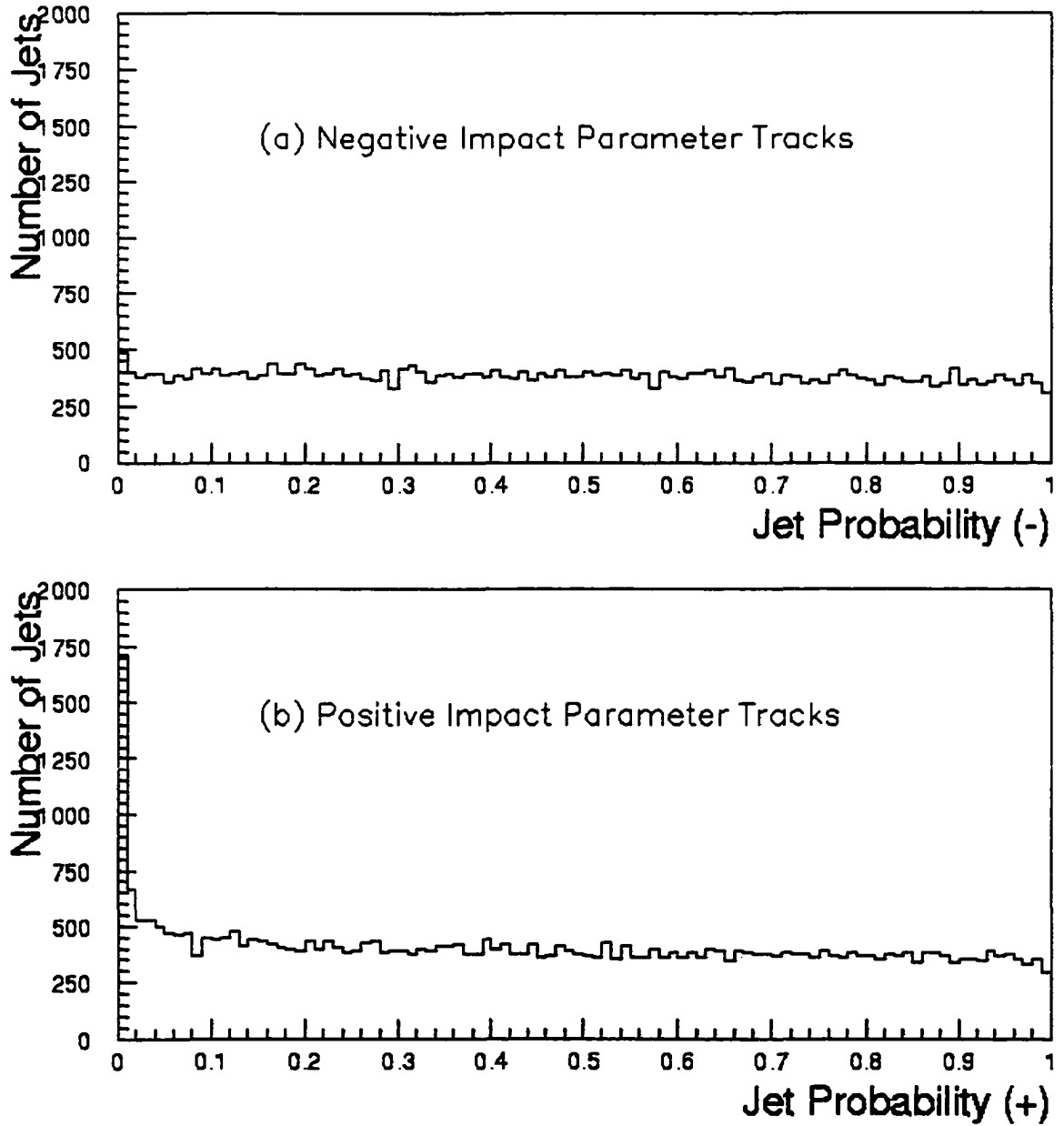
127

Jet Probability for Taggable Jets

Figure 5.4: (a) Negative Jet Probability distribution (JP_-) for QCD sample [80]. (b) Positive Jet Probability distribution $JP_+$of for QCD sample [80].

128

5.1.2 Tracking degradation

The JP tagging efficiency depends on the track reconstruction efficiency. From studies comparing data to MC expectations [81], we find that the initial detector simulation does not reproduce the track finding efficiency correctly. For $JP_+ \leq 0.05$, the ratio of $\epsilon(DATA)/\epsilon(MC) = 0.88 \pm 0.12$ [82]. To account for this loss in efficiency, we employ a *tracking degradation* algorithm on a track-by-track basis. The tracking degradation algorithm gives the probability that a MC track would be reconstructed in data. This probability is a function of the number of other tracks surrounding the track in question. All MC JP plots and numbers in this analysis include tracking degradation. In Sec. 7.1.3 we demonstrate that adding tracking degradation to MC correctly models the JP efficiency.

5.1.3 Optimization

We compute JP_+ for jets with $E_T > 15$ Gev and $|\eta| < 2$ (see Table 4.10). We consider a jet "taggable" [2] if the jet contains ≥ 2 tracks ($\Delta R(track, jet) < 0.4$ [3]) that satisfy the following criteria [80]:

1. $\chi^2_{SVX}/d.o.f \leq 6$

2. $N_{hits} \geq 2$; 2-hit tracks with a hit in Layer 0 of the SVX' are excluded

3. Each track passes a loose set of track quality cuts

4. Tracks are inconsistent with coming from prompt K_s, Λ decays

---

[2] "Untaggable" jets are assigned a JP of 1.

[3] $\Delta R = \sqrt{(\Delta \eta)^2 + (\Delta \phi)^2}$

129

5. $|d| < 0.1$ cm

6. $|\Delta z| < 5$ cm between each track and the primary vertex

7. Track $p_T > 1$ GeV

8. positive impact parameter (if computing JP_+);

   negative impact parameter (if computing JP_-)

Fig. 5.5 shows the JP_+ distributions, normalized to 1, for $\tilde{t}_1\bar{\tilde{t}}_1$ MC events ($M_{\tilde{t}_1} = 110$ GeV/c^2, $M_{\tilde{\chi}_1^0} = 40$ GeV/c^2) after the **Pretagged** requirements are made. Jet 1/2/3, which we require to be "taggable", are ordered by E_T; $E_T^1 > E_T^2 > E_T^3$. The minimum JP_+ of "taggable" jets in the event is called min JP_+. We see a clear peak in min JP_+ at low jet probability. Fig. 5.6 shows the same plots for $\tilde{b}_1\bar{\tilde{b}}_1$ ($M_{\tilde{b}_1} = 140$ GeV/c^2, $M_{\tilde{\chi}_1^0} = 40$ GeV/c^2). We see that the peak at low probability is even more pronounced.

This is to be contrasted with the behavior of our background sources. As we saw in Fig. 5.4, QCD events have only a slight excess of events at low JP_+. Note that the distributions in Fig. 5.4 are <u>not</u> normalized to 1. Fig. 5.7 shows the JP_+ distributions for our QCD MC after the **Pretagged** selection. Fig. 5.8 shows the JP_+ distributions for our $W/Z/t\bar{t}/Diboson$ MC after the **Pretagged** selection.

From Fig. 5.5–Fig. 5.8, we see that JP_+ is an efficient discriminator between signal ($\tilde{t}_1\bar{\tilde{t}}_1$ or $\tilde{b}_1\bar{\tilde{b}}_1$) and background (QCD+$W/Z/t\bar{t}/Diboson$). As our final selection requirement, we demand that the event have min $JP_+ \leq X$. Like Sec. 4.6, we choose the value X by maximizing the $S/\sqrt{B}$. Unlike Sec. 4.6, we do not use the data distribution as our background shape. Instead, we use our MC samples, properly normalized, to model the background. Fig. 5.9 shows $S/\sqrt{B}$ for $\tilde{t}_1\bar{\tilde{t}}_1$ ($M_{\tilde{t}_1} = 110$ GeV/c^2,

130

Figure 5.5: JP_+ distributions for $\tilde{t}_1 \bar{\tilde{t}}_1$. The distributions are normalized to 1. Jet 1/2/3/ are ordered by E_T; $E_T^1 > E_T^2 > E_T^3$. min JP_+ is the minimum JP_+ of the three jets.
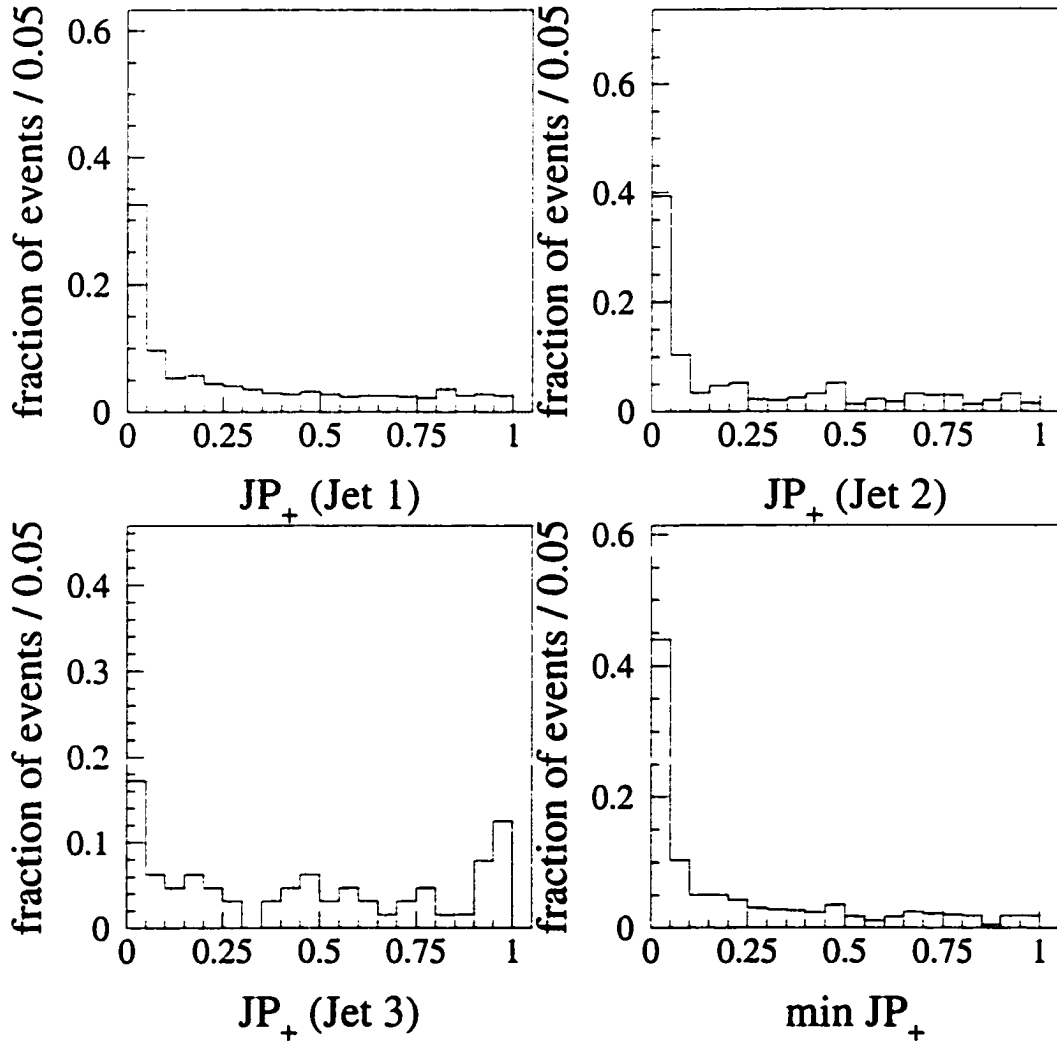
131
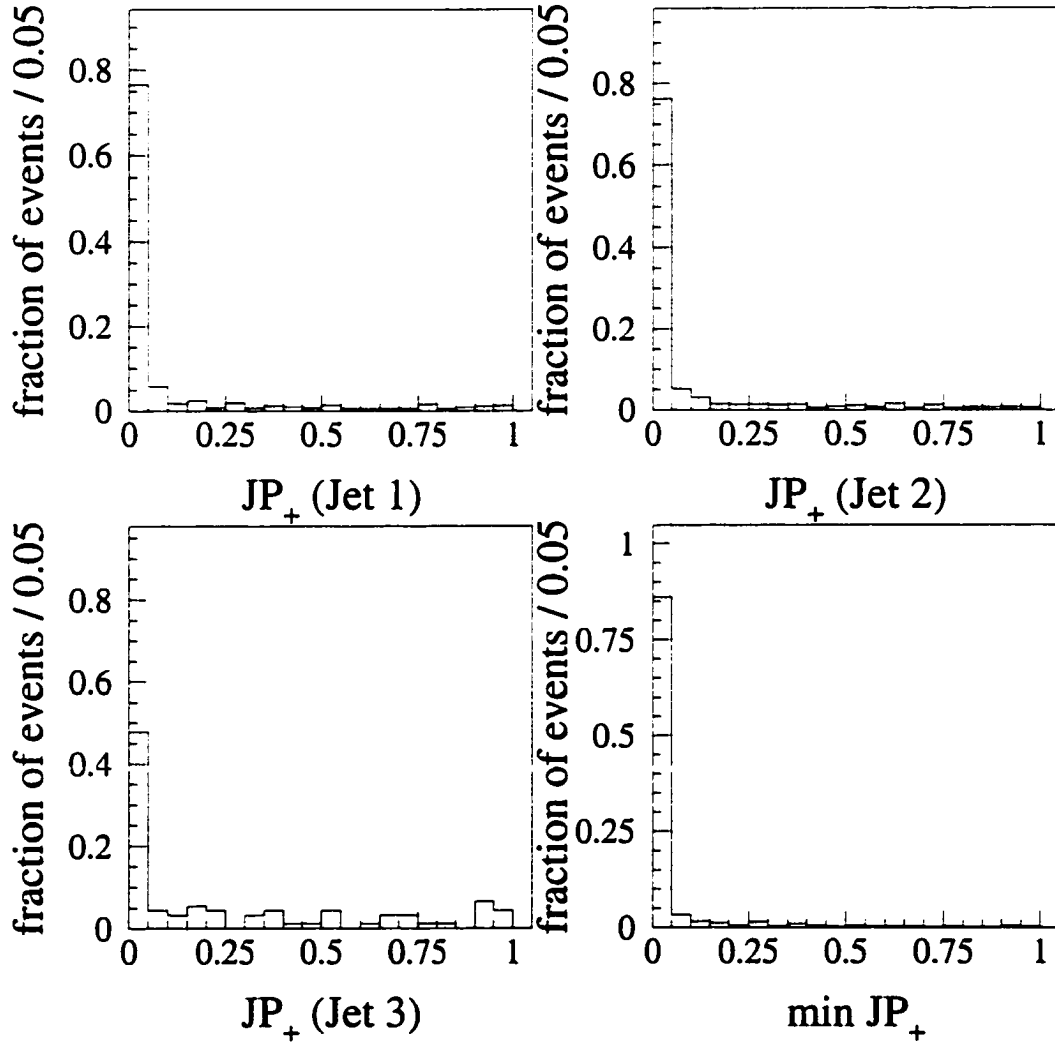
Figure 5.6: JP_+ distributions for $\bar{b}_1\bar{b}_1$. The distributions are normalized to 1. Jet 1/2/3/ are ordered by E_T; $E_T^1 > E_T^2 > E_T^3$. min JP_+ is the minimum JP_+ of the three jets.

132

Figure 5.7: JP_+ distributions for QCD MC. The distributions are normalized to 1. Jet 1/2/3/ are ordered by E_T; $E_T^1 > E_T^2 > E_T^3$. min JP_+ is the minimum JP_+ of the three jets.

133
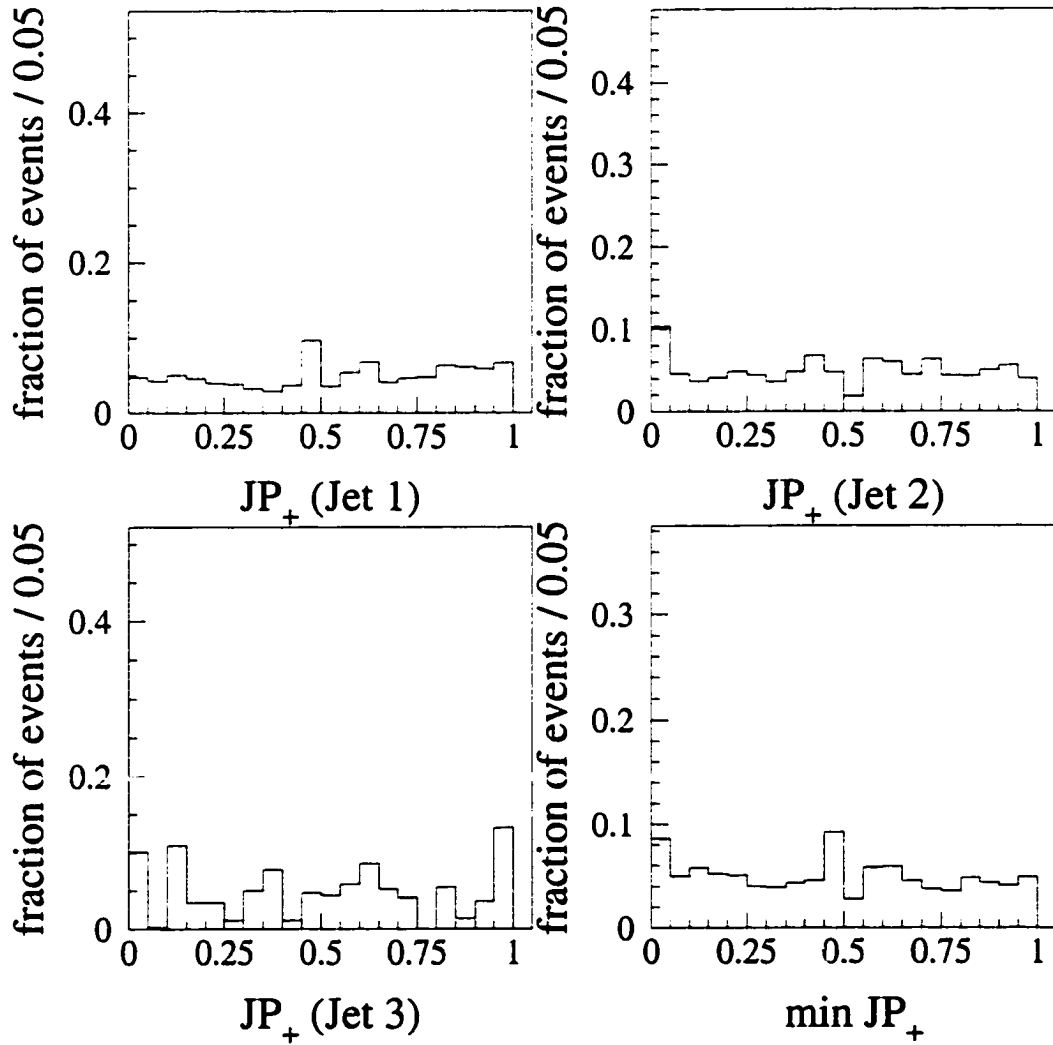
Figure 5.8: JP_+ distributions for $W/Z/t\bar{t}/Diboson$ MC. The distributions are normalized to 1. Jet 1/2/3/ are ordered by E_T; $E_T^1 > E_T^2 > E_T^3$. min JP_+ is the minimum JP_+ of the three jets.
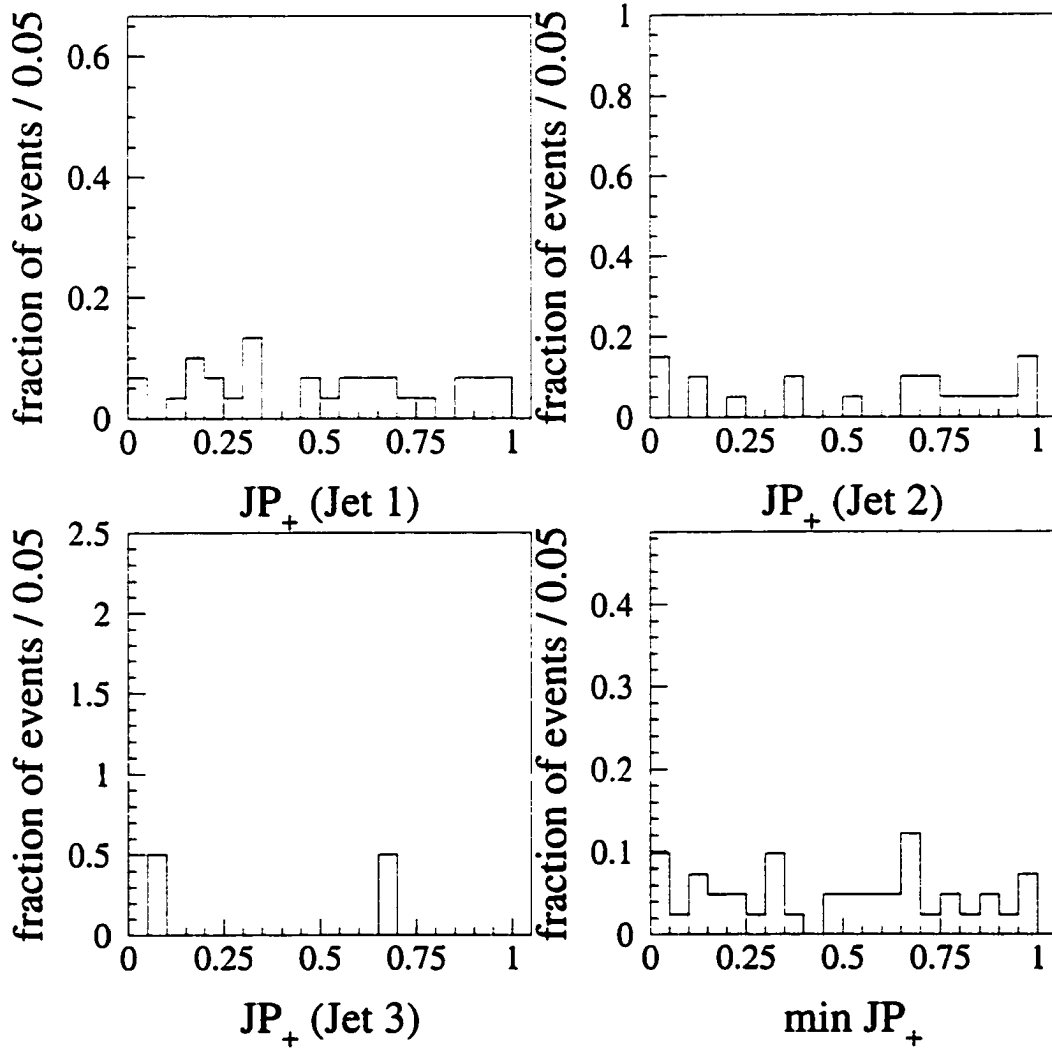
134
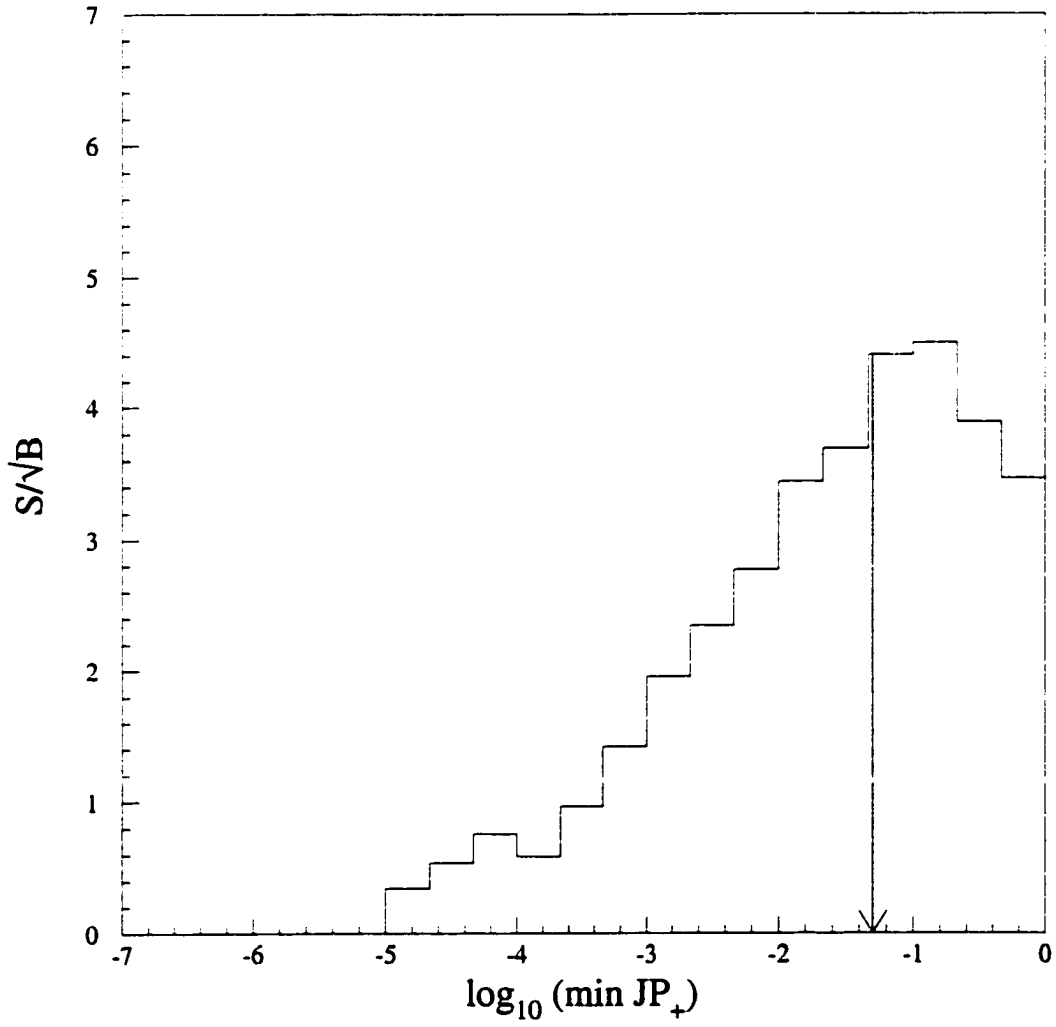
Figure 5.9: Optimization of the min JP_+ requirement for $\tilde{t}_1\bar{\tilde{t}}_1$. The arrow indicates the value chosen. $M_{\tilde{t}_1} = 110$ GeV/c^2, $M_{\tilde{\chi}_1^0} = 40$ GeV/c^2.

135

Figure 5.10: Optimization of the min JP_+ requirement for $\bar{b}_1\bar{b}_1$. The arrow indicates the value chosen. $M_{\tilde{t}_1} = 140$ GeV/c^2, $M_{\tilde{\chi}_1^0} = 40$ GeV/c^2.

136

$M_{\tilde\chi_1^0} = 40$ GeV/c^2) and Fig. 5.10 shows $S/\sqrt{B}$ for $\tilde b_1 \bar{\tilde b}_1$ ($M_{\tilde t_1} = 140$ GeV/c^2, $M_{\tilde\chi_1^0} = 40$ GeV/c^2). Therefore, we require min $JP_+ \leq 0.05$ for the stop analysis and min $JP_+ \leq 0.01$ for the sbottom analysis.

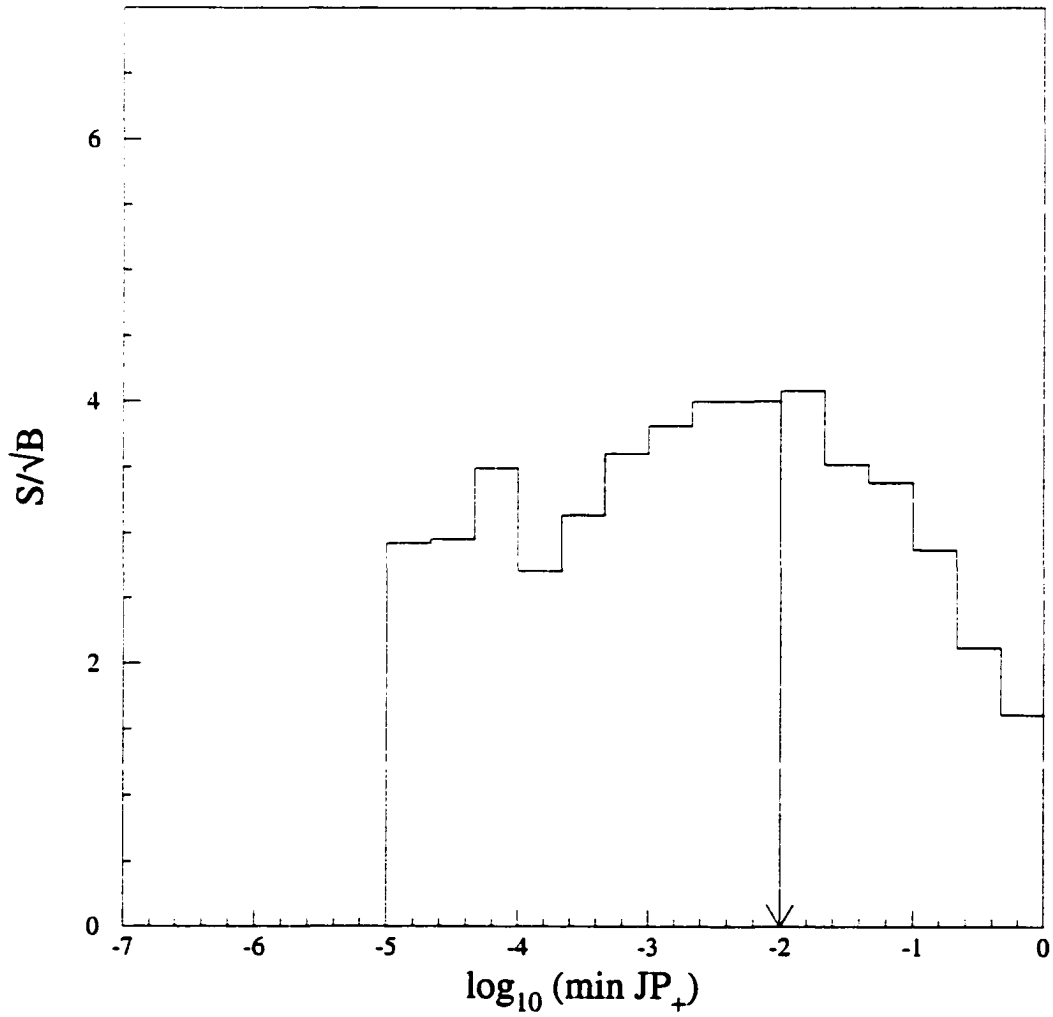As a final point, we note that the min JP_+ requirement is optimized at a single point in ($M_{\tilde q}, M_{\tilde\chi_1^0}$) parameter space. Fig. 5.11 shows the event tag efficiency as a function of $M_{\tilde t_1}$ for constant $M_{\tilde\chi_1^0}$. We define the event tag efficiency as:

$$\epsilon_{tag} = \frac{\#\ events\ with\ min\ JP_+ \leq 0.05}{\#\ events\ pass\ Pretagged\ selection} \tag{5.3}$$

Because not every event has a "taggable" jet, the event tag efficiency is lower than what one would expect based on Fig. 5.5. We see that this requirement is very insensitive to the choice of ($M_{\tilde t_1}, M_{\tilde\chi_1^0}$). Fig. 5.12 shows the same plot for $\bar b \bar b$ signal with ϵ_{tag} defined for min $JP_+ \leq 0.01$. The behavior as a function of ($M_{\tilde b_1}, M_{\tilde\chi_1^0}$) is the same.
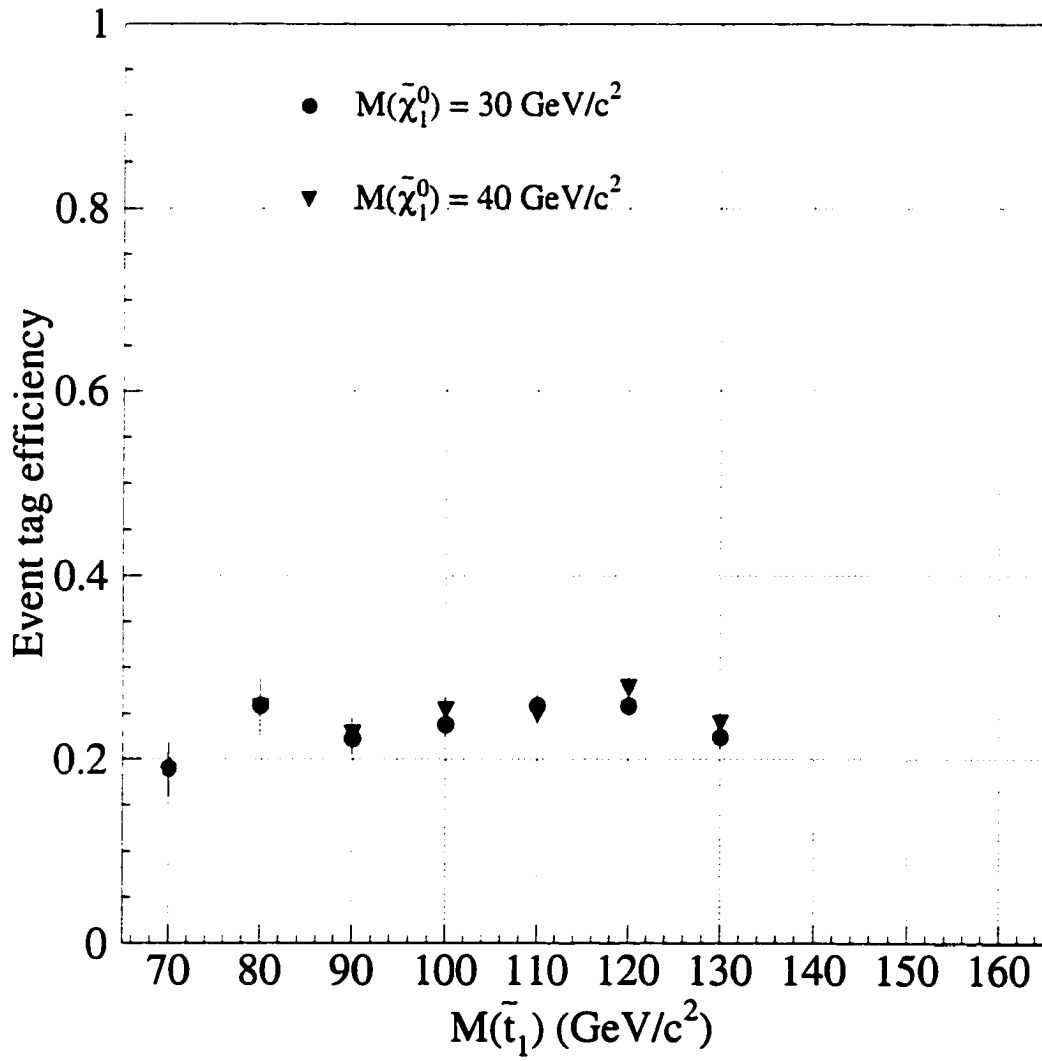
137

Figure 5.11: Event tag efficiency for $\tilde{t}_1\bar{\tilde{t}}_1$. See Eqn. 5.3 for the definition of event tag efficiency.
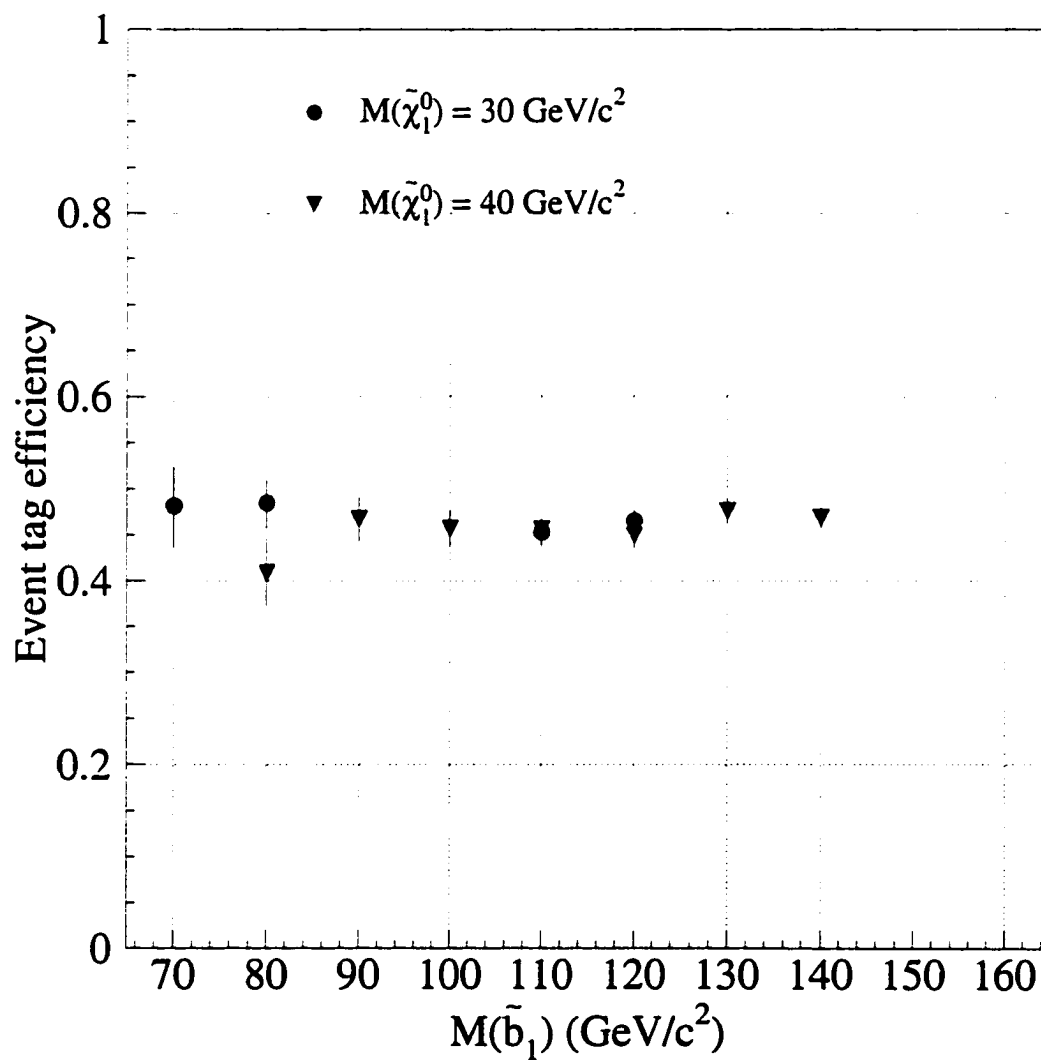
138

Figure 5.12: Event tag efficiency for $\tilde{b}_1\bar{\tilde{b}}_1$. See Eqn. 5.3 for the definition of event tag efficiency.

139

Chapter 6

Tagged Background Estimate

In Chapter 5, we demonstrated that min JP_+ is an efficient variable with which to select scalar quark events. In this chapter, we calculate the expected background from $W/Z/t\bar{t}/Diboson$ and QCD sources for the min $JP_+ \leq 0.05(0.01)$ requirement. We also cross-check the background calculations in a data sample similar to our signal data samples but enriched in background.

6.1 min $JP_+ \leq 0.05$

We estimate the $W/Z/t\bar{t}/Diboson$ background using our MC samples. We apply the min $JP_+ \leq 0.05$ requirement after the **Pretagged** selection and normalize to 88 pb^{-1}. For the min $JP_+ \leq 0.05$ sample, we expect a total of $11.1 \pm 1.8 \pm 3.3$ events from $W/Z/t\bar{t}/Diboson$ sources; the first uncertainty is statistical and the second uncertainty is systematic. Table 6.1 gives a breakdown of the number of events expected from each process.

We estimate the tagged QCD background using a mistag matrix method derived in [83]. The mistag matrix parameterizes the probability that a *jet* has $JP_\pm \leq 0.05$ as a function of the jet E_T and the number of "good", $\pm$i.p. SVX$'$ tracks (see Sec. 5.1.1). The mistag matrix is derived from a data sample of inclusive jets; i.e. events that

140

Sample	N_{exp}
$W^\pm(\to e^\pm\nu_e)+ \geq 2$ jets	$0.3 \pm 0.3 \pm 0.1$
$W^\pm(\to \mu^\pm\nu_\mu)+ \geq 2$ jets	$0.9 \pm 0.5 \pm 0.3$
$W^\pm(\to \tau^\pm\nu_\tau)+ \geq 1$ jets	$7.6 \pm 1.6 \pm 2.2$
$Z^0(\to \nu\bar{\nu})+ \geq 2$ jets	$1.2 \pm 0.4 \pm 0.4$
$t\bar{t}$	$0.7 \pm 0.2 \pm 0.4$
$Diboson~(WW + WZ + ZZ)$	$0.4 \pm 0.1 \pm 0.1$
total $W/Z/t\bar{t}/Diboson$ bkg	$11.1 \pm 1.8 \pm 3.3$
total QCD bkg	3.4 ± 1.7
total expected	14.5 ± 4.2

Table 6.1: The number of expected background events for the min $JP_+ \leq 0.05$ sample. The first error is statistical, the second systematic.

pass the JET20/JET50/JET70/JET100 triggers (see Sec. 4.3) and the SUMET_300 trigger [1] plus some additional cleanup requirements. One of these requirements is $\not{E}_T \leq 40, 50, 60, 70, 120$ for the JET20,JET50,JET70,JET100,SUMET_300 sample. In Sec. 6.3, we show that even though our data sample has $\not{E}_T > 40$ Gev, the mistag matrix is still appropriate for our data sample.

Let $P_\pm^i$ be the mistag matrix probability for jet i. Then the probability that an event with N jets ($E_T \geq 15$ GeV and $|\eta| \leq 2$) has at least one jet with $JP_\pm \leq 0.05$, $P_\pm^{event}$, is:

$$P_\pm^{event} = 1 - \prod_{i=1}^{N}(1 - P_\pm^i)$$

For any given pretagged sample, the sum of the $P_\pm^{event}$ gives us the expected number of events if we require at least one jet with $JP_\pm \leq 0.05$ ($\equiv$ min $JP_\pm \leq 0.05$). In addition,

---

[1]The SUMET_300 trigger is a Level 3 trigger that requires $\sum_{cluster} E_T > 300$ GeV for clusters with $E_T > 10$ GeV.

141

the expected distribution for a kinematic variable (such as $\not{E}_T$ or min $\Delta\Phi(\not{E}_T, j)$) in the tagged sample is equal to the distribution in the pretagged sample with events weighted by $P_\pm^{event}$.

Our strategy for estimating the QCD background is the following:

1. Apply the mistag matrix for $JP_- \leq 0.05$ to the **Pretagged** data; call this $Data(\text{-}matrix)$.

2. Apply the mistag matrix for $JP_- \leq 0.05$ to the **Pretagged** $W/Z/t\bar{t}/Diboson$ MC normalized to 88 pb^{-1}; call this $W/Z/t\bar{t}/Diboson(\text{-}matrix)$.

3. If we assume that the excess of **Pretagged** data events above $W/Z/t\bar{t}/Diboson$ expectations is due to QCD, then:

$$QCD(-matrix) = Data(-matrix) - W/Z/t\bar{t}/Diboson(-matrix)$$

$QCD(\text{-}matrix)$ is our estimate of the number of events in the min $JP_- \leq 0.05$ due to QCD multijets.

The actual numbers are Data($\text{-}matrix$) = 6.38 ± 0.54 and $W/Z/t\bar{t}/Diboson(\text{-}matrix)$ = 5.00 ± 0.44. Therefore, QCD($\text{-}matrix$) = $(6.38 \pm 0.54) - (5.00 \pm 0.44) = 1.38 \pm 0.69$. To get the number of events in the min $JP_+ \leq 0.05$ due to QCD multijets we scale this number by a factor of 2.5 which is the ratio of $JP_+ \leq 0.05$ tagged jets to $JP_- \leq 0.05$ tagged jets in the inclusive jet data from [83]. Thus the number of QCD events expected in the min $JP_+ \leq 0.05$ is 3.4 ± 1.7. If we repeat this procedure using the $JP_+ \leq 0.05$ mistag matrix from [83] we get an estimate of 4.8 ± 1.4. Note that no scale factor is needed for this method.

We use our QCD MC as a further check of our QCD estimate for the min $JP_+ \leq$ 0.05 sample. After the **Pretagged** selection, the min $JP_+ \leq 0.05$ event tag rate is

142

$4 \pm 2\%$. We multiply this tag rate by the excess of events in our **Pretagged** sample (126 ± 83) to get an estimate of 5 ± 4.

We use method 1 ($JP_- \leq 0.05$ mistag matrix) for our QCD background estimate. We make the following observations:

1. All three methods are consistent with each other.

2. All three methods are independent of our estimate of the QCD background in the **Pretagged** data sample. By assuming that the entire **Pretagged** excess is due to QCD, we are placing an upper bound on the QCD contribution to our tagged background.

3. Method 2 is sensitive to our modeling of heavy flavor in Monte Carlo.

4. Method 3 suffers from a lack of statistics in our QCD MC.

We point out that applying the min $JP_+ \leq 0.05$ requirement improves the discovery potential $(S/\sqrt{B})$ for the $\tilde{t}_1 \bar{\tilde{t}}_1$ analysis. Consider the $\tilde{t}_1 \bar{\tilde{t}}_1$ signal for $M_{\tilde{t}_1} = 110$ GeV/c^2, $M_{\tilde{\chi}_1^0} = 40$ GeV/c^2. After the **Pretagged** selection, we expect 70 $\tilde{t}_1 \bar{\tilde{t}}_1$ events and 396 background events. Therefore $S/\sqrt{B} = 70/\sqrt{396} = 3.5$. When we add the min $JP_+ \leq 0.05$ requirement we expect 17 $\tilde{t}_1 \bar{\tilde{t}}_1$ events and a total of 14.5 background events. Therefore, $S/\sqrt{B} = 17/\sqrt{14.5} = 4.5$.

6.2   min $JP_+ \leq 0.01$

We estimate the $W/Z/t\bar{t}/Diboson$ background using our MC samples. We apply the min $JP_+ \leq 0.01$ requirement after the **Pretagged** selection and normalize to 88 pb^{-1}. For the min $JP_+ \leq 0.01$ sample, we expect a total of $4.5 \pm 1.1 \pm 1.2$ events

143

Sample	N_{exp}
$W^{\pm}(\to \tau^{\pm}\nu_{\tau})+ \geq 1$ jets	$3.0 \pm 1.0 \pm 0.9$
$Z^{0}(\to \nu\bar{\nu})+ \geq 2$ jets	$0.8 \pm 0.3 \pm 0.2$
$t\bar{t}$	$0.5 \pm 0.2 \pm 0.2$
Diboson (WW, WZ, ZZ)	$0.2 \pm 0.1 \pm 0.1$
Total $W/Z/t\bar{t}/Diboson$ bkg	$4.5 \pm 1.1 \pm 1.2$
Total QCD bkg	1.3 ± 0.7
Total Expected	5.8 ± 1.8

Table 6.2: The number of expected background events for the min $JP_{+} \leq 0.01$ sample. The first error is statistical, the second systematic.

from $W/Z/t\bar{t}/Diboson$ sources; the first uncertainty is statistical and the second uncertainty is systematic. Table 6.1 gives a breakdown of the number of events expected from each process.

We estimate the QCD background using the mistag matrix method described in Sec. 6.1 with several modifications. The mistag matrix for $JP_{\pm} \leq 0.01$ does not exist. However, as we saw from Fig. 5.4, the JP_{-} distribution is flat. Thus, we can apply the $JP_{-} \leq 0.05$ matrix and divide by 5 to get the $JP_{-} \leq 0.01$ mistag matrix result. In addition, we need to derive the scale factor of $JP_{+} \leq 0.01$ tags to $JP_{-} \leq 0.01$ since the scale factor of 2.5 is no longer appropriate. We compute this scale factor in a sample enriched in QCD events. We create this QCD–enriched sample from the **FILT2** by applying all the **Pretagged** selection <u>except</u> the soft jet veto, $\Delta\Phi(\not{E}_{T}, j_{1}) < 165°$, and $45° < \Delta\Phi(j_{1}, j_{2}) < 165°$. Plus, we require the 35 GeV$\leq \not{E}_{T} < 40$ GeV. There are 3909 data events and we expect 154 $W/Z/t\bar{t}/Diboson$ events. The ratio of $JP_{+} \leq 0.01$ tags to $JP_{-} \leq 0.01$ tags (after subtracting the $W/Z/t\bar{t}/Diboson$ contribution) is 4.8 ± 1.3. Using QCD($-matrix$) $= 1.38 \pm 0.69$ from Sec. 6.1, the QCD estimate for the min

144

$JP_- \leq 0.01$ sample is $(1.38 \pm 0.69) \cdot \frac{1}{5} \cdot (4.8 \pm 1.3) = 1.3 \pm 0.7$.

The improvement in discovery potential for the $\tilde{b}_1\bar{\tilde{b}}_1$ analysis is even greater than the improvement for the $\tilde{t}_1\bar{\tilde{t}}_1$ analysis. For $M_{\tilde{b}_1} = 140\,\mathrm{GeV}/c^2$ and $M_{\tilde{\chi}^0_1} = 40\,\mathrm{GeV}/c^2$, we expect 20 events in the **Pretagged** sample which gives $S/\sqrt{B} = 24/\sqrt{396} = 1.2$. After applying the min $JP_+ \leq 0.01$ requirement, we expect 11.4 $\tilde{b}_1\bar{\tilde{b}}_1$ events and 5.8 background events so that $S/\sqrt{B} = 11.4/\sqrt{5.8} = 4.7$.

6.3 Cross–check

There are several checks we can perform to verify our background estimates. The first is to check the JP_- estimates. For min $JP_- \leq 0.05$, we expect a total of 8.1 ± 2.4 events and we observe 5. Table 6.3 shows the breakdown of the expected background. For min $JP_- \leq 0.01$ we expect a total of 1.6 ± 0.7 events and we observe 1. Table 6.4 shows the breakdown of the expected background. In both cases, we see good agreement between what we observe and what we predict.

We can also look at a data sample which is similar to our final tagged samples but still background–enriched. To this end, we take our **Pretagged** data sample and remove the soft jet veto cut, the $\Delta\Phi(\not{E}_T, j_1) < 165°$ requirement and the $45° < \Delta\Phi(j_1, j_2) < 165°$ requirement (see Table 4.10); we call this sample our QCD–enriched sample. This gives us 5799 data events with an expected background of 1040 ± 218 events from $W/Z/t\bar{t}/Diboson$ processes. For a signal sample of $M_{\tilde{q}} = 110\,\mathrm{GeV}/c^2$, $M_{\tilde{\chi}^0_1} = 40\,\mathrm{GeV}/c^2$, we expect ≈ 150 events. We can therefore assume that the entire data excess above $W/Z/t\bar{t}/Diboson$ expectations before tagging ($= 4759 \pm 231$ events) is due to QCD multijets. We use the methods described above to compute the backgrounds. Table 6.5 shows the observed number of events along with our

145

Sample	N_{exp}
$W^{\pm}(\to e^{\pm}\nu_e)+\geq$ 2 jets	$0.3 \pm 0.3 \pm 0.1$
$W^{\pm}(\to \mu^{\pm}\nu_{\mu})+\geq$ 2 jets	$1.8 \pm 0.7 \pm 0.5$
$W^{\pm}(\to \tau^{\pm}\nu_{\tau})+\geq$ 1 jets	$3.0 \pm 1.0 \pm 0.9$
$Z^0(\to \nu\bar{\nu})+\geq$ 2 jets	$1.0 \pm 0.3 \pm 0.3$
$t\bar{t}$	$0.08 \pm 0.08 \pm 0.03$
Diboson (WW, WZ, ZZ)	$0.3 \pm 0.1 \pm 0.1$
Total $W/Z/t\bar{t}/Diboson$ bkg	$6.5 \pm 1.3 \pm 1.9$
Total QCD bkg	1.6 ± 0.8
Total Expected	8.1 ± 2.4
Total Observed	5

Table 6.3: The number of expected background events for the min $JP_-\leq 0.05$ data sample. The first error is statistical, the second systematic.

Sample	N_{exp}
$W^{\pm}(\to \mu^{\pm}\nu_{\mu})+ \geq$ 2 jets	$0.3 \pm 0.3 \pm 0.1$
$W^{\pm}(\to \tau^{\pm}\nu_{\tau})+ \geq$ 1 jets	$0.7 \pm 0.5 \pm 0.2$
$Z^0(\to \nu\bar{\nu})+ \geq$ 2 jets	$0.1 \pm 0.1 \pm 0.03$
$t\bar{t}$	$0.08 \pm 0.08 \pm 0.03$
Diboson (WW, WZ, ZZ)	$0.09 \pm 0.06 \pm 0.02$
Total $W/Z/t\bar{t}/Diboson$ bkg	$1.3 \pm 0.6 \pm 0.4$
Total QCD bkg	0.26 ± 0.14
Total Expected	1.6 ± 0.7
Total Observed	1

Table 6.4: The number of expected background events for the min $JP_-\leq 0.01$ data sample. The first error is statistical, the second systematic.

146

Tagger	Data	$W/Z/t\bar{t}/Diboson$	Data-$W/Z/t\bar{t}/Diboson$	QCD Matrix
$JP_+ \leq 0.05$	227	45 ± 10	182 ± 18	182 ± 13
$JP_- \leq 0.05$	81	21 ± 5	60 ± 10	61 ± 7
$JP_+ \leq 0.01$	109	24 ± 6	85 ± 12	58 ± 16
$JP_- \leq 0.01$	15	4 ± 1	9 ± 4	12 ± 1

Table 6.5: Expected background composition of the QCD-enriched data sample. The error is equal to the statistical plus systematic.

expectations for background. We draw special attention to columns 4 and 5. We see that, except for the min $JP_+ \leq 0.01$ sample, the number of data events minus our $W/Z/t\bar{t}/Diboson$ prediction agrees well with our QCD estimate. The discrepancy in this sample is most likely due to the scale factor 4.8 ± 1.3. When compared to the systematic uncertainty due to all other sources (Chapter 7) this discrepancy is not an issue. We plot various kinematic quantities for the four tagged samples: Fig. 6.1–Fig. 6.3 for the min $JP_+ \leq 0.05$ sample; Fig. 6.4–Fig. 6.6 for the min $JP_- \leq 0.05$ sample; Fig. 6.7–Fig. 6.9 for the min $JP_+ \leq 0.01$ sample; Fig. 6.10–Fig. 6.12 for the min $JP_- \leq 0.01$ sample.
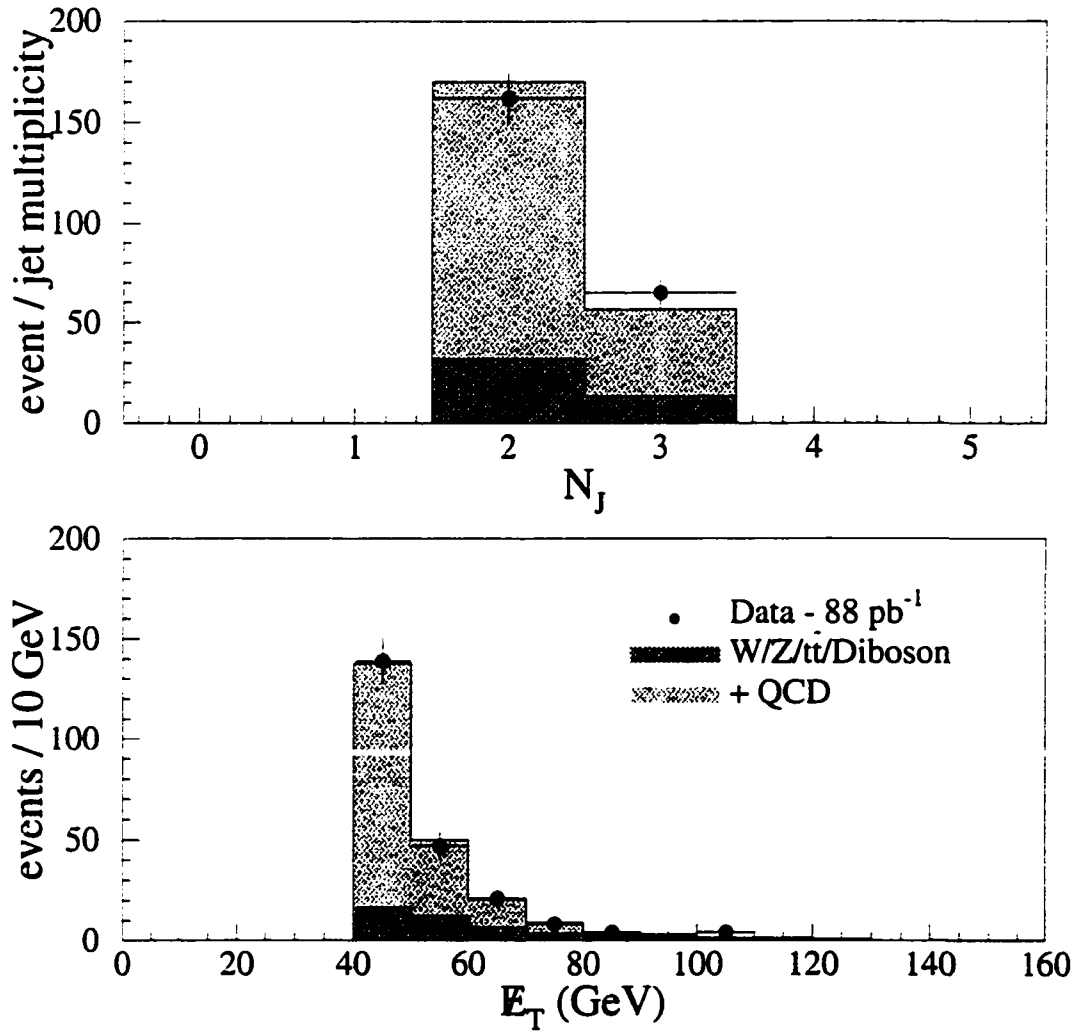
Figure 6.1: Kinematic distributions for events in the QCD-enriched sample.*after* the min $JP_+ \leq 0.05$ requirement.
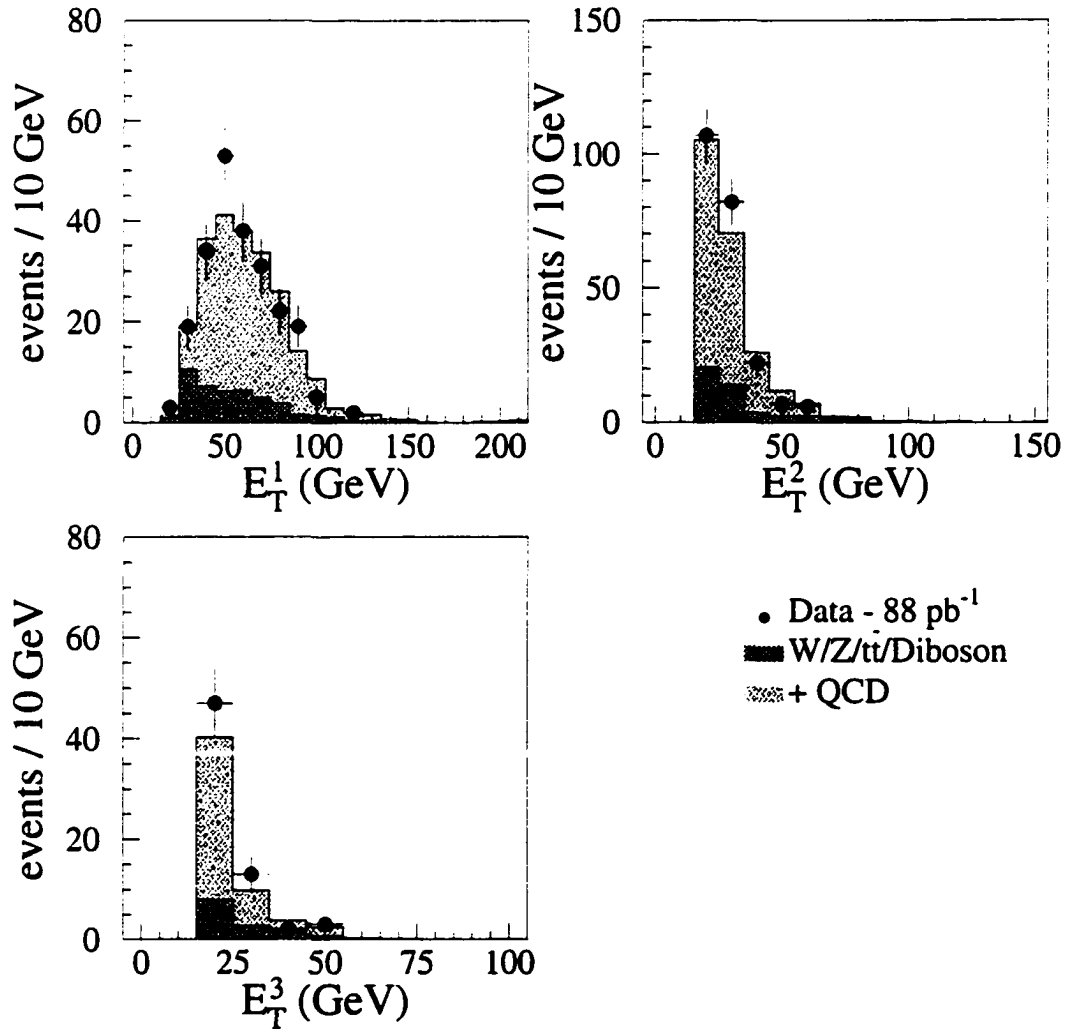
148

Figure 6.2: Kinematic distributions for events in the QCD–enriched sample. *after* the min $JP_+ \leq 0.05$ requirement.
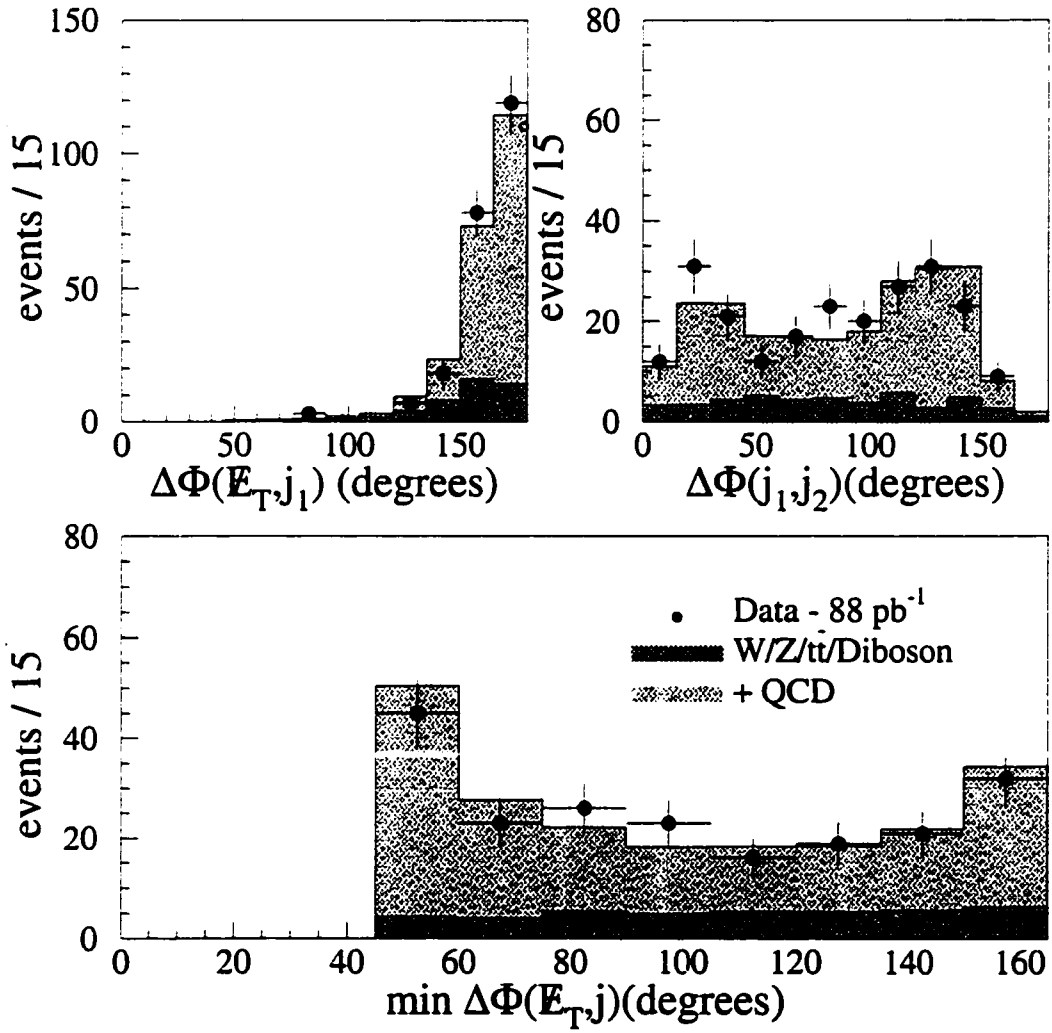
149

Figure 6.3: Kinematic distributions for events in the QCD–enriched sample. *after* the min $JP_+ \leq 0.05$ requirement.

150

Figure 6.4: Kinematic distributions for events in the QCD–enriched sample.*after* the min JP_- ≤ 0.05 requirement.

151

Figure 6.5: Kinematic distributions for events in the QCD–enriched sample.*after* the min JP_- ≤ 0.05 requirement.

152

Figure 6.6: Kinematic distributions for events in the QCD–enriched sample.*after* the min $JP_- \leq 0.05$ requirement.

153
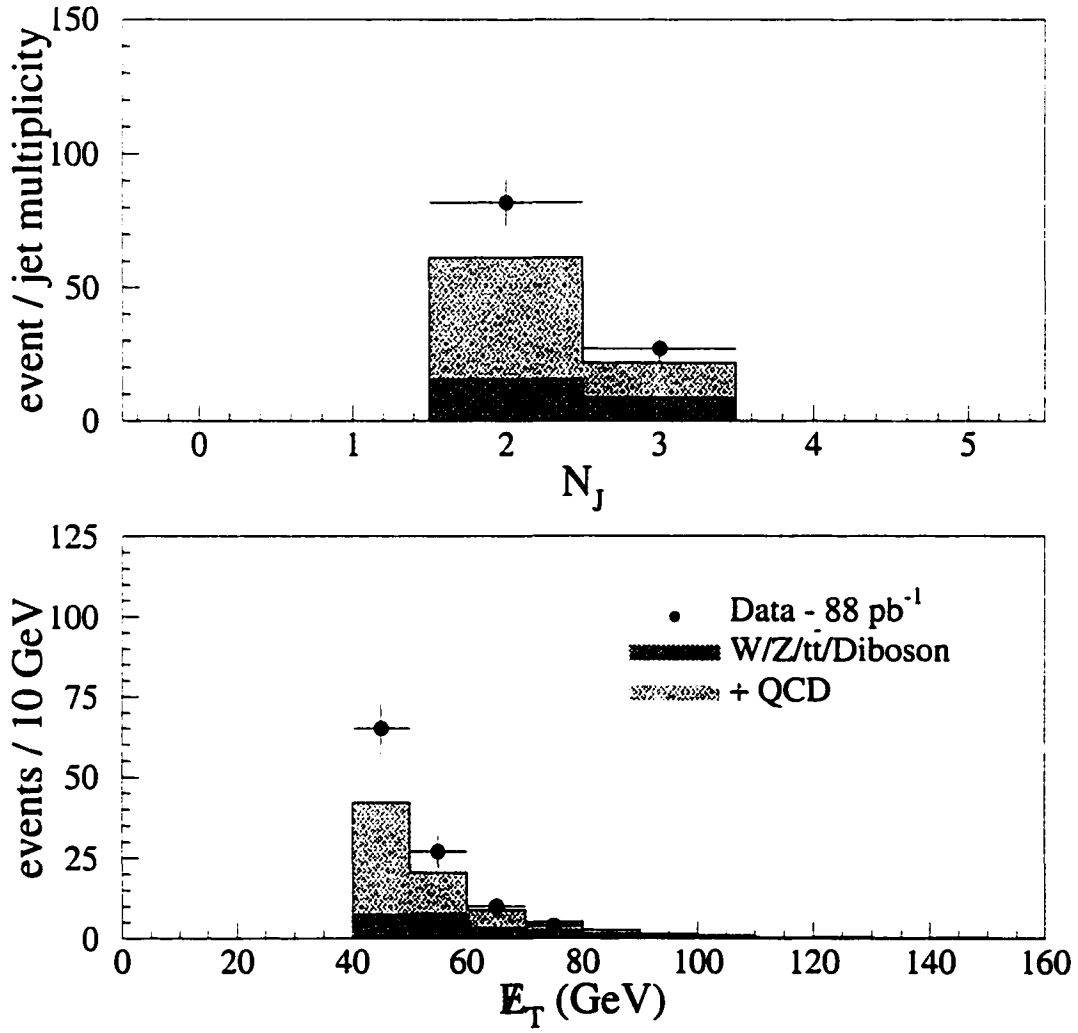
Figure 6.7: Kinematic distributions for events in the QCD–enriched sample. *after* the min $JP_+ \leq 0.01$ requirement.
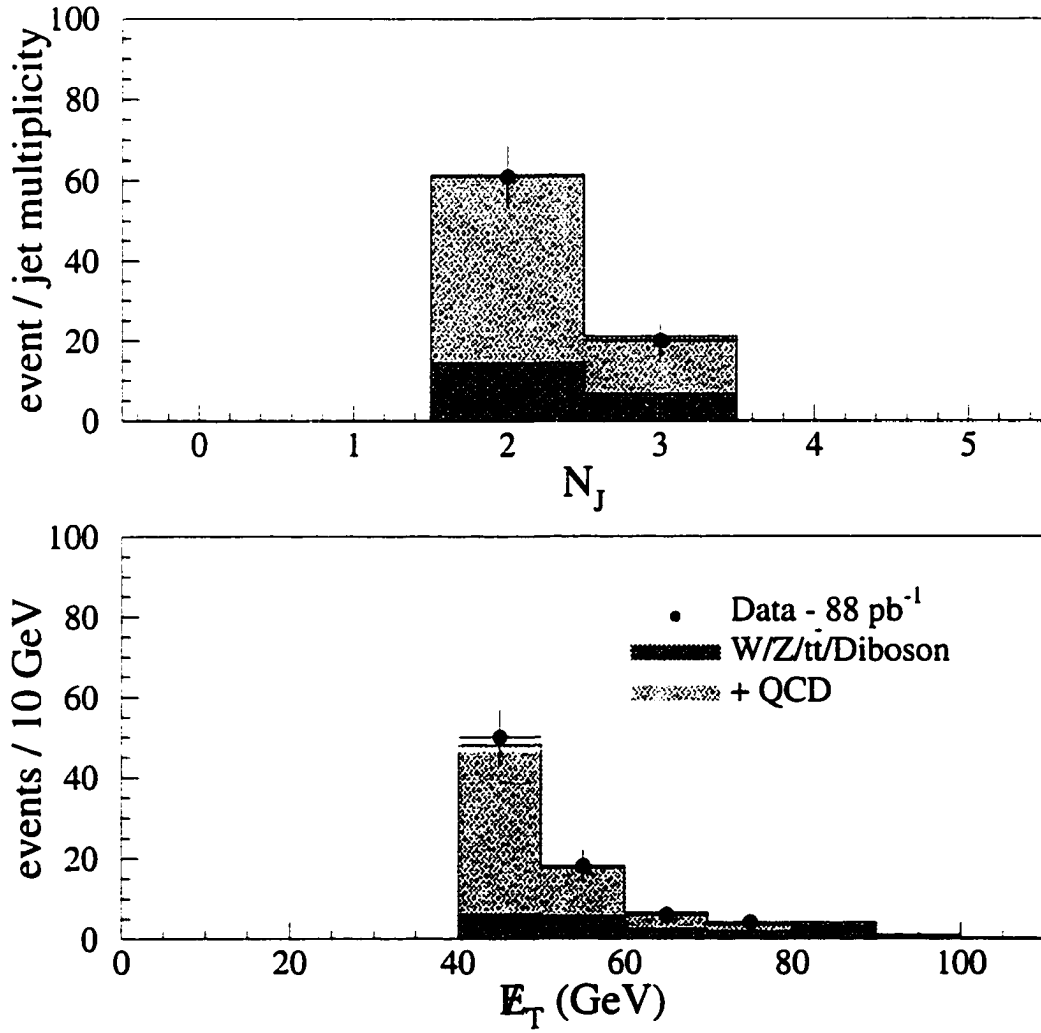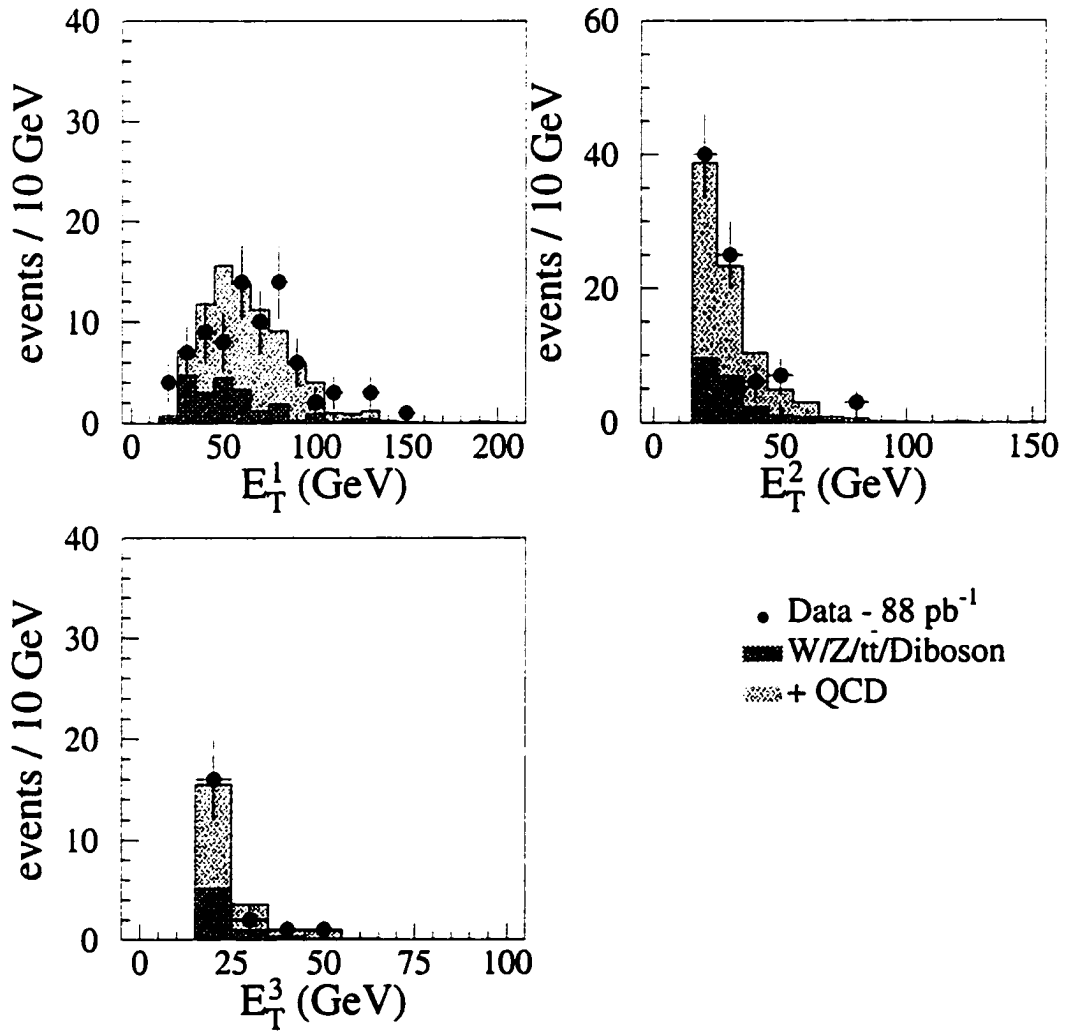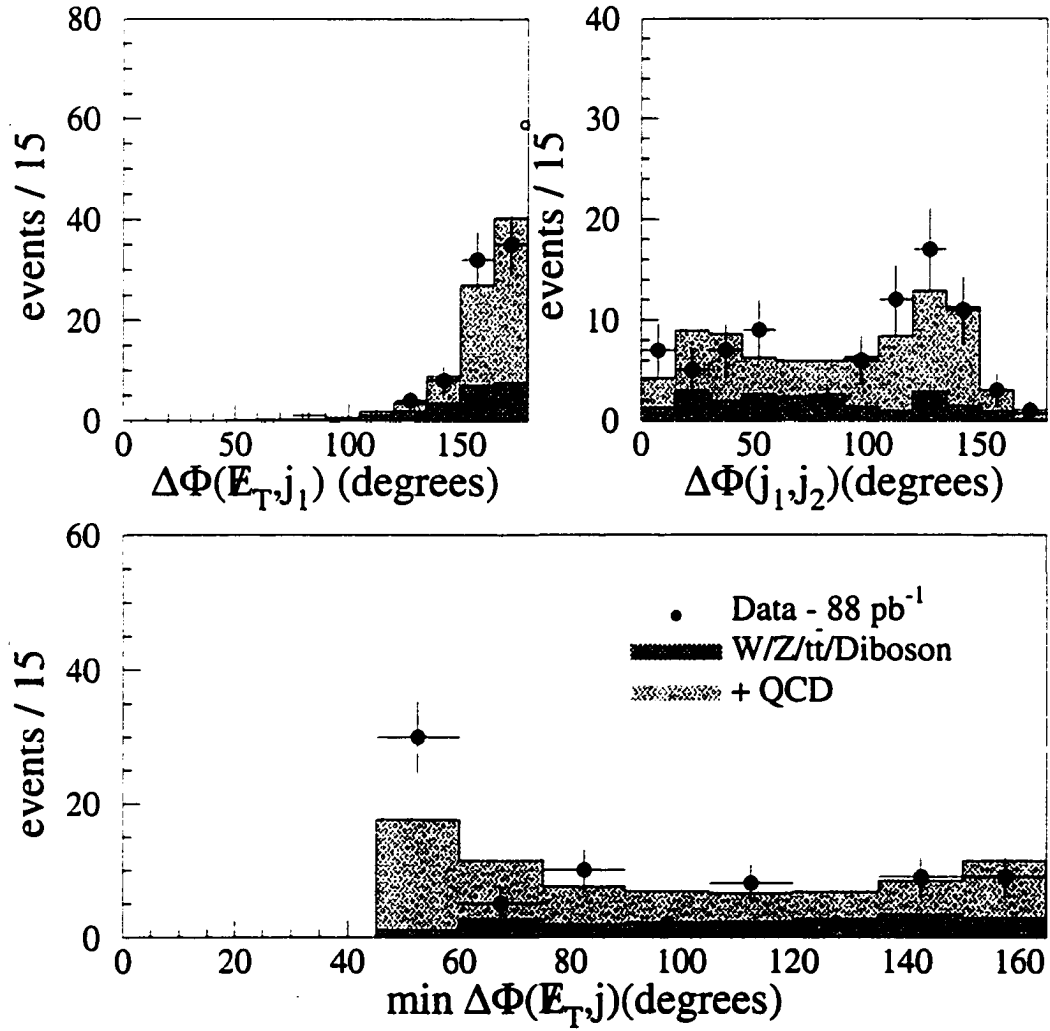
154
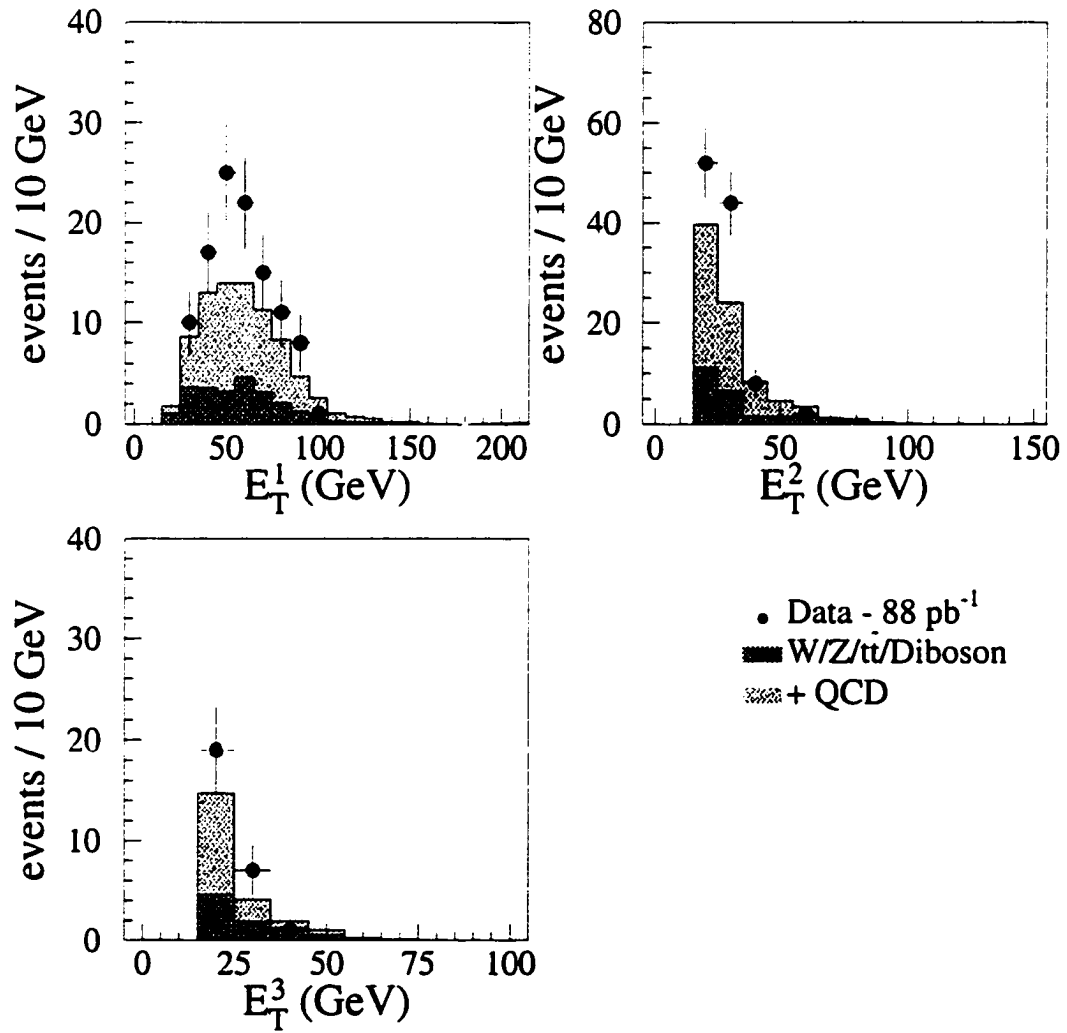
Figure 6.8: Kinematic distributions for events in the QCD–enriched sample.*after* the min $JP_+ \leq 0.01$ requirement.

155

Figure 6.9: Kinematic distributions for events in the QCD–enriched sample. *after* the min $JP_+ \leq 0.01$ requirement.

156

Figure 6.10: Kinematic distributions for events in the QCD–enriched sample. *after* the min JP_- ≤ 0.01 requirement.

157

Figure 6.11: Kinematic distributions for events in the QCD–enriched sample. *after* the min JP_- ≤ 0.01 requirement.

158

Figure 6.12: Kinematic distributions for events in the QCD–enriched sample.*after* the min $JP_- \leq 0.01$ requirement.
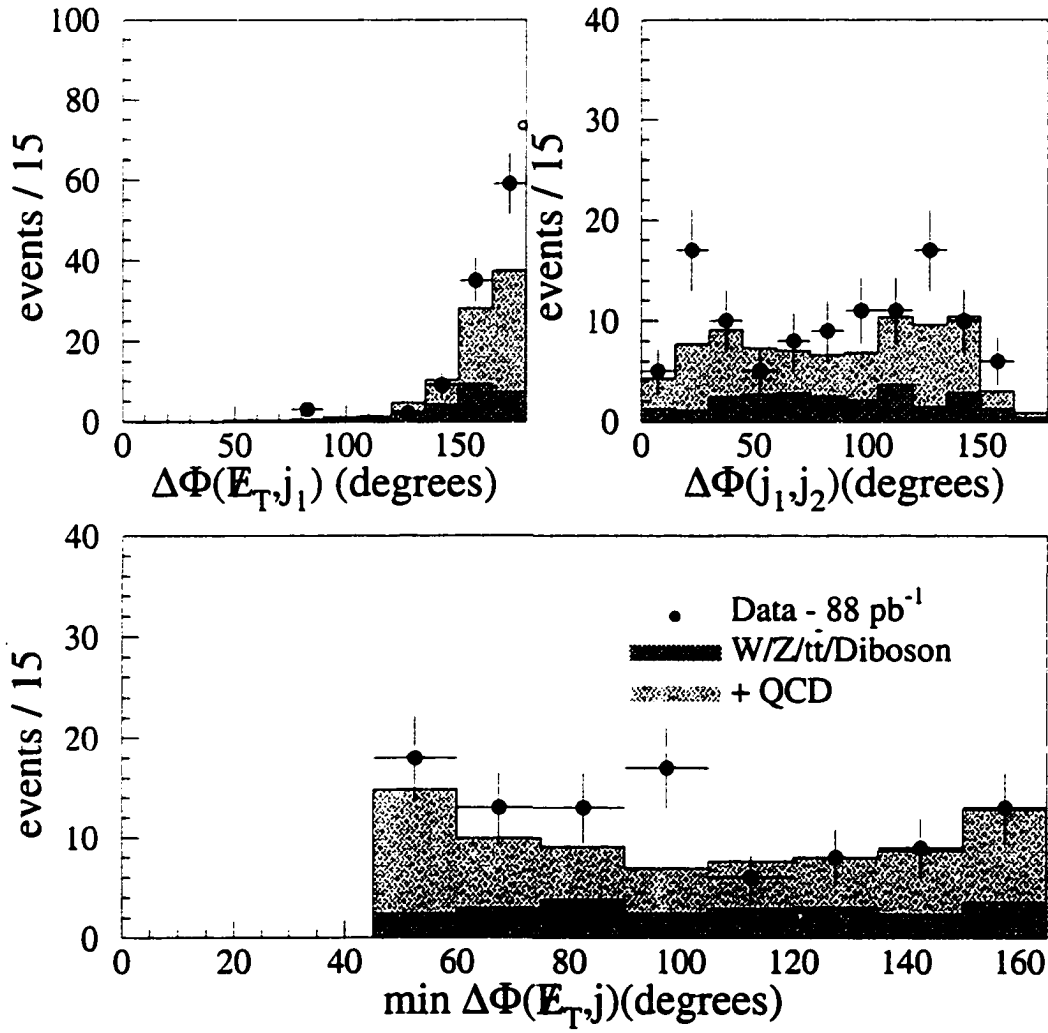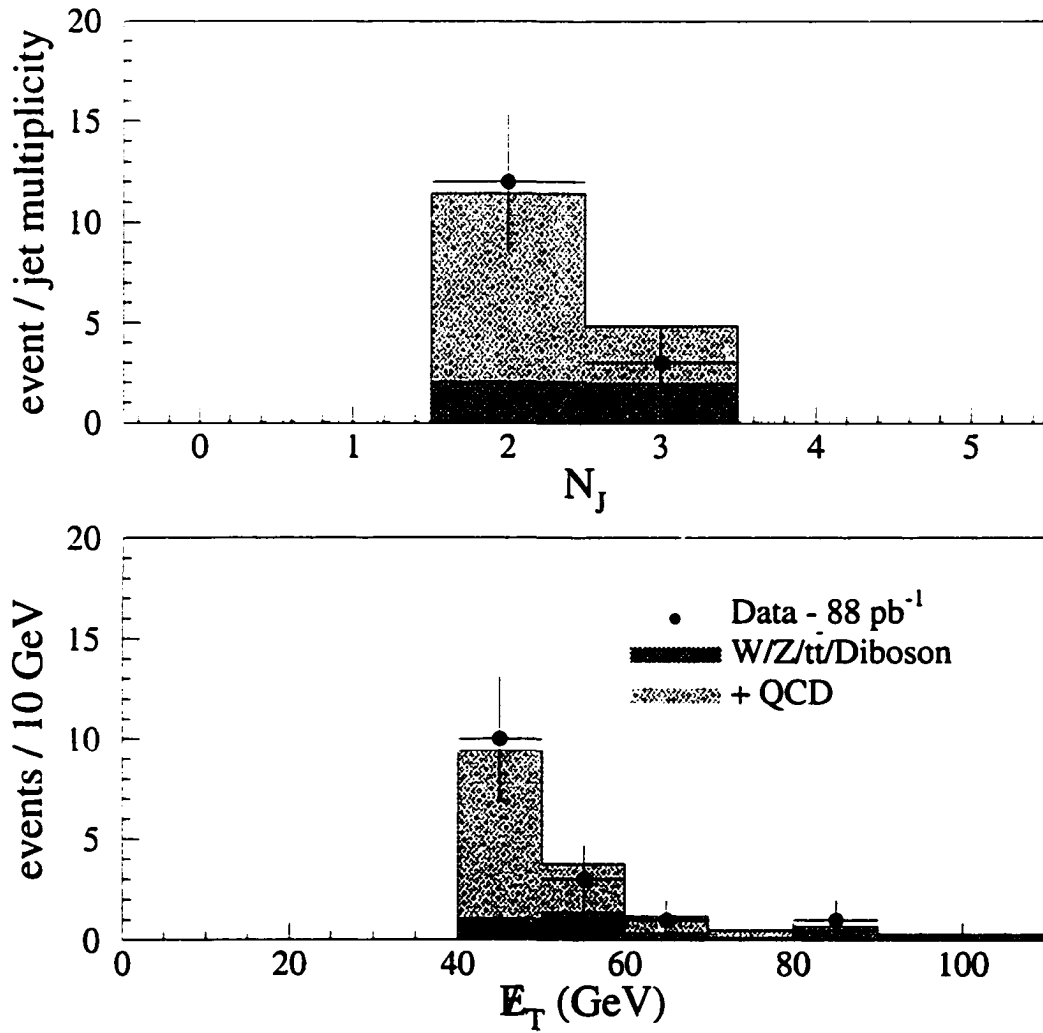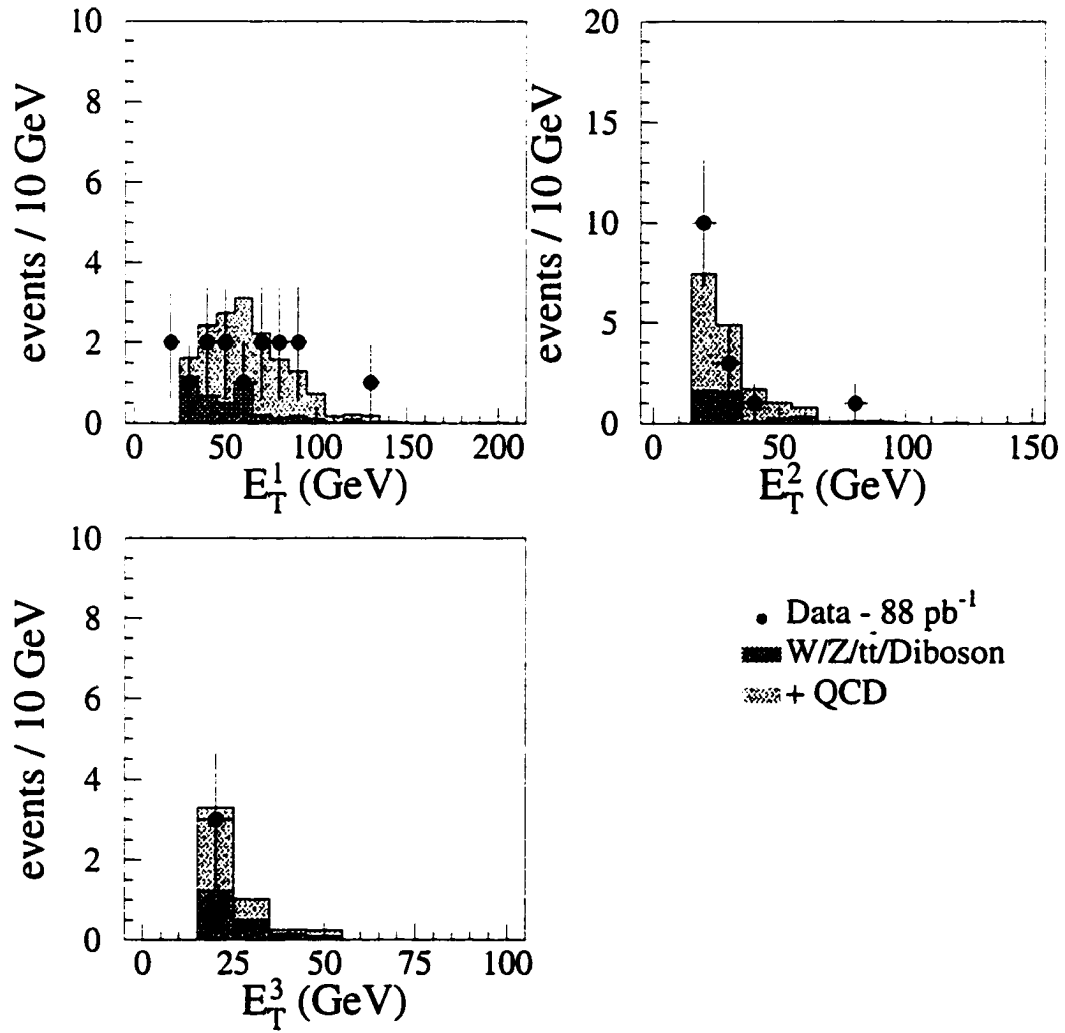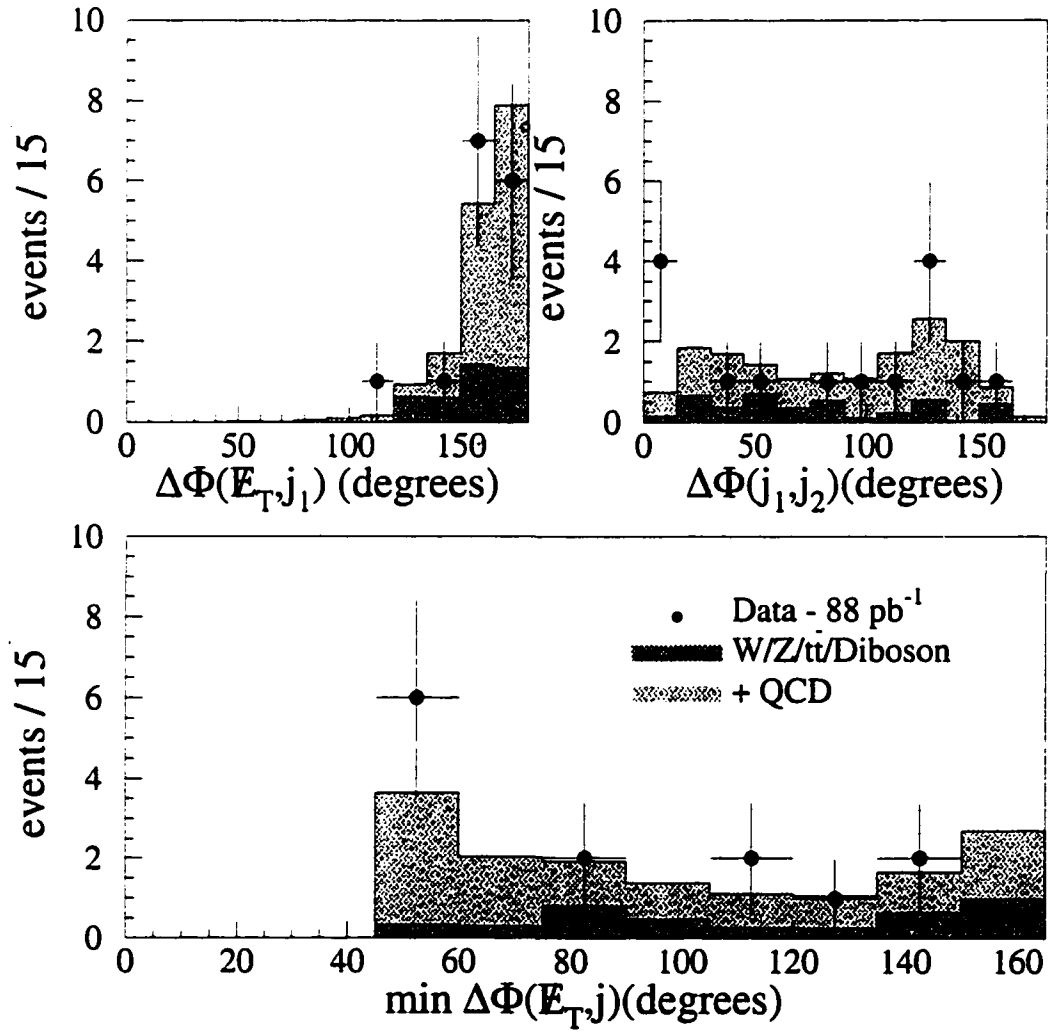
159

Chapter 7

Systematic Uncertainties

In Chapter 8, we apply the min $JP_+ \leq 0.05(0.01)$ requirement. In order to determine whether any excess of data events above our expected background is significant, we must first understand the systematic uncertainties associated with our background and signal estimates.

7.1 Signal Systematics

7.1.1 Cross-section

The NLO squark cross section depends on many parameters: the QCD renormalization scale μ, choice of parton distribution function(PDF) and the various SUSY parameters ($\tan \beta$, μ, A_t, etc.) [42]. The SUSY parameters change the cross section by less than 1%. As we will see, these effects are negligible when compared to the effects of changing the QCD renormalization scale or the PDF.

The nominal choice of PDF is CTEQ 3M [84]. If we use $MRSD0'$ [85], the cross section changes by 2%–7% ($\equiv \delta_{pdf}(m_{\tilde{q}_1})$); see Figure 7.1. The nominal choice for the QCD μ scale is $\mu = M_{\tilde{q}_1}$. We compute $\sigma_{\tilde{q}_1 \tilde{q}_1}$ for $\mu = 2 \cdot M_{\tilde{q}_1}$ and $\mu = 0.5 \cdot M_{\tilde{q}_1}$. Let $\delta_\mu(M_{\tilde{q}_1}) \equiv$ the maximum deviation due to the change in μ for $M_{\tilde{q}_1}$. This is plotted
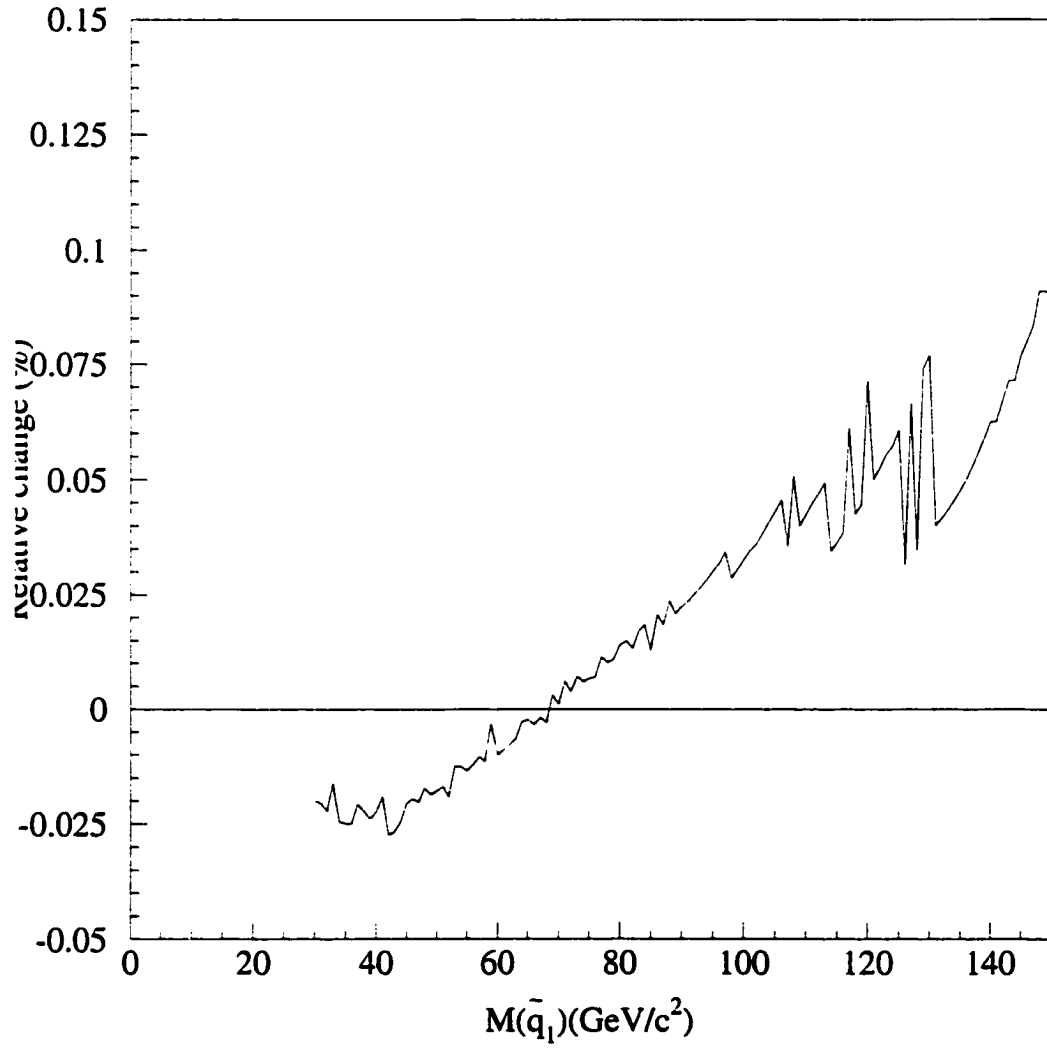
160

Figure 7.1: Plot of the systematic uncertainty in the NLO squark cross section due to the choice of parton distribution function.
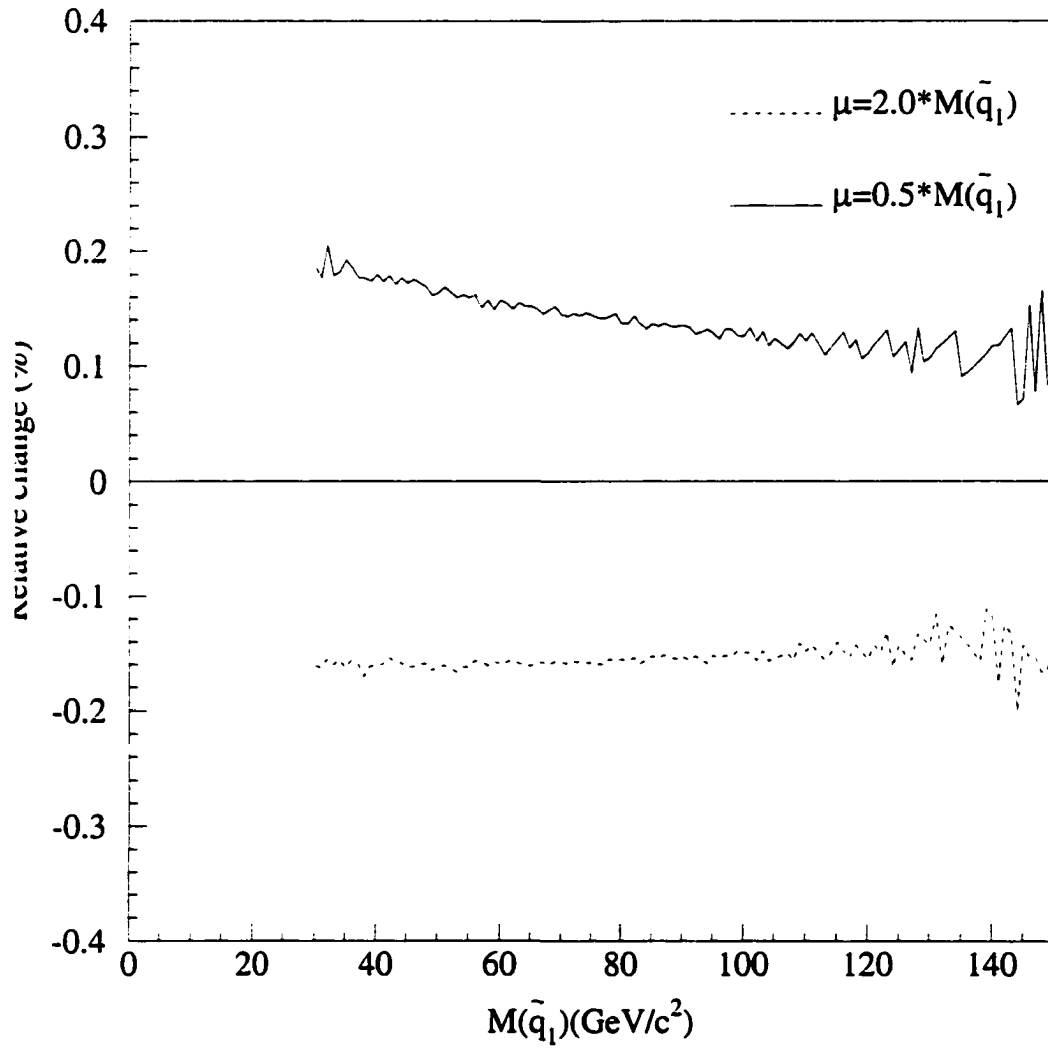
161

Figure 7.2: Plot of the systematic uncertainty in the NLO squark cross section due to the choice of QCD μ scale

162

in Figure 7.2. For each mass point we add δ_{pdf} and δ_μ in quadrature to get the cross section systematic as a function of $M_{\tilde{q}_1}$.

7.1.2 ISR/FSR Radiation

To compute the systematic uncertainty due to initial/final state radiation (ISR/FSR) we follow the method used in the CDF top mass measurement [86]. For our nominal signal efficiencies we use PYTHIA with initial and final state radiation turned ON. We then generate $\tilde{q}_1\overline{\tilde{q}_1}$ MC with ISR ON+FSR OFF and $\tilde{q}_1\overline{\tilde{q}_1}$ MC with FSR ON+ISR OFF. Let $\epsilon(NOISR)$ be the efficiency for the sample with FSR ON+ISR OFF and $\epsilon(NOFSR)$ be the efficiency for the sample with ISR ON+FSR OFF. Then the ISR/FSR systematics are given by:

$$ISR\ systematic\ =\ \frac{\epsilon(nominal) - \epsilon(NOISR)}{2 \times \epsilon(nominal)}$$

$$FSR\ systematic\ =\ \frac{\epsilon(nominal) - \epsilon(NOFSR)}{2 \times \epsilon(nominal)}$$

We find that the change in efficiency due to ISR+FSR, when added in quadrature, is 23%.

7.1.3 Tagging

Since the jet probability requirement is crucial for this analysis, we need to verify that our MC correctly models this distribution. We study jet probability in two different data samples: the first is a charm–enriched data sample [82] and the second is a bottom–enriched data sample [87].

The charm–enriched sample, which we call the D–star sample, is a data sample of events which has the $D^* \rightarrow D^0\pi_s$, $D^0 \rightarrow K^\pm\mu^\mp X^0$ decay chain reconstructed

163
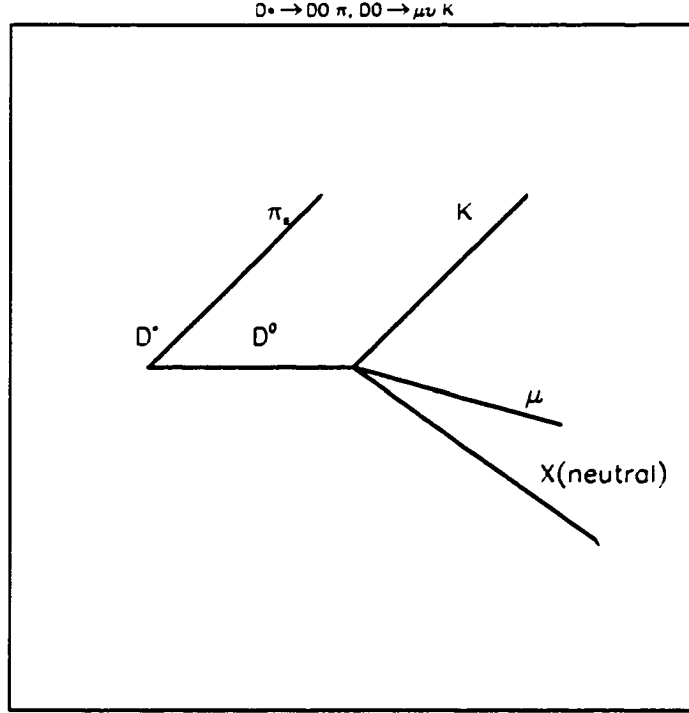
Figure 7.3: Diagram of the $D^* \to D^0 \pi_s$, $D^0 \to K^{\pm} \mu^{\mp} X^0$ decay chain. This sample is used to study the modeling of jet probability for charm jets.

(Fig. 7.3). This sample is a sub–sample of events collected by a Level 3 trigger that requires a single muon with $P_T^{\mu} > 8$ GeV/c. We apply the following requirements to create the D–star sample:

1. $p_T^{\mu} > 8$ GeV/c

2. $p_T^K > 1$ GeV

3. muon and kaon have opposite charge

4. invariant mass of K–μ ($\equiv M_{K\mu}$): $1.2 < M_{K\mu} < 1.8$ GeV/c^2

5. soft pion, π_s, impact parameter significance: $\frac{d_{\pi_s}}{\sigma} < 5.0$

164

From MC studies, we expect this sample to be 90% charm hadrons [82]. We define the jet probability efficiency as:

$$\epsilon(JP_0) = \frac{N_{D^*}(JP_+ < JP_0) - N_{D^*}(JP_- < JP_0)}{N_{D^*}(before\ tag)}$$

Fig. 7.4 compares $\epsilon(JP_0)$ from data to $\epsilon(JP_0)$ from MC without tracking degradation and Fig. 7.5 compares data to MC with tracking degradation (see Sec. 5.1.2). Based on this study, we feel that we understand our tagging for the stop analysis (min $JP_+ \leq 0.05$) to within 10%.

The bottom-enriched sample is also created from a single muon data sample. We demand that the muon pass the following requirements [87]:

- $\chi_x^2(CMU) < 9$;

- $\chi_x^2(CMP) < 9$;

- $\chi_z^2(CMU) < 12$;

- transverse momentum $p_T > 8.0$ GeV/c.

In addition we require the presence of two "taggable" jets (see Sec. 5.1.3) with $E_T \geq$ 15 GeV, one of which is associated with the muon $(\Delta R(jet - \mu) < 0.4)$ and is called a *muon jet*. The other jet is called the *away jet*. We determine the sample composition on the muon side *before* tagging using the shape of the positive jet probability distribution. We find:

$$F_b = 24 \pm 1\%, \quad F_c = 16 \pm 1\%, \quad F_p = 60 \pm 1\%,$$

where F_b is the fraction of muons coming from b-decay, F_c is the fraction of muons coming from c-decay and F_p is the fraction of muons coming from primary jets, mostly fakes [87].

165
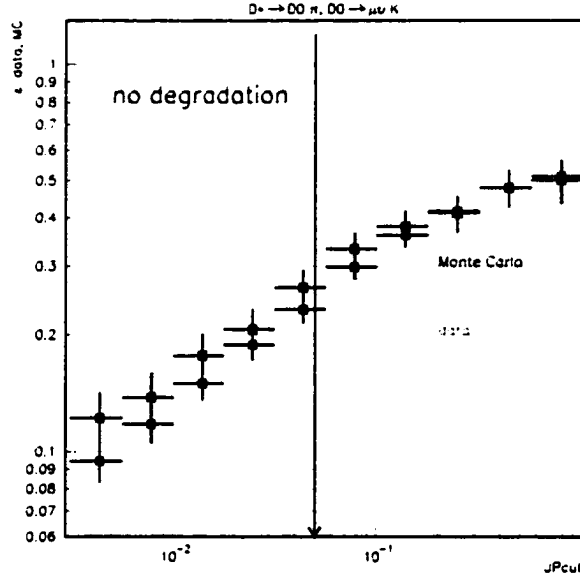
Figure 7.4: Comparison of min JP_+ efficiency between data and MC (without tracking degradation) in the charm-enriched sample.
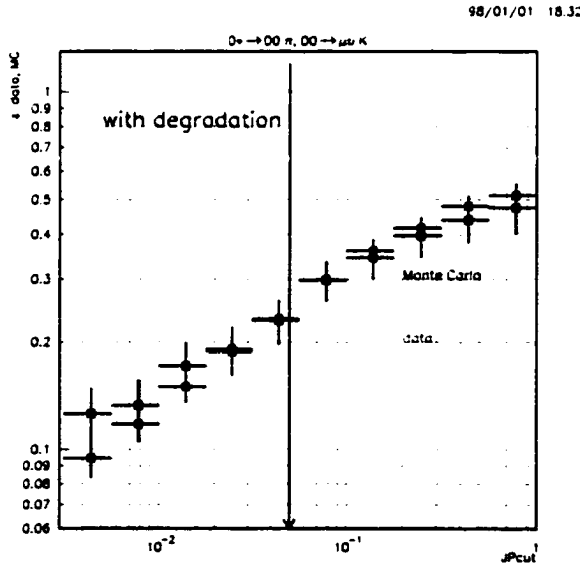
Figure 7.5: Comparison of min JP_+ efficiency between data and MC (with tracking degradation) in the charm-enriched sample.

166
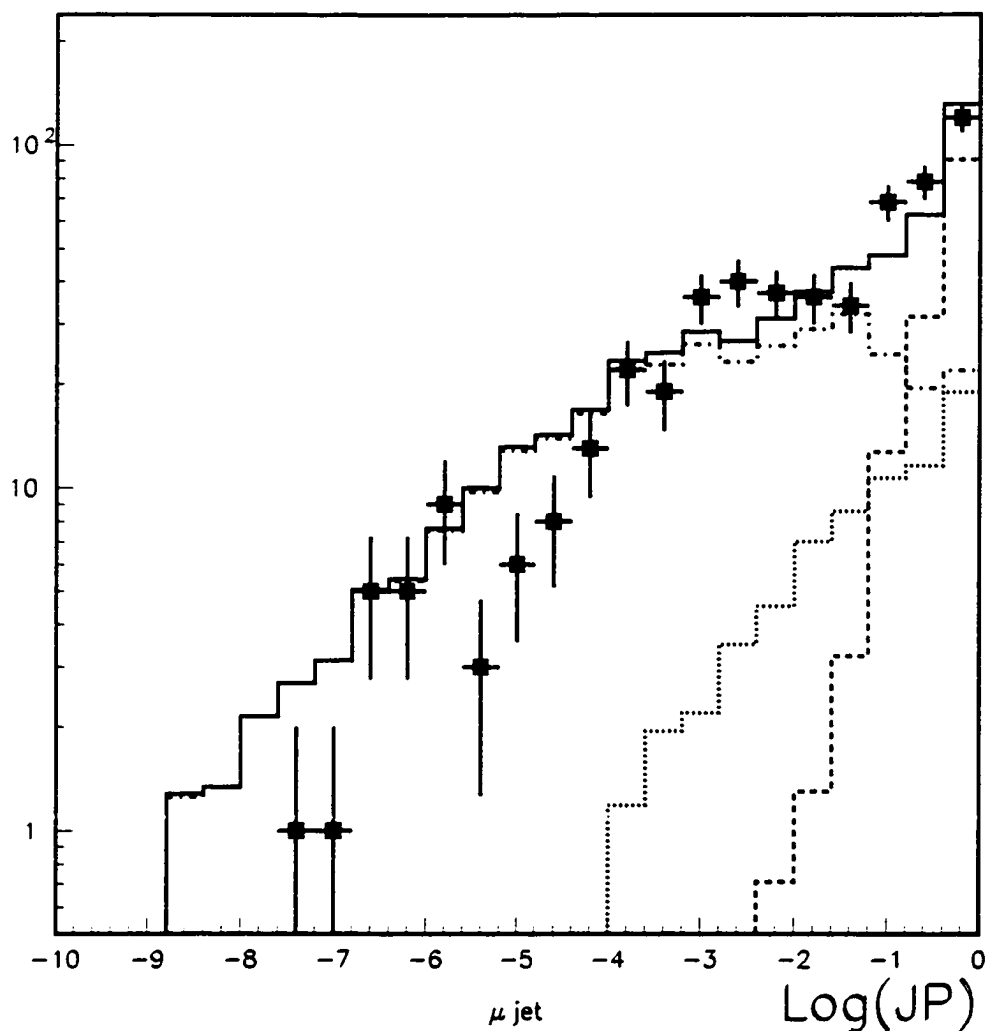
Figure 7.6: The JP_+ distribution of the *muon jet* in the bottom–enriched sample. The points are data and the histograms are the background shapes as determined by MC: the dashed histogram is primary jets, the dotted histogram is charm jets, the dot–dashed histogram is bottom jets, and the solid histogram is the sum of the three components. The calculation of the relative fractions of backgrounds is described in the text.

167

$JP_+ \leq$	# data	# MC
0.05	275	300 ± 30
0.01	205	218 ± 22

Table 7.1: Number of expected and observed events after requiring $JP_+ \leq 0.05(0.01)$ for the *muon jet* in the bottom-enriched sample.

We create the bottom-enriched sample by requiring $JP_+(away\ jet) \leq 0.05$. We then plot the JP_+ of the muon jet. This is shown in Figure 7.6. Points represent data. We need to know the sample composition on the muon side *after* we tag the away jet in order to compare data to MC. We use PYTHIA Monte Carlo to predict the sample composition for the away jet, once the flavor of the muon jet is known. We expect

$$F_b = 61 \pm 6\%,\ F_c = 13 \pm 2\%,\ F_p = 26 \pm 2\%$$

We use these fractions to weight Monte Carlo predictions for the b, c and primary JP_+ shapes. The result is shown in Figure 7.6. The solid histogram represents the sum of the three contributions. The agreement with data is quite good. In Table 7.1, we summarize the number of expected and observed events after requiring $JP_+ \leq 0.05(0.01)$ for the *muon jet*. The numbers agree within statistics and 10% systematics. We therefore assign a 10% systematic for the sbottom analysis (min $JP_+ \leq 0.01$).

7.1.4 Multiple Interactions

Due to the high luminosities achieved during Run IB, there are, on average, 1.6 extra interactions in addition to the primary hard scattering interaction. The total

168

acceptance for the $\tilde{t}_1\bar{\tilde{t}}_1$ and $\tilde{b}_1\bar{\tilde{b}}_1$ is calculated from MC that has exactly one interaction. To model the change in acceptance due to extra interactions, we mix in minimum bias data events with a $\tilde{t}_1\bar{\tilde{t}}_1$ MC sample with $M_{\tilde{t}_1} = 110$ GeV/c^2 and $M_{\tilde{\chi}_1^0} = 40$ GeV/c^2. For each MC event we pick a random number from a poisson distribution with a mean of 1.6 and add that number of minimum bias events to the MC event. We combine the events at the calorimeter tower level and reprocess the MC sample. The dominant effect of multiple interactions is to add soft jets ($7 < E_T < 15$ GeV) to the event. This reduces the efficiency of the soft jet veto requirement: $\epsilon_{soft\ jet}$. The ratio of the soft jet veto efficiency in mixed MC versus unmixed MC is:

$$\frac{\epsilon_{soft\ jet}(mixed)}{\epsilon_{soft\ jet}(unmixed)} = 0.93$$

Therefore, we reduce the total acceptance for all our signal samples by 0.93. The error on this scale factor is 3%. Note that all signal estimates and plots include this MI degradation.

7.1.5 Trigger

For the trigger systematic, we vary the parameters of our L2 MET_35* curve (Sec. 4.3.2) by $\pm 1\sigma$. We find this systematic to be 10% for all mass points.

7.1.6 Jet energy

We account for uncertainties in the absolute jet energy scale by varying the jet E_T's by $\pm 5\%$. This changes the signal acceptance by $\pm 10\%$.

7.1.7 Luminosity

The uncertainty on the integrated luminosity is 4.1% [88].

169

7.2 Background Uncertainties

7.2.1 ISR/FSR Radiation

ISR/FSR

Since ISR/FSR radiation can not be adjusted in VECBOS we assume the uncertainty for background events is the same as for signal events. We therefore assign a 23% systematic uncertainty for ISR/FSR.

7.2.2 VECBOS scale factor

The systematic uncertainty quoted by [73] for the VECBOS normalizations (see Table 4.2) is 10%. Based on the agreement between data and MC for the single lepton samples (see Sec. 4.6.1), a 10% systematic uncertainty is appropriate for our samples.

7.2.3 Trigger

For the trigger systematic, we vary the parameters of our L2 MET_35* curve (Sec. 4.3.2) by $\pm 1\sigma$. We find this changes the background acceptances by $\pm 10\%$

7.2.4 Jet energy

We account for uncertainties in the absolute jet energy scale by varying the jet E_T's by $\pm 5\%$. This changes the background acceptances by $\pm 10\%$.

7.2.5 Tagging

Based on the studies described in Sec. 7.1.3, we assign a 10% systematic uncertainty in the background for the min JP_+ requirement.

170

7.2.6 Luminosity

The uncertainty on the integrated luminosity is 4.1% [88].

171

Chapter 8

Limits

In this chapter, we apply the min JP_+ requirements to our **Pretagged** data sample. For the stop analysis, we look at the min $JP_+ \leq 0.05$ sample and for the sbottom analysis, we look at the min $JP_+ \leq 0.01$ sample. If we see no excess of data events above our Standard Model expectations, we set a 95% Confidence Level (95% C.L.) limit in the $(M_{\tilde{q}}, M_{\tilde{\chi}_1^0})$ parameter space.

8.1 min $JP_+ \leq 0.05$

Fig. 8.1 shows the min JP_+ distribution in the **Pretagged** sample: the points are data, the solid histogram is the $W/Z/t\bar{t}/Diboson$+QCD background estimate. In the region min $JP_+ \leq 0.05$ we see 11 data events. This is consistent with our total Standard Model expectation of 14.5 ± 4.2. We check that the kinematic distributions in the min $JP_+ \leq 0.05$ sample are consistent with our SM expectations. Fig. 8.2 shows the N_J and the $\not{E}_T$ distributions; Fig. 8.3 shows the jet E_T distributions; and Fig. 8.4 shows the $\Delta\Phi$ distributions. All of these distributions are consistent with our SM expectations. Note that the QCD distributions are derived using the negative mistag matrix method described in Sec. 6.1 and <u>not</u> from our QCD MC sample.

172

Sample	N_{exp}
$W^{\pm}(\rightarrow e^{\pm}\nu_e)+ \geq 2$ jets	$0.3 \pm 0.3 \pm 0.1$
$W^{\pm}(\rightarrow \mu^{\pm}\nu_{\mu})+ \geq 2$ jets	$0.9 \pm 0.5 \pm 0.3$
$W^{\pm}(\rightarrow \tau^{\pm}\nu_{\tau})+ \geq 1$ jets	$7.6 \pm 1.6 \pm 2.2$
$Z^0(\rightarrow \nu\bar{\nu})+ \geq 2$ jets	$1.2 \pm 0.4 \pm 0.4$
$t\bar{t}$	$0.7 \pm 0.2 \pm 0.4$
$Diboson$ (WW, WZ, ZZ)	$0.4 \pm 0.1 \pm 0.1$
Total $W/Z/t\bar{t}/Diboson$ bkg	$11.1 \pm 1.8 \pm 3.3$
Total QCD bkg	3.4 ± 1.7
Total Expected	14.5 ± 4.2
Total Observed	11

Table 8.1: The number of expected background events for the min $JP_+ \leq 0.05$ sample. The first error is statistical, the second is systematic.

173

Figure 8.1: The min JP_+ distribution in the **Pretagged** sample.

174
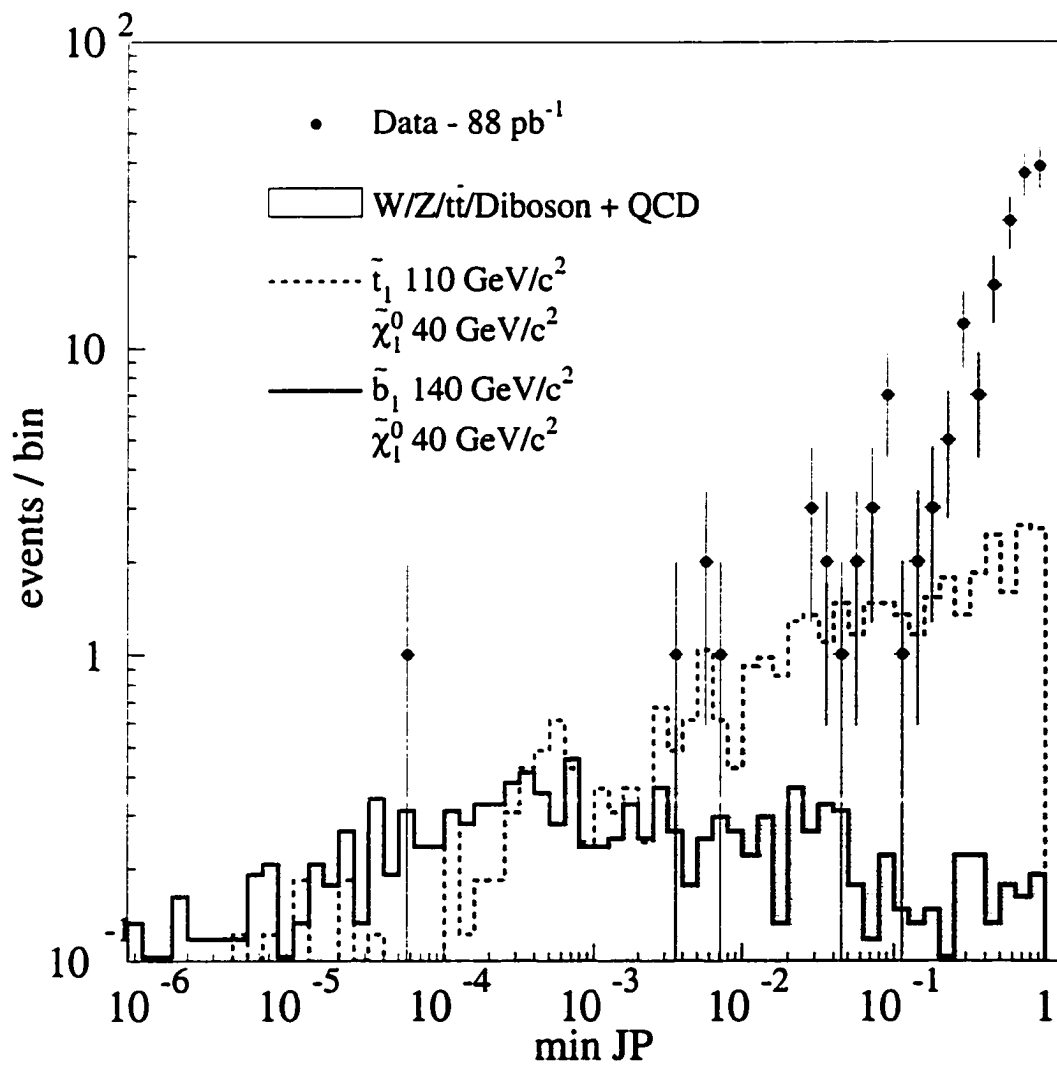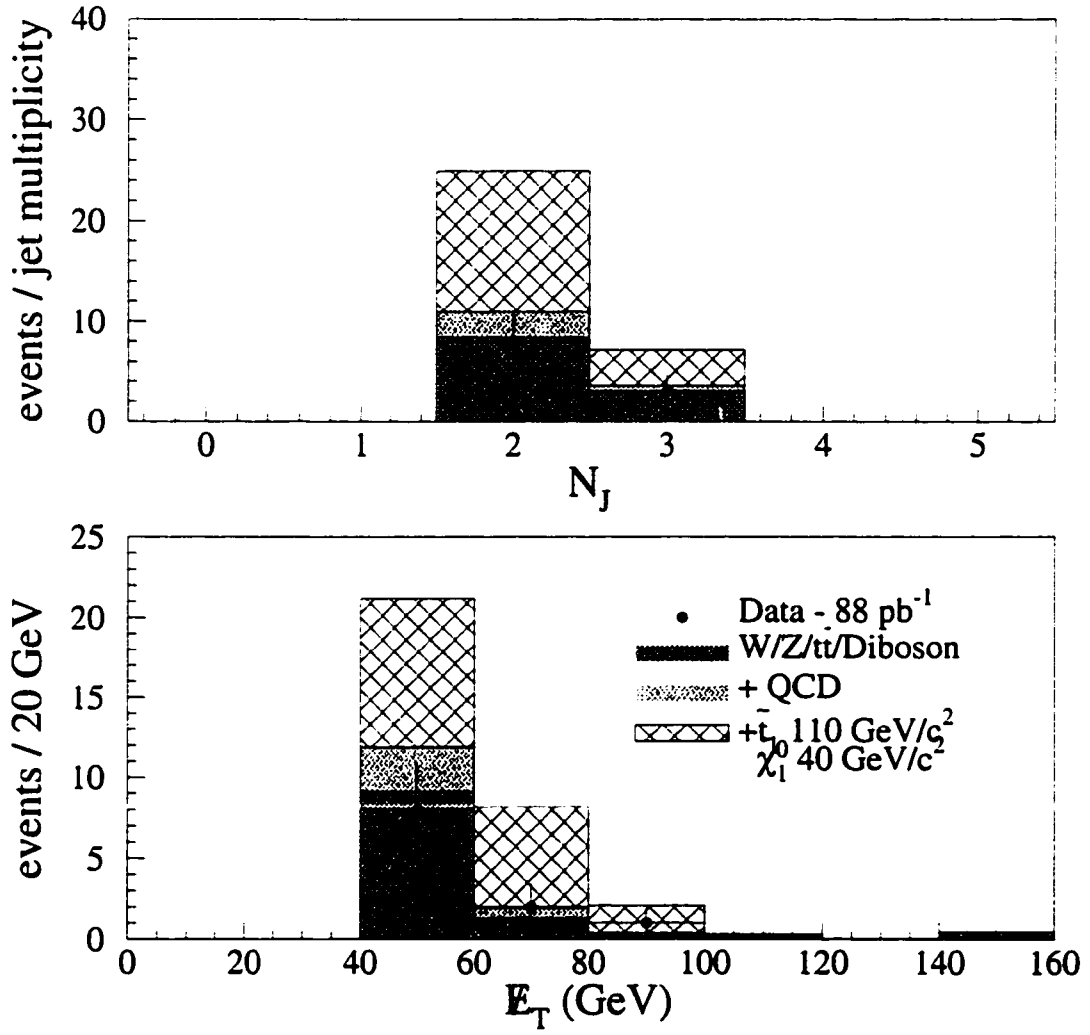
Figure 8.2: Kinematic distributions for events in the min $JP_+ \leq 0.05$ sample. The $\tilde{t}_1\tilde{t}_1$ sample has $M_{\tilde{t}_1} = 110$ GeV/c^2 and $m_{\tilde{\chi}_1^0} = 40$ GeV/c^2.

175
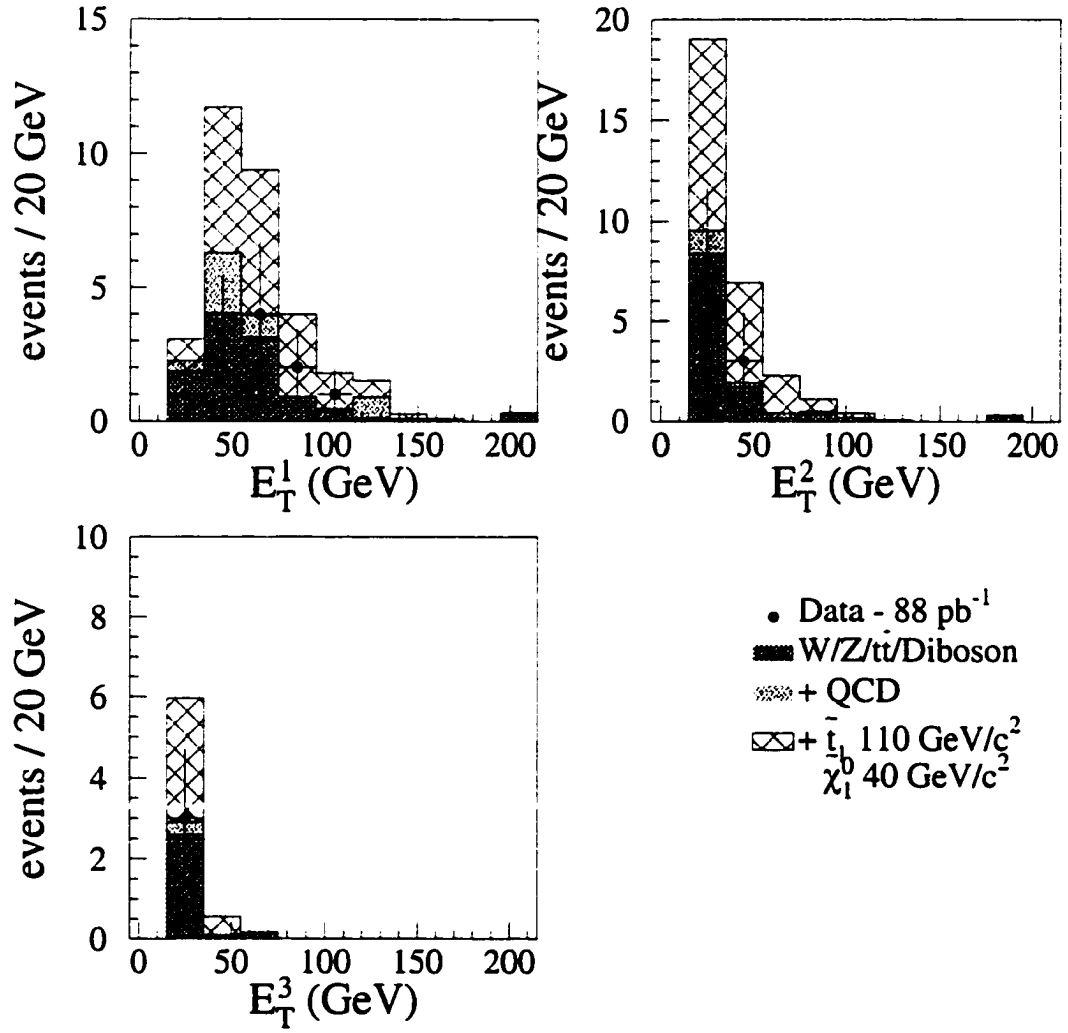
Figure 8.3: Kinematic distributions for events in the min $JP_+ \leq 0.05$ sample. The $\tilde{t}_1\bar{\tilde{t}}_1$ sample has $M_{\tilde{t}_1} = 110$ GeV/c^2 and $m_{\tilde{\chi}_1^0} = 40$ GeV/c^2.

176

Figure 8.4: Kinematic distributions for events in the min $JP_+ \leq 0.05$ sample. The $\tilde{t}_1\bar{\tilde{t}}_1$ sample has $M_{\tilde{t}_1} = 110$ GeV/c^2 and $m_{\tilde{\chi}_1^0} = 40$ GeV/c^2.

177

8.2   min $JP_+ \leq 0.01$

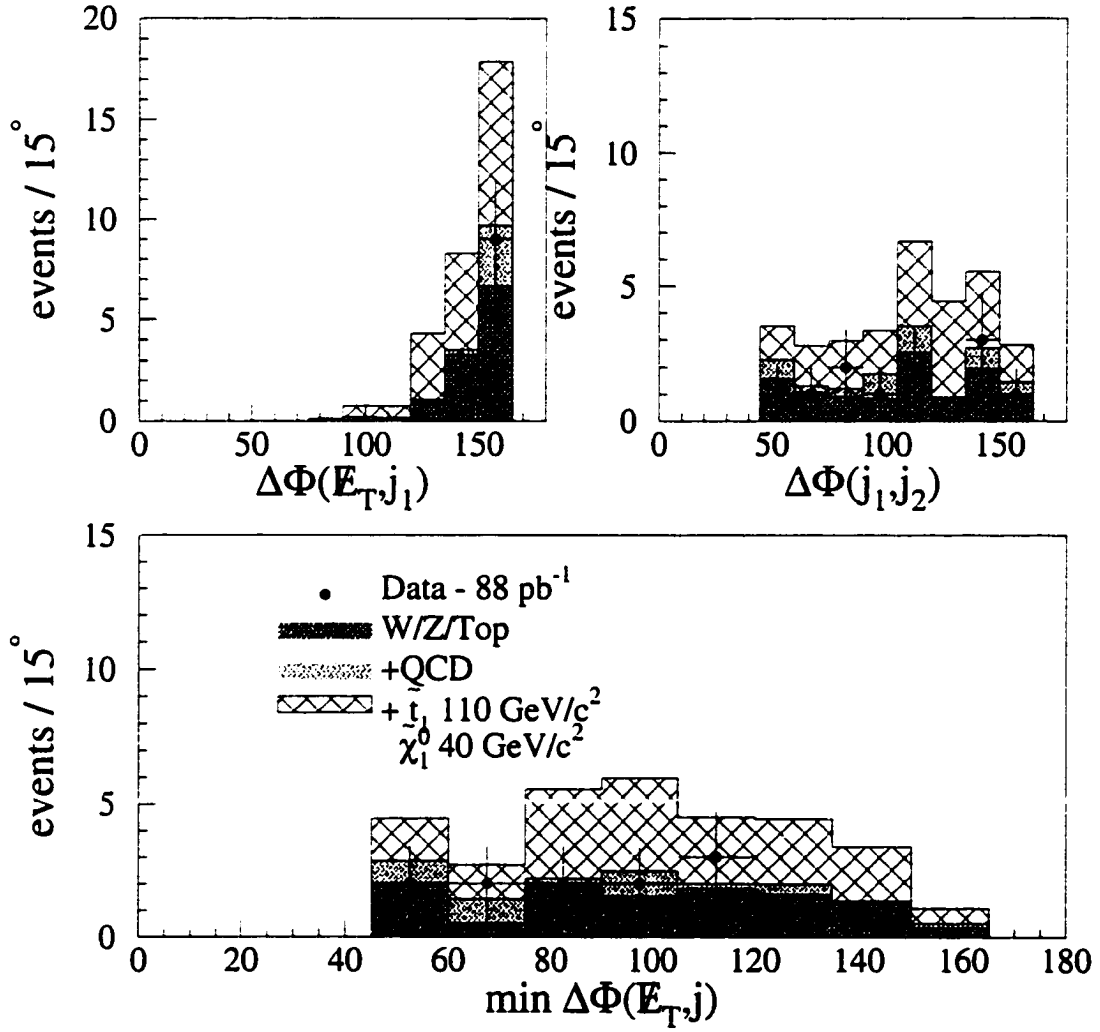In the region min $JP_+ \leq 0.01$ we see 5 data events. This is consistent with our total Standard Model expectation of 5.8 ± 1.8. We check that the kinematic distributions in the min $JP_+ \leq 0.01$ sample are consistent with our SM expectations. Fig. 8.5 shows N_J and the $\not{E}_T$ distributions; Fig. 8.6 shows the jet E_T distributions; and Fig. 8.7 shows the $\Delta\Phi$ distributions. All of these distributions are consistent with our SM expectations. Note that the QCD distributions are derived using the negative mistag matrix method described in Sec. 6.2 and <u>not</u> from our QCD MC sample.

8.3   95% C.L. Method

We do not see an excess of events in our *tagged* samples. We therefore set a 95% C.L. limit using a background-subtraction method [13]. For each point $(M_{\tilde{q}}, M_{\tilde{\chi}_1^0})$ we generate 75K of the following 'pseudo-experiments'. We smear (using a Gaussian distribution) the calculated number of background events and the estimated number of signal events by their respective total uncertainties. We then fluctuate these estimates independently using a Poisson distribution. We reject all pseudo-experiments where the fluctuated number of background events exceeds the number of events observed in the data. We set a 95% C.L. limit by excluding all $(M_{\tilde{q}}, M_{\tilde{\chi}_1^0})$ points when the sum of fluctuated signal and background events exceeds the number of events observed in the data 95% of the time.

We use bilinear interpolation to estimate the acceptance for $(M_{\tilde{q}}, M_{\tilde{\chi}_1^0})$ points where no MC is generated. To determine the uncertainty at an interpolated point, we increase the acceptance of our grid points by $+1\sigma$ and re-calculate the acceptance for the interpolated point. The uncertainty is taken as the difference between these

178

Sample	N_{exp}
$W^{\pm}(\to \tau^{\pm}\nu_{\tau})+ \geq 1$ jets	$3.0 \pm 1.0 \pm 0.9$
$Z^{0}(\to \nu\bar{\nu})+ \geq 2$ jets	$0.8 \pm 0.3 \pm 0.2$
$t\bar{t}$	$0.5 \pm 0.2 \pm 0.2$
$Diboson$ (WW, WZ, ZZ)	$0.2 \pm 0.1 \pm 0.1$
Total$W/Z/t\bar{t}/Diboson$ bkg	$4.5 \pm 1.1 \pm 1.2$
Total QCD bkg	1.3 ± 0.7
Total Expected	5.8 ± 1.8
Total Observed	5

Table 8.2: The number of expected background events for the min $JP_{+} \leq 0.01$ sample. The first error is statistical, the second systematic.

179
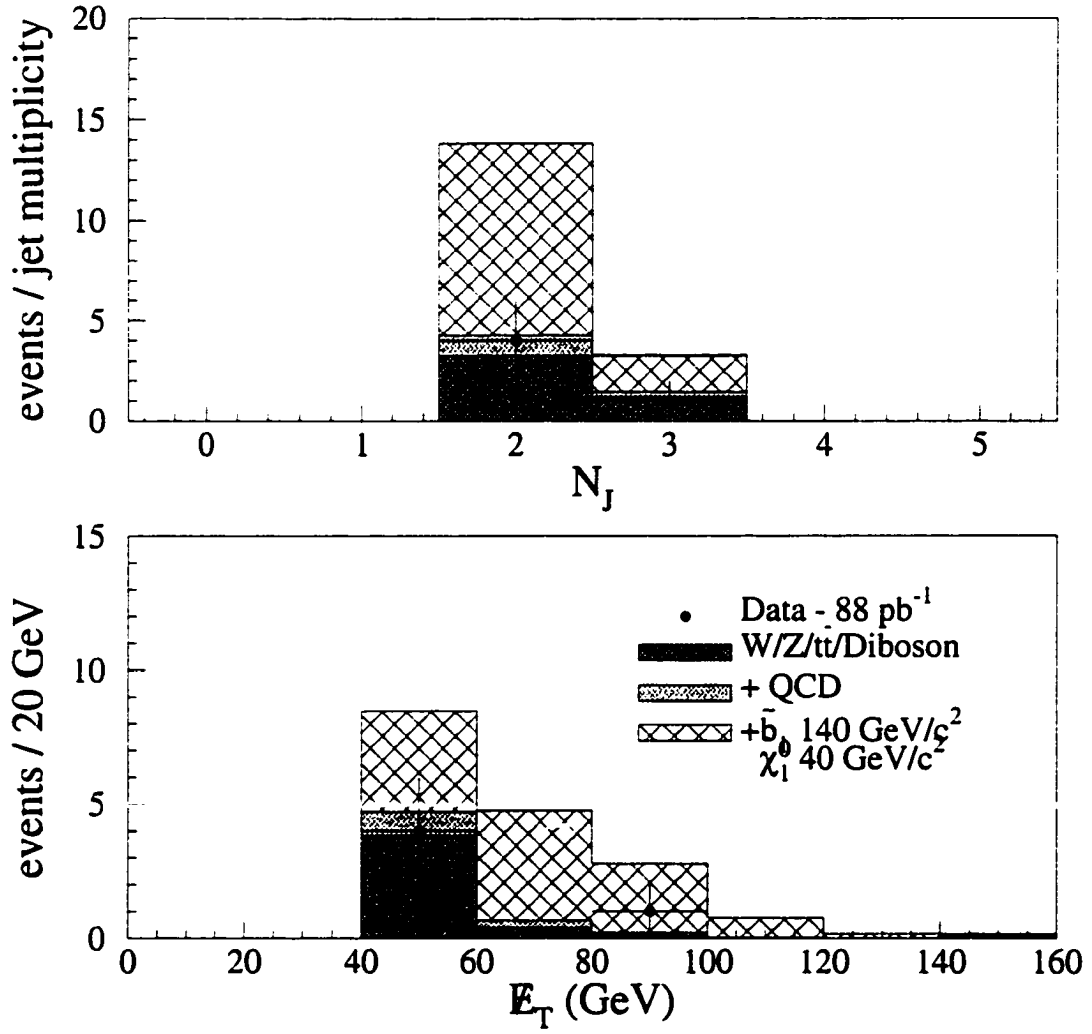
Figure 8.5: Kinematic distributions for events in the min $JP_+ \leq 0.01$ sample. The $\tilde{b}_1\bar{\tilde{b}}_1$ sample has $M_{\tilde{b}_1} = 110$ GeV/c^2 and $M_{\tilde{\chi}_1^0} = 40$ GeV/c^2.

180

Figure 8.6: Kinematic distributions for events in the min $JP_+ \leq 0.01$ sample. The $\tilde{b}_1\bar{\tilde{b}}_1$ sample has $M_{\tilde{b}_1} = 110$ GeV/c^2 and $M_{\tilde{\chi}_1^0} = 40$ GeV/c^2.
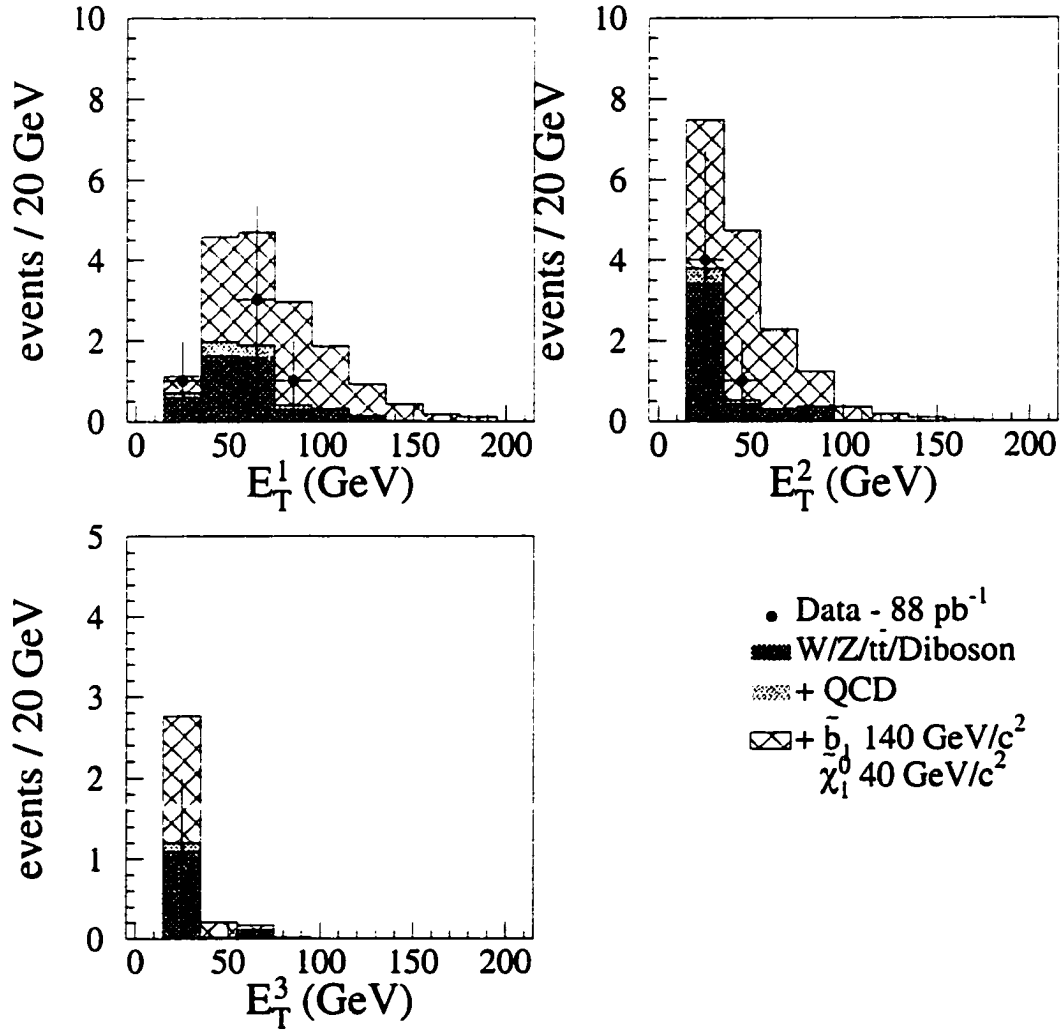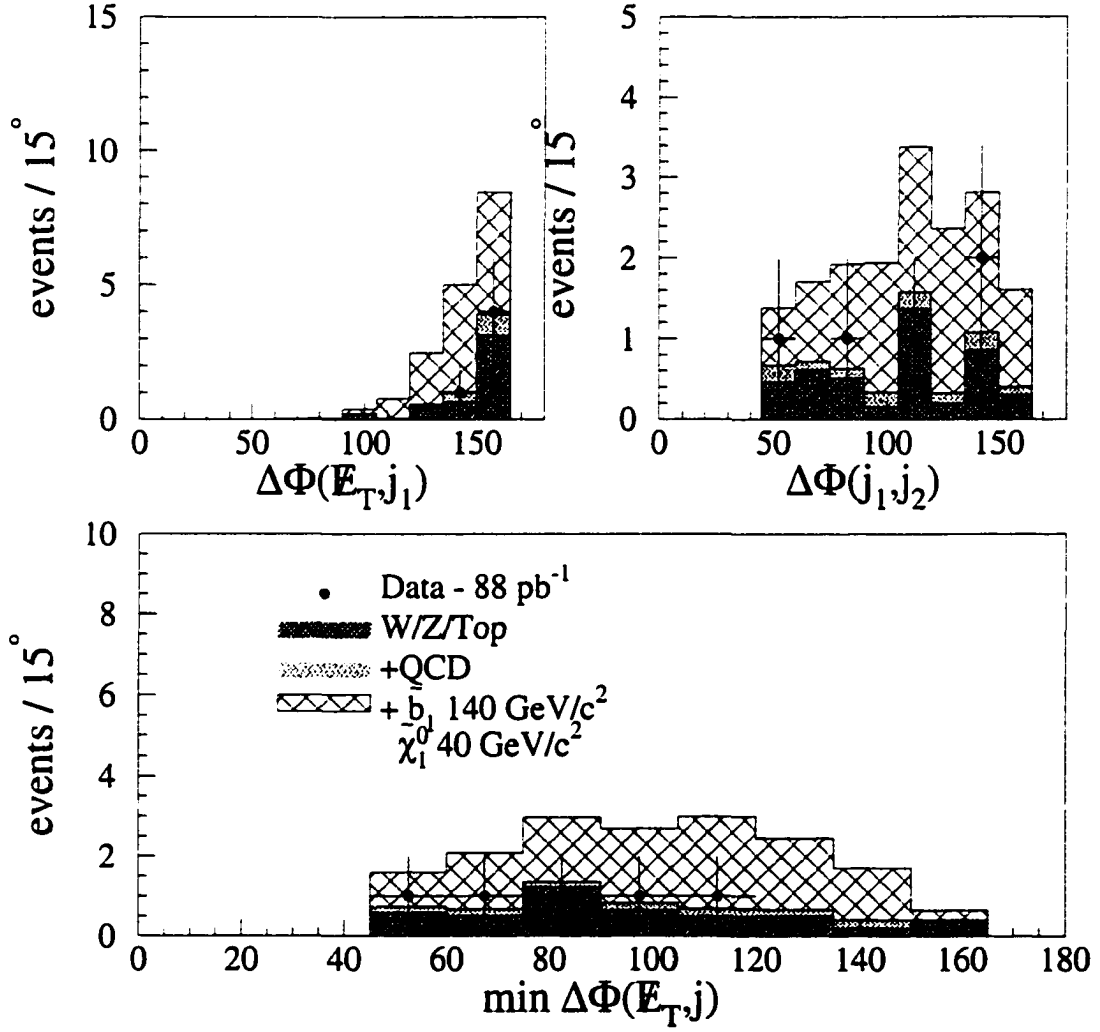
181

Figure 8.7: Kinematic distributions for events in the min $JP_+ \leq 0.01$ sample. The $\tilde{b}_1\bar{\tilde{b}}_1$ sample has $M_{\tilde{b}_1} = 110$ GeV/c^2 and $M_{\tilde{\chi}_1^0} = 40$ GeV/c^2.

182

2 interpolated acceptances.

8.4 Stop limit

Table 8.3 shows the total acceptance for our $\tilde{t}_1\bar{\tilde{t}}_1$ MC samples. We use these acceptances and our background estimate of 14.5 ± 4.2 to set a 95% CL limit. This is shown in Figure 8.8. We only set a limit in the region where the $\tilde{t}_1 \longrightarrow c\tilde{\chi}_1^0$ decay is dominant. This is the region to the left of the line $M_{\tilde{t}_1} = M_W + M_B + M_{\tilde{\chi}_1^0}$. The region to the right is dominated by the decay $\tilde{t}_1 \longrightarrow b\tilde{\chi}_1^+$ to which we are not sensitive. We superimpose the excluded region from both DØ [51] (the other collider experiment at Fermilab) and ALEPH [89] (one of the four experiments at LEP). We see that this analysis extends the excluded parameter space compared to these experiments. In Figure 8.9, we show the cross section excluded by data versus the theory cross section as a function of $M_{\tilde{t}_1}$ for $M_{\tilde{\chi}_1^0}= 40$ GeV/c^2 and $M_{\tilde{\chi}_1^0}= 50$ GeV/c^2.

8.5 Sbottom Limit

Table 8.4 shows the total acceptance for our $\tilde{b}_1\bar{\tilde{b}}_1$ MC samples. With these acceptances and our background estimate of 5.8 ± 1.8 we set a 95% CL limit. This is shown in Figure 8.10. Unlike the $\tilde{t}_1$ analysis, there is no competing decay in our region of interest. Therefore, we do not have to place any restrictions on our excluded region. We superimpose the excluded region from both DØ [52] (the other collider experiment at Fermilab) and ALEPH [89] (one of the four experiments at LEP). We see that this analysis significantly extends the excluded parameter space compared to these experiments. In Figure 8.11, we show the cross section excluded by data versus the theory cross section as a function of $M_{\tilde{b}_1}$ for $M_{\tilde{\chi}_1^0}= 60$ GeV/c^2 and $M_{\tilde{\chi}_1^0}= 80$ GeV/c^2.

183

$M_{\tilde{t}_1}$	$M_{\tilde{\chi}_1^0}$	acceptance(%)
40	0	0.020 ± 0.01
40	10	0.030 ± 0.02
40	20	0.005 ± 0.01
50	0	0.18 ± 0.04
50	10	0.10 ± 0.03
50	20	0.04 ± 0.02
50	30	0.03 ± 0.02
60	20	0.20 ± 0.05
60	30	0.07 ± 0.03
60	40	0.04 ± 0.02
70	20	0.79 ± 0.09
70	30	0.30 ± 0.06
70	40	0.16 ± 0.04
70	50	0.04 ± 0.02
80	30	1.03 ± 0.10
80	40	0.49 ± 0.07
80	50	0.15 ± 0.04

$M_{\tilde{t}_1}$	$M_{\tilde{\chi}_1^0}$	acceptance(%)
90	30	1.53 ± 0.12
90	40	1.14 ± 0.11
90	50	0.69 ± 0.08
100	20	2.78 ± 0.16
100	30	2.39 ± 0.15
100	40	2.12 ± 0.14
100	50	1.30 ± 0.11
110	30	3.18 ± 0.18
110	40	2.87 ± 0.17
110	50	2.07 ± 0.14
120	30	3.57 ± 0.19
120	40	3.26 ± 0.18
120	50	3.32 ± 0.18
130	30	3.67 ± 0.19
130	40	3.75 ± 0.19
130	50	4.08 ± 0.20

Table 8.3: Total acceptance for stop after all requirements. The jet probability requirement is min $JP_+ \leq 0.05$. Note that the degradation due to multiple interactions (see Sec. 7.1.4) is not included.
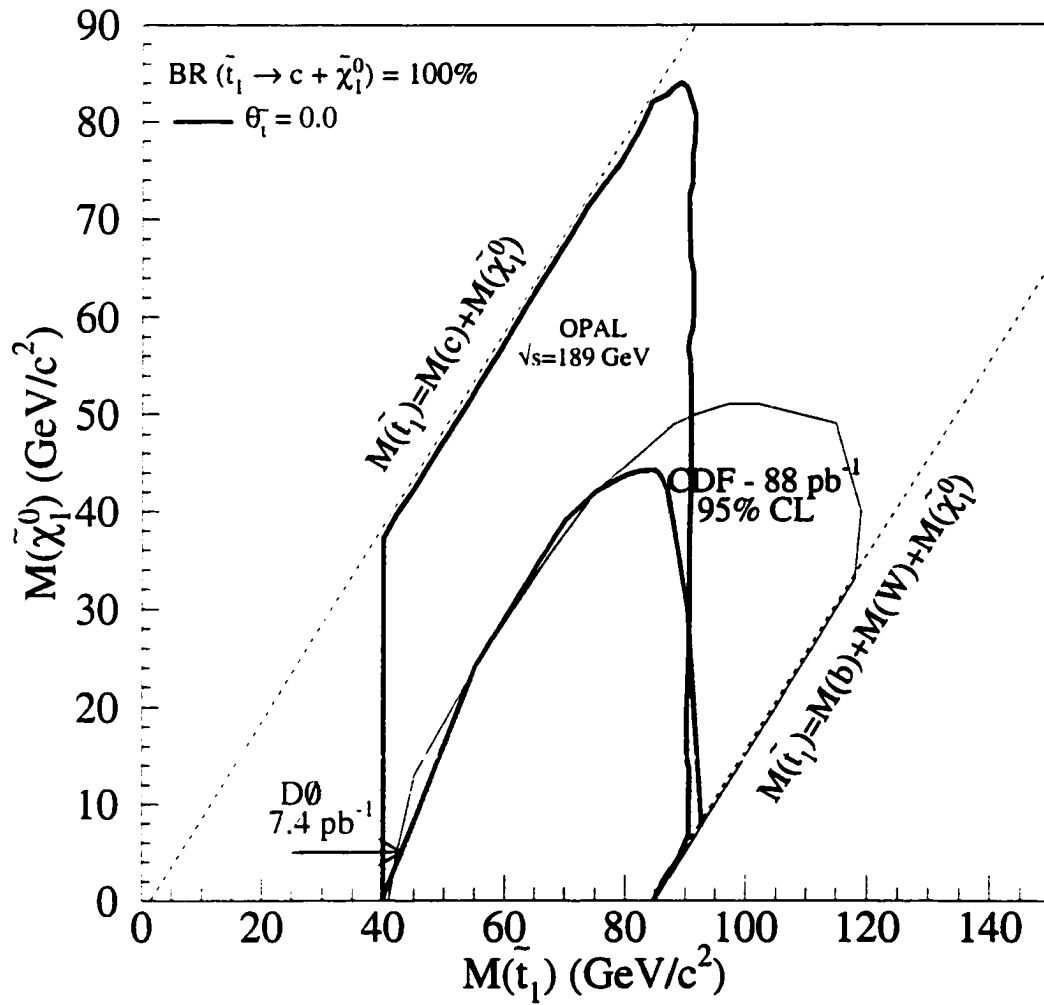
184

Figure 8.8: 95% C.L. limit for $\tilde{t}_1 \longrightarrow c\tilde{\chi}_1^0$. Also show are the limits from DØ [51] and OPAL [89].

185

Figure 8.9: Theory cross section versus cross section excluded by data. The lower data curve corresponds to $M_{\tilde{\chi}_1^0} = 40$ GeV/c^2 and the upper data curve corresponds to $M_{\tilde{\chi}_1^0} = 50$ GeV/c^2. The dotted theoretical curve is the Leading Order (LO) cross section using the program PROSPINO from [42]. The dashed theoretical curve is the Next-to-Leading Order (NLO) cross section using the program PROSPINO with the QCD renormalization scale (μ) set to $m_{\tilde{t}_1}$. We use the CTEQ 3L parton distribution function (PDF) for the LO cross section and the CTEQ 3M PDF for the NLO cross section [84].

186
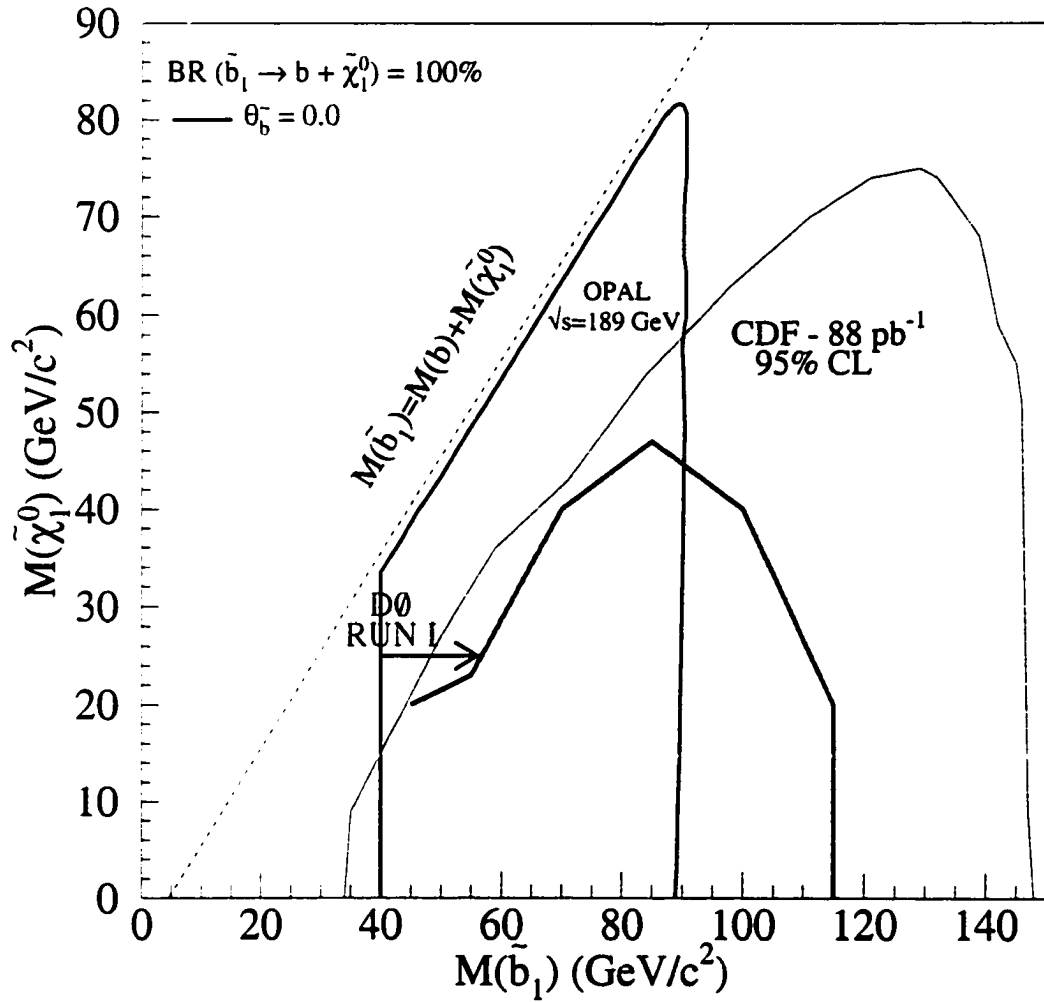
Figure 8.10: 95% C.L. limit for $\bar{b}_1 \longrightarrow b\tilde{\chi}_1^0$. Also show are the limits from DØ [52] and OPAL [89].
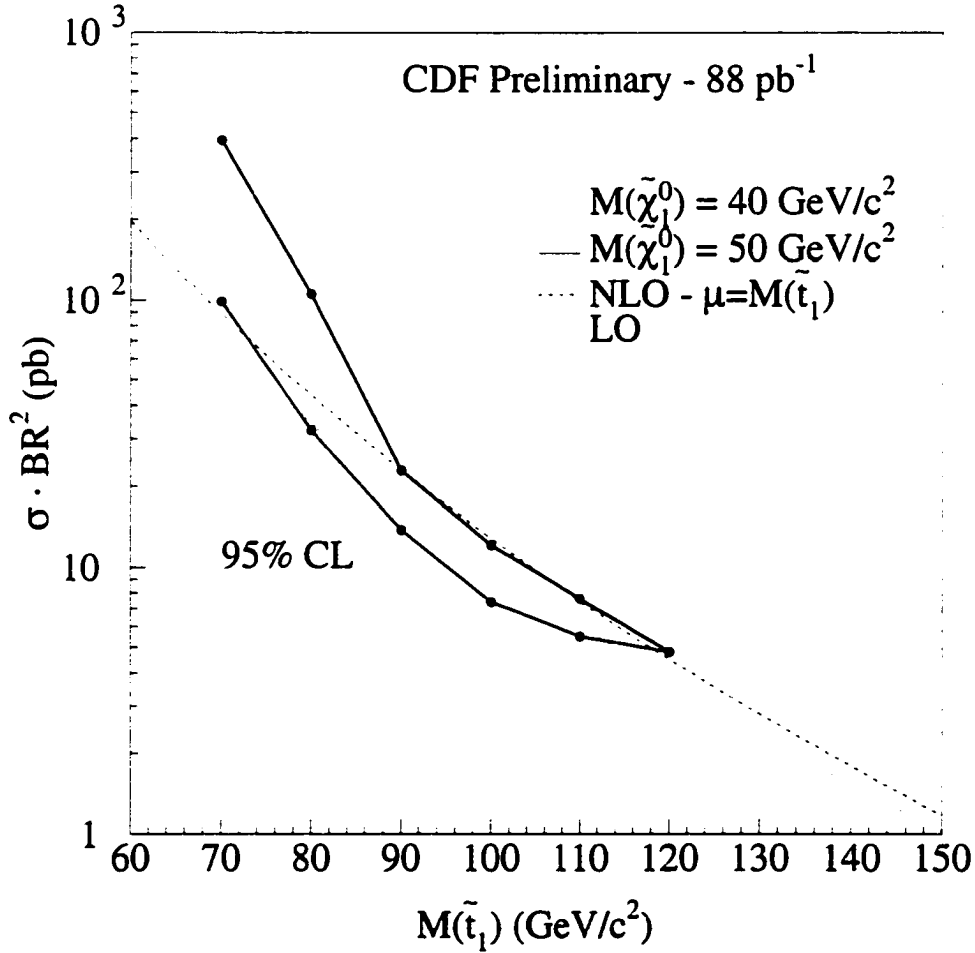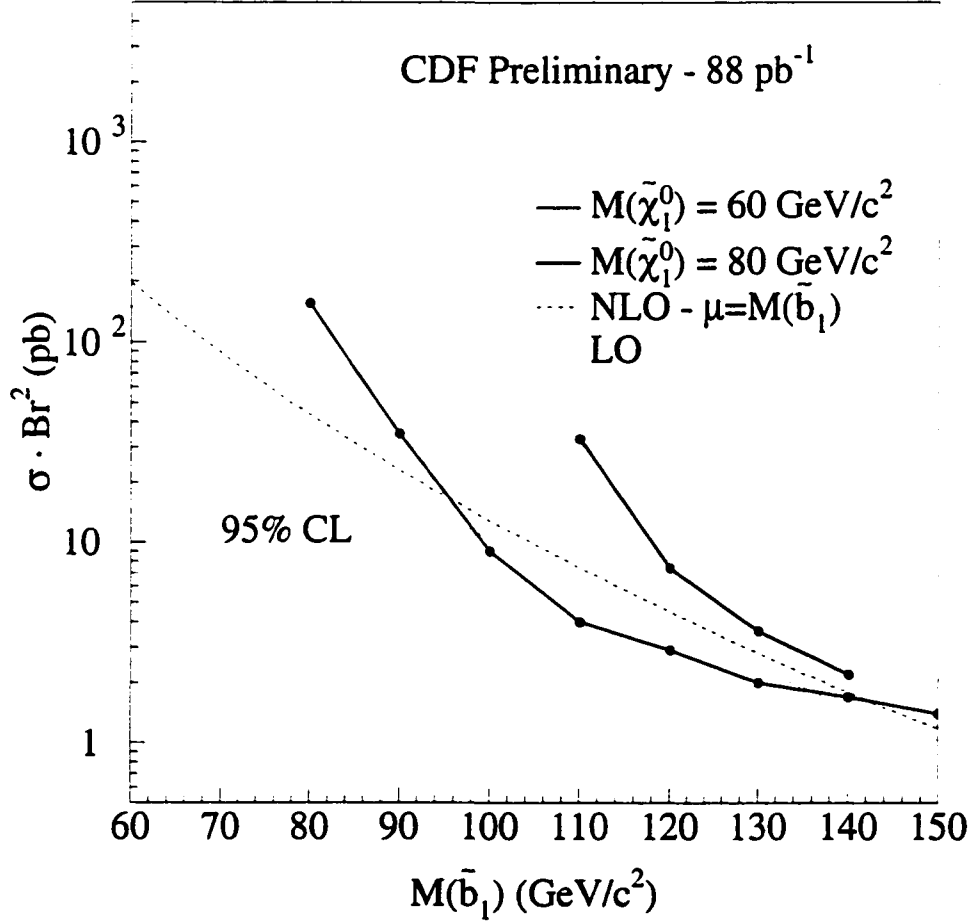
Figure 8.11: Theory cross section versus cross section excluded by data. The lower data curve corresponds to $M_{\tilde{\chi}_1^0} = 60$ GeV/c^2 and the upper data curve corresponds to $M_{\tilde{\chi}_1^0} = 80$ GeV/c^2. The dotted theoretical curve is the Leading Order (LO) cross section using the program PROSPINO from [42]. The dashed theoretical curve is the Next-to-Leading Order (NLO) cross section using the program PROSPINO with the QCD renormalization scale (μ) set to $m_{\tilde{t}_1}$. We use the CTEQ 3L parton distribution function (PDF) for the LO cross section and the CTEQ 3M PDF for the NLO cross section [84].

188

$M_{\tilde{b}_1}$	$M_{\tilde{\chi}_1^0}$	acceptance(%)	$M_{\tilde{b}_1}$	$M_{\tilde{\chi}_1^0}$	acceptance(%)
30	0	0.02 ± 0.01	80	40	0.62 ± 0.08
30	10	0.02 ± 0.01	80	50	0.19 ± 0.04
40	0	0.05 ± 0.02	80	60	0.07 ± 0.03
40	10	0.045 ± 0.015	90	40	1.92 ± 0.14
40	20	0.035 ± 0.013	90	50	0.91 ± 0.10
50	0	0.19 ± 0.04	90	60	0.31 ± 0.06
50	10	0.13 ± 0.04	90	70	0.08 ± 0.03
50	20	0.15 ± 0.04	100	40	3.27 ± 0.18
50	30	0.01 ± 0.01	100	50	2.32 ± 0.15
50	40	0.01 ± 0.01	100	60	1.22 ± 0.11
60	20	0.30 ± 0.06	100	70	0.36 ± 0.06
60	30	0.14 ± 0.04	110	30	5.28 ± 0.22
60	40	0.06 ± 0.02	110	40	4.67 ± 0.21
70	30	0.64 ± 0.08	110	60	2.68 ± 0.16
70	40	0.16 ± 0.04	110	70	1.42 ± 0.12
70	50	0.06 ± 0.02	110	80	0.33 ± 0.06
80	30	1.59 ± 0.13	120	30	6.37 ± 0.24

Table 8.4: Total acceptance for sbottom after all requirements. The jet probability requirement is min $JP_+ \leq 0.01$. Note that the degradation due to multiple interactions (see Sec. 7.1.4) is not included.

189

$M_{\tilde{b}_1}$	$M_{\tilde{\chi}_1^0}$	acceptance(%)	$M_{\tilde{b}_1}$	$M_{\tilde{\chi}_1^0}$	acceptance(%)
120	40	5.64 ± 0.23	140	0	8.48 ± 0.28
120	50	4.92 ± 0.22	140	10	8.12 ± 0.27
120	60	3.75 ± 0.19	140	40	7.74 ± 0.27
120	70	3.01 ± 0.17	140	50	7.33 ± 0.26
120	80	1.47 ± 0.12	140	60	6.39 ± 0.25
130	40	6.86 ± 0.25	140	70	5.57 ± 0.23
130	50	5.90 ± 0.24	150	0	8.71 ± 0.28
130	60	5.39 ± 0.23	150	10	8.35 ± 0.28
130	70	4.49 ± 0.21	150	50	8.15 ± 0.27
130	80	3.07 ± 0.17	150	60	7.92 ± 0.27

Table 8.5: Total acceptance for sbottom after all requirements. The jet probability requirement is min $JP_+ \leq 0.01$. Note that the degradation due to multiple interactions (see Sec. 7.1.4) is not included.

190

Chapter 9

Conclusion

This analysis searches for evidence of two new particles, $\tilde{t}_1$ and $\tilde{b}_1$, predicted by Supersymmetry. We select events with 2 or 3 high-E_T jets, large $\not{E}_T$ and no high-p_T lepton(s). We improve our discovery potential by requiring that at least one jet be inconsistent with coming from the primary vertex. For the $\tilde{t}_1$ analysis, we require at least one jet with $JP_+ \leq 0.05$. For the $\tilde{b}_1$ analysis, we require at least one jet with $JP_+ \leq 0.01$. We find no excess of events above our expectations from Standard Model processes in either case. We observe 11 events and expect 14.5 ± 4.2 events from SM processes when we require min $JP_+ \leq 0.05$. We observe 5 events and expect 5.8 ± 1.8 events from SM processes when we require min $JP_+ \leq 0.01$. Further, the kinematics of the data events in both these samples are consistent with our SM predictions. Therefore, we set a 95% C.L. in the $(M_{\tilde{q}}, M_{\tilde{\chi}_1^0})$ parameter space (see Fig. 8.8 and Fig. 8.10). The maximum excluded $\tilde{t}_1$ mass is 119 GeV/c^2 which corresponds to $M_{\tilde{\chi}_1^0} = 40$ GeV/c^2. The maximum excluded $\tilde{b}_1$ mass is 148 GeV/c^2 which corresponds to a massless $\tilde{\chi}_0^0$.

191

9.1 Run II prospects

Until the Large Hadron Collider (LHC) is completed, the Tevatron will be the preeminent place to search for $\tilde{t}_1$ and $\tilde{b}_1$. In 2000, the Tevatron and CDF will complete their upgrades and begin a new data taking run called Run II. The important changes for these analyses are:

1. The center of mass energy will increase from $\sqrt{s} = 1.8$ TeV to $\sqrt{s} = 2$ TeV. This will increase the scalar squark cross section by 40%.

2. The Main Ring has been dismantled and its function will be taken over by the Main Injector. This means that the detector background due to Main Ring splash (see Sec. 4.4) will no longer exist in Run II.

3. The SVX tracking will be substantially improved providing roughly a factor of 2 increase in tagging efficiency.

Fig. 9.1 shows the expected 3 sigma sensitivity for stop discovery in the $\tilde{t}_1 \longrightarrow c\tilde{\chi}_1^0$ channel in the $(M_{\tilde{t}_1}, M_{\tilde{\chi}_1^0})$ parameter space for three different Run II integrated luminosity values. Fig. 9.2 shows the same plot for the $\tilde{b}_1 \longrightarrow b\tilde{\chi}_1^0$ channel.

9.2 Other Searches

The signature of large $\not{E}_T$ 2 high-E_T jets (with at least one jet due to heavy flavor quarks), and no high-p_T lepton(s) is not unique to Supersymmetry. There are other sources of new physics which have this signature. We now describe two other searches that use the results of the $\tilde{t}_1/\tilde{b}_1$ analyses to place limits on new physics.
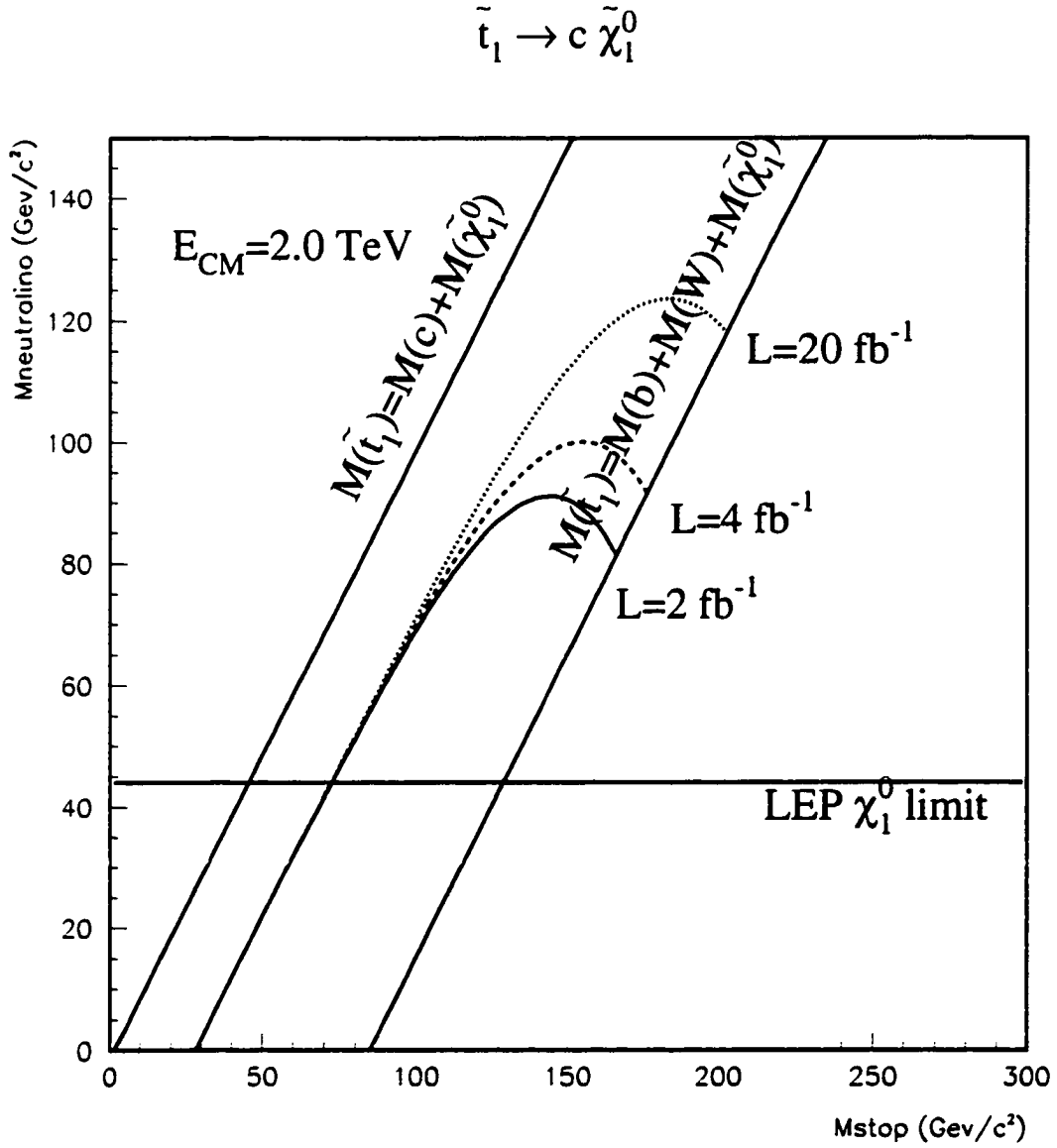
192

$$\tilde{t}_1 \rightarrow c \, \tilde{\chi}_1^0$$

Figure 9.1: Expected discovery potential in Run II of the $\tilde{t}_1 \longrightarrow c\tilde{\chi}_1^0$ search for 3 different values of the total integrated luminosity.
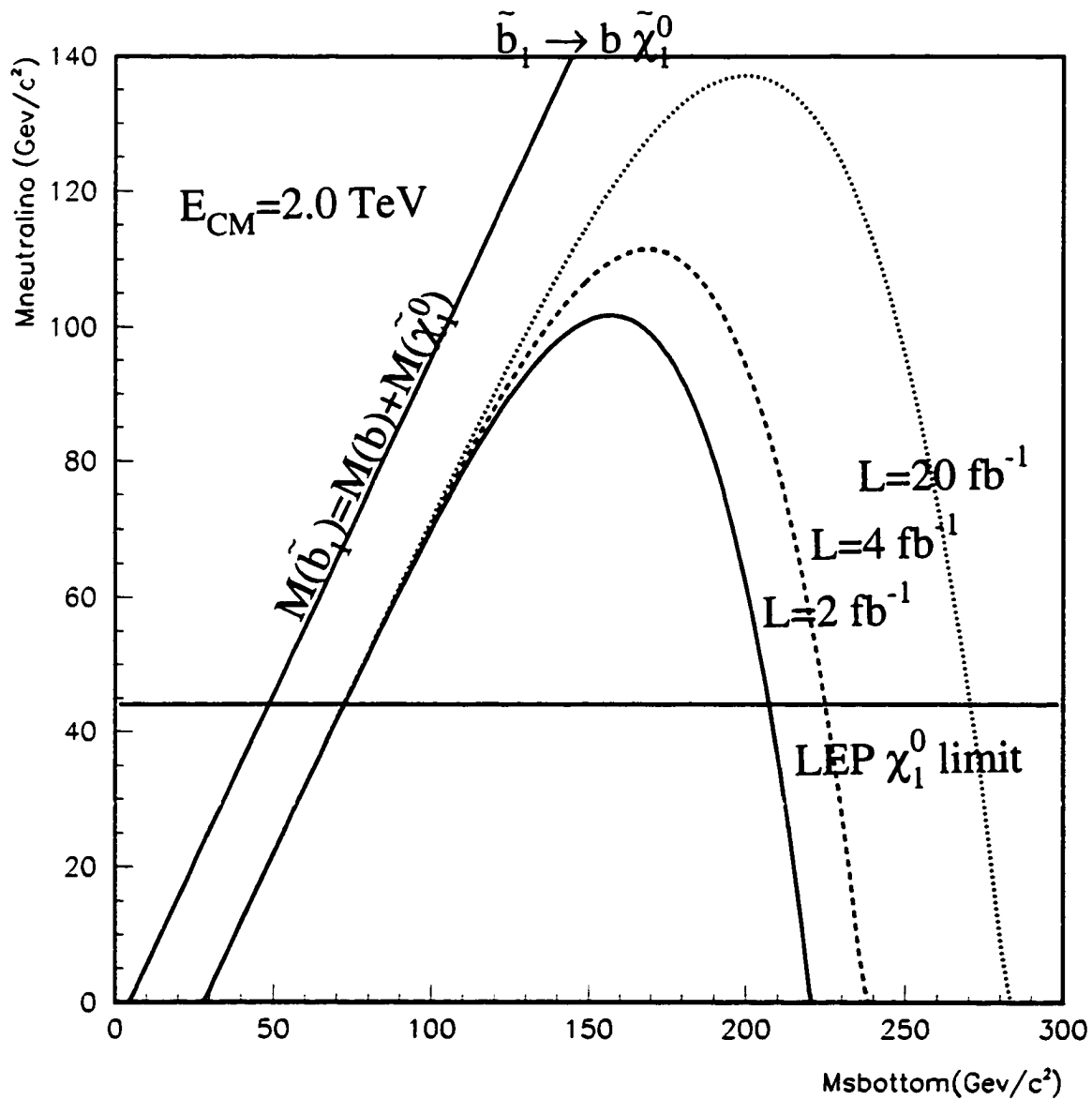
193

Figure 9.2: Expected discovery potential in Run II of the $\tilde{b}_1 \longrightarrow b\tilde{\chi}_1^0$ search for 3 different values of the total integrated luminosity.
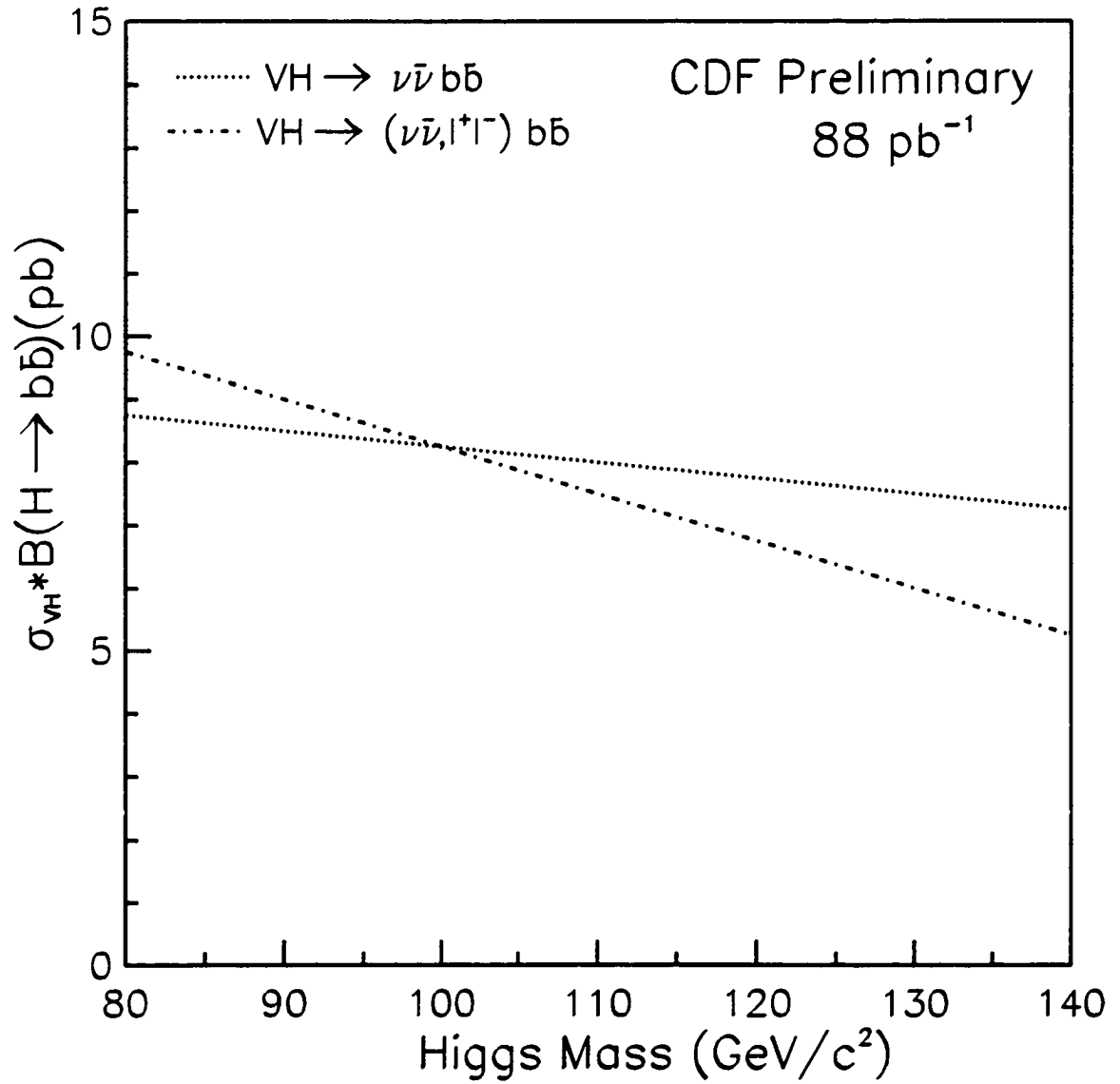
194

Figure 9.3: $\sigma \cdot B$ excluded by data at the 95% C.L. The dotted line is the limit for the $\nu\bar{\nu}b\bar{b}$ search and the dot-dashed line is the limit for the $\nu\bar{\nu}b\bar{b}$ search combined with the $l^+l^-b\bar{b}$ search.

195

9.2.1 Higgs search

One production method for the Standard Model Higgs boson (see Sec. 1.3) at the Tevatron is $p\bar{p} \to ZH^0 \to (\nu\bar{\nu})(b\bar{b})$. This topology is exactly the same as the $\tilde{b}_1\bar{\tilde{b}}_1$ search. Starting from the sample **FILT2** sample, we apply many of the same kinematic requirements [90]. One requirement that is not applied is the soft jet veto. Instead, we require the presence of two heavy flavor jets. The first jet must be tagged by SECVTX [7] while the second tag can be tagged by either SECVTX , $JP_+ \leq 0.05$, or the Soft Lepton Tagger (SLT) [65]. The SLT tagger looks for a low-p_T lepton (electron or muon) associated to a jet coming from the semi-leptonic decay of the b quark. A likelihood analysis is performed on the invariant mass distribution of the two tagged jets. Based on this analysis, we set a 95% C.L. limit on the $p\bar{p} \to ZH^0$ cross section as a function of the Higgs mass (M_{H^0}). This is shown in Fig. 9.3. Also shown in Fig. 9.3 is the combination of the $ZH^0 \to \nu\bar{\nu}b\bar{b}$ search with the $ZH^0 \to l^+l^-b\bar{b}$ search ($l = e/\mu$).

9.2.2 Leptoquark

Leptoquarks (LQ) are new particles, predicted by many Grand Unified Theories (GUT's), which have both lepton and baryon numbers [23–29]. This allows LQ's to mediate the decay of leptons into baryons and vice-versa. The interactions between leptons, quarks, and LQ's can be characterized by an effective lagrangian with the most general dimensionless and $SU(3) \times SU(2) \times U(1)$ invariant couplings [91]. At the Tevatron, LQ's are produced in pairs. When the LQ decays to a quark and a neutrino, the signal topology is 2 jets plus $\not{E}_T$, and no high-p_T lepton. It can be shown [92] that our **Pretagged** selection is also efficient for the LQ analysis. We

196

only consider the case where the LQ decays to a neutrino and a heavy flavor quark $(= c/b)$ [1].

For 2nd and 3rd generation LQ's, we can use our heavy flavor tagger. For the 2nd generation LQ, it can be shown [92] that min $JP_+ \leq 0.05$ is the optimal selection. For the 3nd generation LQ, it can be shown [92] that min $JP_+ \leq 0.01$ is the optimal selection. Therefore, we can use the background numbers from the stop/sbottom analysis for the $2^{nd}/3^{rd}$ generation LQ respectively. In Fig. 9.4 and Fig. 9.5 we plot the cross section excluded at the 95% C.L. versus the theory cross section from several models as a function of the LQ mass.

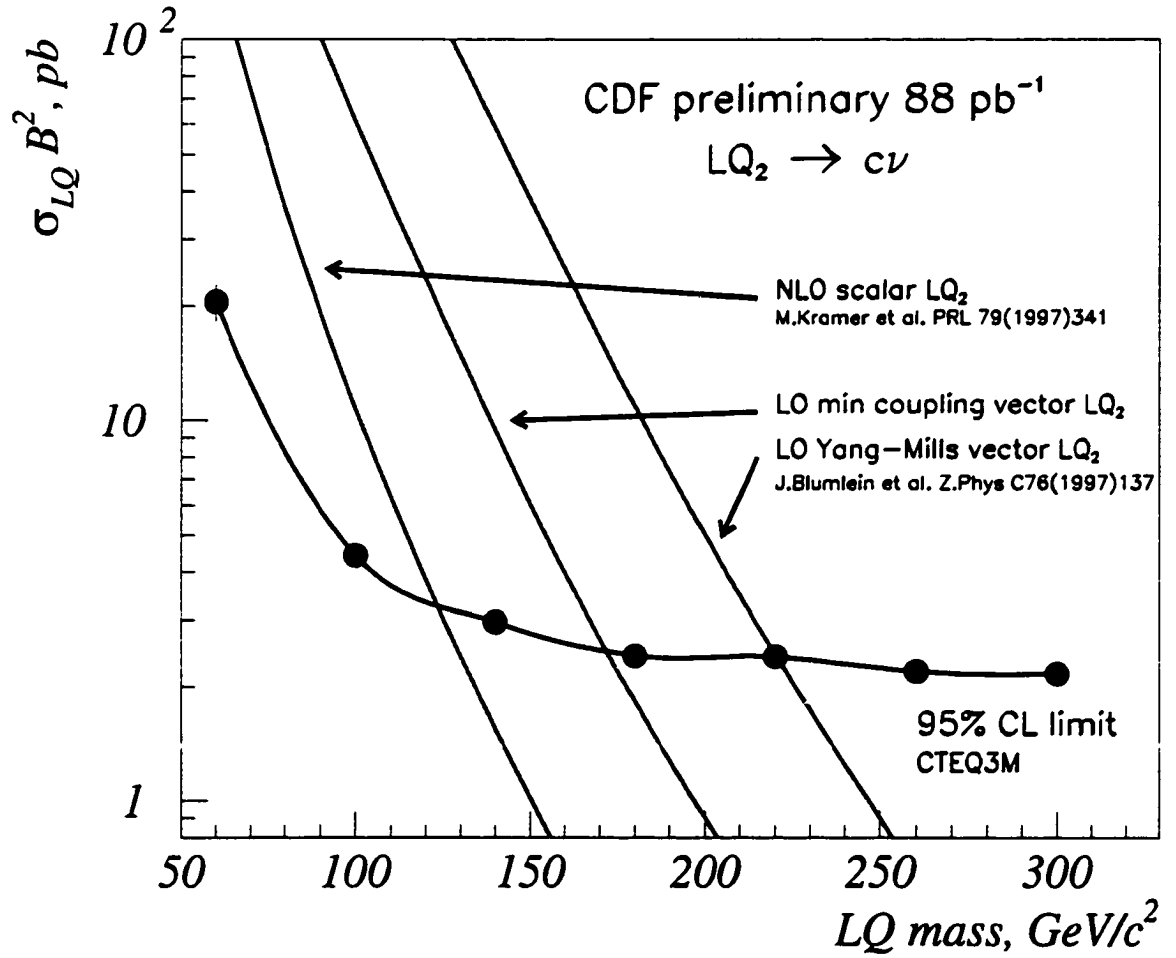[1]We call these LQ's the $2^{nd}/3^{rd}$ generation LQ (LQ_2/LQ_3) respectively.

197

Figure 9.4: $\sigma \cdot B^2$ for LQ_2 pair production excluded by data (points) at the 95% C.L. Also shown are the theoretical predictions (solid lines) for several different models.
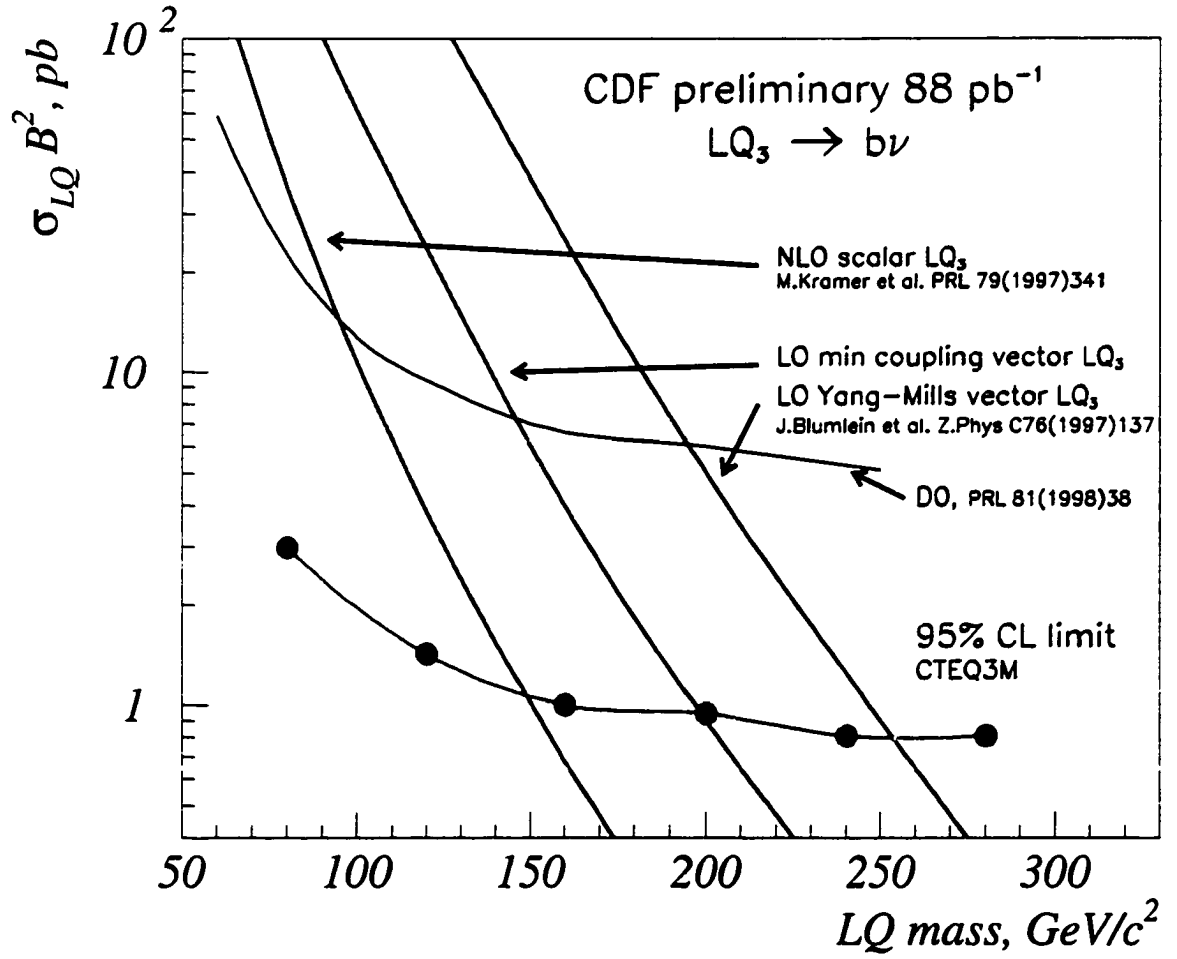
198

Figure 9.5: $\sigma \cdot B^2$ for LQ_3 pair production excluded by data (points) at the 95% C.L. Also shown are the theoretical predictions (solid lines) for several different models. The results from D∅ are also shown [93].

Appendix A

IETA-IPHI tables

ABSOLUTE ETA range	TOWE IETA (negative/positive ETA)
0-0.1308	42/43
0.1308-0.2595	41/44
0.2595-0.3841	40/45
0.3841-0.5033	39/46
0.5033-0.6163	38/47
0.6163-0.7226	37/48
0.7226-0.8225	36/49
0.8225-0.9160	35/50
0.9160-1.0036	34/51
1.0036-1.1000	33/52
1.1000-1.2000	32/53

200

Bibliography

[1] E. Rutherford, Phil. Mag. **21**, 669 (1911).

[2] C. D. Anderson, Science **76**, 238 (1932).

[3] G. Arnison *et al.*, Phys. Lett. **B122**, 103 (1983).

[4] G. Arnison *et al.*, Phys. Lett. **126B**, 398 (1983).

[5] M. Banner *et al.*, Phys. Lett. **122B**, 322 (1983).

[6] M. Banner *et al.*, Phys. Lett. **122B**, 476 (1983).

[7] F. Abe *et al.*, Phys. Rev. Lett. **74**, 2626 (1995).

[8] S. Abachi *et al.*, Phys. Rev. Lett. **74**, 2632 (1995).

[9] V. Barger and R. J. N. Phillips, in *Collider Physics*, Vol. 71 of *Frontiers in Physics*, edited by D. Pines (Addison–Wesley, Redwood City, USA, 1987).

[10] C. Quigg, in *Gauge Theories of the Strong, Weak and Electromagnetic Interactions*, Vol. 56 of *Frontiers In Physics*, edited by D. Pines (Addison–Wesley, Redwood City, USA, 1983).

[11] I. J. R. Aitchison and A. J. G. Hey, in *Gauge Theories in Particle Physics. A Practical Introduction, Graduate Student Series in Physics*, 2nd ed., edited by D. Brewer (Adam Hilger, Bristol, UK, 1989).

[12] Y. Fukuda *et al.*, Phys. Rev. Lett. **81**, 1562 (1998).

[13] C. Caso *et al.*, Eur. Phys. J. **C3**, 1 (1998).

[14] H. Goldstein, *Classical Mechanics, Addison-Wesley Series in Physics*, 2nd ed. (Addison-Wesley Pub. Co., Reading, Mass, 1980).

[15] M. E. Peskin and D. V. Schroeder, *An Introduction to Quantum Field Theory* (Addison-Wesley Pub. Co., Reading, Mass., 1995).

[16] E. Noether, Nachr. Ges. Wiss. Göttingen **2**, 235 (1918).

[17] J. Erler and P. Langacker, *Status of the Standard Model*, hep-ph/9809352, (1998).

[18] T. Kinoshita and W. B. Lindquist, Phys. Rev. Lett. **47**, 1573 (1981).

[19] P. Langacker and M. xing Luo, Phys. Rev. **D44**, 817 (1991).

[20] S. F. King, Rept. Prog. Phys. **58**, 263 (1995).

[21] L. Susskind, Phys. Rev. **D20**, 2619 (1979).

[22] S. Weinberg, Phys. Rev. **D19**, 1277 (1979).

[23] J. C. Pati and A. Salam, Phys. Rev. **D8**, 1240 (1973).

[24] J. C. Pati and A. Salam, Phys. Rev. Lett. **31**, 661 (1973).

[25] J. C. Pati and A. Salam, Phys. Rev. **D10**, 275 (1974).

[26] H. Georgi and S. L. Glashow, Phys. Rev. Lett. **32**, 438 (1974).

[27] B. Schrempp and F. Schrempp, Phys. Lett. **153B**, 101 (1985).

[28] E. Farhi and L. Susskind, Phys. Rept. **74**, 277 (1981).

[29] J. L. Hewett and T. G. Rizzo, Phys. Rept. **183**, 193 (1989).

[30] M. B. Green and J. H. Schwarz, Phys. Lett. **149B**, 117 (1984).

[31] D. J. Gross, J. A. Harvey, E. Martinec, and R. Rohm, Phys. Rev. Lett. **54**, 502 (1985).

[32] P. Candelas, G. T. Horowitz, A. Strominger, and E. Witten, Nucl. Phys. **B258**, 46 (1985).

[33] H. P. Nilles, Phys. Rept. **110**, 1 (1984).

[34] H. E. Haber and G. L. Kane, Phys. Rept. **117**, 75 (1985).

[35] S. P. Martin, A Supersymmetry primer, hep-ph/9709356, (1997).

[36] M. Drees, Pramana **51**, 87 (1998).

[37] P. F. Smith and J. R. J. Bennett, Nucl. Phys. **B149**, 525 (1979).

[38] J. Ellis *et al.*, Nucl. Phys. **B238**, 453 (1984).

[39] K. Inoue, A. Kakuto, H. Komatsu, and S. Takeshita, Prog. Theor. Phys. **68**, 927 (1982).

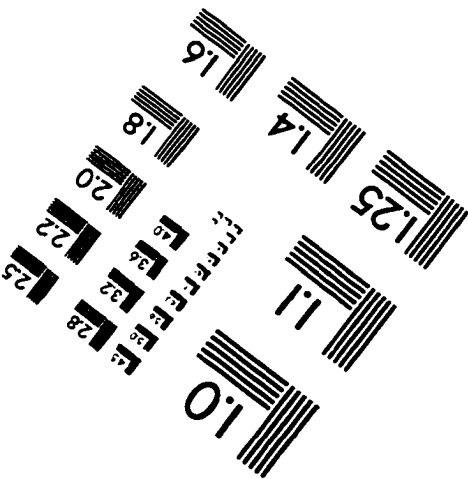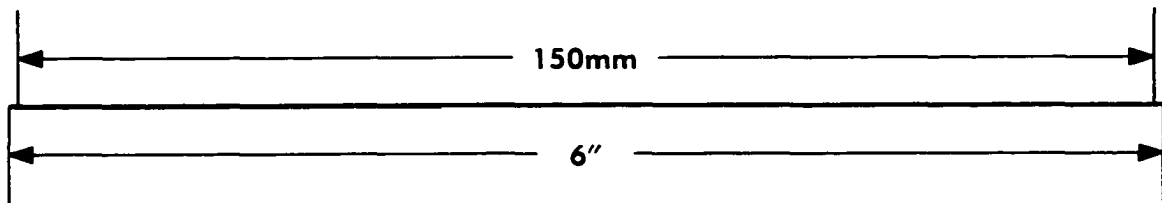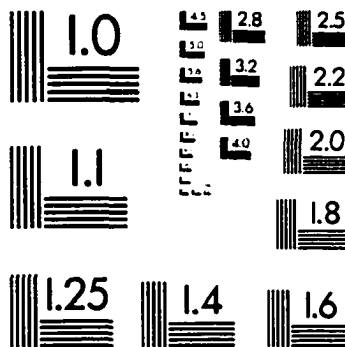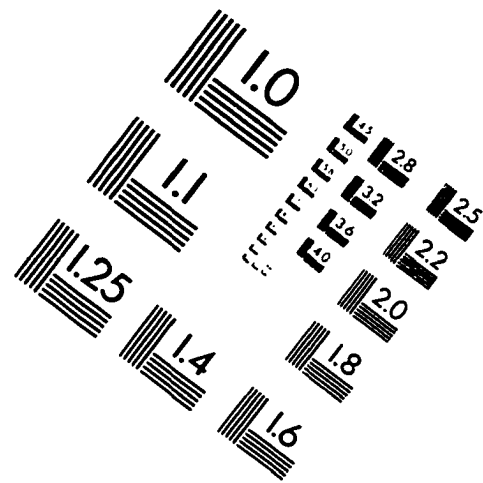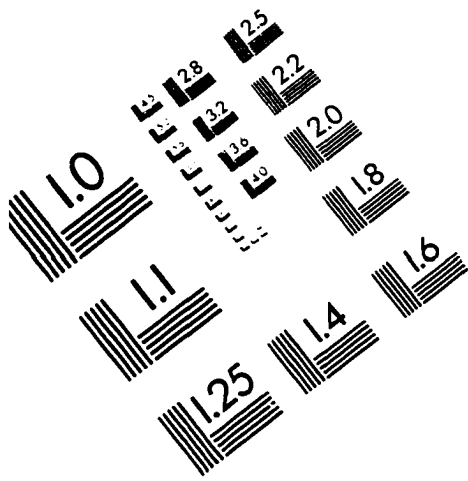[40] K. Inoue, A. Kakuto, H. Komatsu, and S. Takeshita, Prog. Theor. Phys. **71**, 413 (1984).

[41] N. K. Falck, Z. Phys. **C30**, 247 (1986).

[42] W. Beenakker *et al.*, Nucl. Phys. **B515**, 3 (1998).

[43] G. Abbiendi *et al.*, Eur. Phys. J. **C8**, 255 (1999).

[44] F. Abe *et al.*, Phys. Rev. Lett. **76**, 2006 (1996).

[45] G. Abbiendi *et al.*, Search for acoplanar lepton pair events in e+ e- collisions at S**(1/2) = 161-GeV, 172-GeV and 183-GeV, hep-ex/9808036, (1998).

[46] K. ichi Hikasa and M. Kobayashi, Phys. Rev. **D36**, 724 (1987).

[47] W. Porod and T. Wohrmann, Phys. Rev. **D55**, 2907 (1997).

[48] B. Abbott *et al.*, Search for squarks and gluinos in events containing jets and a large imbalance in transverse energy, hep-ex/9902013, (1999).

[49] J. Done *et al.*, *Search for Gluinos and Squarks Using Like–Sign Dilepton Events in Run1A and Run1B*, CDFNOTE 4909 (unpublished).

[50] K. Ackerstaff *et al.*, Eur. Phys. J. **C6**, 225 (1999).

[51] S. Abachi *et al.*, Phys. Rev. Lett. **76**, 2222 (1996).

[52] B. Abbott *et al.*, (1999).

[53] J. Thompson, Introduction to colliding beams at Fermilab, FERMILAB-TM-1909 (unpublished).

[54] M. D. Church and J. P. Marriner, Ann. Rev. Nucl. Part. Sci. **42**, 253 (1993).

[55] D. Amidei *et al.*, Nucl. Instrum. Meth. **A350**, 73 (1994).

[56] S. Cihangir et al., Nucl. Instrum. Meth. **A360**, 137 (1995).

[57] L. S. Groer, Ph.D. thesis, Rutgers University, 1998.

[58] F. Bedeschi et al., Nucl. Instrum. Meth. **A268**, 50 (1988).

[59] L. Balka et al., Nucl. Instrum. Meth. **A267**, 272 (1988).

[60] S. Bertolucci et al., Nucl. Instrum. Meth. **A267**, 301 (1988).

[61] Y. Fukui et al., Nucl. Instr. Meth. **A267**, 280 (1988).

[62] G. Brandenburg et al., Nucl. Instrum. Meth. **A267**, 257 (1988).

[63] S. Cihangir et al., Nucl. Instrum. Meth. **A267**, 249 (1988).

[64] G. Ascoli et al., Nucl. Instrum. Meth. **A268**, 33 (1988).

[65] F. Abe et al., Phys. Rev. **D50**, 2966 (1994).

[66] F. Abe et al., Phys. Rev. **D45**, 1448 (1992).

[67] F. Abe et al., Phys. Rev. **D43**, 2070 (1991).

[68] T. Sjostrand, Comput. Phys. Commun. **82**, 74 (1994).

[69] S. Mrenna, Comput. Phys. Commun. **101**, 232 (1997).

[70] F. A. Berends, H. Kuijf, B. Tausk, and W. T. Giele, Nucl. Phys. **B357**, 32 (1991).

[71] G. Marchesini et al., Herwig version 5.9, hep-ph/9607393, (1996).

[72] H. Baer, F. E. Paige, S. D. Protopopescu, and X. Tata, (1993).

[73] F. Abe *et al.*, Phys. Rev. Lett. **79**, 4760 (1997).

[74] M. Hohlmann *et al.*, *Tau identification in $W \to \tau\nu$ events with TAUFND*, CDFNOTE 3688 (unpublished).

[75] M. Spiropulu *et al.*, *First $\not{E}_T$ Sample for Run1B Squark/Gluino Search* , CDFNOTE 4027 (unpublished).

[76] H. Wenzel, Fitting the Beamline with the SVX, CDFNOTE 1924 (unpublished).

[77] M. Spiropulu *et al.*, *Second $\not{E}_T$ Sample for Run1B Squark/Gluino Search*, CDFNOTE 4143 (unpublished).

[78] F. Abe *et al.*, Phys. Rev. Lett. **79**, 357 (1997).

[79] F. Abe *et al.*, Phys. Rev. **D53**, 1051 (1996).

[80] D. Amidei *et al.*, *Study of the Jet Probability BTAG Algorithm JPBTAG*, CDFNOTE 2091 (unpublished).

[81] G. Unal, *Tracking efficiency and the SVX scale factor*, CDFNOTE 3563 (unpublished).

[82] R. Demina, *Study of Charm Efficiency to Jet Probability Tag*, CDFNOTE 4444 (unpublished).

[83] G. Apollinari *et al.*, *New determination of SECVTX and JPB mistag rates using jet data*, CDFNOTE 3990 (unpublished).

[84] J. Huston *et al.*, Phys. Rev. **D51**, 6139 (1995).

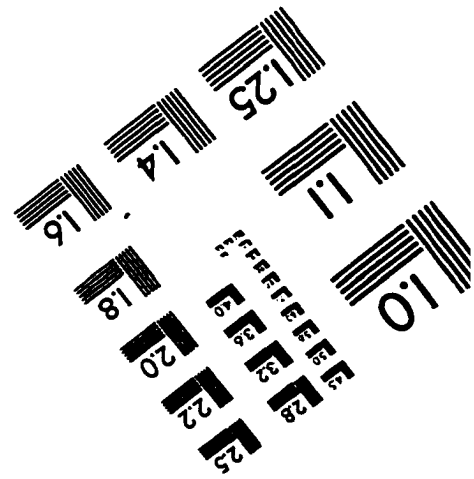[85] A. D. Martin, W. J. Stirling, and R. G. Roberts, Phys. Lett. **B306**, 145 (1993).

[85] A. D. Martin, W. J. Stirling, and R. G. Roberts, Phys. Lett. **B306**, 145 (1993).

[86] S. Aota *et al.*, *Measurement of the top quark mass in the lepton+jets channel*, CDFNOTE 4199 (unpublished).

[87] C. Holck *et al.*, *Search for Direct Production of Scalar Bottom Quark*, CDFNOTE 4870 (unpublished).

[88] D. Cronin-Hennessy and A. Beretvas, *Luminosity at CDF*, CDFNOTE 4721 (unpublished).

[89] G. Abbiendi *et al.*, Phys. Lett. **B456**, 95 (1999).

[90] W. Bokhari *et al.*, *A Search for $ZH \to \nu\nu b\bar{b}$ production*, CDFNOTE 4663 (unpublished).

[91] W. Buchmuller, R. Ruckl, and D. Wyler, Phys. Lett. **191B**, 442 (1987).

[92] A. Nomerotski *et al.*, *Search for 2nd and 3rd generation leptoquarks in MET and HF sample*, CDFNOTE 4877 (unpublished).

[93] B. Abbott *et al.*, Phys. Rev. Lett. **81**, 38 (1998).

IMAGE EVALUATION
TEST TARGET (QA–3)

150mm

6"

Grant of Rights. Author hereby grants to ProQuest the **non-exclusive**, worldwide right to reproduce, distribute, display and transmit the Work (in whole or in part) in such tangible and electronic formats as may be in existence now or developed in the future. Author further grants to ProQuest the right to include the abstract, bibliography and other metadata in the ProQuest Dissertations & Theses database (PQDT) and in ProQuest Dissertation Abstracts International and any successor or related index and/or finding products or services.

ProQuest Publishing Program - Election and Elements. The rights granted above shall be exercised according to the publishing option selected by Author in Section III, Author Options, and subject to the following additional Publishing Program requirements:

- Distribution of the Work. Except as restricted by Author in the publishing option selected, the rights granted by Author automatically include (1) the right to allow sale and distribution of the Work, in whole or in part, by ProQuest and its sales agents and distributors and (2) the right to make the Abstract, bibliographic data and any meta data associated with the Work available to search engines and harvesters.

- Restrictions. ProQuest will use commercially reasonable efforts to restrict the distribution of the Work as provided under the publishing option selected by Author or *as later elected by Author* through direct contact with ProQuest. Such election is subject to Author's Degree Granting Institution Directives. With respect to restrictions requested after submission of the Work, Author acknowledges that ProQuest cannot recall or amend previously distributed versions of the Work.

- Removal of Work from the Program. ProQuest may elect not to distribute the Work if it believes that all necessary rights of third parties have not been secured. Refer to the website http://www.proquest.com/products_umi/dissertations/ for information about copyright and your dissertation or thesis. If Author's degree is rescinded, and/or the degree-granting institution so directs, ProQuest will expunge the Work from its publishing program in accordance with its then current publishing policies.

- Degree Granting Institution Directives. Author is solely responsible for any conflict between policies and directions of Author's degree-granting institution, Author's choice of publishing model, and/or any restriction Author places on the use of the Work. For the avoidance of doubt, ProQuest is not responsible for access to the Work that is provided by Author's degree-granting institution through its library or institutional repository. Author must work directly with Author's degree granting institution to ensure application of any restrictions to access relating to the Work by Author's degree granting institution.

Delivery of the Work. Author shall provide to ProQuest the Work and all necessary supporting documents during the online submission process, according to the Instructions accompanying this agreement.

Rights Verification. Author represents and warrants that Author is the copyright holder of the Work and has obtained all necessary rights to permit ProQuest to reproduce and distribute third party materials contained in any part of the Work, including all necessary licenses for any non-public, third party software necessary to access, display, and run or print the Work. Author is solely responsible and will indemnify ProQuest for any third party claims related to the Work as submitted for publication.

Open Access Publishing Plus
☒ I want the broadest possible dissemination of my work, and I want to provide free global access to the electronic copy of my work via the internet.
☒ I understand that I will not be eligible to receive royalties.

I want major search engines (e.g. Google, Yahoo) to discover my work. Learn more:
http://www.proquest.com/en-US/products/dissertations/google.shtml
☒ Yes
☐ No

Acknowledgment: I have read, understand and agree to this ProQuest Publishing Agreement, including all rights and restrictions included within the publishing option chosen by me as indicated above.

REQUIRED Author's signature _Christopher M Holck_ **Date** 10/21/2017

(Print Name) _Christopher M Holck_

Institution conferring degree _University of Pennsylvania_